

MANTLE CONVECTION, MELT MIGRATION AND THE
GENERATION OF BASALTS AT MID-OCEAN RIDGES

by

MATTHEW JEAN CORDERY

A.B. with Honors, Geophysical Sciences
The College of the University of Chicago
15 June 1985

SUBMITTED TO THE DEPARTMENT OF EARTH, ATMOSPHERIC AND
PLANETARY SCIENCES IN PARTIAL FULFILLMENT OF
THE REQUIREMENTS FOR THE DEGREE OF

DOCTOR OF PHILOSOPHY

at the

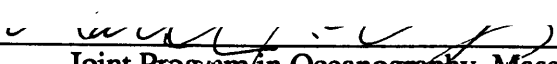
MASSACHUSETTS INSTITUTE OF TECHNOLOGY

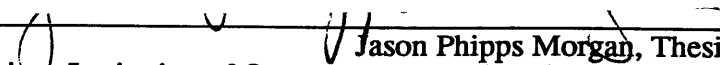
and the

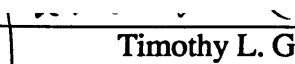
WOODS HOLE OCEANOGRAPHIC INSTITUTION

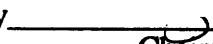
20 May 1991

©Massachusetts Institute of Technology, 1991

Signature of author 
Joint Program in Oceanography, Massachusetts Institute of
Technology and Woods Hole Oceanographic Institution

Certified by 
Jason Phipps Morgan, Thesis Co-Advisor
Scripps Institution of Oceanography, University of California, San Diego

Certified by 
Timothy L. Grove, Thesis Co-Advisor
Massachusetts Institute of Technology

Accepted by 
Chairman, Joint Committee for Marine Geology and Geophysics,
Massachusetts Institute of Technology and Woods Hole Oceanographic Institution

MASSACHUSETTS INSTITUTE
OF TECHNOLOGY
Lindgren WITHDRAWN FROM MIT LIBRARIES Lindgren
MAY 20 1991

MANTLE CONVECTION, MELT MIGRATION AND THE
GENERATION OF BASALTS AT MID-OCEAN RIDGES

by

MATTHEW JEAN CORDERY

Submitted to

the Department of Earth, Atmospheric and Planetary Sciences,
Massachusetts Institute of Technology

and

the Department of Marine Geology and Geophysics
Woods Hole Oceanographic Institution

on 20 May, 1991

in partial fulfillment of the requirements for
the Degree of Doctor of Philosophy

ABSTRACT

In this thesis I develop a thermodynamically self-consistent numerical model of melting, melt migration and mantle flow beneath a mid-ocean ridge. The models I explore consider sub-ridge mantle upwelling to have two components. The plate-spreading divergence of the lithosphere results in an upwelling beneath the ridge axis. Melting-induced density changes also result in a component of upwelling flow. The rate of plate spreading and the nature of the flow field determine the first order temperature structure of the mantle. At some depth, the adiabatically rising mantle crosses its solidus and begins to melt. Loss of latent heat upon melting keeps the mantle temperature on its solidus throughout the melting regime. Melt separates from its host rock and rises to the surface under the influence of buoyancy forces and mantle flow-derived pressure gradients. Advection of heat by the melt carries heat to shallower depths and can result in further melting. Extraction of a basaltic melt from the mantle results in a reduction in the mantle density. Lateral variations in the mantle density due to the finite size of the melting regime result in enhanced upwelling near the ridge axis. This enhanced upwelling results in further melting due to the enhanced advection of thermal energy above the mantle solidus.

The mantle solidus used in this thesis is unique in that it depends not only upon pressure but upon the mantle modal mineralogy and oxide composition as well. I assume explicitly that the mantle mineralogy corresponds to that of a slightly depleted spinel lherzolite defined by the assemblage olivine, orthopyroxene, clinopyroxene, and aluminous spinel. Mantle composition is defined by concentrations of the following oxides: K_2O ,

Na_2O , CaO , FeO , MgO , TiO_2 , SiO_2 , Al_2O_3 . Melt compositions are also defined by these same oxides. Melting is assumed to occur via a fractional mechanism. Melting begins at the pressure where the mantle temperature intersects the solidus and melting ends at the pressure where conductive cooling becomes important or clinopyroxene is lost as a mineral phase. Mantle density is calculated from the proportions of the minerals present and their Fe/Mg ratio.

The effects of heat transport by the melt and of varying the latent heat of melting are isolated by fixing the mantle velocity field to be that due to solely to the spreading of the lithospheric plates. The latent heat of melting causes the mantle temperature to lie along the solidus in accordance with the requirements of thermodynamics. A zero latent heat of melting would result in all of the mantle melting when it reaches a certain depth. A small ($250 \text{ J kg}^{-1} \text{ }^\circ\text{C}^{-1}$) but finite latent heat of melting results in large melt production rates and a melting regime with a finite thickness and melting continues until clinopyroxene is lost as a phase. A more reasonable latent heat ($450 \text{ J kg}^{-1} \text{ }^\circ\text{C}^{-1}$) yields much smaller latent heats of melting because less melting is required for a given amount of energy. As a result, crustal thicknesses are lower for a small latent heat (3.0 vs. 4.7 km) and melting ceases at the pressure where conductive cooling becomes important. Advection of heat by the melt causes melting rates to increase, perhaps substantially depending upon melting rates and the degree to which melt is focussed towards the ridge.

The effects of varying the mantle viscosity, spreading rates and melting-induced buoyancy forces are investigated. Increasing the half-spreading rate from 1 cm yr^{-1} to 8 cm yr^{-1} results in a widening of the melt regime because the depth to which conductive cooling is important becomes shallower. The width over which significant melting occurs, however, is limited by the horizontal distance over which significant vertical mantle flow occurs ($\sim 100 \text{ km}$). The flow field places an physical limit upon the crustal thickness as the spreading rate increases. Again, the minimum depth of melting is defined by the depth at which clinopyroxene is lost as a phase. Melt production rates are determined not only by the advection of heat by the mantle and melt, but by changes in the solidus temperature and its pressure derivative as well.

Melting-induced density changes in the mantle drive convection beneath the ridge. This effect is not important when the half-spreading rate is faster than 4 cm yr^{-1} because viscous stresses dominate the small lateral variations in mantle density. At slow spreading rates (1 cm yr^{-1}), lateral density variations are larger due to the smaller dimensions of the melting regime. For a viscosity of 10^{19} Pa s , the density driven convection is weak resulting in a marked dependence of crustal thickness upon spreading rate. For a viscosity of 10^{18} Pa s , convection is more vigorous at the slowest spreading rate resulting in higher

melting rates. Convection narrows the melting regime at the slow spreading rates but this does not proved an effective mechanism for focussing the melt to the ridge axis, especially at the faster spreading rates where convection is limited. Downwelling in the mantle is extremely limited due to the positive buoyancy of the residual mantle. At this viscosity, the crustal thickness is a constant function of spreading rate. For both viscosities, mantle flow–derived pressure gradients are nominal compared to melt buoyancy forces and the melt rises vertically resulting in broad crustal accretion zones at the surface.

If the mantle viscosity depends upon temperature and pressure then mantle viscosities are high (5×10^{20} Pa s) in the conductive lid overlying the melting regime and low (10^{18} Pa s) within the melting regime itself. The low viscosities in the melting regime allows convection to significantly reduce the spreading rate dependence of crustal thickness. The high viscosity in the conductive lid magnifies pressure gradients in the mantle. It is shown, however, that these enhanced pressure gradients are still an ineffective mechanism for focussing melt to the ridge.

Several geophysical observables (thermal topography, gravity anomalies, seismic travel time) are calculated for each model. For a fixed spreading rate, no detectable differences exist between models with different mantle viscosity parameters. The mantle modal mineralogy is equally homogeneous as is the oxide composition of the aggregate primary melts. This indicates that some parameter other than spreading rate or mantle viscosity structure is responsible for the observed variation in mid–ocean ridge basalt chemistry.

Finally, a model is presented wherein the permeability of the mantle is allowed to be anisotropic. The argument is made that finite strain in the mantle affects the directional permeability of the mantle. If this anisotropy tensor is proportional to the square of the finite strain, then melt can be focussed to the ridge axis regardless of spreading rate.

Thesis co–advisor : Dr. Jason Phipps Morgan
 Title : Professor of Geophysics
 Institute of Geophysics and Planetary Physics
 Scripps Institution of Oceanography
 University of California, San Diego
 La Jolla, California

Thesis co–advisor : Dr. Timothy L. Grove
 Title : Professor of Geology and Geochemistry
 Dept. of Earth, Atmospheric and Planetary Sciences
 Massachusetts Institute of Technology
 Cambridge, Massachusetts

Table of Contents

| | |
|--|----|
| ABSTRACT..... | 2 |
| ACKNOWLEDGEMENTS..... | 8 |
| CHAPTER ONE | |
| INTRODUCTION..... | 13 |
| CHAPTER TWO | |
| THE EFFECTS OF SPREADING RATE AND VARIABLE VISCOSITY ON MANTLE FLOW AND MELT MIGRATION AT MID-OCEAN RIDGES..... | 15 |
| INTRODUCTION..... | 15 |
| Melt Migration and Observations of the Oceanic Crust..... | 15 |
| Broad Melt Zone - Narrow Volcanic Zone Paradox..... | 16 |
| The Effects of Mantle Viscosity..... | 16 |
| The Effects of Buoyancy Forces..... | 19 |
| Parameterizations of Mantle Melting..... | 20 |
| Objectives..... | 21 |
| MODEL DEVELOPMENT..... | 22 |
| Assumptions Regarding Melting and Melt Migration..... | 22 |
| Governing Equations of Momentum, Mass and Energy..... | 26 |
| Parameterization of Melting..... | 30 |
| RESULTS..... | 34 |
| Constant Viscosity - 10^{19} Pa s..... | 34 |
| Constant Viscosity - 10^{18} Pa s..... | 39 |
| Temperature- and Pressure-Dependent Viscosity..... | 40 |
| DISCUSSION..... | 42 |
| Observational Implications..... | 43 |
| Bathymetry..... | 43 |
| Gravity..... | 44 |
| Seismic Wave Travel Time Anomalies..... | 45 |
| Residuum Mineralogy and Aggregate Melt Composition..... | 46 |
| Summary Comments..... | 48 |
| CONCLUSIONS..... | 49 |
| FIGURE CAPTIONS..... | 50 |
| TABLE 2.1 Notation..... | 57 |
| TABLE 2.2 Non-dimensionalization Parameters..... | 59 |
| TABLE 2.3 Experimental Parameters..... | 60 |

| | |
|--|-----|
| TABLE 2.4 Mantle Modal Mineralogy and Oxide Composition..... | 61 |
| TABLE 2.5 Physical Dimensions of Crust and Melting Regime..... | 62 |
| TABLE 2.6 Aggregate Primary Melt Compositions..... | 63 |
| CHAPTER THREE | |
| MELTING AND MANTLE FLOW BENEATH A MID-OCEAN SPREADING CENTER..... | 83 |
| INTRODUCTION..... | 83 |
| MODEL DEVELOPMENT..... | 84 |
| RESULTS..... | 85 |
| The Effect of Latent Heat of Melting..... | 85 |
| The Effect of Advection of Heat via Melt Percolation..... | 86 |
| The Effect of Buoyancy-Drive Flow..... | 87 |
| DISCUSSION..... | 88 |
| CONCLUSIONS..... | 88 |
| FIGURE CAPTIONS..... | 89 |
| TABLE 3.1 Physical Dimensions of Crust and Melting Regime..... | 90 |
| CHAPTER FOUR | |
| ANISOTROPIC PERMEABILITY IN THE OCEANIC UPPER MANTLE AND ITS EFFECT ON THE MIGRATION OF MELT AT MID-OCEAN RIDGES..... | 101 |
| INTRODUCTION..... | 101 |
| Transport of Melt Due to Dynamic Processes in the Mantle..... | 102 |
| Transport of Melt due to Dike Propagation..... | 105 |
| Anisotropy in the Mantle and its Effect upon Melt Migration..... | 107 |
| Objectives..... | 109 |
| MODEL DEVELOPMENT..... | 109 |
| RESULTS..... | 111 |
| DISCUSSION..... | 113 |
| CONCLUSIONS..... | 114 |
| FIGURE CAPTIONS..... | 115 |
| TABLE 4.1 Experimental Parameters..... | 118 |
| TABLE 4.2 Physical Dimensions of Crust and Melting Regime..... | 119 |
| CHAPTER FIVE | |
| CONCLUSIONS..... | 132 |

| | |
|--|-----|
| APPENDIX A | |
| FINITE ELEMENT FORMULATION OF THE GOVERNING EQUATIONS AND THEIR SOLUTION VIA DIGITAL COMPUTERS..... | 138 |
| Introduction..... | 138 |
| The Finite Element Method..... | 139 |
| Table A1..... | 141 |
| The Conjugate Gradient Algorithm..... | 145 |
| Computations on Vector-Concurrent Computers and the Element-By-Element Concept..... | 148 |
| Table A3..... | 152 |
| Discrete Form of the Momentum Equations..... | 152 |
| Discrete Form of the Energy Equations..... | 155 |
| Discrete Form of the Melt Production Rate..... | 159 |
| Discrete Form of the Permeability-Melt Viscosity Ratio Equation..... | 160 |
| Discrete Form of the Advection Equation for Mineralogy and Oxide Composition..... | 165 |
| Discrete Form of the Finite Strain Equation..... | 166 |
| Discrete Form of the Melt Flux Equation..... | 167 |
| FIGURE CAPTIONS..... | 168 |
| TABLE A2 Gaussian Quadrature Rules..... | 170 |
| TABLE A4 Streamline Upwind Advection Matrix..... | 171 |
| BIBLIOGRAPHY..... | 183 |

Acknowledgments

There is no greater desert or wilderness than to be without true friends.

Francis Bacon
Essays, 1612

Any decision we make regarding our lives opens doors to new possibilities and closes those to others. This is no less true with the decision to attend graduate school. Far too often, we complain of what we lose by being graduate students. As we try to compass our way through our own private and self-assumed purgatories, we often lose sight of what we gain. Personally, I have met some of the nicest people. Because this is a scholarly work, I will, perforce, mention my family, my friends, and those people who influenced my academic life. If you find that you are not specifically mentioned here, please do not fret overmuch; whatever particular joys or pains we have shared together are expressed within these pages. The style of my prose and the sustained effort required of me to finish this work are reflections of those people who have shared my life.

First and foremost, I would like to thank my parents, Jean and Carol. To them I am indebted for my laugh, my love, and my particular (some would say peculiar) turn of mind. These are the very wellsprings of my heart and soul; the foundations of what inner strength I possess. To my parents I owe a particular debt of gratitude for allowing me the freedom to compass my own path through life. By degrees, I have learnt the greatness of that gift. They are always there with the necessary words of support and guidance without telling me what to do. Furthermore, by accident or design they raised me in a land of incomparable beauty and spirit. From these, and by sharing them with my family, I have gained something that teaches and sustains and, moreover, a place to call home.

To my thesis advisor, Jason Phipps Morgan, I owe many debts besides the mundanely financial. I only hope that in working together on a scientifically interesting problem we've not completely ruined our future funding opportunities. Throughout all this, you have endured my bouts with frustration, stupidity, and ennui with remarkable equanimity, and praised my occasional glimmers of intelligence (animal and vegetable). Moreover, though, you have been and are my friend. I do not know too many advisors who can be coerced by their students into playing Frisbee on warm summer days or who (try to) teach their students to body surf. I can only hope that I became a better scientist under your guidance. You have constantly reminded me that good science is rigorous, relevant, and simple. Moreover, it needs to be fun to keep it from simply being work. I cannot forget to thank your wife Melanie for her friendship, encouragement and hygiene lessons and your

daughter Ariane for her unbridled enthusiasm and unqualified love. Both have helped to lighten the burden and bring a smile (except the hygiene lessons). By the way, since this is the one part of my thesis you can not edit, I hereby apologize for the prosaic writing style of my acknowledgements.

Tim Grove, my thesis co–advisor, is to be praised for both accepting the responsibility of advisor and for seeing it through to its natural conclusion. His enthusiasm and guidance are greatly appreciated. Few people would be willing to help a wayward geophysicist appreciate some of the subtleties of igneous petrology as well as run the bureaucracy gauntlet on their behalf.

My inexpressible gratitude I offer to Rosamund J. Kinzler for two reasons. First, her thesis formed an important part of my own. Her willingness to teach and answer the same question over and over and over again is greatly appreciated. Second, she is one of those few people whom one meets that is kind, gracious, and possessed of an easy laugh. If I am sorry for one thing, it is that our friendship comes so late in my tenure at MIT. I hope our future work provides opportunities for collaboration for I will surely miss our pleasant and thought–provoking conversations.

We can all name our very best of friends. Those people without whom our lives would acquire an appalling emptiness, an emotional cavity if you will. My very best and most constant of friends is Helen LaCrosse and to her I owe more than I can imagine. Whenever I really hated this place, I could always count on her voice and her friendship to make me feel better; thus girding me for the next day’s battle. At the very least she is a constant source of support, criticism, literature and music. I also must say that our long relationship has been very convenient as well. Not everyone can have their own personal psychoanalyst. Many thanks go to her parents, Thomas and Marjorie LaCrosse, who opened their home to me for holidays and scientific meetings. I will always think kindly of Baltimore because of them.

Paul Filmer has been a blessing as a friend, as a colleague, and as an officemate. Few things on this Earth create a bond between like minds than collusion and guile. Paul’s inherently eclectic nature, reasonably decent education, and mind for interesting trivia made him both distracting and distractible. Perhaps, now that I am gone, he will finish his thesis. If he does not, I just know he will eventually suffer some ineffable fate in this feminist, politically–correct liberal wasteland. I do not want that on my conscience. While I am on the subject of office mates, I must mention Jack Jemsek, who was my office mate at McLean Lab during my WHOI years (under the “aegis” of Richard P. Von Herzen). Jack graciously opened his home to me when I needed a place to stay while trying to literally decipher my own data. The many pizza runs, the few bar–hopping adventures,

and the general late-night schmoozing were greatly appreciated by someone who had no solid roots at either Woods Hole or Cambridge.

Frank M. Richter of the University of Chicago is to be praised for defining my interests in geophysics and concurrently admonished for unknowingly leading me into a cursedly difficult field with an appropriate number of difficult personalities. How things might be different if I had not attended his departmental seminar that day...

I owe particular debts to Mr. Roy Timmreck and Mr. Tom Tunley; the former being my high-school chemistry teacher and the latter being my high-school geology teacher. I thank Roy for having the desire and ability to draw out of me whatever latent intellectual talents I possessed and for giving me free reign of the chemistry lab. He lit the fuse, thus I suppose I should confess to nearly, and somewhat appropriately, turning him, his lab, his students, and a good portion of the school into a brief, but impressive, pyrotechnic display on several occasions. I thank him for the ability to be my friend, my mentor and a good running partner. My lasting thanks go to Tom for giving me something really interesting to do for the rest of my life. I thank him for going the extra mile by encouraging me to pursue something I still consider to be worthwhile. Lucky for you, Tom, that rocks aren't noted for being terribly combustible.

My thanks go to two friends, Maria Harris and Karen Harpp, for their brilliance, their infectious humor, and their hearts of gold. My association with them can, at the very least, be termed providential.

Steve Recca is to be commended for being the most personable incarnation of evil that I have ever met.

Dave McCormick's personality is, in some ways, frighteningly similar to my own. Dave may not be personally responsible for my having acquired a taste for alcohol, but he certainly is guilty of contributing to it. I can not, however, in good conscience judge his effort to be unappreciated or incorrect. My thanks go out to him and his wife for sharing their home, Johnny D's and Bill Plympton. If you want to know, Dave, I'm just having one of those days.

I have to mention Scott King not only because he is a good friend and colleague, but because the similarity in our personal histories borders upon the truly bizarre. Few of our colleagues actually had to live with us during college. I think we all know what that means.

Many thanks also go out to the following for making MIT and WHOI what they are: Jonathon Snow, Bob Grimm, Justin Revenaugh, Lind Gee, Mark Murray, Peter Puster, Will Wilcock, Mark Simons, Greg Beroza, John Goff, Anne Sheehan, Ken Creager, Eric Bergman, Kurt Feigl, Mike Bergman, Randy Mackie, Andrew Gunstensen, Niall Slowey,

Bruce Chapman, Richard Holme, Joanne Frederich, Paula Waschbusch, Sarah Kruse, Tom Juster, D'Arcy Straub, Carolyn Ruppel, Karen Fischer, Duncan Fisher, Peter Kauffman, Cecily Wolfe, Lyle, Bruce Cabral, Dave Dinter, Julio Friedman, Dawn Sumner, Eric Buchovecky, Tom Wagner.

Acta est fabula

*For I have learned,
 To look on nature, not as in the hour
 Of thoughtless youth; but hearing oftentimes
 The still, sad music of humanity,
 Nor harsh nor grating, though of ample power
 To chasten and subdue. And I have felt
 A presence that disturbs me with the joy
 Of elevated thoughts; a sense sublime
 Of something far more deeply interfused,
 Whose dwelling is the light of setting suns,
 And the round ocean and the living air,
 And the blue sky, and in the mind of man:
 A motion and a spirit that impels
 All thinking things, all objects of thought
 And rolls through all things. Therefore am I still
 A lover of the meadows and the woods,
 And mountains; and of all that we behold
 From this green earth; of all the mighty world
 Of eye, and ear, – both what they half create,
 And what perceive; well pleased to recognize
 In nature and the language of the sense
 The anchor of my purest thoughts, the nurse
 The guide, the guardian of my heart, and soul
 Of all my moral being.*

Excerpt from *Lines Composed a Few Miles Above Tintern
 Abbey, on Revisiting the Banks of the Wye during a Tour*
 by William Wordsworth, 13 July, 1798

Chapter One Introduction

It is my intent to beget a good understanding between the chymists and the mechanical philosophers who have hithero been too little acquainted with one another's learning.

Robert Boyle
The Sceptical Chymist

The advent of the plate tectonic theory and the sea–floor spreading hypothesis ushered in a new understanding of the importance of mid–ocean ridges in the development of the Earth's vast ocean basins. These ridges are no longer viewed as curious, unexplained features of the seafloor, but rather as the principal point of origin for the oceanic crust. The rocks forming the crust is known to be igneous in nature. The first–order explanation for how these rocks are formed is that the divergence of the lithosphere causes mantle rock to upwell over some region beneath the ridge axis. As a volume of the mantle rises adiabatically, the pressure exerted by the overlying rock begins to decrease. At some depth, the volume crosses its solidus and begins to melt. This melt then separates from its host rock and migrates to the surface where it cools to form the oceanic crust.

This rather simplistic model, however, does little to illuminate the complex interrelationships between the generation of melt and flow in the mantle. For example, mantle flow determines the temperature structure beneath the ridge. The temperature structure, in conjunction with the mantle solidus, defines the region of melt production and the distribution of melt. Melting creates lateral changes in mantle density and composition. The change in composition changes the mantle solidus and the change in mantle density changes mantle flow patterns. The additional density–driven flow then alters the pattern of melting. Thus, the melt–mantle system beneath a mid–ocean ridge is dynamic and, for this reason, ill–understood. Furthermore, the mechanisms of melt migration are still being debated. Does melt migrate via percolation or via dike propagation? Are non–linear phenomenon such as compaction boundary layers and “magmons” important for melt transport?

The distances and time scales over which these processes occur render a laboratory study impracticable. Remote–sensing techniques (e.g. seismics, gravity, magneto–tellurics) do not provide any insight as to the relative magnitude of forces acting upon the mantle–melt system or their interactions. At present, the only means at our disposal for investigating the dynamics of the upper mantle beneath mid–ocean ridges is through careful numerical experiments. In this thesis, I have developed the numerical tools to explore a thermo–dynamically self–consistent physical model for mantle flow, melting, and melt

migration beneath an oceanic spreading center. I have then applied these tools to better define the geophysical and petrological implications of several potential candidate models of subridge flow and melting.

Chapter Two provides a more detailed discussion of the issues and physics surrounding current investigations of melt migration and mantle flow beneath mid-ocean ridges. A goal within this chapter is to characterize the behavior of the melt-mantle system with changes in the spreading rate of the oceanic lithosphere and changes in the mantle viscosity structure. I examine the efficacy of changes in the mantle viscosity as a means of creating a narrow neovolcanic zone at the ridge axis. I compare each of these models by calculating several surface observables.

Chapter Three presents several numerical experiments that characterize the effect various energy transport mechanisms have upon the generation and distribution melt beneath a mid-ocean ridge axis. The mechanisms investigated include latent heat of melting, advection of heat by the melt phase, and transport of heat by flow in the mantle (both plate-driven and buoyancy-driven).

Chapter Four develops the idea that dynamic forces in the mantle are an inadequate mechanism for focussing melt to a mid-ocean ridge. I present a model that allows the mantle permeability to be anisotropic. The orientation of strain in the mantle (e.g. crystallographic deformation) is related to the permeability and several numerical experiments are performed that show this mechanism can be quite effective at focussing melt to the ridge axis.

Chapter Two

The Effects of Spreading Rate and Variable Viscosity on Mantle Flow and Melt Migration at Mid–Ocean Ridges

Peoples, know then once and for all that nature wanted to protect you from science just as a mother wrests a dangerous weapon from the hands of her child; that all the secrets she hides from you are so many evils from which she is protecting you, and that the difficulty you find in teaching yourselves is not the least of her kindnesses.

Jean–Jacques Rousseau
Discourse on the Arts and Sciences

INTRODUCTION

Mid–ocean ridges are the sites of oceanic crustal genesis, where the crust itself is created by a partial melting event in the mantle immediately beneath the ridge axis. Melting occurs because the divergence of the lithospheric plates and ridge–local buoyancy forces induce flow in the mantle causing hot mantle material to rise above its solidus. The resulting melt migrates through the mantle and eventually reaches the surface and cools to form the oceanic crust. Observations of mid–ocean ridge structure and chemical composition raise a number of questions unanswerable by this rather simple model. For example: What is the lateral extent and depth range of the partial melting regime? What is the distribution of melt fraction in the melt regime? How does the crustal thickness and composition depend upon spreading rate and mantle temperature? What are the important factors that cause melt to be accumulated into a narrow magma chamber at the ridge axis? Seismic, gravimetric, and/or magneto–telluric experiments may someday help constrain these questions but observational data alone do not provide insight into the forces responsible for upwelling, melting and melt migration beneath a spreading center. Theoretical modelling of mid–ocean ridge dynamics will provide this insight so long as our assumptions are reasonable and the results of such models make predictions that can be tested against observation. The coupled physics and chemistry involved in melting, melt migration, and mantle convection are complicated, however, and our studies must proceed carefully and in a systematic fashion if key associations are to be credibly unravelled.

Melt Migration and Observations of the Oceanic Crust

Current geophysical models of melt generation and extraction have their foundations in a seminal paper of *McKenzie* [1984] which presented the physics of melt extraction in a deformable porous medium. Prior to this work, models of melting and melt extraction assumed that a simplified form of D’Arcy’s Law governed melt migration [*Frank*, 1968; *Sleep*, 1974; *Turcotte and Ahearn*, 1978; *Ahearn and Turcotte*, 1979]. In these models,

vertical pressure gradients due to melt buoyancy forces are the only agents available to remove the melt from its solid porous matrix. *McKenzie* [1984] showed that deformation of the mantle in response to the creation of a partial melt results in significant local pressure gradients which can be important in the migration of the melt phase. The physics of mantle deformation in two-phase flow resulted in the discovery of the possibility of such phenomena as compaction boundary layers [*McKenzie*, 1984; *Richter and McKenzie*, 1984; *Ribe*, 1985a] and non-linear travelling waves of porosity [*Scott and Stevenson*, 1984; *Scott and Stevenson*, 1986; *Scott*, 1988; *Richter and Daly*, 1989].

After the development of the compaction theory, several studies applied it to the problem of melt genesis and crustal formation at mid-ocean ridges. The results of these models, however, present a dilemma. Simple calculations imply that the region of melting beneath a mid-ocean ridge is rather broad, approximately 100 km wide [*Reid and Jackson*, 1981; *Phipps Morgan*, 1987; *Scott and Stevenson*, 1989; *Sotin and Parmentier*, 1989]. However, several observations indicate that crustal accretion occurs within a very few kilometers of the ridge axis. *Macdonald* [1982] showed that the neovolcanic zone of mid-ocean ridges is only 3–5 km wide, regardless of plate spreading rate. Seismic evidence also indicates that the oceanic crust is completely formed at the ridge axis [*Detrick et al.*, 1987]. Recent reevaluations of available seismic data indicate that the thickness of the oceanic crust is a constant 6 km [*McClain and Atallah*, 1986] and does not thicken appreciably with age as concluded by *Reid and Jackson* [1981]. Hence, the problem is how to focus the melt from a broad area at depth into a narrow region at the surface. How this focussing occurs is an outstanding problem, the answer to which may depend upon several factors. The results of previous studies of melt migration at mid-ocean ridges touch upon some of these factors. Thus, it will be useful to review these studies both to provide an overview of the important physics and to use as a guide in developing the model I present below. I will restrict my review to those models which assume that melt migration proceeds via porous flow. Models that do not make this assumption will be discussed in the following chapter.

Broad Melt Zone – Narrow Volcanic Zone Paradox:

The Effects of Mantle Viscosity

A current goal in modelling mid-ocean ridge dynamics is to determine the dominant forces or mechanisms that lead to the apparent focussing of a distributed melt source into a very narrow region at the ridge axis. One argument is that pressure gradients caused by the divergence of lithosphere at the ridge axis may be large enough relative to melt buoyancy forces to direct melt to the ridge [*Spiegelman and McKenzie*, 1987; *Phipps Morgan*,

1987, Figure 2.1a]. However, in a constant viscosity mantle, the viscosity required to achieve this effect is 10^{21} Pa s. This value for the mantle viscosity is larger than expected for the upper mantle directly beneath a ridge axis, and a number of arguments may be made against it. First, this viscosity is larger by an order of magnitude than the 10^{20} Pa s value derived from post-glacial rebound studies [Nakada and Lambeck, 1989]. Due to the dependence of mantle viscosity upon temperature and pressure, an even lower viscosity zone is expected beneath mid-ocean ridges and oceanic lithosphere [cf. Buck and Parmentier, 1986]. An upper mantle low-viscosity (10^{18} – 10^{19} Pa s) zone a few hundred kilometers thick is required to match the observed variations of bathymetry and geoid anomalies over mid-plate swells [Robinson *et al.*, 1987; Ceuleneer *et al.*, 1988; McNutt and Judge, 1990]. Studies of geoid anomalies across oceanic fracture zones also seem to require a low-viscosity zone beneath the lithosphere if small-scale convection is the source of their variation with plate age [Craig and McKenzie, 1986; Robinson *et al.*, 1988]. Joint inversions of shear wave travel times, geoid, and depth anomalies along the mid-Atlantic ridge [Sheehan and Solomon, 1991] also weakly indicate the presence of a low-viscosity zone beneath the ridge axis. However, its presence is harder to detect there because along-axis temperature anomalies are generally smaller than those associated with plumes.

A large, constant mantle viscosity also leads to problems in the theoretical study of mid-ocean ridges for, though it allows viscous stresses to focus melt to the ridge axis, it creates a strong dependence of crustal thickness upon spreading rate with low spreading rate ridges having a markedly thinner crust than their faster spreading counterparts—a result in contradiction with observation [Chen and Sandwell, 1990]. This dependence results from the fact that a high-viscosity mantle cannot easily flow in response to the lateral density changes caused by melt extraction. With no component of mantle flow other than that provided by the divergence of the lithosphere, the thickness and width of the melting regime, and hence the crustal thickness, are determined by the depth marking the onset of the thermal boundary layer or the loss of clinopyroxene. Lowering the mantle viscosity allows melting-induced density variations to induce a vigorous component of upwelling directly beneath the ridge axis. Enhanced upwelling raises the isotherms beneath the ridge axis, increases the thickness of the melting regime, and increases the rate of melt production (see Chapter 3). The additional melting markedly reduces the spreading rate dependence of crustal thickness. However, the mantle viscosity is so low that viscous stresses are weak relative to mantle buoyancy forces. Melt will then rise vertically above the melting regime resulting in a broad region of crustal accretion [Figure 2.1b].

One potential means of circumventing the problems outlined above is to assume that the mantle viscosity depends upon both temperature and pressure. The advantage of such a viscosity law is that viscosities are low (10^{18} – 10^{19} Pa s) in regions where melting occurs and high ($\geq 10^{21}$ Pa s) in the thermal boundary layer. Thus, in the melting regime, viscosities are low enough to allow buoyancy forces to induce convection and limit the dependence of crustal thickness upon spreading rate (Figure 2.1c). Conversely, mantle viscosities are high enough near the surface to create pressure forces capable of focussing melt to the ridge axis. The ability of the ridge to focus melt, however, will depend critically upon the thickness of the thermal boundary layer at the ridge as the mantle viscosity decreases exponentially with increasing temperature. Thus, plate–spreading–induced pressure gradients may decrease rapidly with distance from the ridge axis, potentially limiting their usefulness as a focussing agent.

A low–viscosity zone beneath the ridge axis can also influence the focussing of melt by changing the mantle flow field. Lowering the viscosity at some depth beneath the ridge axis creates faster upwelling velocities there because, unlike in models with a constant viscosity mantle, a rigid, “high–viscosity” lithosphere now exists that moves at the plate velocity. The rigid lithosphere increases the lateral flux of mass thus the vertical flux increases in order to conserve mass. Since the vertical flux of mantle must match the horizontal flux caused by the divergence of the lithosphere, the upwelling region becomes narrower. Melting at mid–ocean ridges is a response to vertical motions of the mantle; narrowing the region of upwelling creates a narrower melting region. In this scenario the region of crustal accretion is narrow not because enhanced mantle pressure gradients draw a broadly distributed melt to the ridge axis, but because the region of melting is itself narrow.

To date only a few studies present experiments incorporating a variable viscosity. *Buck and Su* [1989] present a description of a buoyancy–driven flow and melting experiment beneath a ridge that incorporated a temperature–dependent viscosity. They state that melt is not strongly concentrated to the ridge and that the crust continues to thicken out to a distance of 50 km from the axis. This result is similar to that of *Scott and Stevenson* [1989] who lowered the mantle viscosity by a factor of five wherever a melt phase was present [*Cooper and Kohlstedt*, 1984, 1986] and found no significant narrowing of the crustal accretion region. *Buck and Su* [1988] further suggested that, if melt fractions in the mantle can approach 20%, the mantle viscosity will drop by several orders of magnitude. This leads to an extreme narrowing of the melt production regime, and, by their argument, a zone of crustal accretion only a few kilometers wide. It is unlikely, however, that melt fractions reach this magnitude several tens of kilometers below the ridge axis [*Johnson et*

al., 1990] and uncertain that the presence of melt has such a drastic effect upon the mantle viscosity [Cooper and Kohlstedt, 1984, 1986]. From the above discussion, it should be clear that the effect of near-ridge mantle viscosity structure on mantle flow and melt migration have not yet been strongly demonstrated.

The Effects of Buoyancy Forces

The addition of buoyancy terms into the balance of forces will change patterns of mantle flow and mantle pressure gradients. Changing mantle pressure gradients will affect the path melt takes to the surface through D'Arcy's Law. Changing mantle flow fields will alter the size, shape, and distribution of melt in the melt regime by changing (1) the mantle temperature field, (2) the rate at which rock is advected above its solidus, and (3) the path a given mantle sample takes through pressure-temperature-composition space. Three kinds of buoyancy forces operate in the sub-ridge mantle and are caused by lateral variations in porosity, temperature, and composition. Of these three, the effect of variations in porosity is most likely the smallest if melt fractions are small and their effect is dominated by the influence of other forces (buoyancy or viscous) [Scott and Stevenson, 1989]. The effect of thermal buoyancy forces is likely to be negligible near mid-ocean ridges for two reasons. First, the largest lateral variations in temperature occur near the ridge axis (within 100 km) where the effects of conductive cooling become important. In this thermal boundary layer, mantle viscosities will be quite high and thus unlikely to induce any significant convection. Second, the effect of melting is to reduce mantle temperatures to the solidus and thus eliminate lateral variations in temperature everywhere within the melting region. On the other hand, convection due to lateral variations in mantle composition can be quite vigorous. Lateral variations in density due to mantle composition result from the irreversible chemical change in the mantle upon the extraction of the melt phase. While this convection is important at mid-ocean ridges, its magnitude depends upon the degree to which density changes with extent of melting. Unfortunately, how the mantle density changes as melting proceeds is not well characterized. The general effect of this convection, though, is similar to that of a low-viscosity zone beneath the ridge. The source of convection is local to the ridge axis and enhances upwelling there. Just as in the case of a low-viscosity zone, in order to match the mass flux of the diverging plates, the upwelling zone must narrow leading to a narrower region of melting albeit with higher melting rates and a concomitantly higher crustal thickness.

Parameterizations of Mantle Melting

Finally, an issue of fundamental importance in models of mid-ocean ridge dynamics are the assumptions made about the nature of the melting in the oceanic upper mantle. Two of the most important assumptions inherent in all models are (1) whether melting and melt extraction are better idealized as a fractional or batch process and (2) the method of parameterizing the melting process. The assumptions made about melting are important not only because of the physical feedback between melting and mantle dynamics, but also because of the dependence of melt and residuum chemistry upon the path a mantle sample traverses through pressure-temperature-composition space (and thus upon mantle dynamics). So far, models of mid-ocean ridge melting and circulation have assumed a rather simple functional dependence for melt production. Either a certain percentage of melting per degree centigrade above some solidus is assumed [*Reid and Jackson*, 1981; *Phipps Morgan and Forsyth*, 1988; *Sotin and Parmentier*, 1989; *McKenzie and Bickle*, 1988] or a certain percentage of melting per kilobar change in pressure [*Scott and Stevenson*, 1989]. In the latter case, the generation of melt is not strictly thermodynamically controlled.

Given the number of free parameters one may change in this problem, it should not be surprising that widely disparate physical models can all produce 6 km of oceanic crust. Crustal thickness and neovolcanic zone width are thus necessary but not sufficient conditions for the evaluation of any given model. Because the models all produce widely different distributions of melting, however, and because melt composition depends upon pressure and temperature, it should be possible to use petrologic data to constrain further modelling and to evaluate results. In order to perform this task, an adequate parameterization of the melting process is required.

The oceanic upper mantle is a polymineralic, multicomponent system with major contributions to the melt coming from olivine, pyroxene and an alumina-rich phase (plagioclase, spinel or garnet). Even if solid-state phase changes are ignored this is a complex system to characterize thermodynamically. One approach would be to fully characterize the multicomponent phase space for the upper mantle [e.g. *Ribe*, 1985b]. That is, one could fully describe as a function of composition the solidii in the CAMS tetrahedron. Unfortunately, phase proportions and the phases themselves change with both pressure and composition thus rendering this approach somewhat intractable. Another approach is to parameterize the mantle solidus with simple functions of pressure, temperature, composition and melt fraction as done by *McKenzie and Bickle* [1988]. While the results of *McKenzie and Bickle* [1988] are useful for their emphasis of a parametric approach, their results are flawed in several important aspects. First, the data

used to construct their solidus are from batch melting experiments. The work of *Johnson et al.* [1990] on abyssal peridotites strongly suggests that melting beneath mid-ocean ridges is better described as a fractional melting process. Thus, much of the data used to determine the solidus in *McKenzie and Bickle* [1988] do not adequately determine the behavior of mantle melting at small melt fractions. Second, their solidus does not depend upon mantle composition at any given point. As melting proceeds, the phase proportions and composition of the mantle will change as the low-melting-point components are removed. As these components are lost, the temperature at which subsequent melting occurs will rise. The proportion of phases, their composition, and which aluminous phase is present will also determine how much melt is generated for a given temperature increase. Moreover, since mineralogy is an important control on the partitioning of oxides into the melt and residuum, it is important that melt composition be an explicit function of mantle mineralogy. A final important criticism of parameterization of *McKenzie and Bickle* [1988] is that the composition of the melts used to create their solidus are not appropriate for low-melt fraction, primary melts from a MORB source [R. Kinzer and T. Grove, pers. comm.]. Furthermore, the melt fractions in each experiment are quite large (>10%) thus making the use of their solidus at low melt fractions questionable at best.

If chemical variations of abyssal peridotites and mid-ocean ridge basalts are to be used as constraints upon and indicators of mantle dynamics, then an improved model of melting in the sub-ridge mantle must be devised and adopted.

Objectives

In this study, I will develop a self-consistent, fluid-dynamic model of flow and melt migration in the mantle below a mid-ocean ridge. This model is thermodynamically self-consistent in that the generation of melt occurs due to the advection of mantle heat above the mantle solidus. I also include the effects of latent heat of melting and advection of heat by the melt. Finally, I use a petrologically-defined mantle solidus that is controlled not only by pressure, but also explicitly by mantle mineralogy and residue composition. This method allows me to calculate directly the composition of both primary melts and the mantle residuum as melting proceeds. After the model is defined, I will present a suite of numerical experiments aimed at determining the effects of spreading rate and viscosity structure on mid-ocean ridge mantle dynamics, melting and melt migration. I will also explore a number of calculated surface observables (bathymetry, gravity, seismic structure, mantle residuum chemistry and primary melt composition) in order to determine if observable differences exist between models with the same spreading rate but with different viscosity structures.

MODEL DEVELOPMENT

Our goal is to investigate numerically the steady–state thermo–fluid dynamic character of the mantle beneath a mid–ocean ridge. In striving for a semblance of petrologic realism in the suite of numerical experiments presented in the next section, a certain degree of complexity is added to an already complex system. To mitigate this, I make a few simplifying assumptions regarding the governing equations.

Assumptions Regarding Melting and Melt Migration

I explicitly assume that melt migration occurs via porous flow (D’Arcy flow). This is a good approximation to flow through a pre–existing network of grain boundary channels or macroscopic veins, but not for the transport of melt via dike propagation. I assume that the melt phase forms an interconnected network for all melt fractions along grain edges rather than collecting in isolated non–porous pockets. This assumption is manifest in the functional form of the permeability used in previous studies of melt migration. To date, all models assume that the permeability k_φ is proportional to φ^n where φ is the melt fraction and $n > 0$ is some integer (generally $n=2,3$). In this form, the permeability is non–zero for all values of φ ; thus the melt phase forms an interconnected network at all melt fractions no matter how small. However, the morphology of the melt phase is dependent upon several factors.

For a monomineralic crystalline aggregate, the crucial parameter that determines if a partial melt is interconnected is the dihedral, or “wetting”, angle θ . *Bulau et al.* [1979] show that θ is determined by the ratio of two interfacial free energies, i.e.

$$\cos\left(\frac{\theta}{2}\right) = \frac{1}{2} \frac{\sigma_{ss}}{\sigma_{sl}} \quad (2.1)$$

where σ_{ss} is the excess free energy due to atomic misfits at crystal–crystal interfaces and σ_{sl} is the free energy at crystal–liquid interfaces. Furthermore, they show that if $\theta < 60^\circ$ then the melt phase is interconnected via melt channels along triple junctions. If, however, $\theta > 60^\circ$ then the triple junctions are melt–free and the melt accumulates at grain corners forcing the permeability to zero everywhere. Hot–pressing experiments on natural systems of dunite and basalt at upper mantle pressures (~ 1 GPa) and temperatures (~ 1300 °C) are done by placing a basalt within a charge in contact with an olivine matrix and allowing the resulting melt–rock system to achieve an “equilibrium” texture. These experiments show that the median dihedral angle is about 30° – 50° [*Waff and Bulau, 1979; Jurewicz and*

Jurewicz, 1986; Toramaru and Fujii, 1986; Daines and Richter, 1988]. Evidence that the faces of adjacent grains are indeed dry is shown in a series of scanning electron and transmission electron micrographs by *Waff and Bulau [1979]* and *Vaughan and Kohlstedt [1982]*. These images show that the intergranular faces are free of melt to within the resolution of the scanning devices (~2–20 nm). Perhaps the best evidence that the melt forms an interconnected network comes from the hot–pressing experiments of *Daines and Richter [1988]* who doped the melt phase with a radioactive ^{151}Sm tracer and placed it in contact with a dunite matrix. They found that after the system had reached equilibrium, the radioactive tracer was distributed throughout the matrix. By ruling out diffusion of the samarium tracer into the matrix and establishing a one–to–one correspondence in quenched samples between high radiation levels and the melt phase their results allow us to infer a highly connected melt network.

Bulau et al. [1979] assumed isotropic surface energies in their derivation of the dihedral angle equation (2.1). In fact it is possible to show numerically [*von Bargaen and Waff, 1986*] that the melt is interconnected for all melt fractions no matter how small if the surface free energies are isotropic and the dihedral angle is less than 60° . They note it is likely that interfacial free energies are anisotropic and depend upon the orientations of the crystal lattices at phase boundaries. If the effect of this anisotropy is large the melt phase may not be interconnected at low melt fractions. However both *Waff and Bulau [1979]* and *Vaughan and Kohlstedt [1982]* describe the recrystallization growth of the matrix olivine as isotropic. Thus they conclude that in a hydrostatic stress field the effects of surface energy anisotropy on the geometry of the melt phase must be negligible. If the surface energies are anisotropic and cause the connectivity of the melt to diminish the effect would be most significant at low melt fractions i.e. when the crystal faces are close together. The work of *Daines and Richter [1988]* does not support this conclusion because the melt is interconnected even at low melt fractions (~1–2 weight percent) though the possibility of locally isolated melt pockets cannot be ruled out.

The mantle stress field beneath a mid–ocean ridge is not hydrostatic—an assumption made in the experiments outlined above. *Von Bargaen and Waff [1986]* show that it is possible to pinch off melt channels in certain directions depending upon the magnitude and orientation of the deviatoric stress field. However, they also point out that the magnitude of the deviatoric stress field beneath mid–ocean ridges is probably too low (10–40 kPa) to significantly affect the geometry or connectivity of the melt phase thus this effect is also assumed to be negligible.

Finally, I note that the above conclusions are predicated on the assumption that the mantle is composed exclusively of olivine plus a melt phase (basalt). Typical upper mantle

rock is a polymineralic assemblage (olivine, orthopyroxene, clinopyroxene, \pm aluminous phase). Our conclusion that the melt forms an interconnected network is in no small part tied to the observation that the dihedral angle is less than 60° . However, the dihedral angle equation (2.1) assumes that adjoining crystals have the same composition. Thus, the above experiments imply but do not guarantee that the melt will form an interconnected network in rock similar in composition to that found in the sub-oceanic upper mantle. *Toramaru and Fujii* [1986] derived a new set of dihedral angle equations for a mantle composed primarily of olivine (ol), orthopyroxene (opx) and clinopyroxene (cpx) and performed some hot-pressing experiments on a spinel lherzolite. Their dihedral angle measurements indicate that in such an assemblage the only morphologically stable configuration (i.e. one that allows an interconnected melt network) is one in which melt along triple junctions is surrounded on all sides by olivine (ol-ol-ol). By assuming that the melt-filled grain corners are approximately tetrahedral, they were further able to show that the only stable grain corners are ol-ol-ol-ol and ol-ol-ol-opx. Their calculations agree well with their observation that the melt tends to be surrounded by olivine and that pyroxene grains are melt free.

Additional theoretical results also support the assumption of an interconnected melt phase. *Nakano and Fujii* [1989] argue that in a polymineralic system the melt connectivity depends upon both the modal composition and a critical melt fraction below which the melt does not connect along grain edges. They conclude that if the volume percent of olivine in a natural peridotite (ol,opx,cpx) exceeds 63% and the volume percent of melt exceeds 0.8% then the melt will be interconnecting. They further note that as melting proceeds, the effects of the pyroxenes on melt morphology may decrease and thus the critical modal percentage of olivine may decrease as well. Since upper mantle rocks are composed predominantly of olivine and the critical melt fraction seems relatively low I will assume in the following numerical experiments that the melt phase is interconnected beneath mid-ocean ridges at any finite melt fraction.

I also assume that the amount of melt present at any given time is always small, of order a few percent and that melt extraction is a steady-state process. Physical evidence that melt fractions are likely to be small in the melting regime beneath mid-ocean ridges was recently reported by *Johnson et al.* [1990] who showed that the trace element signatures of clinopyroxenes in abyssal peridotites could only be reproduced if melting occurs fractionally. This discovery does not rule out the possibility that melt only begins to migrate when some critical melt fraction ϕ_0 is exceeded. Thus some melting (0-3%) may initially occur as a batch melting process but it is likely that its contribution to the total melt production is small.

The assumption that $\phi \ll 1$ not only simplifies my governing equations but allows me to ignore the effects of compaction on the deformation of the mantle and the possibility of convective flow due to lateral variations in porosity. Simple numerical experiments indicate that the compaction boundary layer expected at the base of the melting regime is likely to be only a few hundred meters thick [e.g. *Ribe, 1985a*] whereas the melt regime itself is of order a few tens of kilometers thick [e.g. *Sotin and Parmentier, 1989*]. Thus the effect of a compaction boundary layer on the overall dynamics of the system is expected to be small. The extraction of melt over a broad region also acts as a sink for mantle mass and has the effect of drawing mantle towards the melting regime. If the melt fraction is small, however, this effect is negligible [*Phipps Morgan et al., 1987*].

The assumption of steady-state melt extraction is a strong constraint on the behavior of the system. For example, it eliminates the existence of non-linear porosity waves or “magmons” in our solutions as these features are inherently time-dependent. These features are not seen in the ridge-like melting environment explored by *Scott and Stevenson [1989]* which implies that such effects are either not important at mid-ocean ridges or not resolvable with their numerical technique. Whether or not buoyancy forces due to porosity can be ignored relative to those due to density reductions in the mantle depends upon their relative strengths. If the density variations from both are approximately the same, then it may not be valid to ignore one in favor of the other. This issue will be discussed later.

My final melt migration assumption is that melt velocities are in general much larger than mantle velocities ($v \gg V$). This allows me to ignore the effects of relative motion between the melt and the mantle ($v - V$). Thus, melt migration paths are determined purely from buoyancy forces and viscous stresses and not by mantle transport. If the melt velocity v is comparable to the mantle velocity V , then lateral and vertical transport of melt by mantle flow may be important in shaping the pattern of surface eruption by focussing or defocussing melt towards or away from the ridge axis. Simple numerical experiments [*Ribe, 1985a*] indicate that, for reasonable mantle parameters, melt may flow at velocities at least 10 times greater than mantle velocities. This result, of course, depends critically upon the mantle permeability which will control the rate at which melt escapes from the mantle. Recent experimental results on olivine-basalt systems indicate that mantle permeabilities may be much higher than previously is assumed [*Riley et al., 1990*] which would imply even faster melt ascent. On the basis of ^{230}Th - ^{238}U ratios in mid-ocean ridge basalts, *McKenzie [1985]* argues both that melt fractions must be everywhere small ($< 2\%$) and that melt ascent rates are of order 1 m yr^{-1} , a value much larger than the rate of mantle upwelling.

Governing Equations of Momentum, Mass and Energy

Given the previous assumptions and the two-phase flow equations of *McKenzie* [1984], non-dimensional equations for the conservation of momentum in the mantle and melt are written as follows

$$\nabla p = \frac{\partial}{\partial x_j} \eta \left(\frac{\partial V_i}{\partial x_j} + \frac{\partial V_j}{\partial x_i} \right) + R_m \Delta \rho \hat{z} \quad (2.2)$$

$$\mathbf{q} = \phi \mathbf{v} = -\mathbf{K} \left(\frac{\nabla p}{R_m} - \delta \rho \hat{z} \right) \quad (2.3)$$

where equation (2.2) describes the viscous fluid response of the mantle to driving forces such as lateral variations in density and plate motions. Equation (2.3) is D'Arcy's Law for the motion of an interstitial fluid through a porous medium. The fluid flows in response to both imposed pressure gradients (in this case pressure gradients due to mantle deformation) and the buoyancy forces caused the differential density between the melt and the mantle. As will be described later, the tensor \mathbf{K} in D'Arcy's Law is the ratio of permeability to melt viscosity. In our case, the melt viscosity is essentially a constant [*Kushiro*, 1986] thus this tensor may be thought of simply as the permeability divided by a constant. The permeability is, in general, a tensor quantity because parameters that effect the permeability, such as channel width and tortuosity, may vary with direction. A description of all notation used in this chapter is provided in Table 2.1. Parameters used to non-dimensionalize all equations are provided in Table 2.2. The non-dimensional factor $R_m = \rho_m g d^2 / U_0 \eta_0$ is similar to a Rayleigh number in that it describes the relative strength of mantle buoyancy forces to viscous stresses. Note that the mantle is assumed to be incompressible and that the standard Boussinesq approximation is made for all density terms. Therefore, mantle density only varies in the second term on the right-hand side of the mantle momentum equation (2.2) and is assumed to be constant elsewhere as in D'Arcy's Law and the energy equation. As stated above, mantle buoyancy forces due to lateral variations in temperature and porosity are ignored and only those due to changes in mantle composition are allowed. The way in which mantle density varies with composition will be discussed below. The density of the basaltic melt is assumed to be a constant though it is known to exhibit an appreciable variation with pressure with the melt density increasing about 100 kg m^{-3} as pressure increases from zero to ten kilobars [*Fujii and Kushiro*, 1977; *Rigden et al.*, 1984].

Note that form of the mantle momentum equation (2.2) allows for a variable viscosity. In this chapter results in which the mantle viscosity is assumed either to be constant or variable will be presented. For a variable viscosity, it is assumed that the mantle viscosity depends upon pressure and temperature and follows an Arrhenius-type law

$$\eta = C_0 \exp\left(\frac{E^* + pV^*}{RT}\right) \quad (2.4)$$

where C_0 is a constant such that the mantle viscosity achieves a certain value at a certain temperature and pressure (see Table 2.3). To calculate viscosities from equation (2.4), temperature is in units of degrees Kelvin and the pressure is assumed to be the hydrostatic pressure $p = \rho_m g z$. Wherever the mantle viscosity is greater than $50\eta_0$, I explicitly fix the mantle velocity to be the plate spreading velocity ($V=(U_0,0)$, see Figure 2.1) thus defining an effectively rigid lithosphere. The total viscosity range in these experiments is from $0.1\eta_0$ to $50\eta_0$ (cf Figure 2.15).

The mantle viscosity might depend upon the presence of melt. These effects, however, are not clearly known at present. *Cooper and Kohlstedt* [1984, 1986] argue that the effect of an interstitial melt phase will lower the mantle viscosity by at best a factor of two to five if creep in the mantle is controlled by diffusion through the lattice. However, if, as is thought, deformation in the upper mantle is controlled by dislocation creep [*Ashby and Verrall*, 1977; *Goetze*, 1978; *Weertman*, 1978] this effect may be even less because mantle deformation rates will be higher for a given stress and thus the enhancement of creep by the melt phase is muted relative to that for diffusion-controlled creep. In fact, *Karato* [1986] suggests that the presence of a small amount of melt will actually strengthen the mantle by preferentially incorporating incompatible elements and fluids into the melt phase. Thus I assume the melt has no effect upon mantle viscosities.

Conservation of energy is described by the following non-dimensional equation for temperature

$$\frac{\partial T}{\partial t} + (V + q) \cdot \nabla T = \frac{1}{Pe} \nabla^2 T - \frac{\rho_f \Delta S_m}{\rho_m C_p} \Gamma \quad (2.5)$$

which correctly incorporates both the loss of latent heat due to melting and the advection of heat due to melt percolation. The non-dimensional factor $Pe = U_0 d / \kappa$ is a Peclet number which describes the relative strength of thermal advection to thermal diffusion. If the advection of heat dominates the transport of heat by diffusion then $Pe > 1$. Note that the

the latent heat of melting L may be written $L = \Delta T \Delta S_m$ and that specific heat capacities of the melt and mantle are the same. In the experiments I present, the latent heat release due to crystallization of the melt phase is not incorporated into the model though it is possible in this formulation.

To complete the expression for D'Arcy's Law (equation (2.3)), the functional form of the permeability needs to be specified. However, if, as is assumed, the mantle does not deform in response to the formation and extraction of the melt and that melt is immediately extracted after it is formed, why then calculate the permeability at all if the melt is not actually present in the calculations? The answer is that while the mechanics of the system may be little affected by the presence of melt, the migration of the melt may transport a considerable quantity of heat. The amount of heat transport by the melt depends not only upon the amount of melt present but upon its velocity as well ($q = \phi v$). Thus, if the melt is moving rapidly relative to the mantle, it may significantly affect both the volume and distribution of melt (see Chapter 3).

As noted before, experiments on a variety of porous materials indicate that the permeability may often be directly related to the porosity via some relationship such as $k_\phi = c_0 \phi^n$ where c_0 and n are some constants (usually, $n = 2, 3$). Such a relation is sometimes referred to as the Blake–Kozeny–Carman equation. Unfortunately, no data exist to determine the constants necessary to make this equation useful and reliable for mantle–melt systems. What data does exist in the geological literature is in all likelihood not a good parameterization of permeability in the mantle [Maaløe and Scheie, 1982]. Furthermore, the melt fraction is not calculated at every point in the models I present, only the melt production rate is known. In order to use the BKC equation to calculate permeability along a melt flowline, I would need to know the melt fraction along that flowline, which I do not. Given the above assumptions, though, the path melt takes on its way to the surface may still be calculated if an appropriate permeability relation can be found that allows the completion of D'Arcy's Law without specifically knowing the melt fraction present.

D'Arcy's Law (equation (2.3)) requires that both the permeability and the melt viscosity be specified. For purpose at hand, it is sufficient to know their ratio. The ratio of permeability to melt viscosity is, in general, a second order tensor which is written as the following linear relation

$$\mathbf{K} = k_\mu \mathbf{A} \quad (2.6)$$

The tensor \mathbf{A} is a symmetric dimensionless anisotropy tensor with the property that $|A_{ij}| \leq 1$ and the scalar k_μ is the magnitude of the permeability–melt viscosity ratio (k_ϕ/μ). The steady–state melt production rate is defined as

$$\rho_f \nabla \cdot \mathbf{q} = \Gamma \quad (2.7)$$

Combining the melt production rate equation (2.7) with D’Arcy’s Law and equation (2.6) yields the following differential equation for k_μ

$$f_1 \frac{\partial k_\mu}{\partial x} + f_2 \frac{\partial k_\mu}{\partial z} + f_3 k_\mu = R_m \Gamma \quad (2.8a)$$

where the coefficients f_1, f_2 and f_3 are as follows

$$f_1 = A_{xx} \left(-\frac{\partial p}{\partial x} \right) + A_{xz} \left(-\frac{\partial p}{\partial z} + R_m \delta \rho \right) \quad (2.8b)$$

$$f_2 = A_{xz} \left(-\frac{\partial p}{\partial x} \right) + A_{zz} \left(-\frac{\partial p}{\partial z} + R_m \delta \rho \right) \quad (2.8c)$$

$$f_3 = -A_{xx} \frac{\partial^2 p}{\partial x^2} + A_{xz} \left(-2 \frac{\partial^2 p}{\partial x \partial z} \right) - A_{zz} \frac{\partial^2 p}{\partial z^2} - \left(\frac{\partial A_{xx}}{\partial x} + \frac{\partial A_{xz}}{\partial z} \right) \frac{\partial p}{\partial x} + \left(\frac{\partial A_{xz}}{\partial x} + \frac{\partial A_{zz}}{\partial z} \right) \left(-\frac{\partial p}{\partial z} + R_m \delta \rho \right) \quad (2.8d)$$

Note that, in deriving equation (2.8d), the buoyancy term $\delta \rho$ is a constant and, thus, no gradients of this term appear. In this chapter, it is assumed that the mantle is isotropic and, therefore, $\mathbf{A} = \mathbf{I}$ where \mathbf{I} is the identity matrix. Experiments with $\mathbf{A} \neq \mathbf{I}$ will be presented in the following chapter.

For basaltic melts, the melt viscosity is essentially a constant 1–10 Pa s [Kushiro, 1986] thus variations in k_μ directly reflect variations in the permeability. Note that the source term for k_μ in equation (2.8a) is the melt production rate. If no melting occurs then the permeability is zero, as for the Blake–Kozeny–Carman equation. Note further that equation (2.8a) has almost the form of a steady–state advection equation with a source term. The source term is the melt production rate. If no melting occurs ($\Gamma = 0$) then the permeability is zero. Only when $\Gamma > 0$ does the permeability become non-zero. The first two terms on the left–hand side of equation (2.8a) are the advection terms and the

coefficients f_1 and f_2 can be regarded as velocities describing the way pressure gradients, buoyancy forces and anisotropy act to direct the permeability. The third term on the left-hand side of equation (2.8a) provides a mechanism for increasing or decreasing the permeability in response to anisotropy.

Parameterization of Melting

To complete my set of equations, the melt production rate needs to be specified as well as how the mantle density varies with extent of melting. As mentioned above, I wish to avoid being overly simplistic as to how the mantle melts if I am to use petrological and geochemical data as indicators of mantle processes. For the reasons stated above, I choose not to implement the parameterization of *McKenzie and Bickle* [1988]. Rather, I choose the parameterization of *Kinzler and Grove* [1991] for its simplicity, its consistency with known melting processes, and its dependence upon both mantle mineralogy and composition. In this parameterization, the mantle is defined by a modal mineralogy vector M and a oxide composition vector O . Observations of abyssal peridotites indicate that the mantle beneath mid-ocean ridges always contains the following minerals in varying proportions: olivine, clinopyroxene, orthopyroxene and an aluminous phase [*Dick et al.*, 1984; *Dick and Fisher*, 1984; *Michael and Bonatti*, 1985; *Johnson et al.*, 1990]. In the mantle, the aluminous phase appears as either plagioclase, spinel or garnet, in order of increasing pressure. The mineralogy and composition of the mantle respond to patterns of mantle flow and thus the vectors M and O satisfy the following differential equations

$$\frac{\partial M}{\partial t} + \mathbf{V} \cdot \nabla M = f_M \quad (2.9)$$

$$\frac{\partial O}{\partial t} + \mathbf{V} \cdot \nabla O = f_O \quad (2.10)$$

where f_M and f_O describe how the abundance of each mantle mineral and oxide responds to melting. Note that diffusion of each mineral and oxide is assumed to be negligible so that species transport is solely by mantle flow.

I assume that the mantle is described by a four phase spinel lherzolite assemblage (olivine, clinopyroxene, orthopyroxene and aluminous spinel) and eight oxides (K_2O , Na_2O , CaO , FeO , MgO , TiO_2 , SiO_2 and Al_2O_3). It should be noted that the assumption of a pervasive spinel lherzolite assemblage (i.e. plagioclase and garnet are absent regardless of pressure) is not an arbitrary one. First, it simplifies an already complex system. The

primary goal of this study is to investigate the physics of melt migration and mantle deformation. The secondary goal is to determine if melt and residuum compositions can be used as a discriminant between various extant physical models. If calculated compositions do not agree with observations then I can determine that melting of additional phase assemblages is required. Little data exist to constrain melting in the higher pressure garnet lherzolite field though it may be argued some melting must occur at such higher pressures [Salters and Hart, 1989; Johnson *et al.*, 1990]. Finally, little melting will actually occur in the lower pressure plagioclase lherzolite field. If plagioclase is left in the residue at the end of melting, then we might expect to observe significant europium anomalies in the trace element patterns of mid-ocean ridge basalts (negative Eu anomalies) and abyssal peridotites (positive Eu anomalies). That these anomalies are not observed in either the basalts or the peridotites argues against melting in the plagioclase field. Furthermore, experimentally determined melts for the lower pressure plagioclase lherzolite assemblage typically have higher SiO₂ and lower MgO, CaO and Al₂O₃ proportions than primary melts from the higher pressure spinel lherzolite assemblage. These latter melts are closer in composition to the most primitive mid-ocean ridge basalts and thus the inference is that much of the melt that formed the oceanic crust is generated in the spinel lherzolite stability regime.

Given the mantle composition, *Kinzler and Grove* [1991] calculate the melt fraction at any given pressure and any temperature above the spinel solidus with the following relation

$$1155 + 16p - 50(1 - \text{Mg}\#) - 129\text{NaK}\# - T = 0 \quad (2.11)$$

where the pressure p is in kilobars and temperature T is in degrees centigrade. The two compositional parameters, Mg# (Mg/(Mg + Fe)) and NaK# ((Na + K)/(Na + K + Ca)), are non-dimensional parameters describing the compositional state of the melt. Both of these latter parameters depend upon the melt fraction in the following way. For small melt fractions, fractional melting and batch melting produce very similar results with regard to melt and residuum chemistry. Thus, the concentration of a melt component in equilibrium with the mantle is given by the batch melting equation where the melt increment ϕ is finite but small

$$C_l = \frac{C_0}{D_B + \phi(1 - P_B)} \quad (2.12)$$

In this equation, C_l is the concentration of a melt component (e.g. Na₂O) in the melt, C_0 is the initial concentration of that component in the solid, D_B is the bulk partition coefficient

between the solid and melt for that component weighted by the initial mode of the solid, and P_B is the bulk partition coefficient between the solid and the melt, for that component, weighted by the fraction of each mode entering the melt (non-modal melting). Since equation (2.12) depends upon melt fraction, so does equation (2.11). I use a simple bisection technique to iterate for the melt fraction ϕ in equation (2.11). A further complication of this procedure is that the Mg# of the melt is not the Mg# at the beginning of melting but at its conclusion. The Mg# of the melt is determined from the initial olivine composition of the solid, thus fixing its value during the iterative procedure. The Mg# of olivine is determined iteratively, as well, by solving mass balance equations for Mg and Fe [Langmuir and Hanson, 1980; Kinzler and Grove, 1991]. As long as the melt fraction is small this procedure yields reasonably good estimates for the melt Mg#.

One difficulty encountered in solving the solidus equation (2.11) for the melt fraction is that complete extraction of sodium and potassium in the solid causes the NaK# to be zero, regardless of the melt fraction. Thus, at point where sodium is lost, equation (2.11) cannot be used to solve for the melt fraction since pressure, temperature, and melt Mg# are fixed and the NaK# is zero. To overcome this problem, I make a simple thermodynamic argument that, at any point, the melt fraction may not exceed that determined by the following energy balance

$$\rho_m C_p T = \rho_m C_p T_s + \phi \rho_f L \quad (2.13)$$

where T_s is the solidus temperature determined by equation (2.11). Once melt fraction is known, the melt production rate Γ is simply $\Gamma = \partial\phi/\partial t$.

Once the melt fraction is known, the residual mantle mineralogy and composition may be calculated as well as the melt composition. The residual mantle mineralogy is determined by subtracting from the mantle mode vector an experimentally-constrained amount of each mineral per unit amount of melt. The coefficients of this mantle melting reaction are given by Kinzler and Grove [1991] for a spinel lherzolite assemblage

$$0.81 \cdot Cpx + 0.40 \cdot Opx + 0.06 \cdot Sp - 0.27 \cdot Ol = 1.00 \cdot Liquid \quad (2.14)$$

Melt oxide compositions are determined with the parameterization of Kinzler and Grove [1991]. The new mantle oxide composition is simply the starting oxide composition less the amount of each component now in the melt times the melt fraction. As a final point, if the weight percent of clinopyroxene drops below 1%, then the melt fraction is set to zero. This is my effective 'cpx-out' criterion. My assumption that melting ends when

clinopyroxene is lost does not necessarily mean that this is the point at which melting ceases in the Earth's mantle. In fact, evidence exists that some amount of melting continues to occur even after clinopyroxene is lost [H.J.B. Dick, pers. comm.]. One reason for requiring melting to end when clinopyroxene is lost is that no data exist to constrain the melting reaction (2.14) and solidus (2.11) when only olivine and orthopyroxene occur as mantle phases. However, we do expect that when the low melting-point components are lost, the latent heat of melting will increase sharply and melting will effectively cease at the point of 'cpx-out'.

Mantle density is, in general, a function of pressure (compressibility), temperature (thermal expansion), composition (Fe/Mg ratio) and mineralogy. For the purposes of this work, I will initially ignore the variation of mantle density with pressure and temperature. The mantle density at any point is the simple sum of densities for all mineral phases present. The density of each mineral phase is determined by its Fe/Mg ratio and the density of the magnesium- and iron-bearing end-members or that mineral. For our purposes, the Mg-Fe end-member pairs are olivine : forsterite (3325 kg m^{-3}) – fayalite (4400 kg m^{-3}), clinopyroxene : diopside (3277 kg m^{-3}) – hedenbergite (3632 kg m^{-3}), orthopyroxene : enstatite (3190 kg m^{-3}) – orthoferrosillite (4005 kg m^{-3}), and spinel : spinel (3583 kg m^{-3}) – hercynite (4265 kg m^{-3}). The appropriate Mg# for each mineral is determined by the Mg# of olivine and appropriate Fe/Mg distribution coefficients [Langmuir and Hanson, 1980; Kinzler and Grove, 1991]. Note that because there is no spinel-plagioclase phase transition in my model, there is also no corresponding density jump at the phase transition. Finally, I do not consider crystallization of the melt phase as its temperature falls below its liquidus.

Numerical solutions to the differential equations presented above are obtained using the finite-element method. The computational geometry and boundary conditions for each experiment are summarized in Figure 2.1. The computational domain has dimensions 400 km (horizontal) x 150 km (vertical). The computational grid has a variable spacing with a minimum horizontal resolution of 3 km at the ridge axis and a minimum vertical resolution of 3 km above 60 depth. The total number of nodes is 73 in the horizontal direction and 37 in the vertical. Experimental run parameters are listed in Table 2.3 and the initial mantle mineralogy and composition, M_0 and C_0 respectively, are listed in Table 2.4. Mantle which has not lost any basaltic components will be referred to as "fertile" mantle with no other isotopic or geochemical interpretations implied. Mantle that experiences a loss of basaltic components will be referred to as "residual" mantle or simply "residuum".

RESULTS

In this section, I present the results of nine numerical experiments, all of which are described in Table 2.3. I choose a mantle temperature of 1340 °C in order to obtain a reasonable crustal thickness across the suite of experiments. In the presentation that follows, I will proceed by fixing the mantle viscosity and describing the salient features that appear as I increase the lithospheric half-spreading rate. I will offer comparative descriptions for models with different viscosity structures as the opportunity arises.

Constant Viscosity – 10^{19} Pa s

My goal in this section is to present a description of the steady-state mantle/melt system without the complicating factor of compositionally-driven convection. Plots of several melt- and mantle-related variables for experiments with half-spreading rates of 1, 4 and 8 cm yr⁻¹ are shown in Figures 2.3, 2.4 and 2.5, respectively. At this viscosity, the mantle flow field is almost completely determined by the spreading of the lithospheric plates. This is clearest in the 1 cm yr⁻¹ model (Figure 2.3) which shows significant lateral variations in residual mantle density indicating that viscous stresses due to the divergence of the lithosphere dominate buoyancy forces. The dominance of viscous stresses depends upon the magnitude of the density reduction experienced by the mantle after extraction of the melt phase. If the average density change is large, then buoyancy forces may dominate viscous stresses. If the density change is much less, then viscous stresses may dominate. For example, *Sotin and Parmentier* [1989] observe significant compositionally-driven convection beneath the ridge at this same mantle viscosity. This difference in behavior results from the fact that their maximum change in residual mantle density $\Delta\rho$ is about 50 kg m⁻³ whereas the maximum change in all models I present is about 10 kg m⁻³ (a change from 3328 kg m⁻³ to 3318 kg m⁻³). Thus my ratio of buoyancy forces to viscous stresses is lower and plate behavior dominates despite the lower viscosity.

The reason that the density changes are markedly different between my model and others resides in the different means by which the aggregate densities are determined. Ideally, we should have experimentally determined densities of abyssal peridotites as a function of extent of melting. The range of mantle densities will depend upon both the mineral phases present as well as their proportion and composition. Most current experimentally determined mantle density functions are for a garnet lherzolite assemblage taken from kimberlite xenolith samples [*Boyd and McCallister, 1976; Jordan, 1979*]. Removal of a melt component from these samples yields an estimated density change of about 50 kg m⁻³ after approximately 20% melting. Such large density changes result from the loss of the dense garnet phase which is present in xenoliths in significant quantities. As

argued above, little melting is expected to occur in the garnet stability field thus bringing the use of this data throughout the melting regime into serious question. Since no data exist for a spinel lherzolite assemblage, we calculate the densities directly from the mantle modes and their Fe/Mg ratio. That is, the Mg# of each mode is calculated via mass balance, then the density of each mode is simply $Mg\# \cdot \rho_{Mg} + (1-Mg\#) \cdot \rho_{Fe}$ where ρ_{Mg} is the density of the Mg-rich end-member of a particular mineral and ρ_{Fe} is the density of the Fe-rich end-member of that mineral. The bulk density of the mantle is then the sum of all mode densities weighted by their weight fraction at any point. The high-density spinel phase is present in much lower quantities in the spinel lherzolite (Table 2.4) than garnet in the xenoliths (2.5 weight % vs. 10 weight %). Most of the density change in the models I present is associated with the removal of clinopyroxene which has a density closer to those of the coexisting phases, resulting in much smaller density changes.

The maximum density changes obtained in these models should be considered a lower limit. Petrologic evidence suggest that some small amount of melting is likely to occur in the higher pressure garnet lherzolite field [Salters and Hart, 1989; Johnson et al., 1990]. Since garnet contains an abundance of heavy oxides that are lost upon melting (e.g. Al_2O_3), then small amounts of melting in the garnet field may cause the maximum density change to be larger than if melting occurred in the spinel field alone. An increase in the range of densities will result in an increase in the ratio of buoyancy forces to viscous stresses (R_m). For this ratio to remain constant, and thus the pattern and magnitude of convection, the mantle shear viscosity must be increased. For example, factor of five increase in the range of mantle densities (from 10 kg m^{-3} to 50 kg m^{-3}) results in a factor of five increase in the mantle shear viscosity—an amount certainly within reason and uncertainty. Thus, even if a discrepancy exists between theoretical and observed melting-induced density changes, the relative density differences are small enough such that reasonable changes in the mantle shear viscosity produce the same ratio of buoyancy forces to viscous stresses and therefore the same pattern of mantle flow.

Since melting controls much of the interesting physics, it is worthwhile to investigate its distribution in some detail. Referring again to Figures 2.3, 2.4 and 2.5, I note that melt production rates increase with the velocity of the overriding plates. This is expected behavior because as upwelling velocities increase the rate at which mantle rock is advected above its solidus increases. Since the pressure change per unit time increases, the rate at which melt is produced must increase in order for the mantle to remain on the same temperature–pressure phase boundary.

The maximum and minimum pressures of melting for each model are listed in Table 2.5. The maximum pressure of melting for all models is 15.7 kbar and is fixed by both the

mantle temperature and the fertile mantle mineralogy and composition. Since the starting composition and mantle temperature are the same across all models, the onset of melting begins at the same pressure for each. Beneath the ridge axis, the minimum pressure of melting is determined by one of two phenomena : either the effects of conductive cooling become important and melting ceases or clinopyroxene melts out ($cpx < 1\%$). In all but one experiment (run 1), the minimum pressure of melting is determined by the depth at which clinopyroxene melts out (about 4 kbar). This is in agreement with *McKenzie and Bickle* [1988] who argue that conductive cooling does not contribute significantly towards limiting the amount of melt produced beneath a ridge. In contrast to their work, however, I clearly do not observe melting continuing all the way to the surface.

In all cases, I observe that melt production rate beneath the ridge axis increases as pressure decreases. This trend can be explained by considering the steady-state energy balance in the melting regime. If the effects of diffusion are negligible in the melting regime, then the advection of heat by the melt and mantle $((V+q)\cdot\nabla T)$ is balanced by the latent heat term $(\rho_f\Delta S_m/\rho_m C_p)$ in the thermal energy equation (equation(2.5)). Consider for a moment the situation where the mantle flow is purely vertical, as beneath the ridge axis, and there is no flux of melt ($q=0$). If the mantle solidus depended solely upon pressure and if the upwelling rate were constant, then the melt production rate would be constant as well. The additional flux of heat due to the buoyantly rising melt could account for the increase of melt production rate with decreasing pressure, but the same trend is seen for models in which the flux of melt heat is ignored (Chapter 3). If the upwelling velocity were not constant but increased through the melting regime, a result perhaps of enhanced flow due to compositionally-driven convection, then the melt production rate would increase as the velocity increased much like the effect of spreading rate upon the rate of melting. Again, however, the trend of melting rate with depth is the same if the flow is driven solely by the plates and the mantle velocity is constant through the melting regime (Chapter 3). Thus, while flow of the mantle and melt do affect the distribution of melt (Chapter 3), neither one accounts for the observed trend of melting.

The only remaining explanation for the melting trend, therefore, must be that the slope of the solidus is changing with pressure. If the coefficient of the pressure dependence is constant, as it is here, then any changes in the shape of the solidus with pressure must result from changes in the mantle composition. Recall that the solidus I am using in this study depends upon both alkali content through the NaK# of the melt and upon the Fe/Mg ratio through the Fe# (1-Mg#) of the melt. Since I have the melt composition at every point, I can calculate the NaK# and Fe# of the melt then calculate their respective pressure derivatives. Multiplying these derivatives by their coefficients in the solidus equation

(equation (2.11)) yields the curves in Figure 2.7a which show how changes in mantle alkali content and the Fe/Mg ratio affect the pressure derivative of the solidus. The effect of alkali content on the slope of the solidus clearly dominates the effect of iron content. Furthermore, changes in the solidus due to alkali content of the melt are clearly reflected in the variation of melt production rate (Figure 2.7b); exposing their role in trend of melt production rate with pressure. The effect of the alkalis decreases as melting proceeds because the alkalis are strongly incompatible in the spinel lherzolite mantle and their depletion dominates any ancillary pressure effects.

As the spreading rate increases (Figures 2.4 and 2.5), the top of the melting regime is delimited by the loss of clinopyroxene both beneath the ridge axis and for some distance away from it. Thus a zone of harzburgitic residue exists above the melting regime and acts as a barrier to further melting. (Recall that the cessation of melting upon the loss of clinopyroxene is an assumption built into the model. Some small amount of melting may occur after clinopyroxene is lost but I am unable to model the melting process beyond that point.) The width of the melting regime increases with spreading rate because mantle isotherms become shallower thus raising the temperature of previously sub-solidus mantle above its melting point. Increasing the width of the melting regime results in the mantle density having less lateral variation than it would at slower spreading rates (Figures 2.4 and 2.5). This effect, along with the increased plate velocity, acts to limit the effect of mantle buoyancy forces on the mantle flow field and hence the melting regime and crustal thickness.

Melt production rates decrease with distance from the ridge axis simply because the mantle flow becomes increasingly horizontal. In the absence of down-stream temperature increases or upwelling (e.g. mantle plumes) the horizontal advection of mantle will not result in melting. Except at the slowest spreading rate where melting is laterally delimited by conductive cooling, most of the melt at the faster spreading rates is produced where significant upwelling occurs. These controls on melting can be applied towards understanding the asymptotic relationship between crustal thickness and spreading rate shown in Figure 2.6 and previously described by *Sotin and Parmentier* [1989]. At the faster spreading rates, where buoyancy forces are negligible, crustal thicknesses are approximately the same because the melt production regimes at these spreading rates are determined by the depth at which clinopyroxene is lost and the region over which significant upwelling occurs. Since the patterns of flow are the same, the amount of crust produced for each model is about the same. At 1 cm yr^{-1} , any enhanced flow due to convection is not sufficient to offset the effects of conductive cooling and thus the crustal thickness decreases.

An examination of the magnitude and orientation of the melt flux vectors and contours of permeability–melt viscosity ratio clearly show that melt is rising vertically under the sole influence of melt buoyancy forces. Mantle viscous stresses have little effect upon melt migration paths at this viscosity. A similar conclusion was reached by *Phipps Morgan* [1987] who showed that little focussing of melt to the ridge axis is to be expected unless the mantle viscosity is about 10^{21} Pa s. The permeability–melt viscosity ratio increases along the vertical melt paths for two reasons. First, the permeability must increase in order to allow both melt produced locally and melt rising from below to escape. Second, the melt production rate increases with height. Outside of the melting regime, the permeability no longer increases because no further melting occurs and thus the permeability remains constant along the melt paths. The average permeability increases with spreading rate because melt production rates increase concurrently.

If the melt viscosity is about 1 Pa s [*Kushiro*, 1986] then the average permeabilities in these models are about 10^{-14} m². *Scott and Stevenson* [1989] relate the permeability to the melt fraction via the relation $k_{\phi} = k_0 \phi^2$ where $k_0 = 10^{-10}$ m². Using this relation and the average permeabilities I obtain an estimate of the melt fraction of about 1% which is in agreement with my assumption of a small melt fraction. If the melt fractions are about 1%, then the maximum melt velocities in these models are of order 10–100 times the half–spreading rate across the suite of models presented in this section. Thus, the permeability–melt viscosity relation yields reasonable results despite the fact that it does not depend upon any particular phenomenology (i.e. melt channel geometry). The constant in Scott and Stevenson’s permeability equation, however, is not necessarily valid in the mantle. A change in this constant by a factor of ten yields a corresponding change in the melt fraction by about a factor of three if k_{ϕ} is held constant. My conclusion that melt fractions must be small given an uncertain permeability–melt fraction relation must be interpreted with caution.

The distances over which crustal accretion are important can be seen in Figure 2.8a (also Table 2.5) which shows non–dimensional crustal thickness versus distance from the ridge axis. The accumulation of crustal material is significant out to several tens of kilometers from the ridge axis in contradiction to the observation that oceanic crust is emplaced entirely at the ridge axis. This result is a consequence of the fact that the melt is rising vertically and therefore the width of the zone of crustal accretion reflects the width of the melting regime. The width over which accretion is important increases with spreading rate simply because the lateral dimensions of the melting regime increase concurrently. However, there is less relative difference between models as the spreading rate increases

because most of the melt is produced near the ridge axis where significant upwelling occurs.

Constant Viscosity – 10^{18} Pa s

Lowering the mantle viscosity to 10^{18} Pa s (Figures 2.9, 2.10 and 2.11) causes the relative magnitude of mantle buoyancy forces to mantle viscous stresses to increase. At this viscosity, the effects of compositionally-driven convection manifest themselves in a number of ways, primarily in the slowest spreading rate models.

Previously, the 1 cm yr^{-1} model exhibited clear lateral variations in density. Now, because the mantle viscosity is much lower, the resulting buoyancy forces are much stronger, resulting in a significant component of upwelling flow. Enhanced mantle upwelling increases the melt production rate by advecting more heat above the solidus than would be possible by plate-driven flow alone. The additional advection of heat due to convection has raised the isotherms above the melting regime and thus lowered the minimum pressure of melting thereby causing more melting to occur. This effect, in conjunction with the higher rates of melting and greater average extents of melting, causes the crustal thickness to increase thus eliminating the marked variation of crustal thickness with spreading rate observed at higher viscosities (Figure 2.6). This result is in agreement with that of *Sotin and Parmentier* [1989] though our values are different due to differences between the models.

As convection becomes more important, the width of the melting regime narrows (Table 2.5), as is observed elsewhere [*Rabinowicz et al.*, 1984; *Scott and Stevenson*, 1989; *Sotin and Parmentier*, 1989; Chapter 3]. The width of the melting regime contracts when convection occurs because of conservation of mass. When flow is driven solely by the plates, a certain amount of mass is advected through the region defined by the edges of the melting regime. Enhanced upwelling due to buoyancy-driven flow increases mantle velocities through this region. Evidence for this is seen in the higher crustal thickness of the 1 cm yr^{-1} model relative to the previous model with the same spreading rate but higher viscosity. The higher velocities do not lead to more mass being advected through the melting regime, however. Rather, the residual mantle, being lighter than the unmelted mantle below it, forces mantle that has passed through the melting regime to be constrained to depths less than or equal to the depth of initial melting (see Figure 2.9). In order for the mass of mantle rising up through the melting regime to equal that transported laterally in the depleted harzburgite residuum, the width of the melting regime must narrow. The crustal thickness increases, however, because the average extent of melting throughout the melting regime is higher.

The total mass of mantle passing through the melting regime must match the mass of mantle advected away by the lithosphere to both sides. The relative amount of narrowing decreases with spreading rate, however, because lateral variations in density become progressively weaker, as noted before, and plate–spreading–induced stresses become more important. Note that the additional flow causes the density fields in each model to be almost stably stratified. Any downward flow that may exist is resisted by the positive buoyancy of the light residuum overlying the denser fertile mantle. For the same reason, upward flow of the mantle is resisted and the mantle density field becomes stably stratified [Scott and Stevenson; 1989; Sotin and Parmentier, 1989].

Narrowing of the melt regime can also be seen in the width of the crustal accretion zone at the surface (Table 2.5, Figure 2.8). The mantle viscosity is even lower than before, further diminishing the effects of mantle viscous stresses on the migration of the melt phase. Hence, the melt rises vertically only in response to melt buoyancy forces. The reduced width of the crustal accretion zone, relative to the higher viscosity models, can be directly attributed to the narrowing of the melting regime by convection. Despite this narrowing, however, the model crustal accretion zone is still 50–150 kilometers in wide.

Temperature– and Pressure–Dependent Viscosity

As shown above, a mantle viscosity of order 10^{18} Pa s is required if there are to be no strong variations of crustal thickness with spreading rate. With such a low viscosity mantle pressure gradients are too weak to focus melt to the ridge axis. Realistically, mantle viscosities are not constant but depend upon both temperature and pressure (equation (2.4)) with viscosity decreasing with temperature and increasing with pressure. In the sub–ridge mantle, this dependence leads to a high–viscosity lithosphere underlain by a low–viscosity zone. The low viscosity in the sub–lithospheric mantle will cause buoyancy forces to dominate viscous stresses resulting in compositionally–driven convection thereby reducing the dependence of crustal thickness upon spreading rate. Arguably, the high viscosities in the lithosphere above the melting regime could enhance mantle pressure gradients to the point where significant focussing of melt to the ridge may occur.

Experimental runs at the same spreading rates as before but with a variable viscosity are presented in Figures 2.12, 2.13 and 2.14. A meaningful presentation of the salient points in these figures requires a knowledge of the viscosity structure of the mantle which are shown Figure 2.15 for all spreading rates. In all runs, the reference mantle viscosity is assumed to be 10^{19} Pa s at 150 km depth and 1340 °C. An upper limit of 5×10^{20} Pa s is also imposed which is close to the value of 10^{21} Pa s used by Phipps Morgan [1987] and

Spiegelman and McKenzie [1987]. Underlying the high-viscosity lithosphere is a low-viscosity zone with a minimum viscosity of about 10^{18} Pa s.

Perhaps the most obvious statement that can be made about the variable viscosity experiments is that there is little discernable difference between the flow fields shown in this series and those of the constant viscosity experiments. There is no dramatic reduction in the width of the melting region relative to the models at 10^{18} Pa s. However, some differences exist. The crustal thickness (Figure 2.6, Table 2.5) clearly shows a modest spreading rate dependence due to the fact that the sub-lithospheric mantle is not a constant low viscosity (i.e. 10^{18} Pa s). Thus the influence of buoyancy forces on the flow field is somewhat reduced by the high viscosity lid.

Contours of permeability and the melt flux vectors indicate that enhanced focussing due to viscous stresses does occur because of the presence of the high-viscosity lithosphere above the melting regime. The amount of focussing increases with the spreading rate because the magnitude of viscous stresses scales with the spreading rate. At 1 cm yr^{-1} , the crustal accretion zone is 15 km narrower than for the model with a constant viscosity of 10^{18} Pa s and the same spreading rate. At 8 cm yr^{-1} , the reduction in the width of the crustal accretion zone is about 50 km when compared to the model with a constant viscosity of 10^{18} Pa s. Even at 8 cm yr^{-1} , however, the amount of focussing due to viscous stresses is insufficient for concentrating most of the melt into a narrow region at the ridge axis. This can be seen more clearly in Figure 2.8c which shows that the crustal accretion zone is still quite broad, of order several tens to a couple of hundred kilometers. The inability of the high-viscosity lithosphere to efficiently focus the melt to the ridge axis can be understood as follows. The divergence of the lithosphere at the ridge axis creates a region of low pressure at the surface centered about that axis. Along with the pressure gradients due to buoyancy-driven convection, pressure gradients due to this lithospheric divergence are what drive melt migration in D'Arcy's Law (equation (2.3)). Within the region of thermal conduction near the surface, the mantle viscosity is high due to its strong temperature-dependence and thus pressure gradients are high. However, temperatures increase rapidly with depth through the conduction boundary layer resulting in a rapid decrease in mantle viscosity (Figure 2.15). The rapid decrease in viscosity with depth causes the magnitude of plate-spreading-derived pressure gradients to decrease rapidly with distance from the ridge axis. Thus, enhanced pressure gradients do aid in focussing melt to the ridge, but only near the surface. If melt is to be drawn in to the ridge from throughout the melting regime, relatively high pressure gradients must exist across its entire expanse. As shown here, this result is not possible indicating that other forces or factors need to be considered.

DISCUSSION

In this chapter, I have developed a thermodynamically-consistent model of melting, melt migration and mantle convection beneath a mid-ocean ridge. The results presented in the previous section illustrate the importance of a number of factors on melt production, the distribution and migration of the melt phase, and on crustal accretion. Though the work I present above is a considerable advance in the study of mid-ocean ridge dynamics, it is a worthwhile task to evaluate the results in light of the approximations I made in the model.

One of the effects I ignore is convection that results from lateral variations in mantle density due to the presence of a lighter melt phase. The effect of the increased density change would be to enhance upwelling beneath the ridge axis and thus narrow the melting regime. However, it is important to recall that the efficacy of density variations in enhancing mantle upwelling is dictated by the ratio of buoyancy forces to viscous stresses. Since melt fractions are likely to be small beneath a ridge axis the resulting density differences between dry mantle and mantle with an interstitial melt phase will likewise be small. For a melt fraction of 1%, the bulk density of the melt and mantle would be about 6 kg m^{-3} lighter than for dry mantle. This density change is about the same order as the maximum change ($\sim 10 \text{ kg m}^{-3}$) in the mantle density at the end of melting for the models presented here. Enhanced upwelling due to this increase in the density change can be countered by increasing the mantle viscosity resulting in patterns of mantle flow that are the same as for models with a lower maximum density change and lower mantle viscosities. Since flow in the mantle strongly determines the distribution of melt, the incorporation of buoyancy forces due to lateral variations in porosity is not likely to change the major observations or results presented here.

The results of *Scott and Stevenson* [1989], however, indicate that while melt-driven convection does enhance flow beneath the ridge, it is not a sufficient mechanism for focussing melt to the ridge axis.

Thermal buoyancy forces will enhance vertical mantle flow beneath the ridge axis because the primary mass flux will be cold, down-welling plumes moving in the direction of plate spreading [*Sotin and Parmentier*, 1989]. However, the effect at the ridge axis of thermal plume descent depends upon several factors. One of these is the distance from the ridge axis where down-welling plumes first appear. This distance is, in turn, determined by the point at which the increase in mantle density due to conductive cooling becomes more important than the positive buoyancy forces in the light harzburgitic layer. Because of the relatively low density changes produced by this model, thermal buoyancy forces could be important in the constant viscosity models. However, beneath a mid-ocean ridge,

the viscosity structure is likely to depend upon temperature and pressure. The presence of a high viscosity lithosphere will tend to inhibit downwellings. Furthermore, the only significant lateral temperature variations will occur along the base of the thermal boundary layer and, within the melting region, these variations will be buffered by the presence of melt. Thus, thermal buoyancy forces are likely to have little effect near ridge axes.

Observational Implications

As shown above, different viscosity structures can lead to differences in the behavior of the mantle–melt system. It is a useful exercise, therefore, to determine if these differences can be observed with measurements of bathymetry, gravity, teleseismic event travel times, abyssal peridotite composition or in the aggregate melt compositions.

Bathymetry

Seafloor bathymetry near mid–ocean ridges is influenced by a number of mantle processes. The thickening of the thermal boundary layer with distance from the ridge axis results in the well–known deepening of the seafloor with age [*Parsons and Sclater, 1977*]. Conversely, variations in the mantle density due to changes in mineralogy and composition cause the seafloor to rise in order to restore the isostatic balance of forces at depth. Dynamic topography is caused by stresses resulting from flow due to plate spreading and flow due to convection. These effects of dynamic topography are likely to be greatest near the ridge axis where the pattern of flow is primarily upward. However, I choose to neglect its effects for two reasons. First, for any given spreading rate, the largest differences between models are for those with the slowest plate speed. The near–ridge topography at slow spreading rates is dominated not so much by viscous mantle processes but rather by plastic and elastic deformations [*Lin and Parmentier, 1989*] which cannot be directly determined from the models. Second, by fixing the mantle velocity within the rigidly moving lithosphere as I do, it is difficult to calculate the viscous stresses at all. Therefore, I choose to simply calculate the isostatic topography due to variations in mantle temperature and composition. If I ignore variations in crustal thickness at the top of the mantle, then the variation of bathymetry with distance, $b(x)$ is calculated as follows

$$b(x) = \frac{\rho_m \alpha}{(\rho_m - \rho_w)} \int (T(x,z) - \Delta T) dz + \frac{1}{(\rho_m - \rho_w)} \int (\rho_m - \rho(x,z)) dz \quad (2.15)$$

Bathymetry as a function of the square root of age for each model are shown in Figure 2.16. At any spreading rate, there is little variation between models with different mantle

viscosities and the bathymetric signals are clearly dominated by the mantle thermal structure. Thus, bathymetry is not a strong discriminant between these models.

Beyond about 1 myr. from the ridge axis, the mantle is moving horizontally and the bathymetric curves vary linearly with the square root of age in agreement with theory and observation [Parsons and Sclater, 1977]. Nearer to the ridge axis, however, the flow field is no longer horizontal and the effects of conductive cooling become important resulting in a flattening of the bathymetry curves for ages younger than 1 myr. The curves for 4 and 8 cm yr⁻¹ have two distinctly different bathymetry trends for ages less than 1 myr. Between the ridge axis and the older lithosphere lies a region with an intermediate slope. The only phenomenon that could cause this change in slope is the change in mantle temperature upon melting.

The effect of variations in the mantle density due to changes in composition is small because the maximum density change from fertile to residual mantle is only about 10 kg m⁻³. This density change corresponds to a temperature change of approximately 100 °C which is much less than the total variation in mantle temperature. Furthermore, the mantle density field is approximately horizontally stratified thus the compositionally-derived density variations produce only a constant, small offset in the bathymetry curves. The effect of composition may become more important if convection due to lateral variations in porosity occurs since this will tend to displace upward isopleths of mantle residuum density [Scott and Stevenson, 1989].

Gravity

As with bathymetry, I assume that the total vertical gravity is solely the sum of variations in mantle temperature and composition. Since I am only interested in discriminating between models whose differences arise from variations in mantle parameters, I do not consider the effect of bathymetry or crustal thickness upon the gravity field. The flattening of the bathymetry with age near the ridge axis is not likely to be important for gravimetric investigations of mid-ocean ridge crustal structure because these studies directly correct for observed seafloor bathymetry.

Gravity is calculated using an analytic expression for the gravity signal of a rectangular region at depth [Telford et al., 1976]. The rectangular regions used are the elements in the finite element grid. Densities are assigned to each element by taking the average of the densities of each node in the element. In order to avoid edge effects, I subtract from every point the mantle temperature and residuum densities along the edge of the computational regime. This procedure eliminates contributions to the gravity field from mass beyond the

edges of the computational regime. The resulting gravity anomalies $\Delta g(x)$ are calculated along a line 6 km above the top of the mantle.

The total contribution of temperature and composition to the gravity field is shown in Figure 2.17. The effect of composition on the gravity is negligible because mantle densities are horizontally stratified thus essentially all of the gravity signature in each of the curves shown is the result of variations in temperature. The gravity anomaly at the ridge axis is greater than at any other point because the relative difference between temperatures at the edge of the computational regime and the ridge axis is the largest. As distance from the ridge axis increases, lateral variations in temperature decrease due to the thickening of the thermal boundary layer and, furthermore, the distance from the lighter density ridge axis increases. Both of these results combine to cause the mantle gravity anomaly to decrease with distance. The peak-to-trough amplitude of the anomalies decreases with spreading rate simply because conductive cooling becomes less important causing the maximum temperature differences between the ridge axis and the edge of the computational regime to decrease.

As with the bathymetry calculations, little differences are seen between the gravity anomalies of any two models at a given spreading rate. At best, there is a few milligals difference between some curves but nothing that may be considered measurable or even diagnostic of differences in mantle flow or rheology.

Seismic Wave Travel Time Anomalies

Shear wave travel times have been used by *Sheehan and Solomon* [1991] to determine variations in temperature and composition along the mid-Atlantic Ridge. Similarly, my intent here is to look for any systematic variations in shear wave travel times that result from the effects of melting in the mantle. The velocity of shear waves in the mantle is a function of a number of parameters including temperature and composition. Other factors which may be important in determining the velocity, and hence travel time, are anisotropy and the presence of an interstitial melt phase. I will defer a discussion of the effects of seismic anisotropy to the following chapter. Also since the effect of melt upon seismic wave velocities is not well understood or constrained I choose to ignore its influence. I assume that the shear wave velocity $v_s(x)$ is given by the following linear relation

$$v_s(x) = v_s^0 + \frac{\partial v_s}{\partial T} (T - \Delta T) + \frac{\partial v_s}{\partial Mg\#} \Delta Mg\# \quad (2.16)$$

where v_s^0 is the reference mantle shear wave speed (5 km s^{-1}). The partial derivatives in equation (3.16) are the variation of shear wave speed with temperature and Mg# of the mantle, respectively. I subtract a reference mantle temperature ($1340 \text{ }^\circ\text{C}$) and a reference mantle Mg# (fertile mantle) at every point.

Teleseismic wavefronts will arrive at the surface along nearly vertical raypaths thus I approximate the travel time anomalies at any point along the surface by the vertical integral of travel time

$$\delta t(x, z=0) = \frac{\partial v_s}{\partial T} \int_{150 \text{ km}}^{0 \text{ km}} \frac{(T(x) - \Delta T)}{v_s^2(x)} dz + \frac{\partial v_s}{\partial \text{Mg}\#} \int_{150 \text{ km}}^{0 \text{ km}} \frac{\Delta \text{Mg}\#(x)}{v_s^2(x)} dz \quad (2.17)$$

Sheehan and Solomon [1991] give values of $\partial v_s / \partial T = -6.0 \times 10^{-4} \text{ km s}^{-1} \text{ }^\circ\text{C}^{-1}$ and $\partial v_s / \partial \text{Mg}\# = 1.8 \times 10^{-2} \text{ km s}^{-1} \text{ Mg}\#^{-1}$. Note that shear wave speed decreases with temperature and increases as the Mg content of the mantle increases.

Curves of travel time anomalies as a function of distance from the ridge axis for all models are shown in Figure 2. 18. The positive values of the travel time anomalies indicate that the vertically-rising wavefront arrives earlier than it would if the mantle temperature and composition were constant. This can be understood by realizing that the residual mantle has a faster shear wave velocity than the fertile mantle. Also, because of the lower temperatures in the conductive boundary layer, shear wave velocities also increase. As with gravity and bathymetry, the curves of travel time anomalies are dominated by temperature effects. The horizontally stratified residual mantle causes a wavefront to arrive, at best, 0.03 seconds early regardless of distance from the ridge axis. Variations in arrival time due to changes in mantle temperature are small and considering the error (~ 1 sec) in determining seismic arrival times also undetectable. Almost certainly, sensitive tomographic methods will be required to image the temperature, composition and melt structure beneath the ridge.

Residuum Mineralogy and Aggregate Melt Composition

As I discussed in the development of this model, the normative mineralogy and composition of the primary melts generated in these numerical experiments depend upon temperature, pressure, and the modal mineralogy of the mantle residuum. Thus, the melt chemistry, and thus the residuum mineralogy and composition, are determined by the temperature and pressure path taken by any mantle sample. Variations in the pattern of

mantle flow, therefore, should result in observable variations in the nature of the derived melts and residual mantle.

Different trends in the mineralogy of the mantle residuum are well-documented [Dick *et al.*, 1984] and are inferred to be the result of along-axis variations in mantle chemistry. Here, I apply the same approach as Dick *et al.* [1984] and plot the proportions of olivine, orthopyroxene and clinopyroxene along a cross-section beneath the ridge axis on an appropriate ternary diagram (Figure 2.19). The trends clearly show the evolution of the mantle from a lherzolite mineralogy to a harzburgite mineralogy as it upwells beneath the ridge. As melting proceeds, the mantle mineralogy moves directly away from the melting reaction point (not shown) which changes with pressure, temperature, and mantle composition. The resulting trends are qualitatively and quantitatively similar to those shown by Dick *et al.* [1984] for abyssal peridotites with the residual mantle losing clinopyroxene and orthopyroxene as pressure decreases until the end of melting at point whereupon clinopyroxene is lost. Otherwise, no discernable differences exist between trends for different models at the same spreading rate. This is true even for the slowest spreading rate model which shows the greatest sensitivity to the effects of lateral density variations. It may be that discernable variations exist for mantle flow paths that do not intersect the ridge axis, however, there is little chance of actually observing rocks from such paths.

The resident melt in the crustal magma chamber at mid-ocean ridges is an aggregate of all melts produced throughout the melting regime. McKenzie and Bickle [1988] refer to such a mixture as an “aggregate primary melt” reflecting the fact that, so far, no melt added to the aggregate, or the aggregate itself, has undergone any fractionation process that would change its composition or normative mineralogy. There are two advantages to looking at the melt aggregate rather than individual melts. First, the aggregate gives an average view of the entire melting field the shape of which will be determined in large part by the mantle flow field. Second, the melt aggregate, to first order, is the parent source of mid-ocean ridge basalts. Any successful model of mid-ocean ridge dynamics must be able to reproduce the variety of MORB’s observed globally [Bryan and Dick, 1982; Dick *et al.*, 1984; Klein and Langmuir, 1987; Klein and Langmuir, 1989]. Aggregate primary melt compositions for all runs are shown in Table 2.6. For all models, the oxide compositions indicate that the aggregate melts have somewhat low concentrations of sodium and iron indicating that the fertile mantle mineralogy and composition used in this chapter is too depleted in basaltic components to yield a more reasonable primary melt composition. In fact, the aggregate melts are close in composition to some depleted melts produced by Elthon [1989]. Otherwise, except for the model that produced only 4 km of crust, there is

little difference between any two of these melts for a suite of runs. This lack of difference between aggregate melt composition is due to the fact that the mantle flow fields in each of the models presented are similar and yield essentially constant average pressures of melting (Table 2.5).

In order to understand the global array of MORB composition, it seems clear that we need to investigate not only the effects of temperature and three-dimensional mantle flow upon melt composition, but that of mantle mineralogy and mantle oxide composition as well. The assumption that any one of these variables accounts for all of the observed variation in MORB composition is likely to be incorrect.

Summary Comments

In the previous sections, I've shown that, from the perspective of surface observations, there is little difference in models with different viscosity structures. However, there is abundant evidence that the sub-ridge mantle varies as a function of spreading rate. The presence of transform faults clearly indicate a three-dimensional structure of mantle upwelling as do variations in along-axis depth. Spacings between transform offsets and non-transform offsets also appear to vary as a function of spreading rate [cf. *Kuo and Forsyth, 1988; Blackman and Forsyth, 1990; Lin et al., 1990*]. Along-axis variations in crustal thickness are clearly evident at fracture zones [*Cormier et al., 1984; Mutter et al., 1984*] where the crust is thinner than normal indicating a heterogeneous environment for melting and melt production. Mantle Bouguer anomalies along the Mid-Atlantic Ridge clearly indicate that mantle upwelling beneath the ridge-axis is variable and three-dimensional [*Kuo and Forsyth, 1988; Lin et al., 1990*]. *Klein and Langmuir [1987]* show that along-axis variability in the average pressure of melting leads to changes in the along-axis chemistry of basalts [*Dick et al., 1984*]. Furthermore, composition is correlated with variations in axial-depth which they interpret as being indicative of along-axis variations in mantle temperature. From a theoretical perspective, *Parmentier and Phipps Morgan [1991]* show that, at low spreading rates (1 cm yr^{-1} half-rate) and low viscosities (10^{18} Pa s), a two-dimensional mantle flow structure maybe no longer stable and inherently breaks up into a three-dimensional flow with discrete upwelling zones.

Variations in the along-axis average pressure of melting can occur because increasing (decreasing) the mantle temperature causes the pressure at which the mantle intersects its solidus to increase (decrease) [*Klein and Langmuir, 1987*]. However, mantle temperature variations are not the sole means by which to attain variations in average pressure of melting. First, variations in mantle composition and modal mineralogy may change the pressure slope of the solidus [*Kinzler and Grove, 1991*] and the pressure at which phase

changes occur. Variations in mantle composition are clearly documented in abyssal peridotites [Dick *et al.*, 1984; Michael and Bonatti, 1985]. These studies also indicate that the degree of depletion varies along-axis whereas in this study the sub-ridge mantle always melted to the point where clinopyroxene was lost. Variations in extent of melting can occur not only from pressure and composition but from changes in the pattern of mantle flow as well. Numerical studies of three-dimensional mantle flow beneath two ridge axes offset by a transform fault show that mantle upwelling becomes progressively weaker near the ridge-transform intersection [Phipps Morgan and Forsyth, 1988]. The weaker upwelling zone results in lower melt production rates, lower extents of melting and higher average pressures of melting. The primary point here is that variations in mantle temperature should not be used indiscriminately to account for variations in melt and mantle composition as this may increase the range of inferred mantle temperatures. Additional factors with equal or smaller effects and acting alone or in concert may yet account for some significant fraction of the global variation of parameters along axis. The effect of these factors have yet to be studied in detail.

CONCLUSIONS

1. I have developed a thermodynamically self-consistent model of melting, melt migration and mantle convection beneath a mid-ocean ridge. Melting is explicitly controlled by the flux of thermal energy above a mantle solidus. The mantle solidus depends upon pressure, mantle mineralogy and mantle composition. As the extent of melting increases, the mantle solidus temperature rises and its pressure derivative changes as the mantle becomes more depleted in its basaltic components. The latent heat of melting controls how much melting occurs locally for a given temperature increase. Advection of heat by the melt will increase melting rates as will convection.
2. The pattern of melt production will depend both upon (1) the rate of heat advection and therefore local mantle velocities and (2) changes in the solidus temperature and its pressure derivative.
3. Beneath the ridge axis, melting ceases at the depth where clinopyroxene is lost as a phase. This effect results in a depleted harzburgitic layer above the minimum depth of melting. The harzburgite layer acts as a barrier to further melting away from the ridge axis. Melting occurs between 4 and 16 kbar depth with an average pressure of melting of 10 kbar.

4. Much of the melt that forms the oceanic crust is created within several tens of kilometers of the ridge axis where significant mantle upwelling occurs. For medium to fast spreading rate ridges, flow driven by density gradients is small compared to flow driven by the plates. Since there is little difference between flow fields these spreading rates, and most of the melt is generated where vertical flow is significant, the thickness of the crust trends towards a constant value as spreading rate increases.

5. Convection due to lateral variations in residuum density becomes increasingly important as spreading rate decreases for two reasons. First, the lateral dimensions of the melting regime are increasingly delimited by the onset of conductive cooling. The smaller width leads to larger lateral variations in density which are the driving force for convection. Second, the magnitude of viscous stresses decreases relative to buoyancy forces because of their dependence upon spreading rate.

6. If mantle viscosities are of order 10^{18} – 10^{19} Pa s, then the flowpaths of the melt phase will be little affected by pressure gradients due to viscous stresses and the melt will rise vertically resulting in a broad region of crustal accretion. Enhancement of these pressure gradients by the use of a temperature– and pressure–dependent viscosity is not a sufficient mechanism for focussing melt to the ridge axis.

7. Comparing several geophysical observables (bathymetry, gravity, seismic travel time) shows that, for any given spreading rate, there are no detectable differences between models with different viscosity structures. A comparison of mantle residual mineralogy and aggregate primary melt compositions show that there is also little difference in these observables between models with different spreading rates and viscosity structures. The fact that significant differences in these variables do exist between mid–ocean ridges implies that changes are required in other parameters, such as mantle temperature, composition and perhaps variations in the mantle flow field due to ridge–transform offsets, ridge migration, or asymmetric spreading.

FIGURE CAPTIONS

Fig. 2.1 Diagram showing the effect of mantle viscosity upon mantle flow and migration of the melt. Mantle flow lines are shown by solid lines terminated with large arrows. Melt flow lines are shown by solid lines terminated by small arrows. The speckled area is the region of melting. Unmelted mantle is indicated by dark–banded layering. For a high viscosity mantle (*a*), mantle flow is dominated by the flow generated by the lateral motions

of the lithosphere. The high mantle viscosity results in strong viscous stresses which focus melt to the ridge axis. Crustal thickness depends strongly upon spreading rate. For a low viscosity mantle (*b*), a significant component of mantle flow is driven by lateral variations in mantle density caused by melting and melt extraction. The low mantle viscosity mantle results in weak viscous stresses and melt buoyancy forces cause the melt to rise vertically. Crustal thickness does not depend upon spreading rate. For a mantle with a low–viscosity asthenosphere and a high–viscosity lid (dotted region) (*c*), convection can occur such that crustal thickness does not depend upon spreading rate. The high–viscosity lid may create viscous stresses that are strong enough to focus melt to the ridge.

Fig. 2.2 The diagram shown is a description of both the computational geometry and the boundary conditions used in the numerical experiments presented. Boundary conditions for velocities are presented to the right of the ridge axis. Boundary conditions for all other variables are presented to the left of the ridge axis. Velocity boundary conditions are prescribed not only on the boundaries, but in the interior of the computational regime as well. The hatched region in the interior defines an area of the mantle that is moving with the surface velocity, i.e. as a rigid plate with velocities $U = U_0$ and $V = 0$. The area encompassing the rigid lithosphere is defined in the following way. For both constant and variable viscosity models, it is possible to calculate a pressure– and temperature–dependent viscosity structure, $\eta(T,p)$, for the mantle using equation (2.4). Wherever the viscosity is calculated to be greater than 50 times the reference viscosity η_0 , the plate is defined to be moving rigidly. To avoid computational difficulties, the rigid behavior of the mantle is assumed to terminate within a distance $0.1d$ (15 km) of the ridge axis. Along the side boundaries and below the hatched region, mantle velocities are prescribed using the analytic solutions for isoviscous plate–driven flow [Batchelor, 1967]:

$$U_{ps}(x,z) = \frac{2U_0}{\pi} \left[\tan^{-1}\left(\frac{x}{z}\right) - \frac{xz}{x^2 + z^2} \right]$$

$$V_{ps}(x,z) = \frac{2U_0}{\pi} \left[\frac{z^2}{x^2 + z^2} \right]$$

Note that the frame of reference for each of these equations is as follows. The origin of the horizontal coordinate x is fixed to the ridge axis. The origin of the vertical coordinate z is fixed to the base of the plate, $z_l(x)$, at the edge of computational domain.

Fig. 2.3 A plot pair showing results for experiment #1 (1 cm yr⁻¹ half-rate, $\eta = 10^{19}$ Pa s). The computational domain is divided in half down the ridge axis and variables pertaining to the melt phase are plotted in (a) and those pertaining to the mantle are plotted in (b). (a) Dimensional melt production rate is shown as levels of grey. Contours of melt production rate are {0.25 (lightest gray shown), 0.50 0.75, 1.0 (darkest gray shown)} $\times 10^{-11}$ kg m⁻³ s⁻¹. Solid black contour lines show contours of the permeability–melt viscosity ratio $k_{\mu} = k_{\phi}/\mu$. Contours are {0.1, 0.2, 0.3, 0.4, 0.5, 0.6} $\times 10^{-14}$ m². Black arrows show direction and magnitude of melt flux q . Melt flux vectors are scaled to the labelled arrow above the plot. The label next to the arrow shows the scaling flux for the remaining arrows as a fraction of the plate velocity U_0 . The scaling flux is taken to be the maximum flux magnitude. (b) Filled arrowheads show direction and magnitude of mantle velocity (V). Mantle flow vectors are scaled to the arrow above the plot. The scaling velocity is shown next to the arrow. Solid lines are contours of mantle temperature with dimensional contour values 200, 400, 600, 800, 1000, and 1200 °C. Mantle density is shown as levels of grey. Contours of density are 3326 (lightest gray shown), 3324, 3322, and 3320 (darkest gray shown) kg m⁻³.

Fig. 2.4 Experiment #2 (4 cm yr⁻¹ half-rate, $\eta = 10^{19}$ Pa s). (a) Dimensional melt production rate is shown as levels of grey. Contours of melt production rate are {0.01 (lightest gray shown) 0.50, 1.00, 1.50 (darkest gray shown)} $\times 10^{-11}$ kg m⁻³ s⁻¹. Solid black contour lines show contours of the permeability–melt viscosity ratio $k_{\mu} = k_{\phi}/\mu$. Contours are (0.5, 1.0, 1.5, 2.0, 2.5, 3.0) $\times 10^{-14}$ m². (b) Solid lines are contours of mantle temperature with dimensional contour values of 200, 400, 600, 800, 1000, and 1200 °C. Mantle density is shown as levels of grey. Contours of density are 3326 (lightest gray shown), 3324, 3322, and 3320 (darkest gray shown) kg m⁻³.

Fig. 2.5 Experiment #3 (8 cm yr⁻¹ half-rate, $\eta = 10^{19}$ Pa s). (a) Dimensional melt production rate is shown as levels of grey. Contours of melt production rate are {0.05 (lightest gray shown) 1.0, 2.0, 3.0 (darkest gray shown)} $\times 10^{-11}$ kg m⁻³ s⁻¹. Solid black contour lines show contours of the permeability–melt viscosity ratio $k_{\mu} = k_{\phi}/\mu$. Contours are (1.0, 2.0, 3.0, 4.0, 5.0, 6.0) $\times 10^{-14}$ m². (b) Solid lines are contours of mantle temperature with dimensional contour values of 200, 400, 600, 800 and 1200 °C. Mantle density is shown as levels of grey. Contours of density are 3326 (lightest gray shown), 3324, 3322, and 3320 (darkest gray shown) kg m⁻³.

Fig. 2.6 Crustal thickness versus half–spreading rate for the models defined in Table 2.3. The different viscosity structures are differentiated by the symbols shown in the legend. Solid lines connect results from models with the save viscosity structure.

Fig. 2.7 (a) The curves in this plot show the effect of varying mantle composition on the pressure (depth) derivative of the mantle solidus. Values used are from experiment #4 (1 cm yr⁻¹, $\eta_0 = 10^{19}$ Pa s) and show a vertical cross section through the melting regime beneath the ridge axis. If variations in mantle chemistry do not affect the the rate at which the mantle solidus increases with pressure, then these curves would lie along the dashed line of zero slope. The curve labeled “NaK effect” is calculated from the composition of the melts in the melting regime and shows the effect of varying alkali composition (Na₂O, K₂O, CaO). The curve labeled “Fe effect” is similar but shows the effect of varying the Fe–Mg ratio. Both curves are calculated as follows

$$\begin{aligned} \text{“NaK effect”} &= -129 \frac{\partial \text{NaK}\#}{\partial p} \\ \text{“Fe effect”} &= -50 \frac{\partial (1 - \text{Mg}\#)}{\partial p} \end{aligned}$$

where the coefficients are taken from equation (2.11). (b) Non–dimensional melt production rate along the same vertical cross section showing the correlation between increasing melt production rate and increases in the slope of the solidus due to the progressive loss of alkalis during melting. See text for further explanation.

Fig. 2.8 Normalized crustal thickness vs. distance from the ridge axis for all models. Each curve is calculated by integrating the flux of melt, q , at the surface ($z=0$ km) and assuming that the total integrated flux of melt from the ridge axis ($x=0$ km) to the edge of the box ($x=200$ km) equals the crustal thickness, h . Curves are shown for three different viscosity structures: (a) 10^{19} Pa s, half–spreading rate of each model is shown by the numbers next to each curve, (b) 10^{18} Pa s, (c) temperature– and pressure dependent viscosity.

Fig. 2.9 Experiment #4 (1 cm yr⁻¹ half–rate, $\eta = 10^{18}$ Pa s). (a) Dimensional melt production rate is shown as levels of grey. Contours of melt production rate are {0.25 (lightest gray shown), 0.50, 0.75, 1.0 (darkest gray shown)} $\times 10^{-11}$ kg m⁻³ s⁻¹. Solid black contour lines show contours of the permeability–melt viscosity ratio $k_\mu = k\phi/\mu$.

Contours are $\{0.50, 1.0, 1.5, 2.0\} \times 10^{-14} \text{ m}^2$. (b) Solid lines are contours of mantle temperature with dimensional contour values of 200, 400, 600, 800, 1000, and 1200 °C. Mantle density is shown as levels of grey. Contours of density are 3326 (lightest gray shown), 3324, 3322, 3320 (darkest gray shown) kg m^{-3} .

Fig. 2.10 Experiment #5 (4 cm yr^{-1} half-rate, $\eta = 10^{18} \text{ Pa s}$). (a) Dimensional melt production rate is shown as levels of grey. Contours of melt production rate are $\{0.01$ (lightest gray shown), 0.50, 1.0, 1.50 (darkest gray shown) $\} \times 10^{-11} \text{ kg m}^{-3} \text{ s}^{-1}$. Solid black contour lines show contours of the permeability–melt viscosity ratio $k_{\mu} = k_{\phi}/\mu$. Contours are $(0.5, 1.0, 1.5, 2.0, 2.5, 3.0) \times 10^{-14} \text{ m}^2$. (b) Solid lines are contours of mantle temperature with dimensional contour values of 200, 400, 600, 800, 1000, and 1200 °C. Mantle density is shown as levels of grey. Contours of density are 3326 (lightest gray shown), 3324, 3322, and 3320 (darkest gray shown) kg m^{-3} .

Fig. 2.11 Experiment #6 (8 cm yr^{-1} half-rate, $\eta = 10^{18} \text{ Pa s}$). (a) Dimensional melt production rate is shown as levels of grey. Contours of melt production rate are $\{0.05$ (lightest gray shown), 1.0, 2.0, 3.0 (darkest gray shown) $\} \times 10^{-11} \text{ kg m}^{-3} \text{ s}^{-1}$. Solid black contour lines show contours of the permeability–melt viscosity ratio $k_{\mu} = k_{\phi}/\mu$. Contours are $(1.0, 2.0, 3.0, 4.0, 5.0, 6.0) \times 10^{-14} \text{ m}^2$. (b) Solid lines are contours of mantle temperature with dimensional contour values of 200, 400, 600, 800, 1000, and 1200 °C. Mantle density is shown as levels of grey. Contours of density are 3326 (lightest gray shown), 3324, 3322, and 3320 (darkest gray shown) kg m^{-3} .

Fig. 2.12 Experiment #7 (1 cm yr^{-1} half-rate, $\eta = \eta(T,p)$). (a) Dimensional melt production rate is shown as levels of grey. Contours of melt production rate are $\{0.25$ (lightest gray shown), 0.50, 0.75, 1.0 (darkest gray shown) $\} \times 10^{-11} \text{ kg m}^{-3} \text{ s}^{-1}$. Solid black contour lines show contours of the permeability–melt viscosity ratio $k_{\mu} = k_{\phi}/\mu$. Contours are $\{0.5, 1.0, 1.5, 2.0\} \times 10^{-14} \text{ m}^2$. (b) Solid lines are contours of mantle temperature with dimensional contour values of 200, 400, 600, 800, 1000, and 1200 °C. Mantle density is shown as levels of grey. Contours of density are 3326 (lightest gray shown), 3324, 3322, and 3320 (darkest gray shown) kg m^{-3} .

Fig. 2.13 Experiment #8 (4 cm yr^{-1} half-rate, $\eta = \eta(T,p)$). (a) Dimensional melt production rate is shown as levels of grey. Contours of melt production rate are $\{0.01$ (lightest gray shown), 1.0, 2.0, 3.0 (darkest gray shown) $\} \times 10^{-11} \text{ kg m}^{-3} \text{ s}^{-1}$. Solid black contour lines show contours of the permeability–melt viscosity ratio $k_{\mu} = k_{\phi}/\mu$.

Contours are $(0.5, 1.0, 2.0, 3.0, 4.0) \times 10^{-14} \text{ m}^2$. (b) Solid lines are contours of mantle temperature with dimensional contour values of 200, 400, 600, 800, 1000, and 1200 °C. Mantle density is shown as levels of grey. Contours of density are 3326 (lightest gray shown), 3324, 3322, and 3320 (darkest gray shown) kg m^{-3} .

Fig. 2.14 Experiment #9 (8 cm yr^{-1} half-rate, $\eta = \eta(T,p)$). (a) Dimensional melt production rate is shown as levels of grey. Contours of melt production rate are $\{0.10$ (lightest gray shown) $2.0, 4.0, 6.0$ (darkest gray shown) $\} \times 10^{-11} \text{ kg m}^{-3} \text{ s}^{-1}$. Solid black contour lines show contours of the permeability–melt viscosity ratio $k_\mu = k_\phi/\mu$. Contours are $(0.10, 2.0, 4.0, 6.0) \times 10^{-14} \text{ m}^2$. (b) Solid lines are contours of mantle temperature with dimensional contour values of 200, 400, 600, 800, 1000, and 1200 °C. Mantle density is shown as levels of grey. Contours of density are 3326 (lightest gray shown), 3324, 3322, and 3320 (darkest gray shown) kg m^{-3} .

Fig. 2.15 Gray–shade image of mantle viscosity (η) for (a) $U_0 = 1 \text{ cm yr}^{-1}$, (b) $U_0 = 4 \text{ cm yr}^{-1}$ and (c) $U_0 = 8 \text{ cm yr}^{-1}$. Viscosity is calculated using the temperature– and pressure–dependent viscosity equation (2.4). Contour levels of $\log_{10}(\eta)$ are shown in the gray–scale bar to the right of each plot.

Fig. 2.16 Isostatic bathymetry b (thermal + compositional) as a function of the square root of age ($\text{myr}^{1/2}$) from the ridge axis. No reference depth is added to the curves as only relative differences are important. Shown are calculations for experiments with (a) $U_0 = 1 \text{ cm yr}^{-1}$, (b) $U_0 = 4 \text{ cm yr}^{-1}$ and (c) $U_0 = 8 \text{ cm yr}^{-1}$. Within each plot are curves for experiments with different viscosity structures: $\eta = 10^{19} \text{ Pa s}$ (solid line), $\eta = 10^{18} \text{ Pa s}$ (long dash line), $\eta = \eta(T,p)$ (short dash line).

Fig. 2.17 Gravity anomalies Δg due to variations in temperature and composition as a function of distance from the ridge axis. As mentioned in the text, the temperature and composition profiles along the edge of the computational regime are subtracted from the mantle temperature and composition at every other point before gravity is calculated. Shown are calculations for experiments with (a) $U_0 = 1 \text{ cm yr}^{-1}$, (b) $U_0 = 4 \text{ cm yr}^{-1}$ and (c) $U_0 = 8 \text{ cm yr}^{-1}$. Within each plot are curves for experiments with different viscosity structures: $\eta = 10^{19} \text{ Pa s}$ (solid line), $\eta = 10^{18} \text{ Pa s}$ (long dash line), $\eta = \eta(T,p)$ (short dash line).

Fig. 2.18 Travel-time anomalies δt due to variations in temperature and composition as a function of distance from the ridge axis. As mentioned in the text, travel times are calculated after subtracting a constant mantle temperature (ΔT) from the temperature field and the Mg# of the fertile mantle from the Mg# of the depleted mantle. Shown are calculations for experiments with (a) $U_0 = 1 \text{ cm yr}^{-1}$, (b) $U_0 = 4 \text{ cm yr}^{-1}$ and (c) $U_0 = 8 \text{ cm yr}^{-1}$. Within each plot are curves for experiments with different viscosity structures: $\eta = 10^{19} \text{ Pa s}$ (solid line), $\eta = 10^{18} \text{ Pa s}$ (long dash line), $\eta = \eta(T,p)$ (short dash line).

Figure 2.19 (a) The full olivine–orthopyroxene–clinopyroxene ternary. Darkened inset shows the subsection of the ternary shown in *b–d*. (b) The filled circles in this subsection of the ol–opx–cpx ternary show the proportions of the mantle modal mineralogy along a vertical cross-section beneath the ridge axis. The spreading rate is 1 cm yr^{-1} . Phase proportions are renormalized after projection from spinel. The color of the filled circles indicate the mantle viscosity of the appropriate experiment: white– 10^{19} Pa s , gray– 10^{18} Pa s , black– $\eta(T,p)$. (c) Same as *b* except experiments for which the spreading rate is 4 cm yr^{-1} are shown. (d) Same as *b* except experiments for which the spreading rate is 8 cm yr^{-1} are shown.

TABLE 2.1 Notation

| Variable | Description | Value | Units |
|--------------|---|-------------------|---|
| A | Permeability anisotropy tensor | | |
| C_p | Specific heat at constant pressure | 1000 | $\text{J kg}^{-1} \text{C}^{-1}$ |
| d | Length scale | 1.5×10^5 | m |
| ΔS_m | Change of entropy upon melting | 450 | $\text{J kg}^{-1} \text{C}^{-1}$ |
| ΔT | Temperature difference between surface and mantle | | C |
| E | Finite strain tensor | | |
| E^* | Activation energy | | |
| g | Gravitational acceleration | 9.81 | m s^{-2} |
| h | Crustal thickness | | km |
| I | Identity tensor | | |
| K | Permeability–melt viscosity tensor | | m^2 |
| k_ϕ | Permeability | | m^2 |
| k_μ | Permeability–melt viscosity ratio | | $\text{m}^2 \text{Pa}^{-1} \text{s}^{-1}$ |
| L | Velocity gradient tensor | | |
| M | Mantle modal assemblage vector | | |
| O | Mantle oxide assemblage vector | | |
| o | Melt oxide assemblage vector | | |
| p | Pressure | | Pa |
| Pe | Peclet number | | |
| q | $= (\phi v)$ Melt percolation velocity vector | | m s^{-1} |
| R | Universal gas constant | 8.314 | $\text{J mol}^{-1} \text{C}^{-1}$ |
| R_m | Buoyancy force–viscous stress ratio | | |
| T | Temperature | | C |
| t | Time | | s |
| U_0 | Plate velocity (half–rate) | | m s^{-1} |
| V | $= (U, V)$ Mantle velocity vector | | m s^{-1} |
| v | $= (u, v)$ Melt velocity vector | | m s^{-1} |
| V^* | Activation volume | | |
| x | Horizontal coordinate | | m |
| z | Vertical coordinate | | m |

| | | | |
|--------------|--|-----------|----------------------------------|
| Γ | Melt production rate | | $\text{kg m}^{-3} \text{s}^{-1}$ |
| η | $= \eta(T, p)$ Mantle shear viscosity | | Pa s |
| η_0 | Reference mantle shear viscosity | 10^{19} | Pa s |
| κ | Mantle thermal diffusivity | 10^{-6} | $\text{m}^2 \text{s}^{-1}$ |
| μ | Shear viscosity of melt | | Pa s |
| φ | Melt fraction | | |
| ρ | $= \rho(M, O)$ Mantle density | | kg m^{-3} |
| ρ_f | Melt density | 2700 | kg m^{-3} |
| ρ_m | Reference mantle density | 3328 | kg m^{-3} |
| $\Delta\rho$ | $= (\rho_m - \rho)$ Density difference between unmelted and melted mantle | | kg m^{-3} |
| $\delta\rho$ | $= (\rho_m - \rho_f)$ Density difference between unmelted mantle and melt | 628 | kg m^{-3} |

TABLE 2.2 Non-dimensionalization Parameters

| Variable | Parameter | Units |
|--------------|----------------|---|
| V | U_0 | m s^{-1} |
| (x,z) | d | m |
| t | d/U_0 | s |
| T | ΔT | $^{\circ}\text{C}$ |
| g | g | m s^{-2} |
| η | η_0 | Pa s |
| ρ | ρ_m | kg m^{-3} |
| p | $\eta_0 U_0/d$ | Pa |
| Γ | $\rho_f U_0/d$ | $\text{kg m}^{-3} \text{s}^{-1}$ |
| \mathbf{K} | $U_0/\rho_m g$ | $\text{m}^2 \text{Pa}^{-1} \text{s}^{-1}$ |

TABLE 2.3 Experimental Parameters

| Run # | U_0^a (cm yr ⁻¹) | ΔT (°C) | Pe^b | R_m^c ($\times 10^3$) | η (Pa s) |
|-------|-----------------------------------|--------------------|--------|------------------------------|-----------------------|
| 1 | 1 | 1340 | 47 | 232 | 10 ¹⁹ |
| 2 | 4 | 1340 | 190 | 58 | 10 ¹⁹ |
| 3 | 8 | 1340 | 380 | 29 | 10 ¹⁹ |
| 4 | 1 | 1340 | 47 | 2,320 | 10 ¹⁸ |
| 5 | 4 | 1340 | 190 | 580 | 10 ¹⁸ |
| 6 | 8 | 1340 | 380 | 290 | 10 ¹⁸ |
| 7 | 1 | 1340 | 47 | 232 | Variable ^d |
| 8 | 4 | 1340 | 190 | 58 | Variable ^d |
| 9 | 8 | 1340 | 380 | 29 | Variable ^d |

^a U_0 is the half-spreading rate of the surface plates.

^b Peclet number : $U_0 d / \kappa$.

^c R_m : $\rho_m g d^2 / U_0 \eta_0$.

^d Mantle viscosity depends upon both temperature and pressure. A suitable pre-exponential factor is chosen such that the viscosity has a value of 10¹⁹ Pa s at 150 km depth and temperature ΔT . See text for explanation.

TABLE 2.4 Mantle Modal Mineralogy and Oxide Composition

| Mantle Modes | |
|---------------|-----------------|
| Mode | Weight Fraction |
| Clinopyroxene | 0.185 |
| Orthopyroxene | 0.240 |
| Olivine | 0.550 |
| Spinel | 0.025 |

| Mantle Oxides | |
|--------------------------------|----------------|
| Oxide | Weight Percent |
| K ₂ O | 0.0035 |
| Na ₂ O | 0.2510 |
| CaO | 3.1430 |
| FeO | 7.6675 |
| MgO | 38.6945 |
| TiO ₂ | 0.1665 |
| SiO ₂ | 46.3240 |
| Al ₂ O ₃ | 3.7545 |

TABLE 2.5 Physical Dimensions of Crust and Melting Regime

| Run # | η Pa s | h^a (km) | w^b (km) | Pressure of Melting | | |
|-------|----------------|---------------|---------------|---------------------|-------------------|--------------------------------|
| | | | | Minimum (kbar) | Maximum (kbar) | Average ^c (kbar) |
| 1 | 10^{19} | 3.8 | 35 | 5.9 | 15.7 | 10.4 |
| 2 | 10^{19} | 5.9 | 113 | 3.9 | 15.7 | 9.8 |
| 3 | 10^{19} | 6.4 | 153 | 3.9 | 15.7 | 9.8 |
| 4 | 10^{18} | 6.1 | 50 | 3.9 | 15.7 | 9.6 |
| 5 | 10^{18} | 6.3 | 114 | 3.9 | 15.7 | 9.8 |
| 6 | 10^{18} | 6.4 | 162 | 3.9 | 15.7 | 9.8 |
| 7 | $\eta(T,p)$ | 5.7 | 36 | 3.9 | 15.7 | 9.8 |
| 8 | $\eta(T,p)$ | 6.5 | 90 | 3.9 | 15.7 | 9.7 |
| 9 | $\eta(T,p)$ | 6.7 | 117 | 3.9 | 15.7 | 9.7 |

^a Crustal thickness. To form the crust, all melt is assumed to contribute to the total crustal thickness. By simple mass balance, the total thickness of the crust h is given by

$$h = \frac{1}{2\rho_f U_0} \iint \Gamma \, dx dz$$

^b The width of the neovolcanic zone, w , is defined by the flux of melt out of the top of the computational regime. If the total integrated flux of melt out of half of the box is equal to the crustal thickness h , then the neovolcanic zone width may be defined as twice the distance x_0 ($w = 2x_0$) such that the following integral has a value of $0.90h$

$$f = h \int_0^{x_0} \|q(x,z=0)\| \, dx / \int_0^{200 \text{ km}} \|q(x,z=0)\| \, dx$$

^c The average pressure of melting, \bar{p} , is the integral over the hydrostatic pressure weighted by the melt production rate

$$\bar{p} = \iint \Gamma \rho_m g z \, dx dz / \iint \Gamma \, dx dz$$

TABLE 2.6 Aggregate Primary Melt Compositions

| Oxide | 1 | 2 | 3 | 4 | 5 | 6 | 7 | 8 | 9 |
|--------------------------------|-------|-------|-------|-------|-------|-------|-------|-------|-------|
| K ₂ O | 0.03 | 0.02 | 0.02 | 0.02 | 0.02 | 0.02 | 0.02 | 0.02 | 0.02 |
| Na ₂ O | 1.82 | 1.44 | 1.40 | 1.43 | 1.42 | 1.38 | 1.51 | 1.42 | 1.37 |
| CaO | 12.18 | 12.53 | 12.57 | 12.54 | 12.56 | 12.59 | 12.46 | 12.55 | 12.59 |
| FeO | 7.48 | 7.56 | 7.58 | 7.56 | 7.57 | 7.59 | 7.54 | 7.57 | 7.60 |
| MgO | 11.84 | 12.20 | 12.25 | 12.20 | 12.28 | 12.28 | 12.12 | 12.22 | 12.27 |
| TiO ₂ | 0.80 | 0.72 | 0.71 | 0.72 | 0.71 | 0.71 | 0.74 | 0.71 | 0.71 |
| SiO ₂ | 49.81 | 49.96 | 49.94 | 50.05 | 49.99 | 49.99 | 49.94 | 49.99 | 49.99 |
| Al ₂ O ₃ | 16.05 | 15.56 | 15.52 | 15.49 | 15.49 | 15.49 | 15.62 | 15.51 | 15.45 |

The aggregate value of each melt oxide, \bar{o}_i , is the integral of that oxide over the melt regime weighted by the melt production rate

$$\bar{o}_i = \iint \Gamma o_i \, dx dz / \iint \Gamma \, dx dz$$

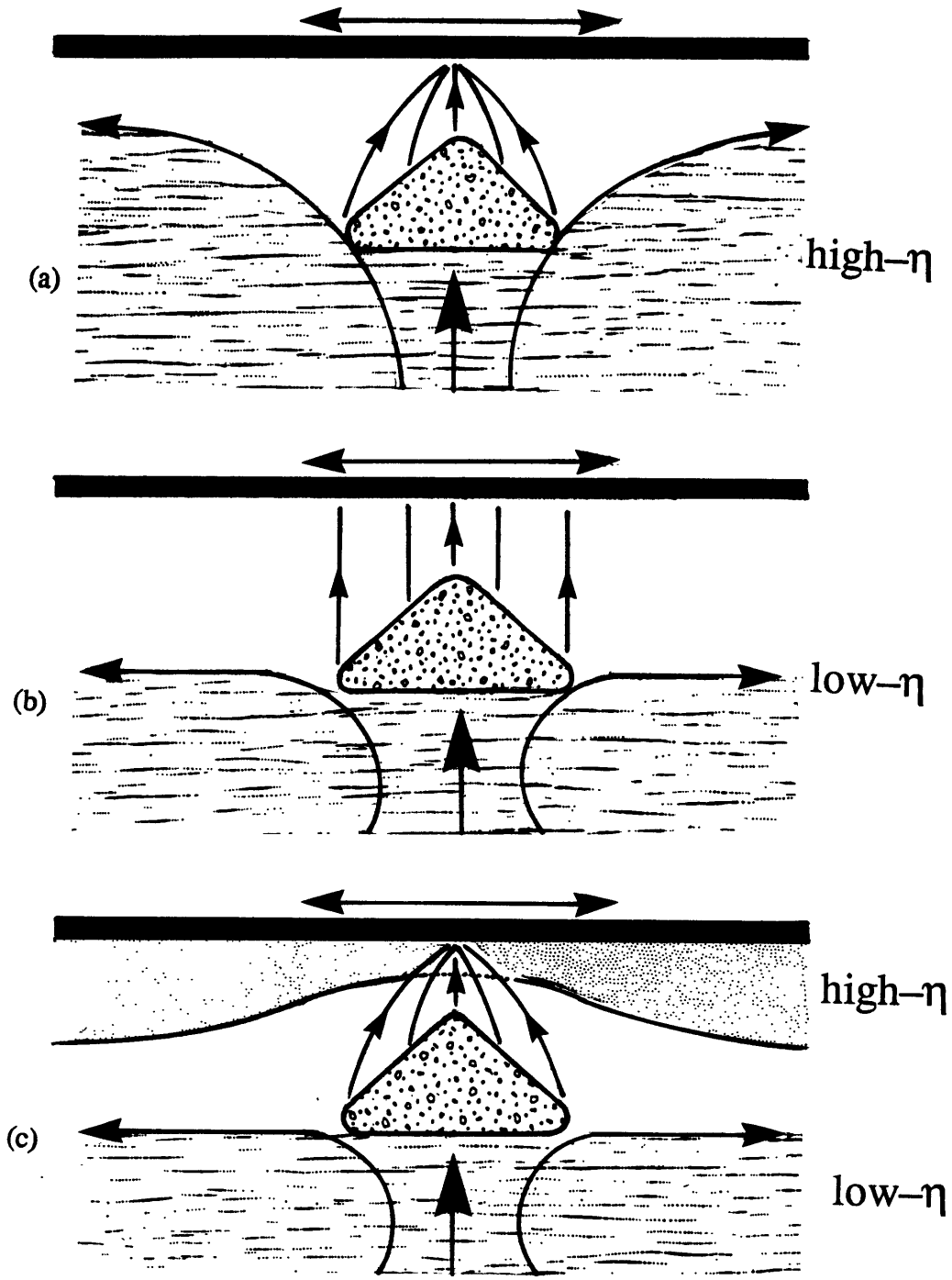


Figure 2.1

Boundary Conditions

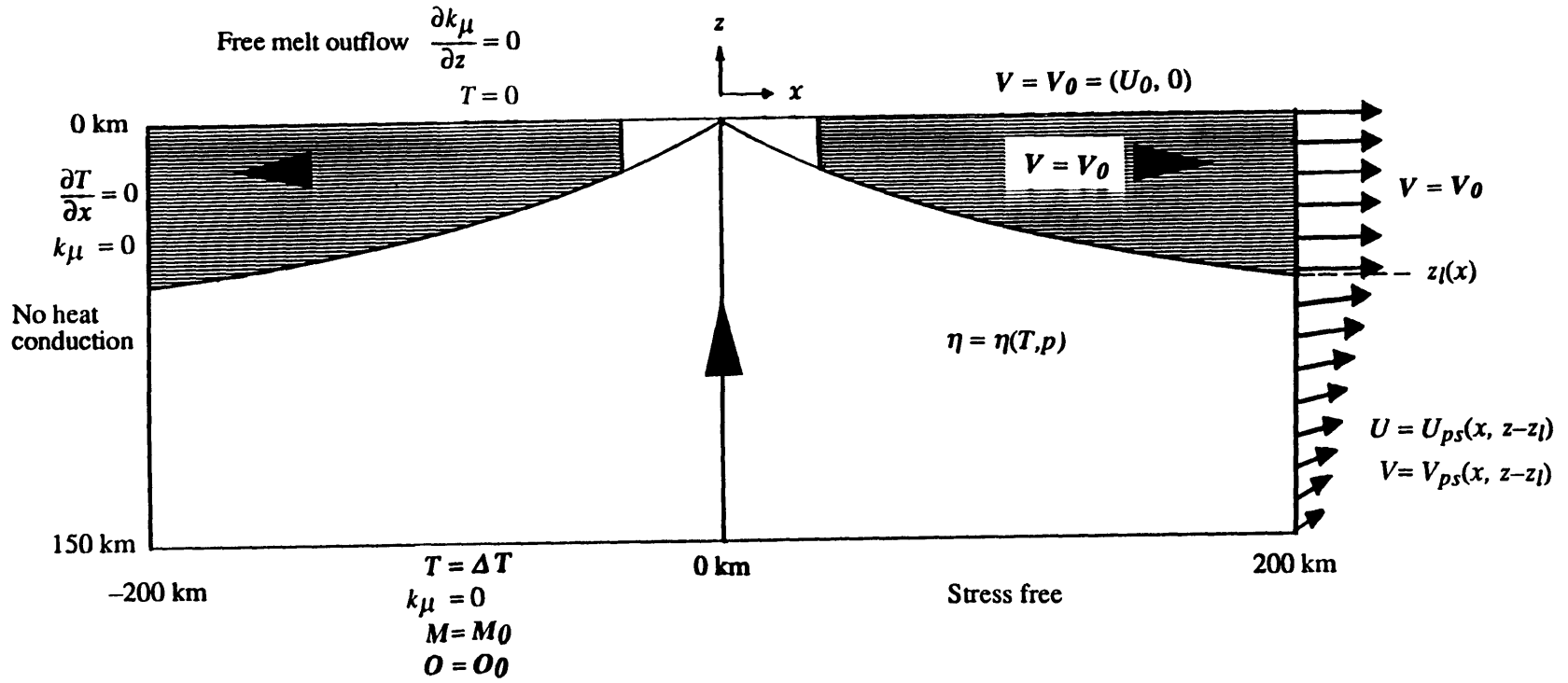


Figure 2.2

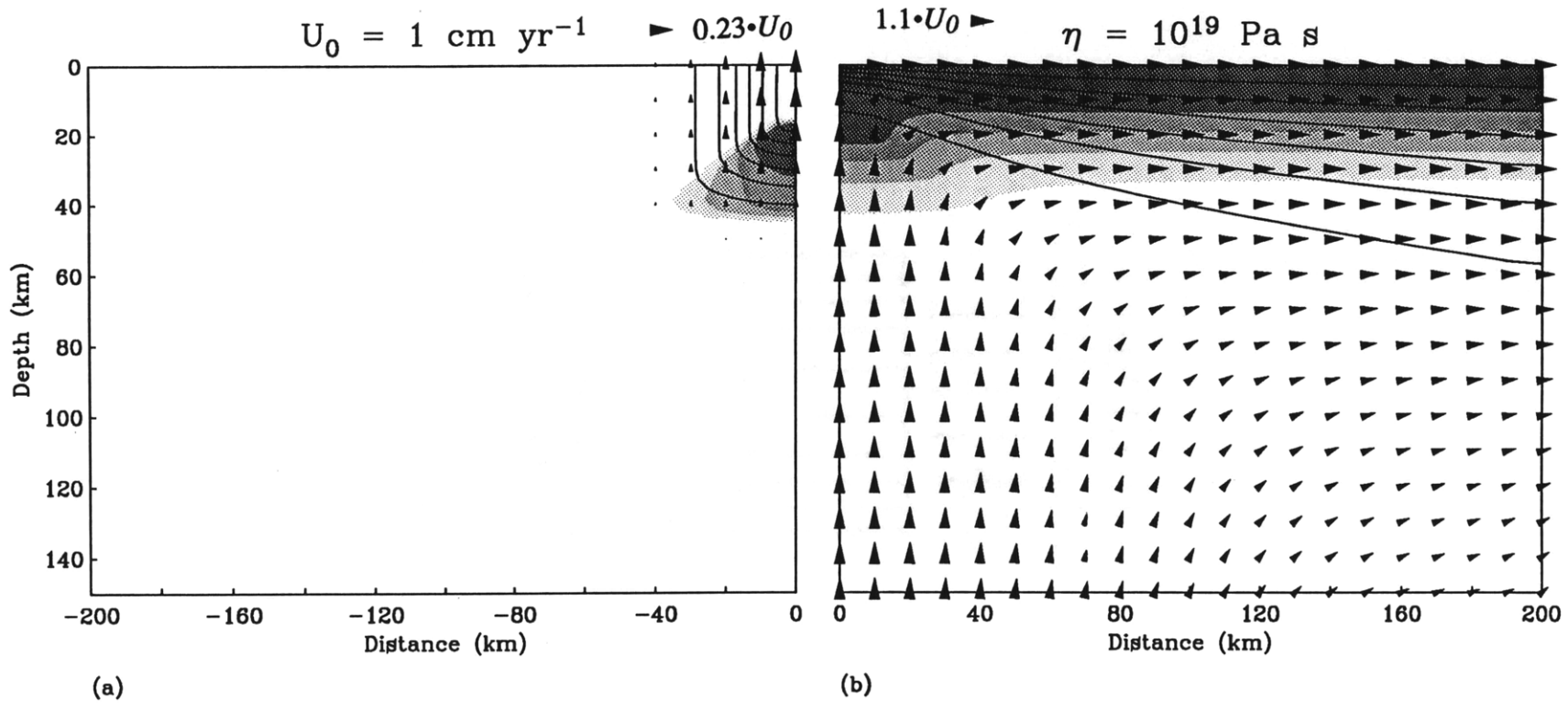


Figure 2.3

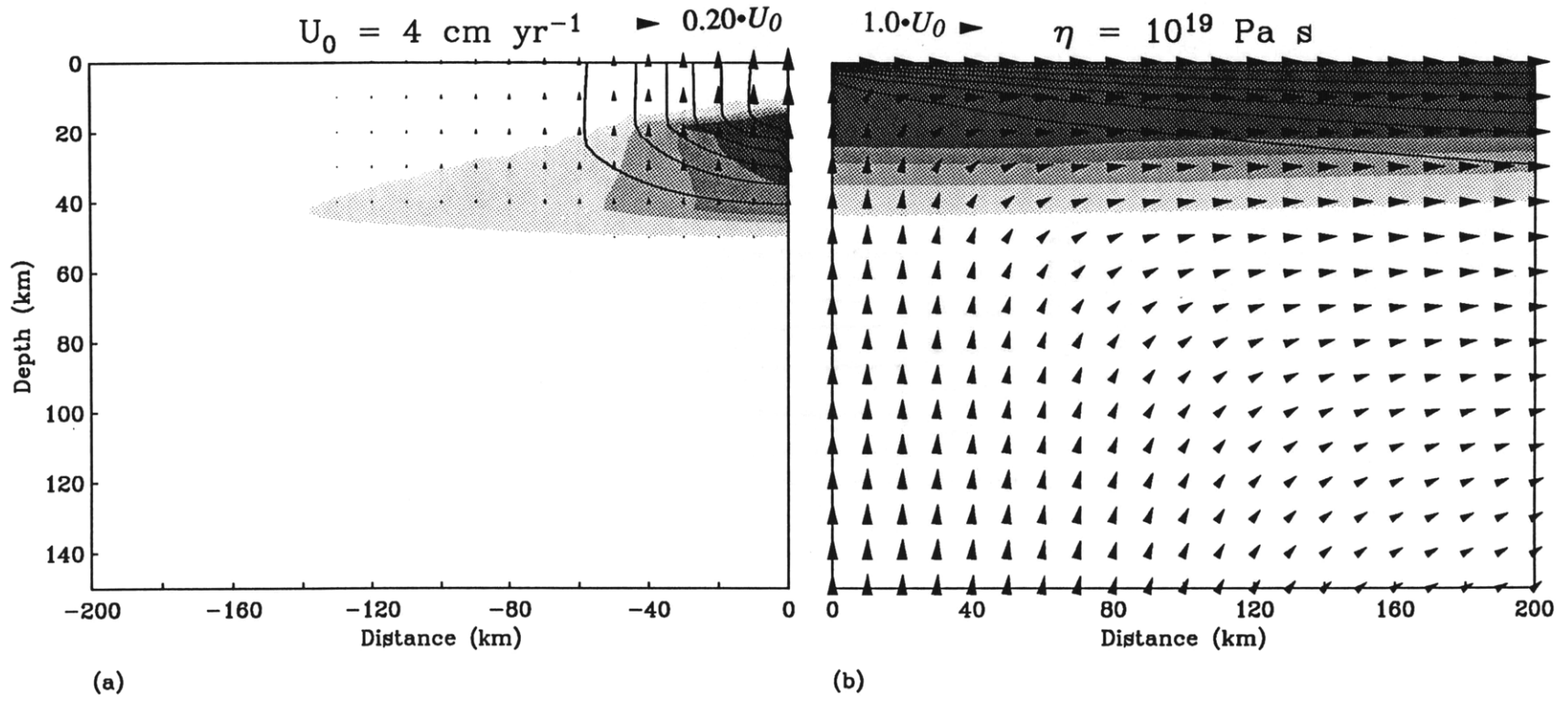


Figure 2.4

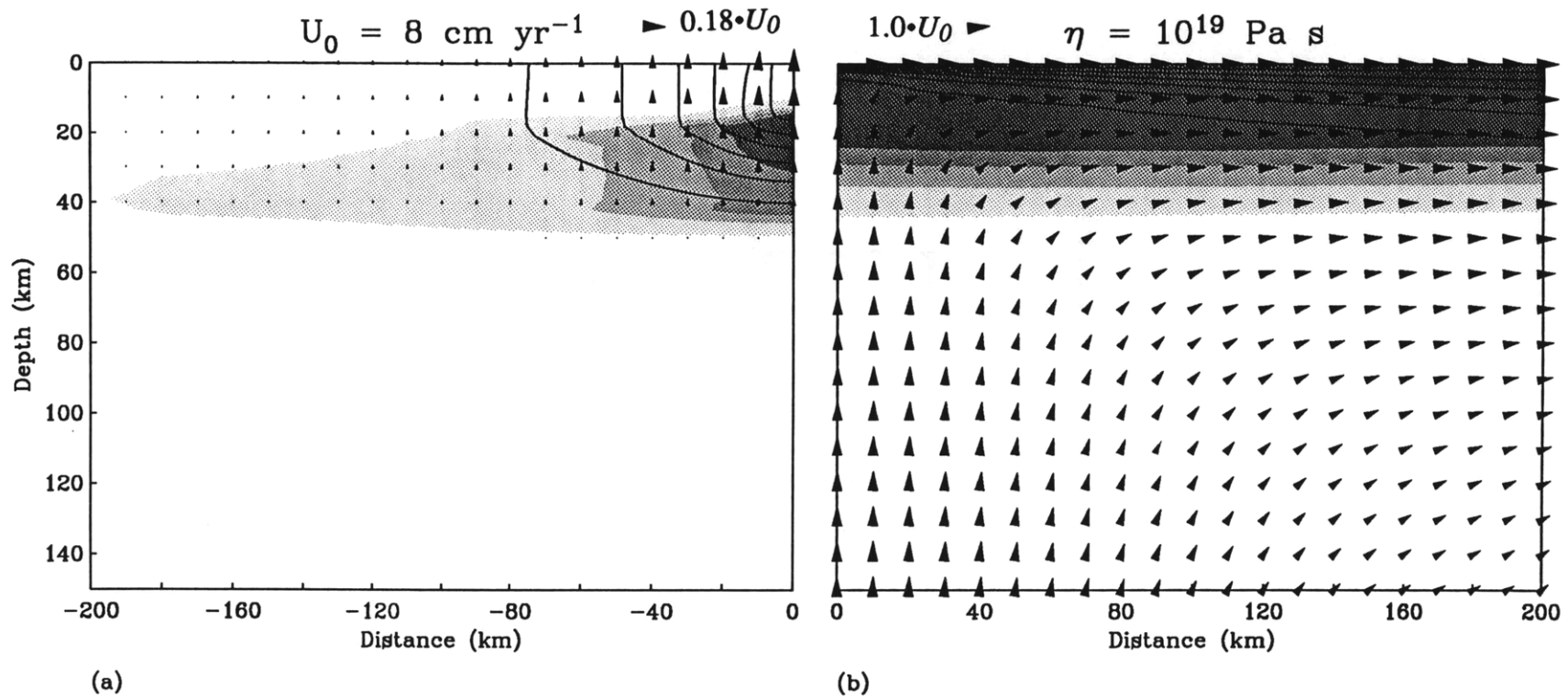


Figure 2.5

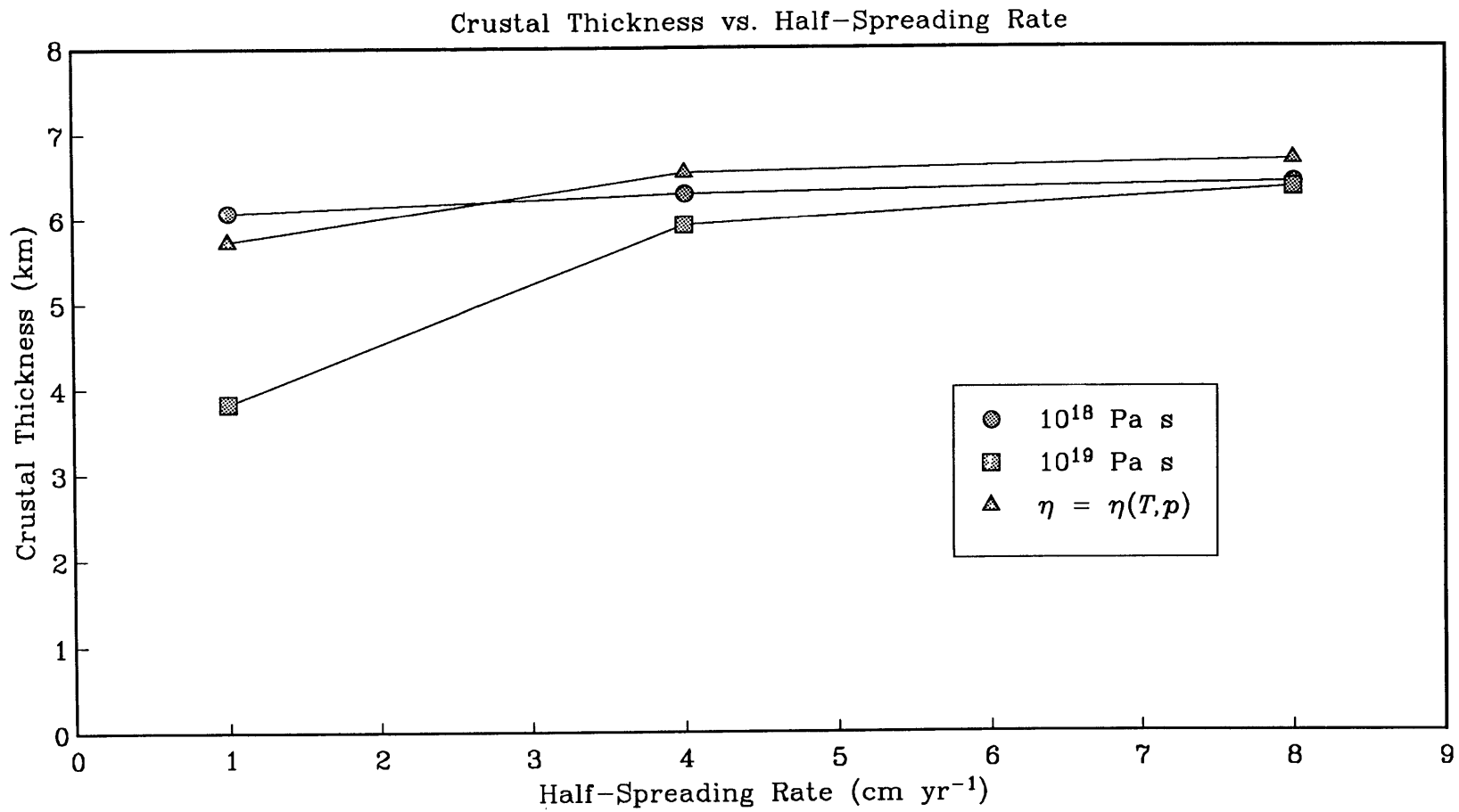


Figure 2.6

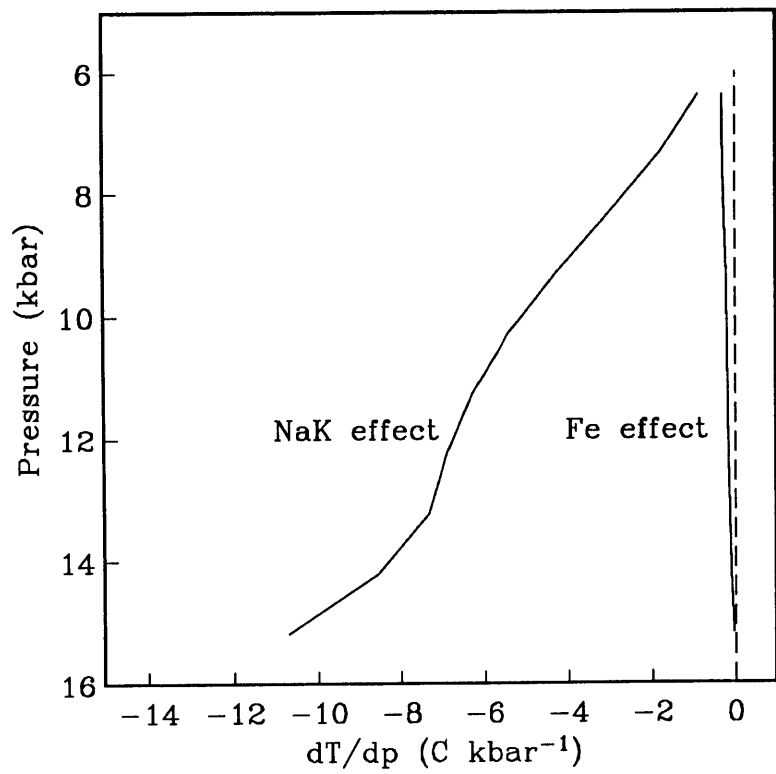
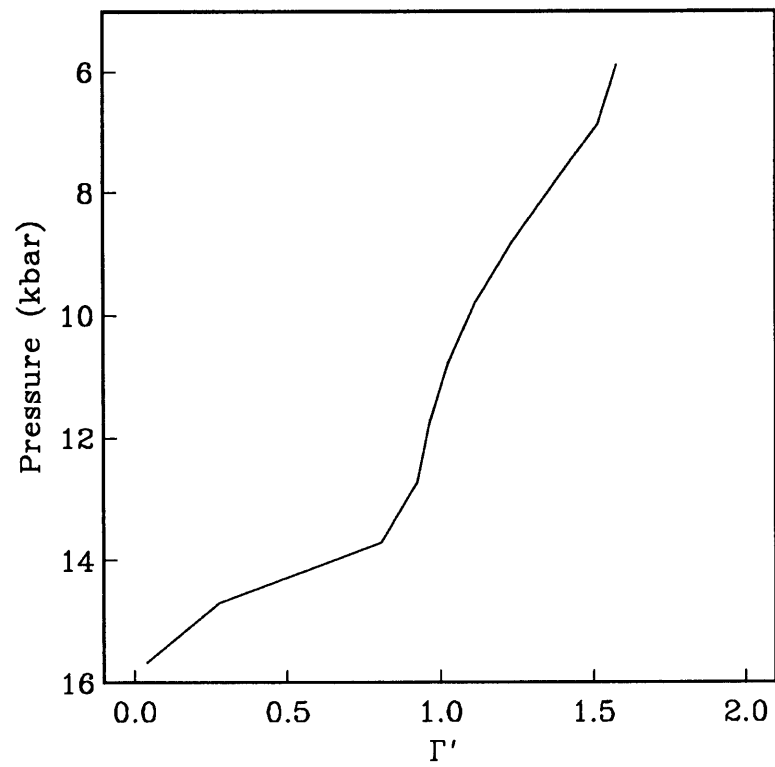


Figure 2.7



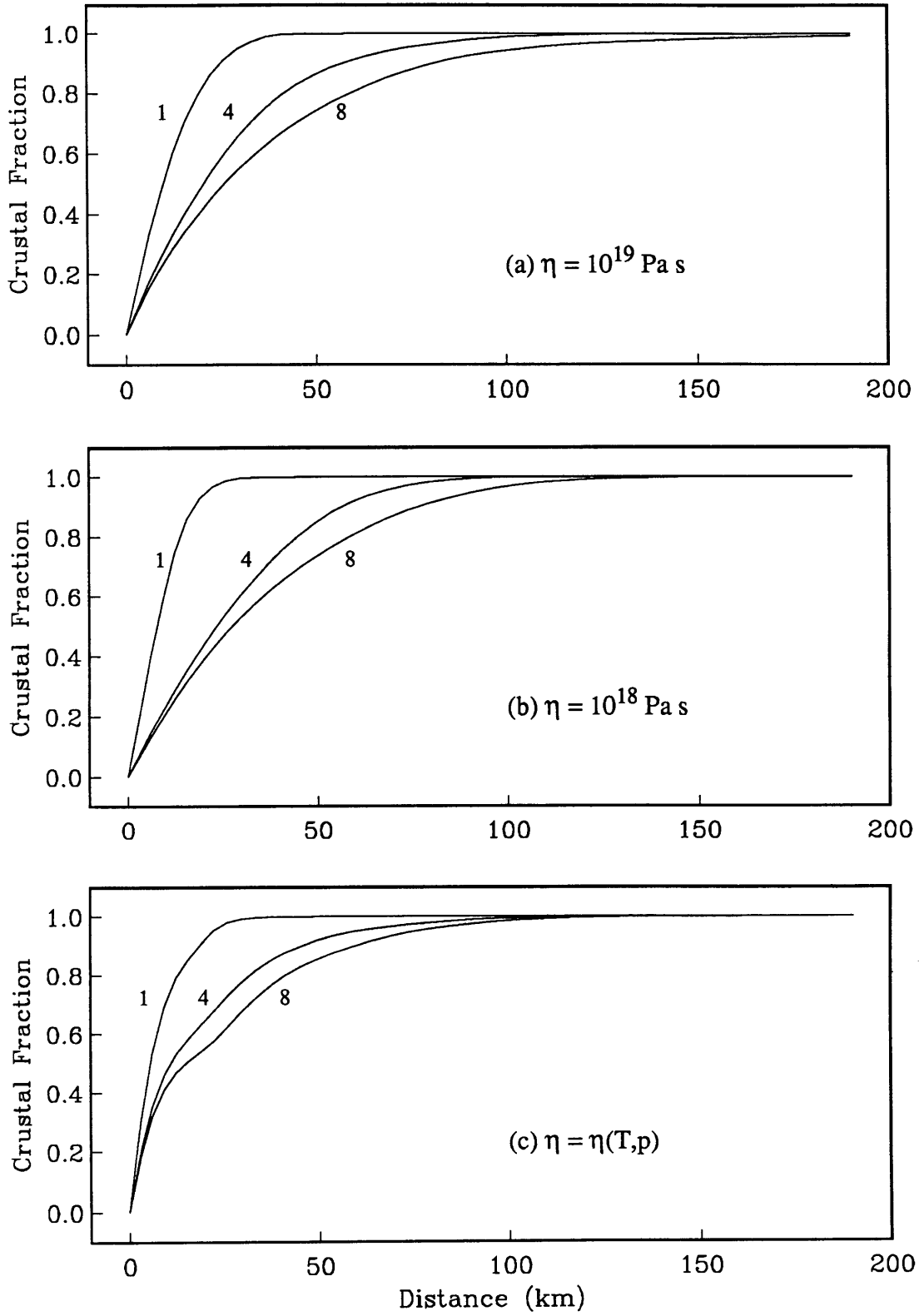


Figure 2.8

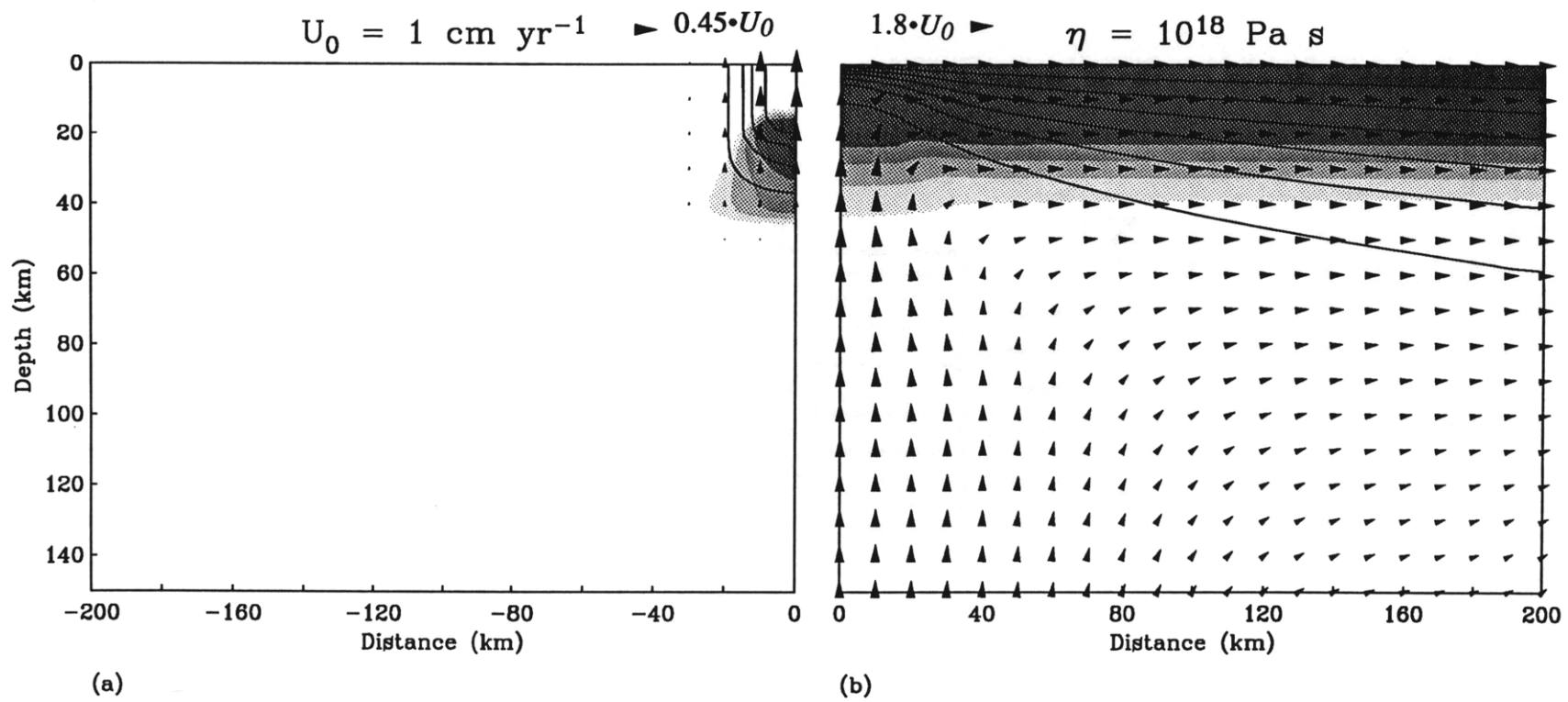


Figure 2.9

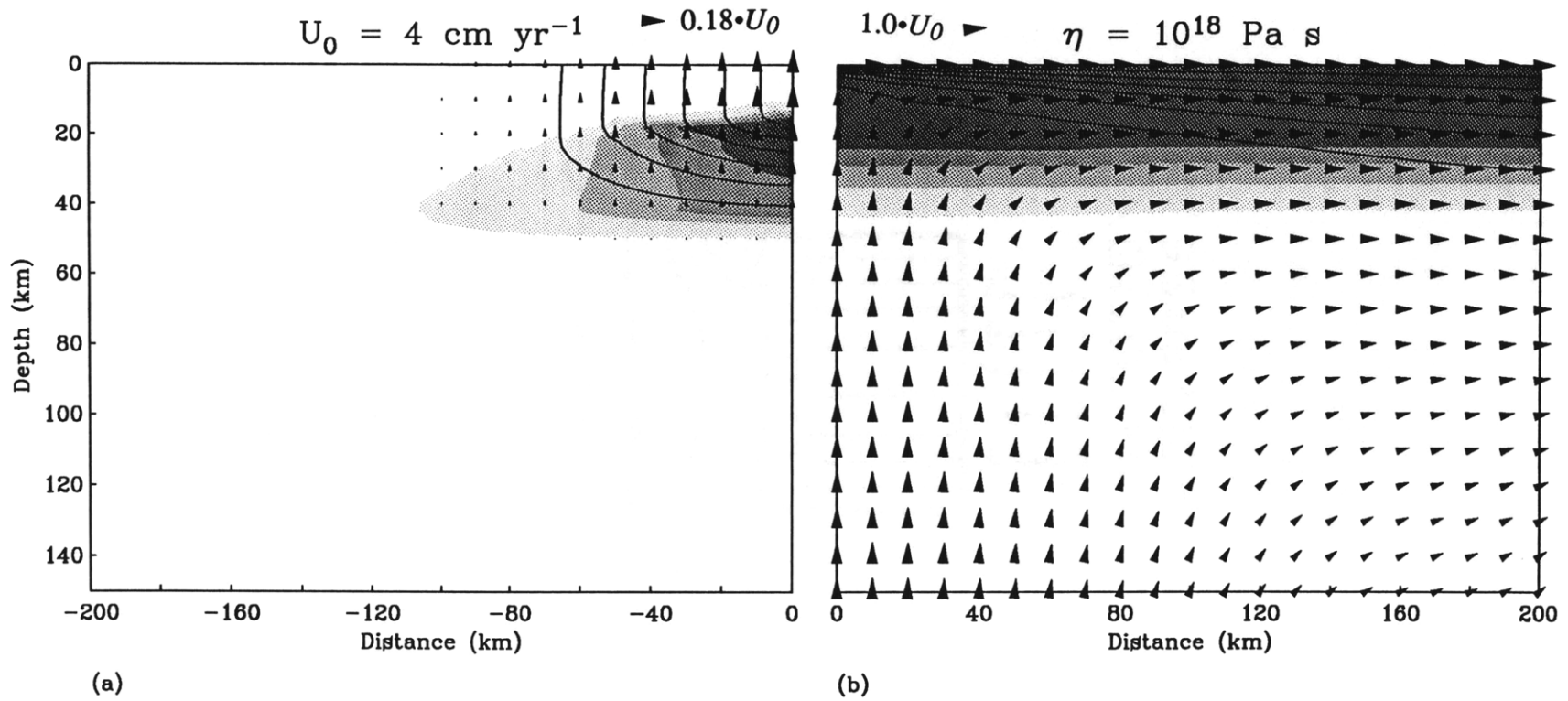


Figure 2.10

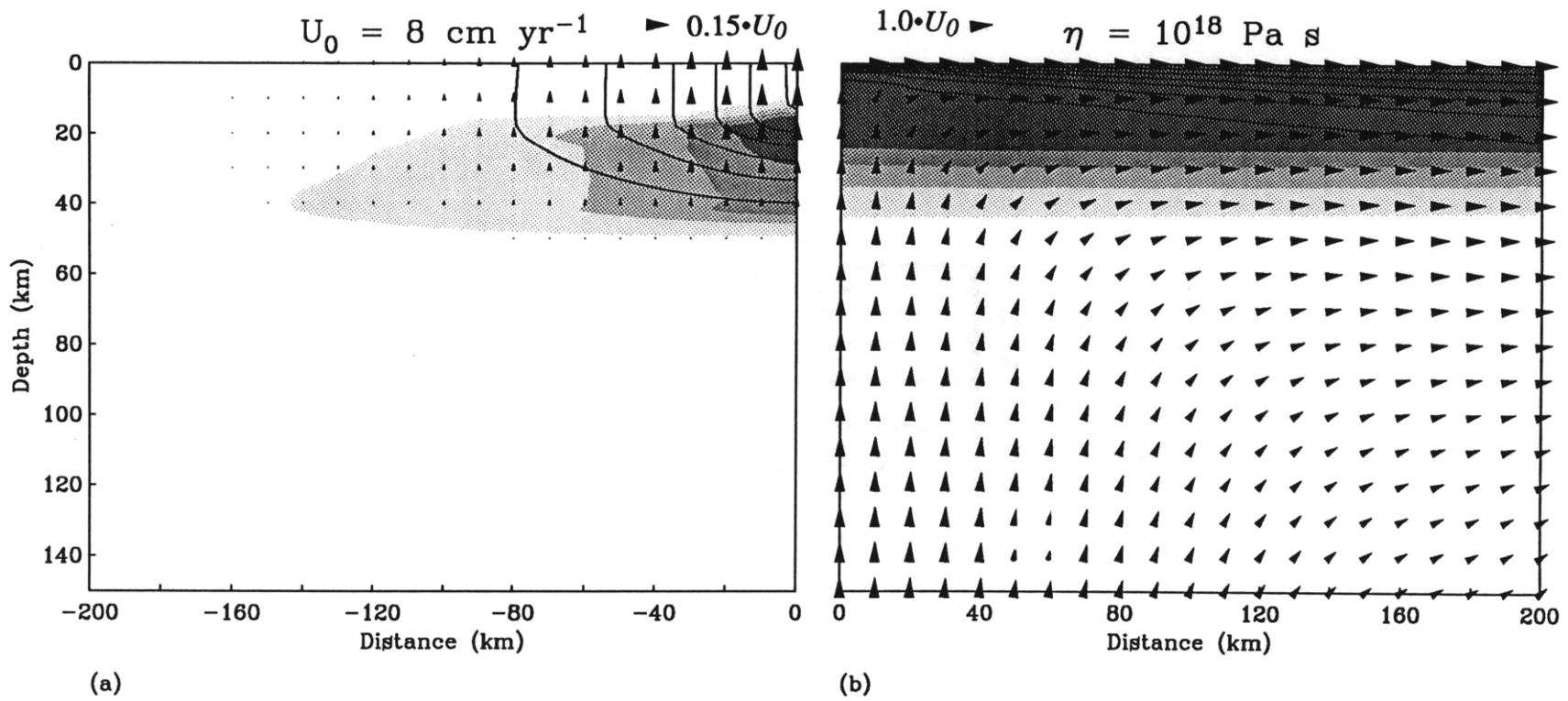


Figure 2.11

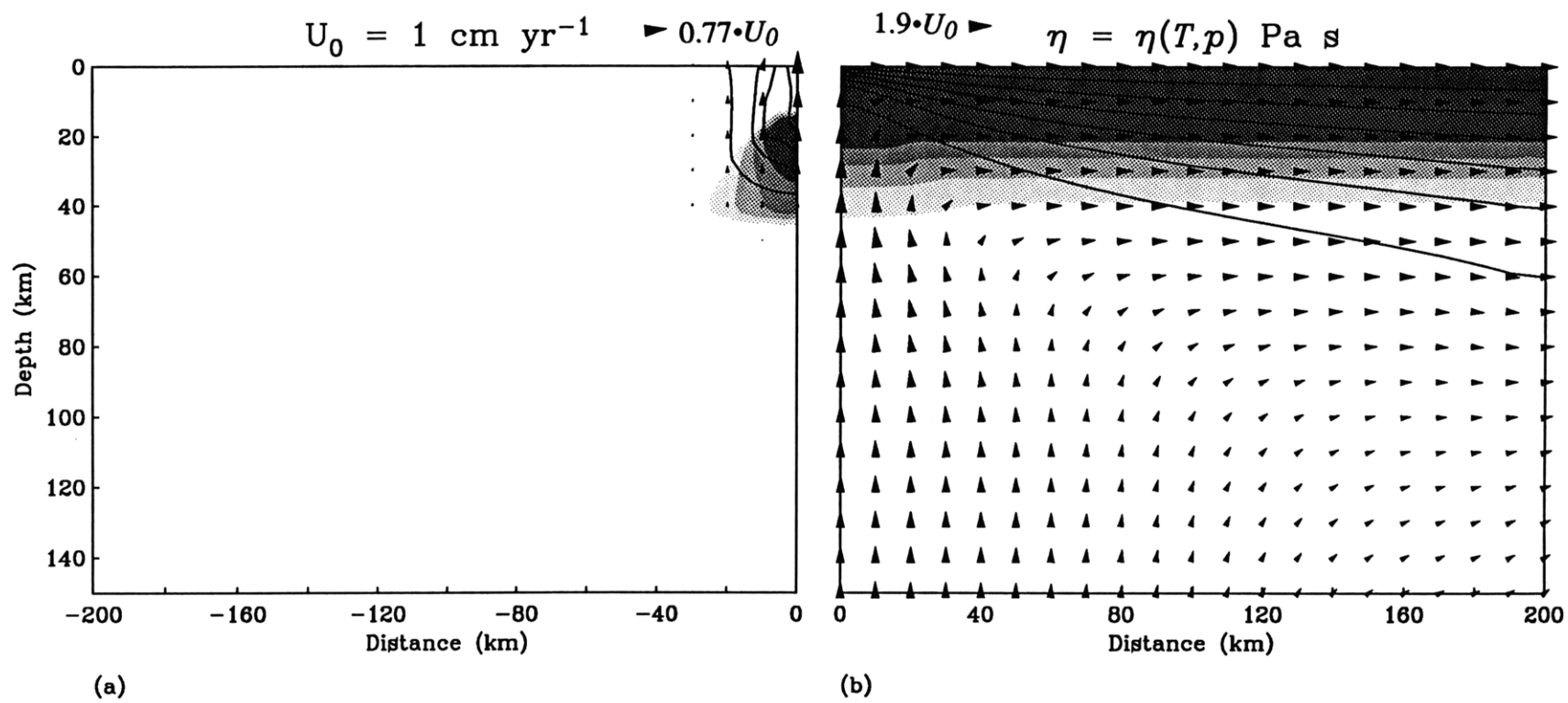


Figure 2.12

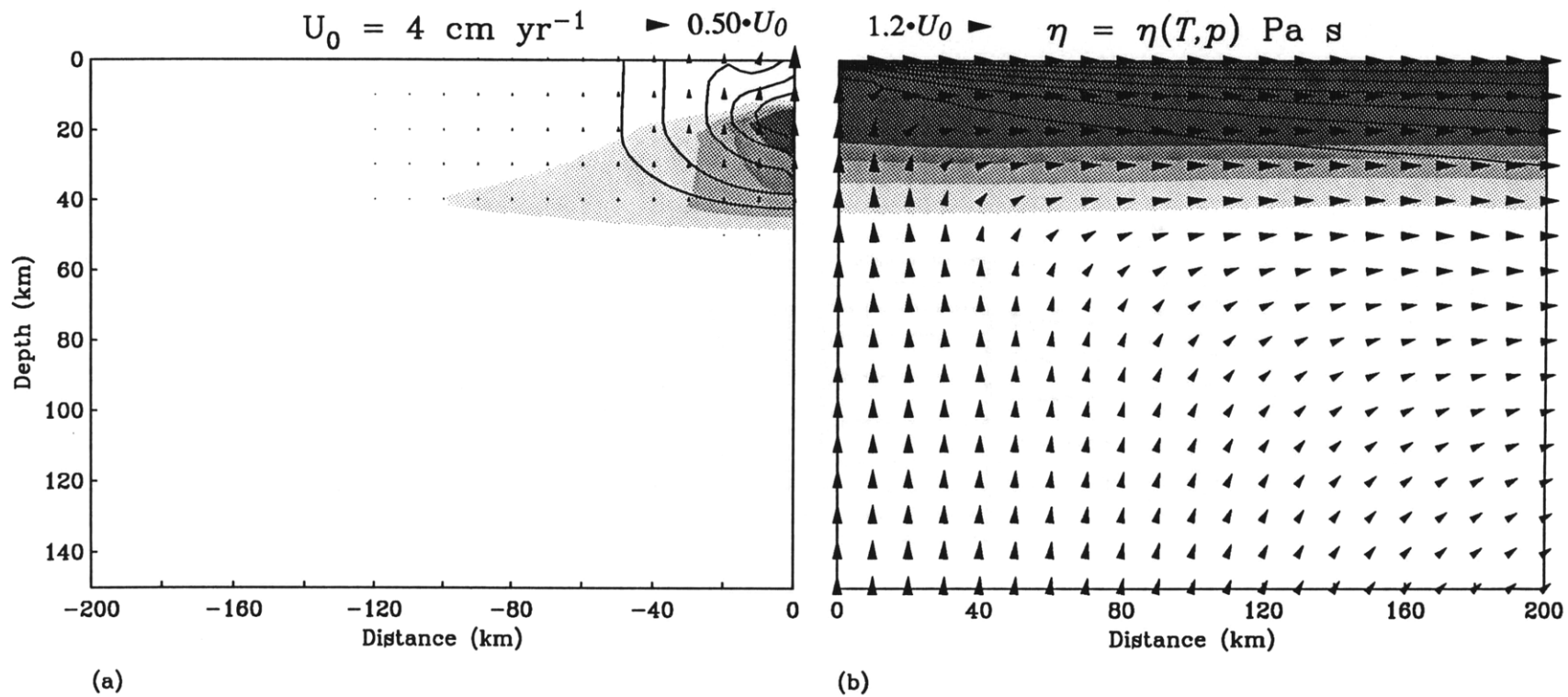


Figure 2.13

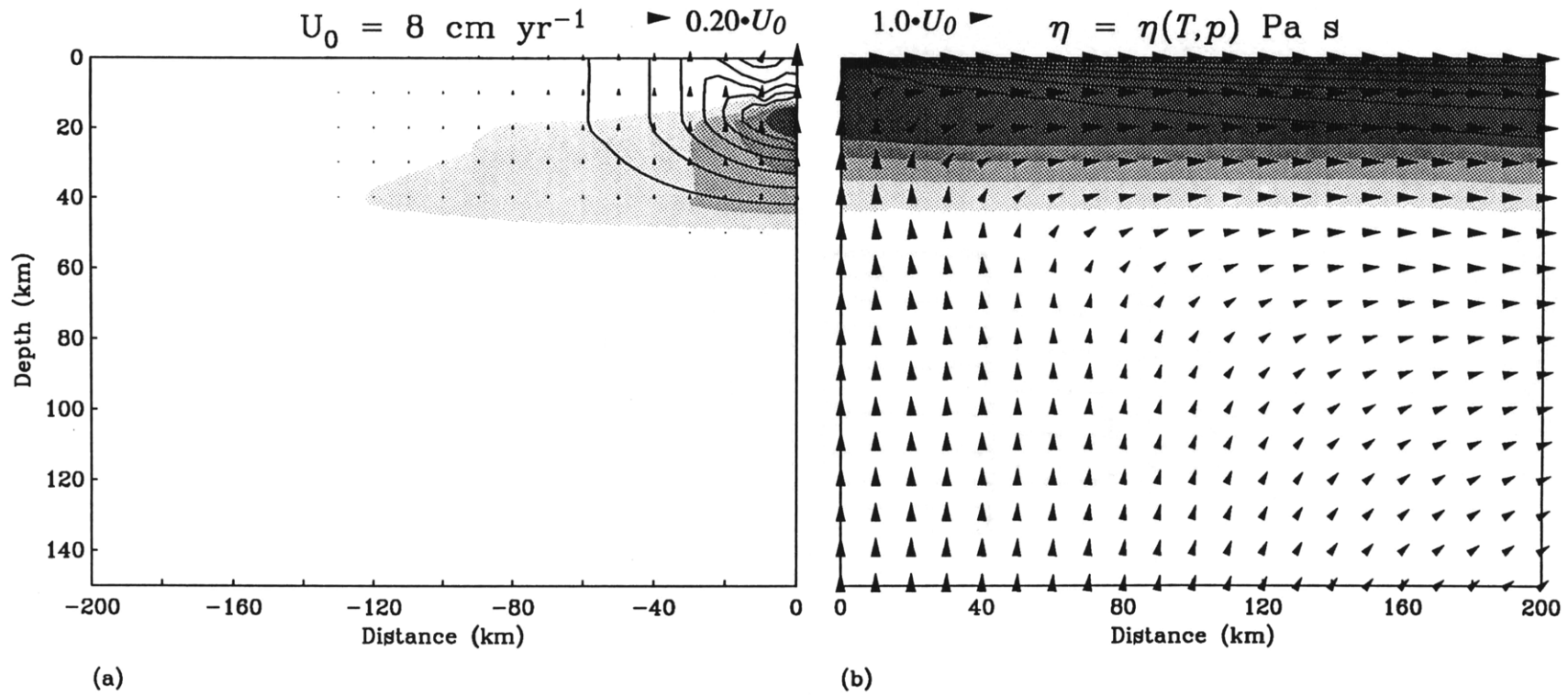


Figure 2.14

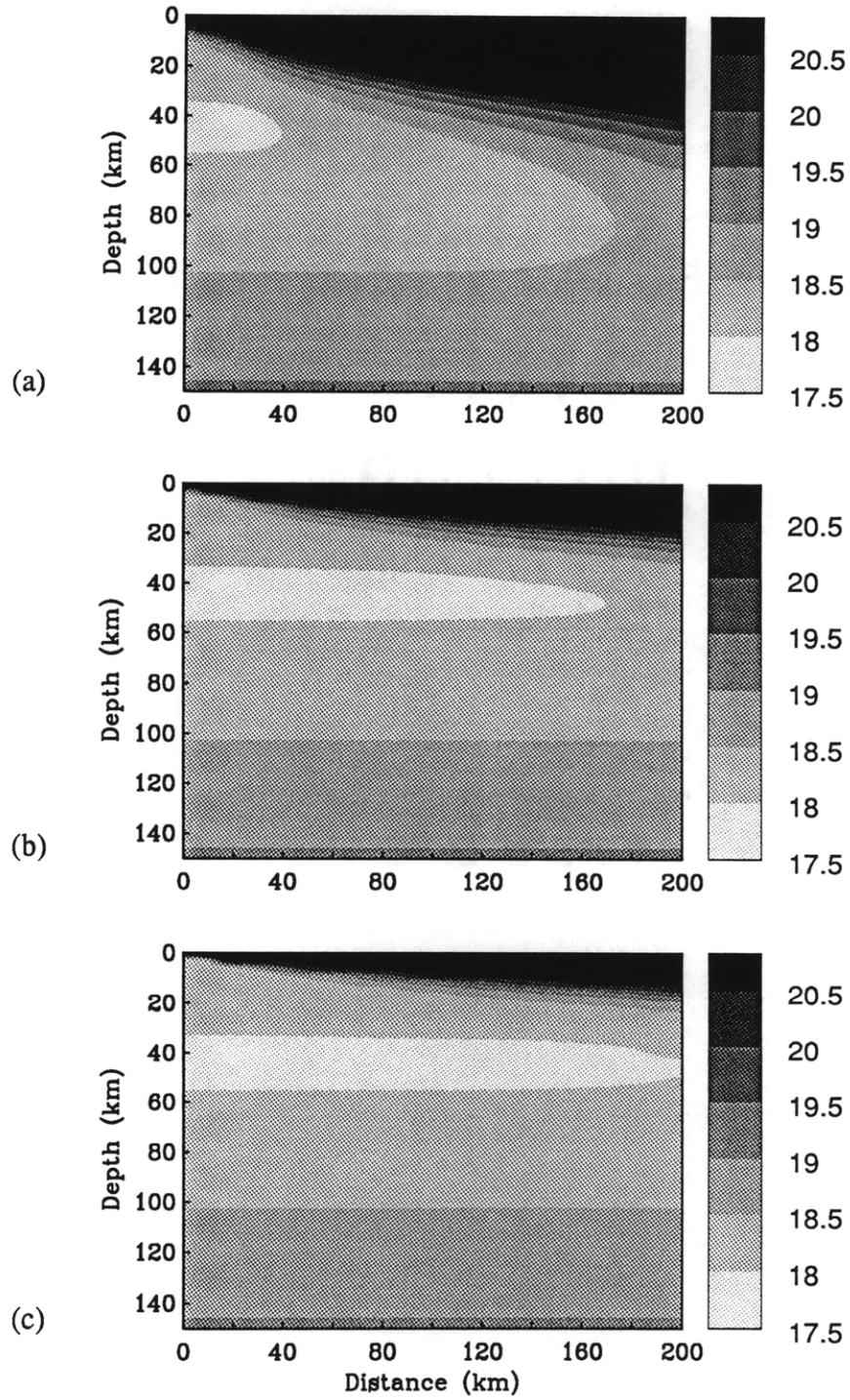


Figure 2.15

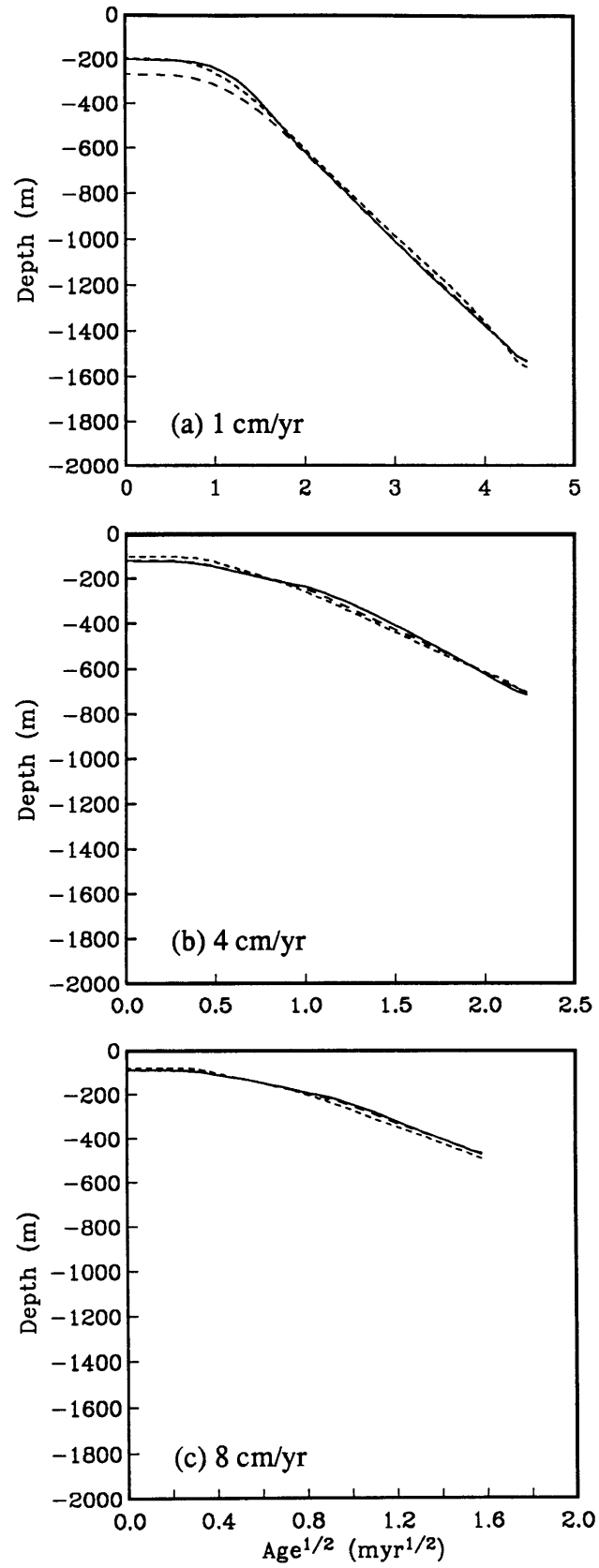


Figure 2.16

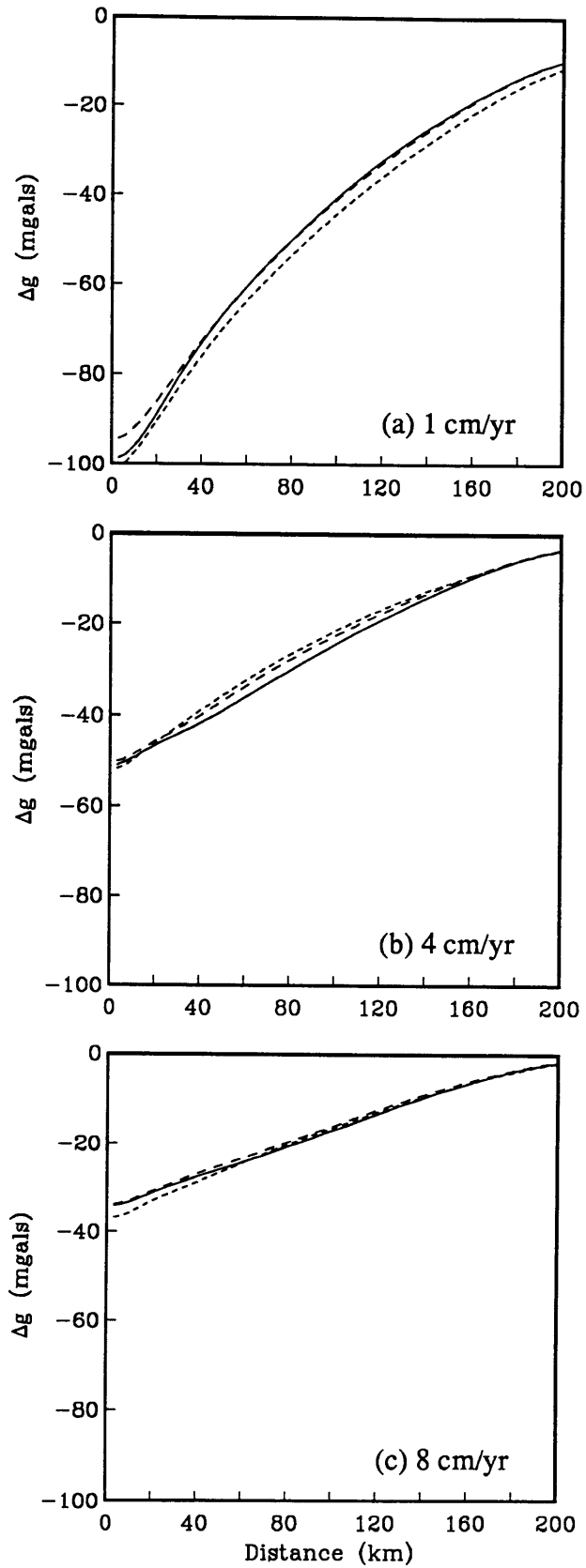


Figure 2.17

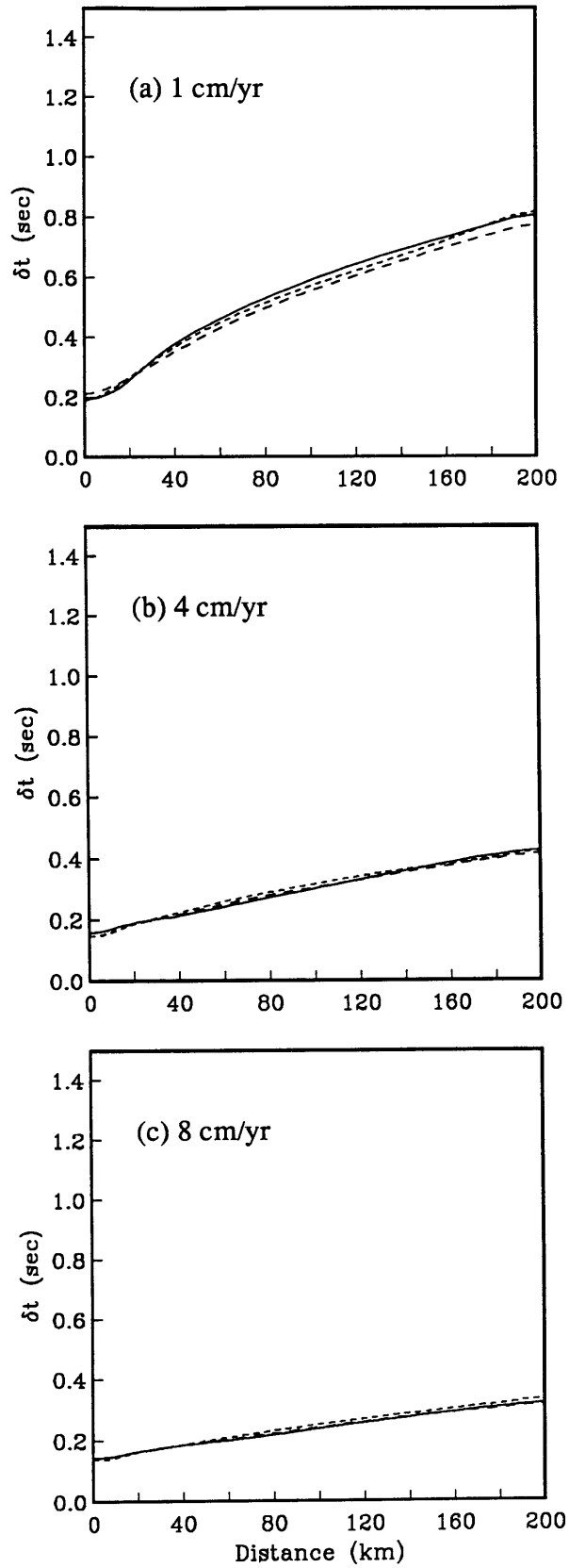


Figure 2.18

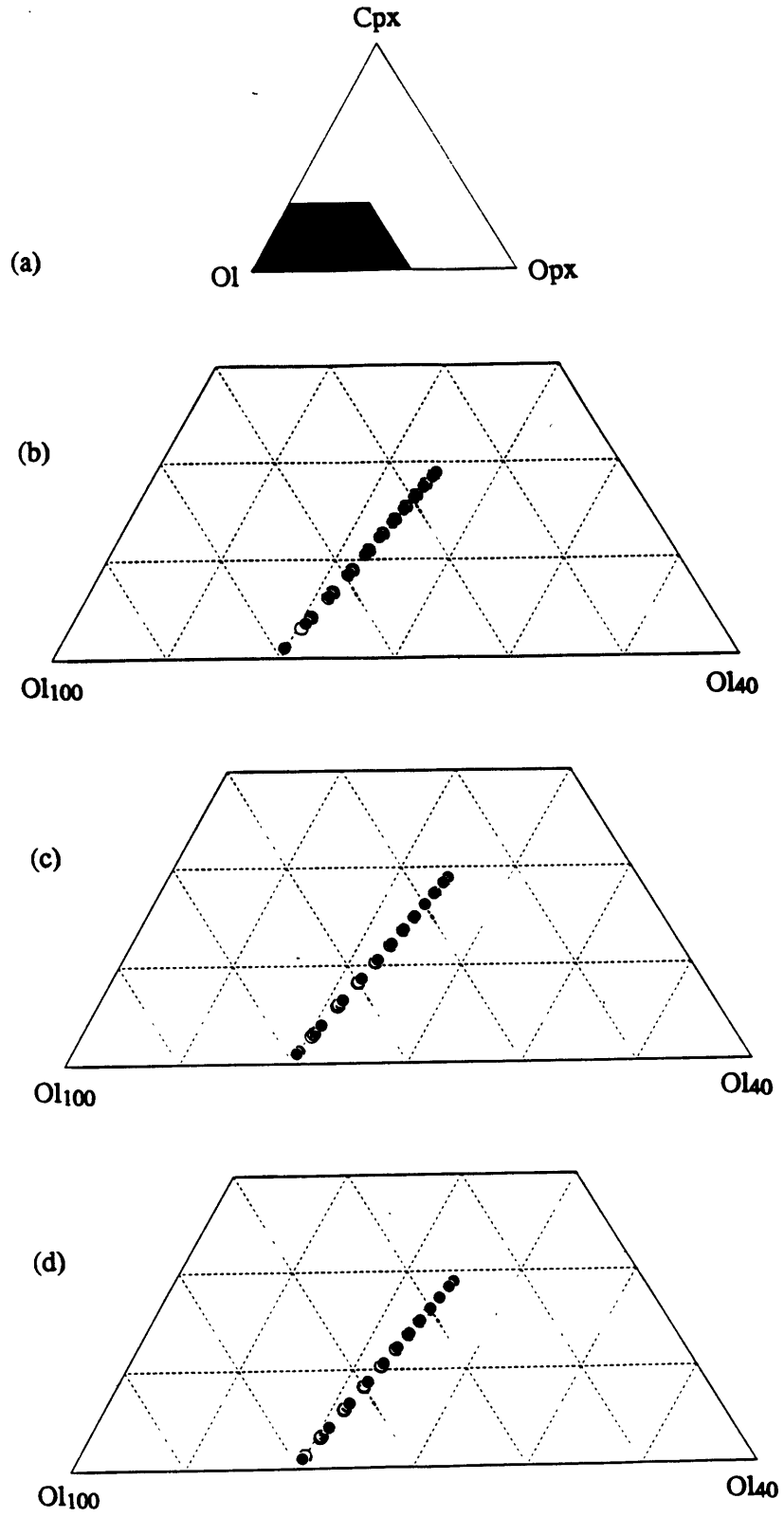


Figure 2.19

Chapter Three

Melting and Mantle Flow beneath a Mid–Ocean Spreading Center

“The best thing for being sad” , replied Merlyn, beginning to puff and blow, “is to learn something. That is the only thing that never fails. You may grow old and trembling in your anatomies, you may lie awake at night listening to the disorder of your veins, you may miss your only love, you may see the world about you devastated by evil lunatics, or know your honour trampled in the sewers of baser minds. There is only one thing for it then – to learn. Learn why the world wags and what wags it. That is the only thing which the mind can never exhaust, never alienate, never be tortured by, never fear or distrust, and never dream of regretting” .

T.H.White
The Once and Future King

INTRODUCTION

Each year approximately 20 km³ of new oceanic crust is created at mid–ocean ridges making them the predominant source of new crustal material on the Earth. Oceanic crust is the product of partial melting in the upper mantle beneath the ridge axis. The first–order description for this process is that beneath the ridge axis mantle rock rises adiabatically and begins melting at the pressure where its temperature exceeds that of its solidus. The resulting melt, lighter than its parental rock, rises buoyantly to the surface where it crystallizes to form the crust. This model, however, does little to illuminate the thermal, mechanical and chemical interactions between the melt and the mantle. These interactions at depth may likely exert a strong influence on observations at the surface. For example, melting and the advection of heat via melt percolation may alter the near–ridge mantle temperature, density, and viscosity structure and lead to significant changes in mantle flow as well as in patterns of melt production and percolation. Changes in these variables may result in observable variations in crustal thickness, bathymetry and basalt chemistry.

Melting is also the source of significant density variations in the mantle. The extraction of a melt from the mantle acts to lower the mantle density by removing the denser iron–bearing minerals [O’Hara, 1975; Boyd and McCallister, 1976; Oxburgh and Parmentier, 1977]. The resulting melt extraction–induced density variations are comparable in magnitude to temperature–induced density variations; providing a significant driving force for flow in the vicinity of the ridge axis. In addition, unlike thermal density variations, these compositional density changes are irreversible and work toward generating a layered compositional structure with the lightest and most depleted mantle overlying progressively less melted, denser, layers. Melt extraction–enhanced convection will also change patterns of melt production by altering both the flow field and the amount of heat advected into the melt production regime.

The above interrelationships suggest that there may be strong links between convection in the mantle and the generation and transport of melt. In the last few years much work in this area concentrated on the physics of extracting a melt from a porous matrix via compaction [McKenzie, 1984; Richter and McKenzie; 1984; Ribe, 1985a]. Recently, more efforts have been made towards applying the above theories to the problem of mantle flow and melt generation and migration beneath a mid-ocean ridge [Phipps Morgan, 1987; Rabinowicz and Ceuleneer, 1987; Spiegelman and McKenzie, 1987; Buck and Su; 1989; Scott and Stevenson, 1989, Sotin and Parmentier, 1989]. This study presents another step in understanding mantle upwelling and melting beneath a spreading center. The computational tool I have developed is the first truly self-consistent model of melt generation and migration because it simultaneously considers the effects of melting, melt migration, and mantle flow on the thermal structure. In this sense it bridges the gap between Scott and Stevenson [1989] (who treat melt migration and buoyant mantle flow but not the thermal structure) and Sotin and Parmentier [1989] (who treat buoyant mantle flow and thermal structure but assume rapid melt migration and neglect the effects of heat transport by melt migration on the thermal structure). In this study I apply this tool to investigate several first order questions raised by these previous studies, in particular: (1) What are the effects of the latent heat of melting? (2) How much heat is advected by the melt relative to the mantle and does this shape the melt production region? (3) Can melting-induced changes in the dynamics of the mantle by themselves account for the narrow width of the neovolcanic zone? I approach these questions by treating the various aspects of convection and melt migration beneath mid-ocean ridges in a systematic fashion.

This paper will initially examine the effects of a latent heat of melting, advection of heat by the melt and their effects on the temperature field, melt production rate and total extent of melting (the amount of depletion experienced by the mantle after the onset of melting, not to be confused with the melt fraction). Finally, I will address the effects of melt-extraction induced flow beneath a spreading center.

MODEL DEVELOPMENT

In the previous chapter, I developed a set of simplified governing equations for two-phase flow and melt generation in the oceanic upper mantle. In this chapter, I will use the same equations with no modifications.

Numerical solutions to the differential equations presented above are obtained using the finite-element method. The computational geometry and boundary conditions for each experiment are summarized in Figure 3.1. The computational domain has dimensions 400 km (horizontal) x 150 km (vertical). The computational grid has a variable spacing with a

minimum horizontal resolution of 3 km at the ridge axis and a minimum vertical resolution of 3 km above 60 depth. The total number of nodes is 73 in the horizontal direction and 37 in the vertical. In all models, the half-spreading rate is $U_0 = 1 \text{ cm yr}^{-1}$, the mantle temperature is $1340 \text{ }^\circ\text{C}$, and the mantle viscosity is 10^{18} Pa s .

RESULTS

In this section I present a suite of four calculations designed to illustrate the effects of latent heat of melting, advection of heat by the melt, and compositionally-driven convection. To better compare these effects, I will assume a constant half-spreading rate of 1 cm yr^{-1} . My first goal is to investigate the effects of incorporating the latent heat of melting into the energy equation. Next, I will present a model that also incorporates the effect of advection of heat due to melt migration. The final model includes melt extraction-induced density variations that also shape sub-ridge flow. As mentioned above, I will ignore the effects of various thermal phenomena and compaction of the mantle due to the mass loss resulting from melt extraction [current work by *Parmentier and Phipps Morgan* (unpub.) show these effects to be small].

The Effect of Latent Heat of Melting

To properly investigate the effects of the latent heat of melting, I would like compare two steady-state models: one with a low latent heat of melting and the other with a latent heat close to a reasonable mantle value. I will compare the results of two models with finite but significantly different latent heats of melting ($\Delta S_m = 250 \text{ J kg}^{-1} \text{ }^\circ\text{C}^{-1}$ and $\Delta S_m = 450 \text{ J kg}^{-1} \text{ }^\circ\text{C}^{-1}$). As mentioned above, the first model (model *P-L250*, $\Delta S_m = 250 \text{ J kg}^{-1} \text{ }^\circ\text{C}^{-1}$) is an extremely simple one. Compositional buoyancy forces are neglected; thus flow in the mantle, and flow-induced advection of mantle heat, are driven solely by surface plate motions. Figure 3.2 shows the resulting flow field along with the temperature, melt production rate, and total extent of melting. The maximum pressure of melting is defined by the depth where the mantle first intersects the solidus. The minimum pressure of melting is defined by the point where clinopyroxene is lost as a phase ($\text{cpx} < 1\%$). Melt production rates increase monotonically through the melting regime up to the cessation of melting. The cross-sections of temperature and melt production rate in Figure 3.3 allow us to see the points outlined above more clearly. Table 3.1 also lists some useful parameters describing the melt production regime. Note that this model produces 4.7 km of crust and that it achieves a maximum extent of melting of 20% beneath the ridge axis.

My next model increases the entropy of melting to $450 \text{ J kg}^{-1} \text{ }^\circ\text{C}^{-1}$ (model *P-L450*), a value more reasonable for the mantle. Figure 3.4 and Table 3.1 show that the dimensions

of the melting regime are essentially the same as in the previous model. However, the minimum pressure of melting is higher because melting in this model ceases due to the onset of conductive cooling rather than the loss of clinopyroxene. The different distribution and lower extents of melting between these models are reflected in the smaller crustal thickness (3.0 km). Figure 3.4 shows that melting is more uniformly distributed about the melt production regime though the maximum melt production rates do occur beneath the ridge axis, as expected. Melt production rates are lower than in the previous model because the entropy of melting is now twice as large as before. More energy is required to produce a given amount of melt and thus melt production rates decrease. Another factor is that heat is extracted through melting without accounting for advection of heat via the melt. As shown below, however, heat advection via the melt in these models is smaller than the effects of the latent heat of melting.

The Effect of Advection of Heat via Melt Percolation

In my next model, I include the effects of advection of heat due to migration of the melt. The advection of heat due to the melt raises the isotherms above the melt production region (Figure 3.5, model $P-L+Q$). Similarly, the melt production rate also increases because the advection of heat due to the melt provides an energy source for additional melting at shallower depths. Why the melt production rate increases can be explained by considering a cross-section of temperature beneath the ridge axis. At some depth in the melting regime, a small, finite amount of melt is formed. Let this melt be transported vertically to a point within the melting regime but at a lower pressure. Perforce, the temperature at that point is lower because of the solidus' pressure dependence and, hence, so is the total energy at this point ($\rho_m C_p T$). The additional energy provided by the presence of the melt ($\phi \rho_f L$) results in an increase in the mantle temperature and thus the melt production rate increases. The crustal thickness increases by 20% (0.9 km, maximum extent of melting ~10%).

Both the permeability (actually the permeability–melt viscosity ratio but the melt viscosity is nearly a constant) and the melt flux vectors (Figure 3.5) show that, at this low mantle viscosity of 10^{18} Pa s, the mantle pressure gradients due to the divergence of the surface plates are small relative to the buoyancy of the melt and, hence, are not large enough to focus melt to the ridge axis [cf. *Phipps Morgan, 1987*]. The melt rises vertically and this is mimicked in the contours of k_μ . Note further that k_μ increases with height through the melting regime. This is a consequence of the fact that the equation for k_μ is essentially an advection equation with a source term that is the melt production rate. Thus, as melt rises in the melt regime, k_μ must increase in order to accommodate both local

melt production and the advection of melt from below. Above the melt regime there are no more sources of melt and k_{μ} is a constant along the melt flowpaths (I can, but do not, include the effect of melt solidification). It is interesting to note that the maximum dimensional value for the permeability is $4.1 \times 10^{-14} \text{ m}^2$ if the melt viscosity is taken to be 10 Pa s. This is certainly within the range of values given by *Maaløe and Scheie* [1982].

In this model, where the mantle viscosity is 10^{18} Pa s, melt buoyancy forces dominate mantle pressure gradients in D'Arcy's Law and melt rises vertically. The vertical advection of melt and the broad width of the melting regime result in a 117 km-wide "neovolcanic" zone.

The Effect of Buoyancy-Driven Flow

In my final model (model *CC-L+Q*), melting-induced variations in mantle density also drive convection. Because of the low viscosity used, the effect of this flow is to eliminate horizontal variations in density clearly shown in the previous three models [cf. Figure 3.6; *Sotin and Parmentier*, 1989] Unlike thermal buoyancy forces, the effect of compositional convection is limited to the region near the ridge axis. Beneath the ridge, convection causes mantle rock to be drawn through a region approximately the width of the melting regime. Within a few kilometers of the melting regime, where the total extent of melting (density) is no longer changing, the mantle begins moving laterally along paths of constant density. Were a mantle parcel to deviate from this path, differential buoyancy forces would return it to its original depth because the mantle density field is now stably stratified (excluding thermal effects of course).

This convection sharply increases melt production rates because more mass is now advected above the solidus. Accordingly, the crustal thickness and the maximum extent of melting increase to 6.1 km and 19%, respectively and melting beneath the ridge ceases when clinopyroxene is lost. Mantle temperatures above the melting regime increase sharply (up to 200 °C) reflecting the thinning of the thermal boundary layer (cf. Figures 3.5 and 3.6).

The melting region in this model narrows from 117 km to 66 km. This is due to the fact that convection has caused upwelling beneath the ridge to be confined into a narrower region than in the previous models. Since the region of vertical mantle flow is narrower, and upwelling is the main cause of mantle melting, the melting regime narrows. The thinning of the thermal boundary layer causes the melt regime to thicken by 6 km (Table 3.1). Note that melt production no longer has a low production 'tail' away from the ridge axis as in Figure 3.2. Also, the maximum dimensional permeability has increased by almost an order of magnitude to $1.8 \times 10^{-13} \text{ m}^2$; reflecting the higher melt production rates.

The ratio of heat advection by melt vs. mantle flow is shown in Figure 3.7. Maximum melt heat transport is about 30% of the upward mantle transport above the melting region, suggesting that melt migration does significantly affects the sub-ridge thermal structure above the melting region.

Finally, note that the additional pressure gradients caused by the presence of melt extraction-induced flow are not capable of focussing melt to the ridge axis. Both the permeability and the melt flux vectors indicate that melt again rises essentially vertically.

DISCUSSION

A primary goal in modelling mantle dynamics at mid-ocean ridges is an understanding of the relative effect various forces and parameters have upon mantle flow, melting and melt migration. Much of the interesting physics, such as compaction and compositionally-driven convection, is determined by the nature of melting and the magnitude and distribution of melt production. In its turn, deformation and flow in the mantle and the heat transported by it influence how the mantle melts. As this chapter has shown, incorporating the effect of latent heat of melting and the advection of heat by the melt are important parameters controlling the magnitude and distribution of the melt phase. The total amount of melting will also determine the crustal thickness. The work I present here clearly indicates that melting and melt migration in models of mid-ocean ridge dynamics needs to be properly parameterized and accounted for in the energy balance if a constraint such as crustal thickness is to be used as discriminant between various models.

CONCLUSIONS

(1) A large impediment to further progress in studies of melt migration at mid-ocean ridges is our uncertainty in the functional dependence of permeability upon melt fraction. The rate at which both mass and heat may be transported by the the melt are critically dependent upon the permeability. As the transport of heat via the melt may affect melt production rates, the extent of melting, etc., it is important that this parameter be well determined. For steady-state melt migration, we are able to derive an equation for the ratio of permeability to melt viscosity from a set of simplified governing equations. This equation lets the permeability adjust for both local production of melt and the advection of melt from other regions. Also, our formulation allows for the potential effects of anisotropy.

(2) The effect of latent heat of melting is to reduce mantle temperatures to the solidus wherever sufficient heat is advected to cause melting. Lowering the latent heat of melting causes both the total amount of melting and the melt production rates to increase. The latent

heat also has an effect on the variation of melt production rate with depth. Small latent heats yield high melt production rates. More mantle-like latent heats decrease melt production rates because less heat is required to keep the mantle temperature on its solidus for a given amount of melt. Differences in the latent heat of a factor of two can lead to large differences in the thickness of the crust. For low latent heats ($250 \text{ J kg}^{-1} \text{ }^\circ\text{C}^{-1}$), melt production rates are high and melting continues until clinopyroxene is lost as a phase. Since most of the basaltic component is melted out for this value of the latent heat, the crustal thickness is higher than for a high-latent heat model ($450 \text{ J kg}^{-1} \text{ }^\circ\text{C}^{-1}$) where melting ceases due to the onset of conductive cooling.

(3) The advection of heat due to the melt increases melt production rates by providing additional energy for melting at shallower depths. Outside the melting region, melt heat advection raises isotherms and provides a means for changing the thickness of the melting region by providing additional energy for melting at lower pressures. These may be important effects where melt is focussed into a narrow region. In my simple plate spreading models, the combined effects of low melt production and vertically rising melt combine to produce a small effect on the temperature and melt production rate fields. However, when crustal thicknesses become appreciable ($\sim 6 \text{ km}$), advection of melt heat may be a factor that cannot be ignored in any self-consistent study.

(4) Compositionally-driven convection increases crustal production by a factor of 1.5–2 over the non-dynamic models and significantly changes both the width and thickness of the melting regime by (i) constricting the upward flow of mantle into a narrower region and (ii) thinning the conductive boundary layer beneath the ridge. This result confirms the result of *Sotin and Parmentier* [1989].

(5) The narrowing of the melt regime and the additional pressure gradients resulting from compositional convection are insufficient to focus melt to the ridge axis when the sub-ridge viscosity is low enough for significant compositionally driven flow to occur.

FIGURE CAPTIONS

Fig. 3.1 The diagram shown is a description of both the computational geometry and the boundary conditions used in the numerical experiments presented. Boundary conditions for velocities are presented to the right of the ridge axis. Boundary conditions for all other variables are presented to the left of the ridge axis. Velocity boundary conditions are prescribed not only on the boundaries, but in the interior of the computational regime as well. The hatched region in the interior defines an area of the mantle that is moving with the surface velocity, i.e. as a rigid plate with velocities $U = U_0$ and $V = 0$. The area encompassing the rigid lithosphere is defined in the following way. For both constant and

variable viscosity models, it is possible to calculate a pressure- and temperature-dependent viscosity structure, $\eta(T,p)$, for the mantle using equation (3.4). Wherever the viscosity is calculated to be greater than 50 times the reference viscosity η_0 , the plate is defined to be moving rigidly. To avoid computational difficulties, the rigid behavior of the mantle is assumed to terminate within a distance $0.1d$ (15 km) of the ridge axis. Along the side boundaries and below the hatched region, mantle velocities are prescribed using the analytic solutions for isoviscous plate-driven flow [Batchelor, 1967]:

$$U_{ps}(x,z) = \frac{2U_0}{\pi} \left[\tan^{-1}\left(\frac{x}{z}\right) - \frac{xz}{x^2 + z^2} \right]$$

$$V_{ps}(x,z) = \frac{2U_0}{\pi} \left[\frac{z^2}{x^2 + z^2} \right]$$

Note that the frame of reference for each of these equations is as follows. The origin of the horizontal coordinate x is fixed to the ridge axis. The origin of the vertical coordinate z is fixed to the base of the plate, $z_l(x)$, at the edge of computational domain.

Fig. 3.2 A plot pair showing results for run *PP-L250* (1 cm yr⁻¹ half-rate, $\eta = 10^{18}$ Pa s, $\Delta S_m = 250$ J kg⁻¹ °C⁻¹). The computational domain is divided in half down the ridge axis and variables pertaining to the melt phase are plotted in (a) and those pertaining to the mantle are plotted in (b). (a) Dimensional melt production rate is shown as levels of grey. Contours of melt production rate are {0.20 (lightest gray shown) 0.40, 0.60 0.8 (darkest gray shown)} $\times 10^{-11}$ kg m⁻³ s⁻¹. (b) Filled arrowheads show direction and magnitude of mantle velocity (V). Mantle flow vectors are scaled to the arrow above the plot. The scaling velocity is shown next to the arrow. Solid lines are contours of mantle temperature with dimensional contour values of 200, 400, 600, 800, 1000, and 1200 °C. Mantle density is shown as levels of grey. Contours of density are 3326 (lightest gray shown), 3324, 3322, and 3320 (darkest gray shown) kg m⁻³.

Fig. 3.3 (a) Vertical cross sections of mantle temperature beneath the ridge axis for all models. (b) Vertical cross sections of non-dimensional melt production rate (Γ^*) beneath the ridge axis for all models.

Fig. 3.4 A plot pair showing results for run *PP-L450* (1 cm yr⁻¹ half-rate, $\eta = 10^{18}$ Pa s, $\Delta S_m = 450$ J kg⁻¹ °C⁻¹). (a) Dimensional melt production rate is shown as levels of grey. Contours of melt production rate are {0.1 (lightest gray shown), 0.2, 0.3, 0.4 (darkest

gray shown)) $\times 10^{-11} \text{ kg m}^{-3} \text{ s}^{-1}$. (b) Solid lines are contours of mantle temperature with dimensional contour values of 200, 400, 600, 800, 1000 and 1200 °C. Mantle density is shown as levels of grey. Contours of density are 3326 (lightest gray shown), 3324, 3322, and 3320 (darkest gray shown) kg m^{-3} .

Fig. 3.5 A plot pair showing results for run *PP-L450+Q* (1 cm yr^{-1} half-rate, $\eta = 10^{18}$ Pa s, $\Delta S_m = 450 \text{ J kg}^{-1} \text{ °C}^{-1}$). (a) Dimensional melt production rate is shown as levels of grey. Contours of melt production rate are {0.15 (lightest gray shown), 0.30, 0.45, 0.60 (darkest gray shown)} $\times 10^{-11} \text{ kg m}^{-3} \text{ s}^{-1}$. Solid black contour lines show contours of k_μ . Dimensional contours are (0.1, 0.2, 0.3, 0.4, 0.5, 0.6) $\times 10^{-14} \text{ m}^2$. Black arrows show direction and magnitude of q . Melt flux vectors are scaled to the labelled arrow above the plot. The label next to the arrow shows the scaling flux for the remaining arrows as a fraction of the plate velocity U_0 . The scaling flux is taken to be the maximum flux magnitude. (b) Solid lines are contours of mantle temperature with dimensional contour values of 200, 400, 600, 800, 1000, and 1200 °C. Mantle density is shown as levels of grey. Contours of density are 3326 (lightest gray shown), 3324, 3322, 3320 (darkest gray shown) kg m^{-3} .

Fig. 3.6 A plot pair showing results for run *CC-L450+Q* (1 cm yr^{-1} half-rate, $\eta = 10^{18}$ Pa s, $\Delta S_m = 450 \text{ J kg}^{-1} \text{ °C}^{-1}$). (a) Dimensional melt production rate is shown as levels of grey. Contours of melt production rate are {0.25 (lightest gray shown), 0.50, 0.75, 1.00 (darkest gray shown)} $\times 10^{-11} \text{ kg m}^{-3} \text{ s}^{-1}$. Solid black contour lines show contours of k_μ . Dimensional contours are (0.5, 1.0, 1.5, 2.0) $\times 10^{-14} \text{ m}^2$. (b) Solid lines are contours of mantle temperature with dimensional contour values of 200, 400, 600, 800, 1000, and 1200 °C. Mantle density is shown as levels of grey. Contours of density are 3326 (lightest gray shown), 3324, 3322, and 3320 (darkest gray shown) kg m^{-3} .

Fig. 3.7 Contours of $|q_z|/|V|$ for the model *CC-L450+Q*. Dimensional melt production rate is shown as levels of gray. Contour levels of the flux ratio are (0.01, 0.1, 0.2, 0.3). This plot may be thought of as a ratio of the heat advected by the melt to that advected by the mantle. Ratios higher than 0.3 exist but are not shown in order to highlight areas within the region of melt production.

TABLE 3.1 Physical Dimensions of Crust and Melting Regime

| Run | h^a (km) | w^b (km) | Pressure of Melting | | |
|------------------|---------------|---------------|---------------------|-------------------|--------------------------------|
| | | | Minimum (kbar) | Maximum (kbar) | Average ^c (kbar) |
| <i>PP - L450</i> | 3.0 | 107 | 6.9 | 15.7 | 11.0 |
| <i>PP - L250</i> | 4.7 | 107 | 5.9 | 15.7 | 10.8 |
| <i>PP-L450+Q</i> | 3.9 | 117 | 5.9 | 15.7 | 10.5 |
| <i>CC L450+Q</i> | 6.1 | 66 | 3.9 | 15.7 | 9.6 |

^a Crustal thickness. To form the crust, all melt is assumed to contribute to the total crustal thickness. By simple mass balance, the total thickness of the crust h is given by

$$h = \frac{1}{2\rho_f U_0} \iint \Gamma \, dx dz$$

^b Maximum width of the melting regime.

^c The average pressure of melting, \bar{p} , is the integral over the hydrostatic pressure weighted by the melt production rate

$$\bar{p} = \iint \Gamma \rho_m g z \, dx dz / \iint \Gamma \, dx dz$$

Boundary Conditions

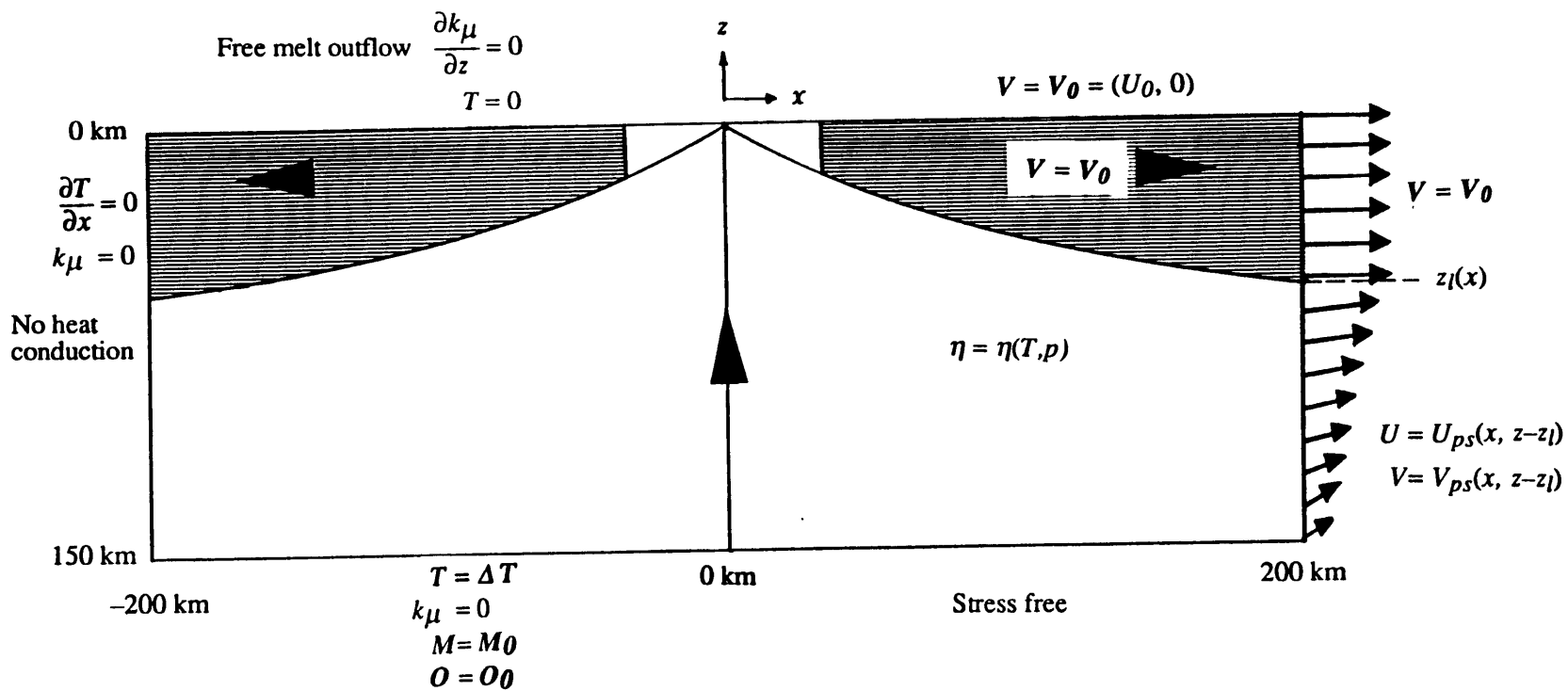


Figure 3.1

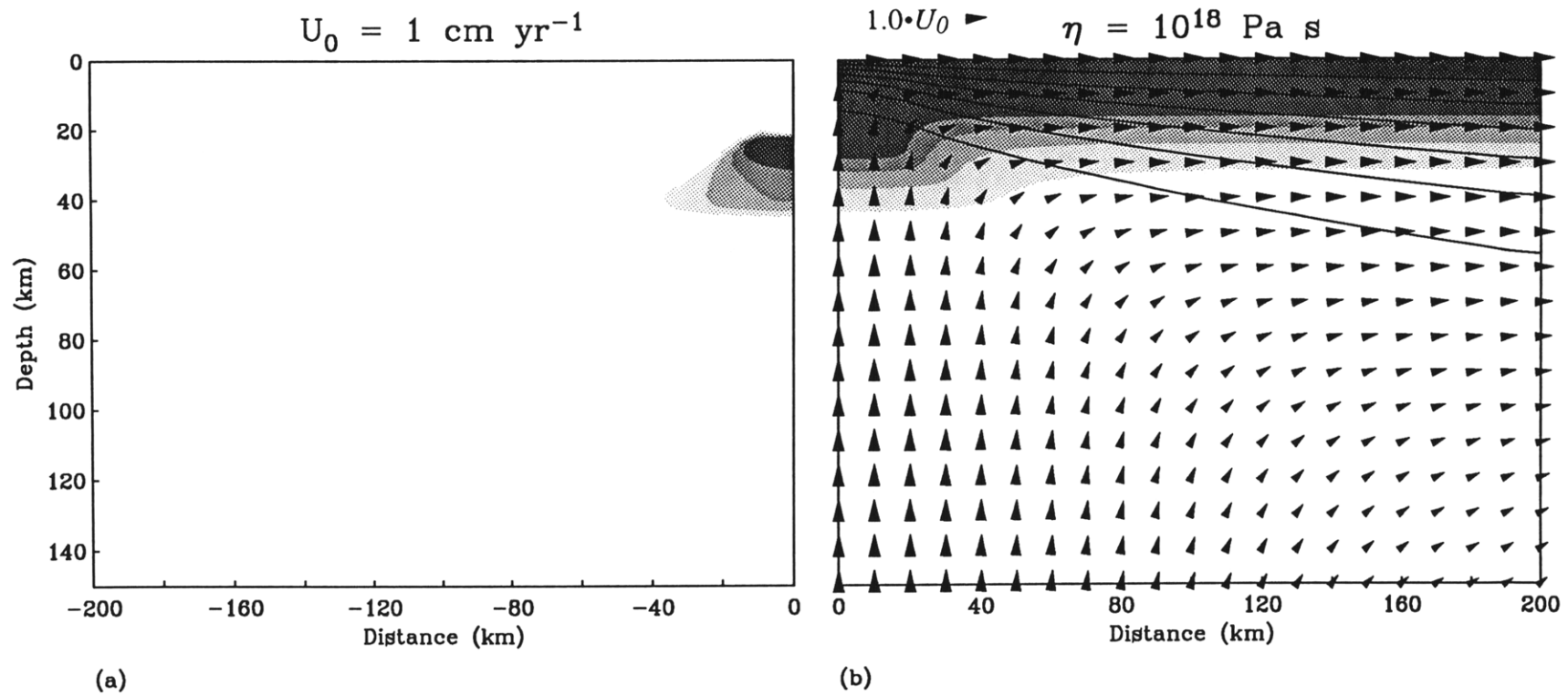


Figure 3.2

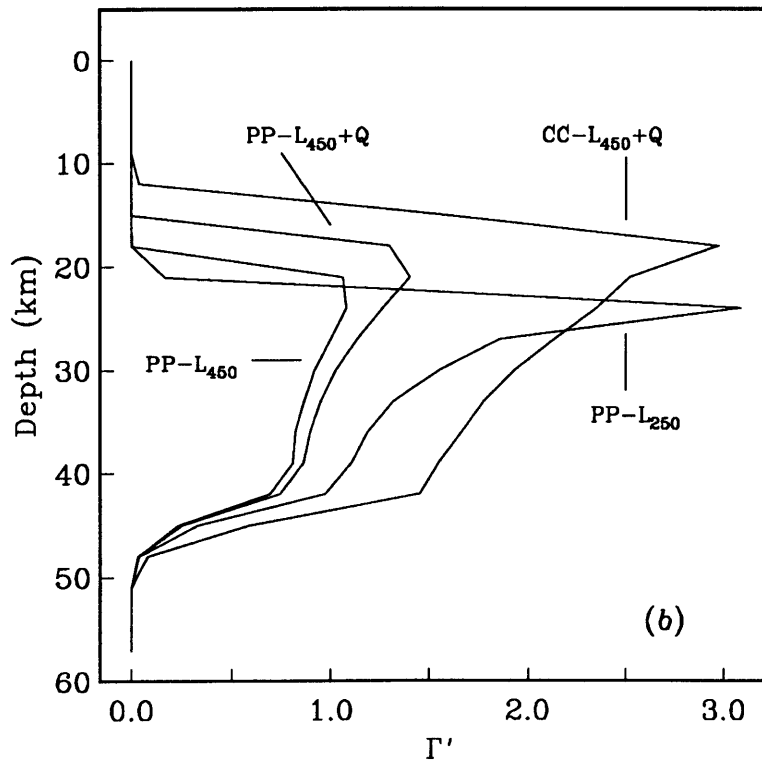
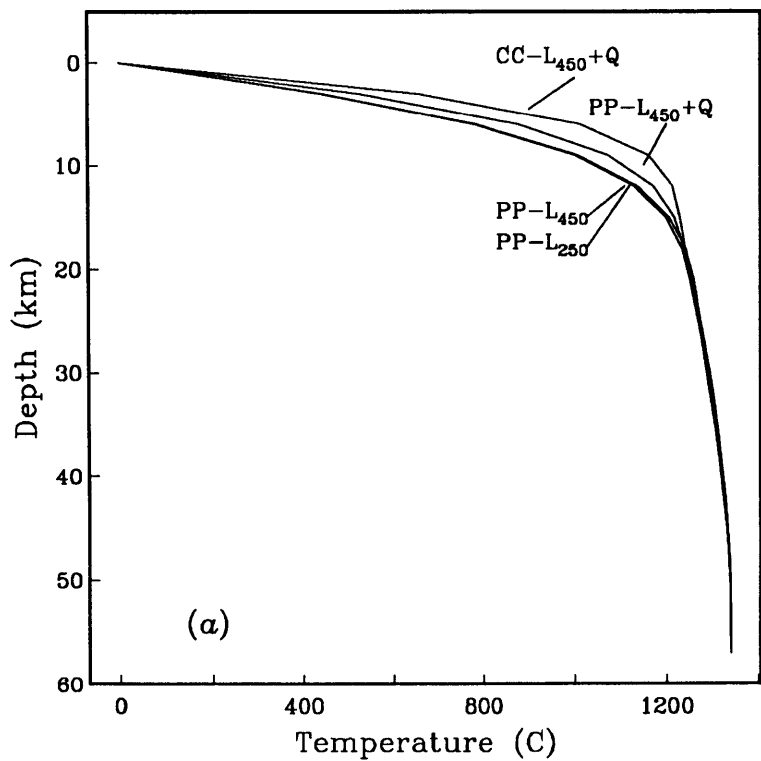
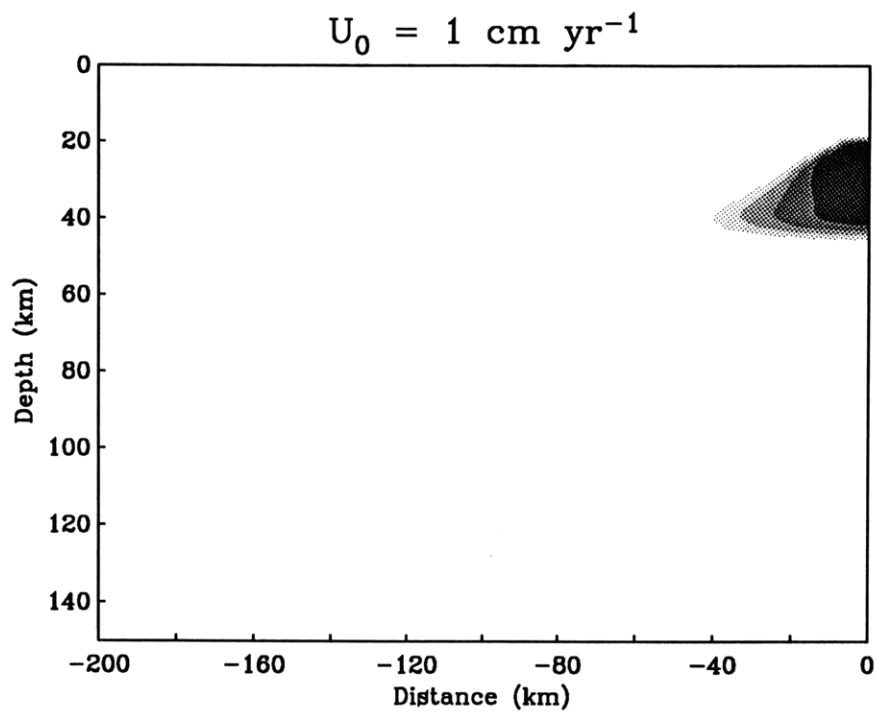
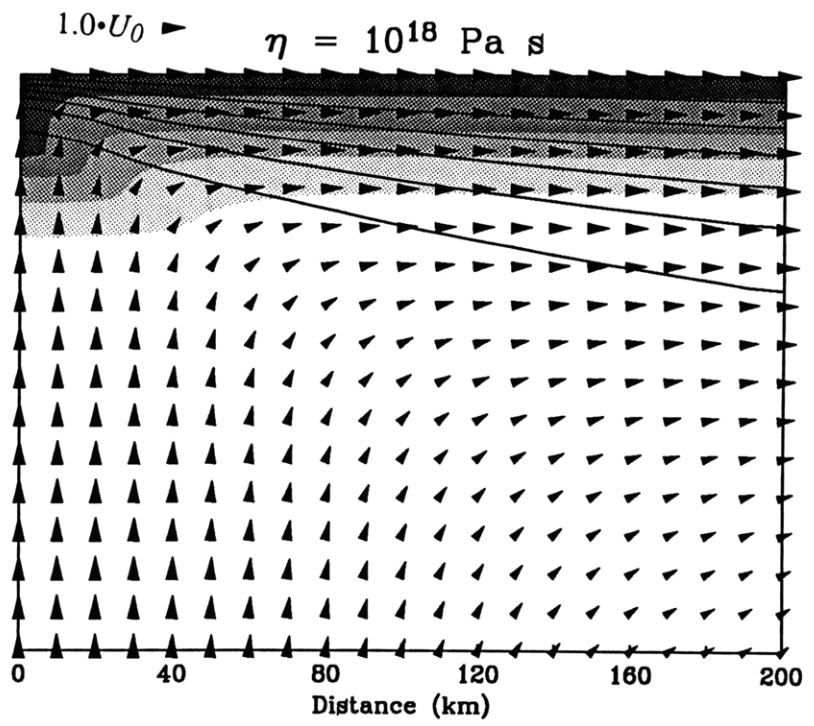


Figure 3.3



(a)



(b)

Figure 3.4

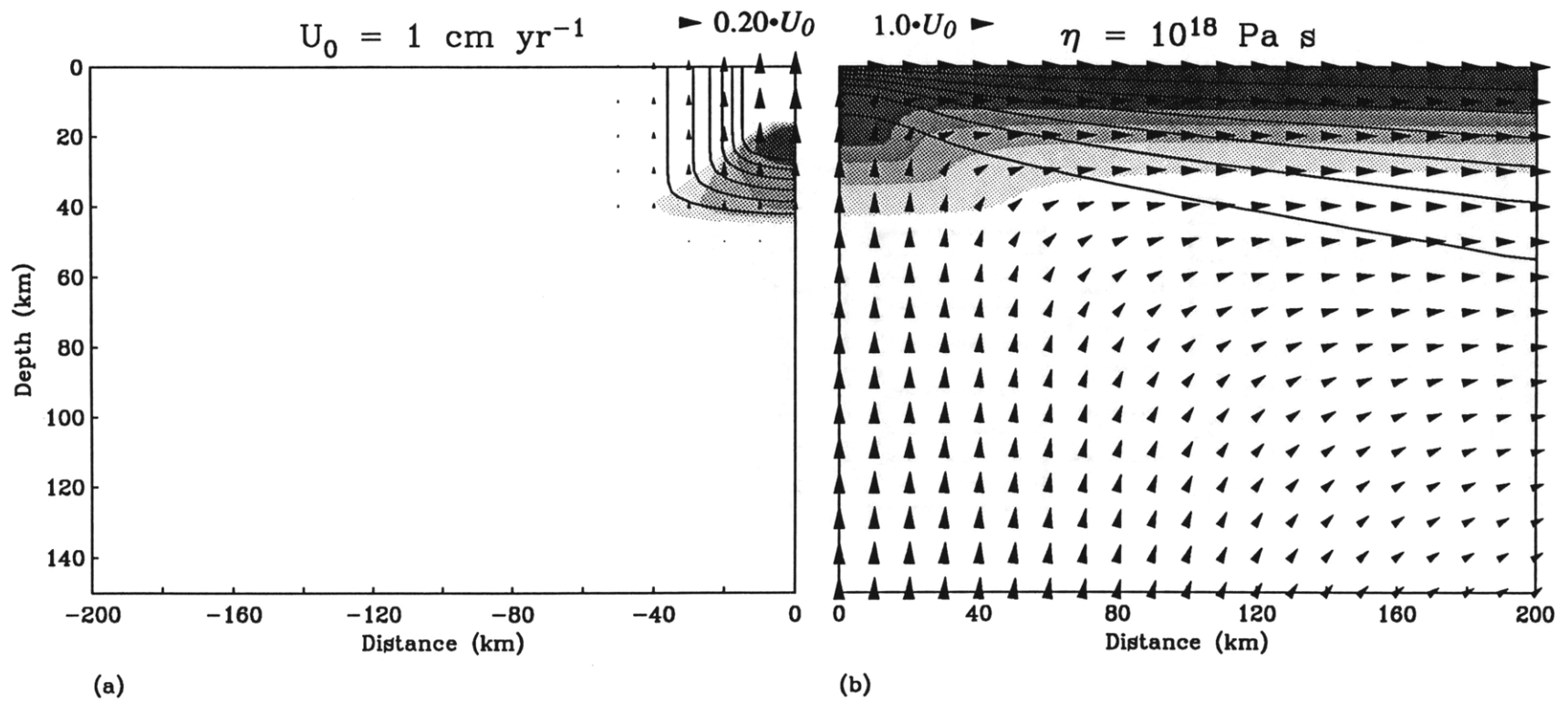


Figure 3.5

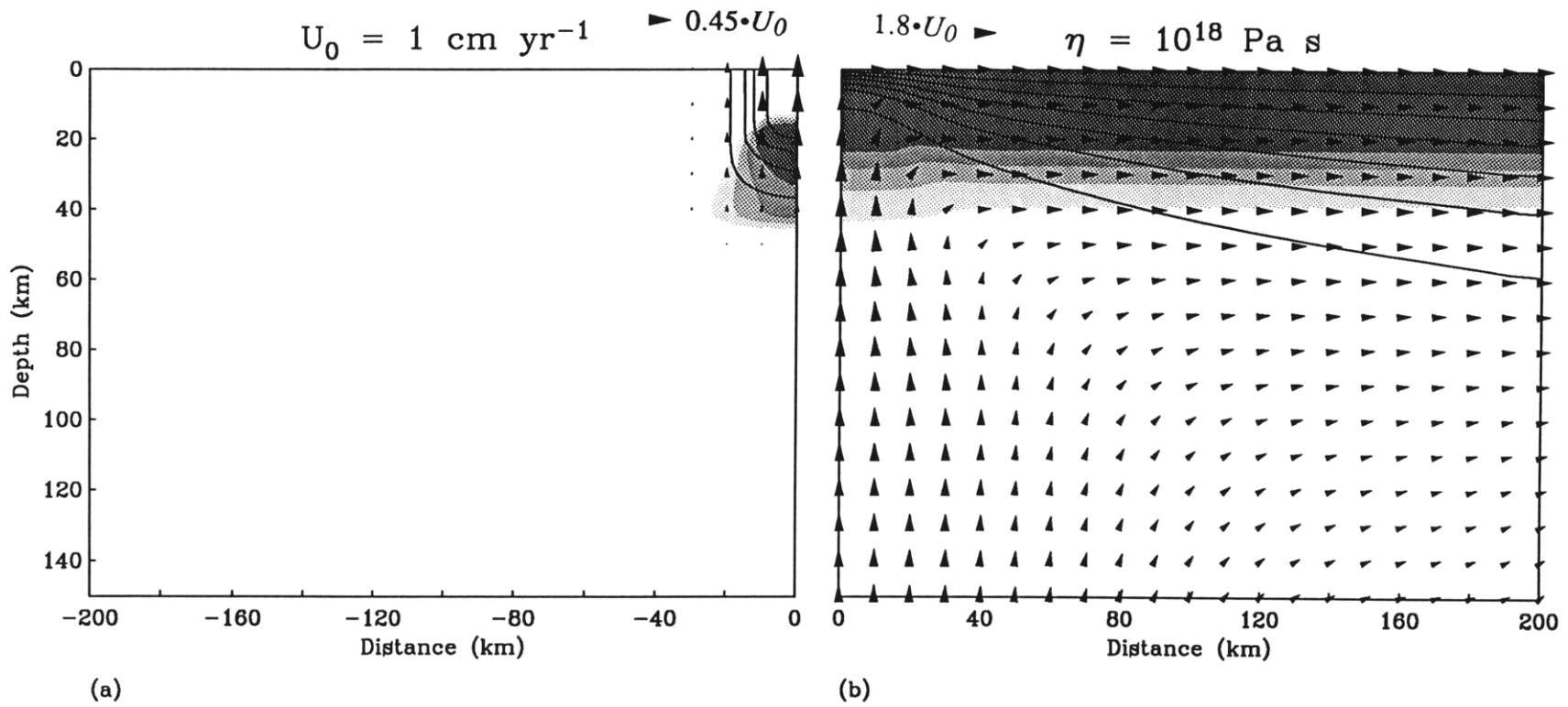


Figure 3.6

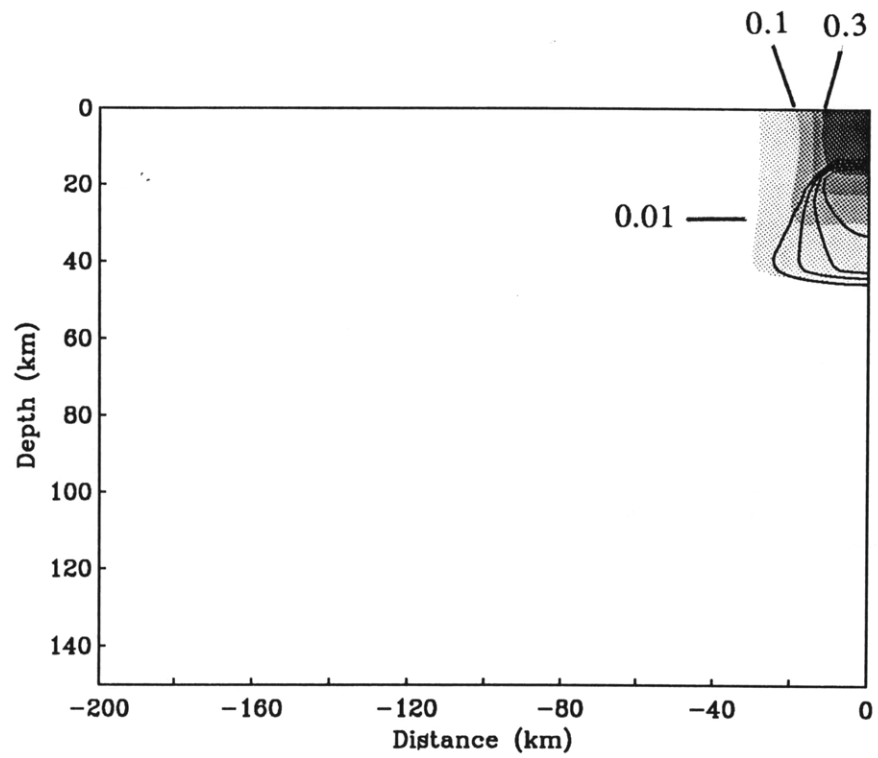


Figure 3.7

This page intentionally left blank

Chapter Four

Anisotropic Permeability in the Oceanic Upper Mantle and its Effect on the Migration of Melt at Mid–Ocean Ridges

Amid all the revolutions of the globe the economy of Nature has been uniform, and her laws are the only things that have resisted the general movement. The rivers and the rock, the seas and the continents have been changed in all their parts; but the laws which direct those changes and the rules to which they are subject, have remained invariably the same.

John Playfair
Illustrations of the Huttonian Theory of the Earth

INTRODUCTION

An outstanding first–order problem in the study of mid-ocean ridge dynamics is the mechanism by which partial melts generated over a broad region beneath the ridge axis are transported into a relatively narrow band along the ridge axis. Detailed morphologic studies of mid-ocean ridge axial valleys clearly show that constructional volcanism occurs only within a few kilometers of the ridge axis proper [e.g. *Macdonald*, 1982]. Seismic reflection and refraction data from the last two decades clearly shows that the mean crustal thickness is about 6 km regardless of spreading rate [Figure 4.1, *Chen and Sandwell*, 1990]. At slow–spreading rate ridges, the scatter in the data increases due to the influence of closely spaced transform faults and non-transform offsets where the oceanic crust is observed to thin by about 2 km [*Detrick and Purdy*, 1980; *Cormier et al.*, 1984; *Mutter et al.*, 1984]. In the mean, however, the data from slow–spreading ridges yields about the same crustal thickness as that from faster spreading ridges.

The oceanic crust is not only possessed of a constant thickness (at fast spreading ridges) but the seismic reflection from the Moho can be traced to within a few kilometers of the ridge-axis whereupon it is truncated by the appearance of an axial magma chamber [*Detrick et al.*, 1987]. The narrow width of the neovolcanic zone and the continuity of the Moho reflector to within a few kilometers of the ridge axis clearly indicates that essentially all magma that eventually becomes the oceanic crust is emplaced entirely at the ridge axis.

Two-dimensional numerical calculations of melting beneath mid-ocean ridges often show, however, that the width of the melting regime beneath a mid-ocean ridge is of order 100 km [*Reid and Jackson*, 1981; *Phipps Morgan and Forsyth*, 1988; *Phipps Morgan*, 1987; *Scott and Stevenson*, 1989; *Sotin and Parmentier*, 1989]. If all of the melt formed beneath a mid-ocean ridge is used to create the oceanic crust and if this melt is entirely emplaced at the ridge axis, then the problem becomes how to laterally transport such a broadly distributed melt over several tens of kilometers into a narrow zone at the ridge axis.

Transport of Melt Due to Dynamic Processes in the Mantle

A number of factors may influence the transport of the melt phase to the ridge axis. Among these are the pattern of mantle flow beneath the ridge axis and the pressure gradients resulting from that flow. If I assume that the mechanism of the melt migration is by porous flow, then the pattern of melt percolation is specified by D'Arcy's Law

$$\mathbf{q} = \varphi(\mathbf{v} - \mathbf{V}) = -\frac{k_{\varphi}}{\mu}(\nabla p - \delta\rho g\hat{z}) \quad (4.1)$$

where φ is the melt fraction, \mathbf{v} is the melt velocity, \mathbf{V} is the mantle velocity, k_{φ} is the permeability of the mantle, μ is the melt shear viscosity, p is the deviatoric mantle pressure, and $\delta\rho$ is the density difference between the mantle and the melt. The second term on the right-hand side states that melt will simply rise vertically by virtue of it being lighter than the surrounding mantle. The first-term on the right-hand side is a statement that deviatoric pressure gradients resulting from flow in the mantle can influence melt flowpaths. In a viscous mantle, these pressure gradients result from velocity shear gradients as described by Stokes' equation expressing conservation of momentum of the mantle

$$\nabla p = \frac{\partial}{\partial x_j} \eta \left(\frac{\partial V_i}{\partial x_j} + \frac{\partial V_j}{\partial x_i} \right) + f \quad (4.2)$$

In this equation, η is the mantle shear viscosity and f is a source term that generally involves buoyancy forces. Note that pressure gradients due to compaction of the mantle have been ignored. *Scott and Stevenson [1989]* show that time-dependent features such as magma solitons are not observed in the mantle flow field beneath mid-ocean ridges. The generation of magma solitons requires that a zone of low melt fraction be underlain by a zone of high melt fraction. Beneath a mid ocean ridge, this situation does not occur because the production of melt and its subsequent migration cause the melt fraction to increase monotonically or remain constant as it migrates to the ridge.

If mantle flow is driven solely by the motions of the lithospheric plates, then the mantle deviatoric pressure field is dominated by a strong pressure sink located at the ridge axis that decays rapidly (as r^{-2}) with distance from the axis [*Batchelor, 1967; Phipps Morgan, 1987*]. This low-pressure zone acts to draw melt to the ridge and thus is a possible mechanism for producing a narrow melt accumulation zone. The efficacy of deviatoric pressure gradients at focussing melt depends critically upon the magnitude of the mantle shear viscosity η in Stokes' equation (4.2).

Both *Spiegelman and McKenzie* [1987] and *Phipps Morgan* [1987] show that, if the mantle viscosity is low (10^{18} - 10^{19} Pa s) then melt buoyancy forces dominate mantle pressure gradients and melt will rise vertically, resulting in a broad region of crustal accretion. Not until the mantle shear viscosity reaches a value of 10^{21} Pa s are mantle pressure gradients comparable to the natural buoyancy force of the melt and thereby capable of focussing a considerable quantity of melt to the ridge axis. However, large mantle viscosities lead to a marked dependence of crustal thickness upon spreading rate [*Sotin and Parmentier*, 1989; Chapter 3]. This dependence arises because, as the mantle viscosity increases, buoyancy forces are dominated by mantle viscous stresses and thus any convection that might arise due to lateral density variations is dominated by the plate-driven flow. At slow spreading rates, conductive cooling then becomes important in defining the dimensions of the melting regime. The resulting decrease in the size of the melt regime lowers the crustal thickness. At faster spreading rates, crustal thickness is largely determined by the plate-driven flow field and the pressure at which clinopyroxene is lost (Chapter 3). To eliminate the spreading rate dependence upon crustal thickness, convection is required to both increase the thickness of the melting regime and raise melt production rates. Lowering the mantle viscosity to 10^{18} - 10^{19} Pa s will result in convection driven by melting-induced density variations. The resulting enhanced mantle upwelling will markedly reduce the spreading rate dependence but only at the expense of defocussing the melt away from the ridge. This negatively correlated behavior between mantle viscosity/ melt focussing and crustal thickness presents a dilemma. From the above discussion, it seems that what is required is a mantle viscosity that is relatively low within and about the melting regime and relatively high otherwise. The low viscosity about the melt regime would allow convection to occur while the high viscosities above the melt regime might focus melt to the ridge.

Such a pathology in the variation of mantle viscosity can be obtained by assuming that the viscosity has strong temperature- and pressure-dependence. Mantle viscosities that depend upon these two variables will have large values in the conductive boundary layer above the melting regime, and low viscosities below. Numerical models (Chapter 3) of mid-ocean ridge dynamics incorporating this viscosity structure do indeed show that compositionally-driven convection occurs in the low-viscosity asthenosphere. Unfortunately, while the high viscosities in the lithosphere do enhance mantle pressure gradients, they do so only within the thermal boundary layer. Outside of that layer, low mantle viscosities reduce the magnitude of mantle pressure gradients about and within the melting regime. The resulting effect upon melt flowpaths is limited because relatively large pressure gradients are confined to the region where conductive cooling is important

(Chapter 3). For the high pressure gradients in the lithosphere to be effective in focussing the melt, their influence needs to be distributed over the entire region through which the melt is percolating.

Convection driven by melting-induced lateral variations in mantle density also acts to focus melt to the ridge axis but in a fashion different from mantle pressure gradients. The density variations may be due to changes in mantle porosity, mantle temperature, or loss of dense basaltic components upon melting. The convection induced by these density changes acts to reduce the width of the melting regime because mantle upwelling velocities in the melting regime increase. In order to match the lateral flux of mass transported by the lithosphere, the width of the melting regime must decrease. Because the width of the melting regime decreases, the zone of crustal accretion must decrease as well. However, several studies that incorporate the effect of buoyancy terms into the balance of forces [Scott and Stevenson, 1989; Sotin and Parmentier, 1989; Chapters 2 and 3] clearly show that the resulting narrowing of the melting regime and lateral transport of melt by the mantle are insufficient mechanisms for creating a narrow zone of surface volcanism.

Buck and Su [1989] suggested that, if melt fractions in the mantle can approach 20%, the mantle viscosity will drop by several orders of magnitude. This leads to an extreme narrowing of the melt production regime, and, by their argument, a zone of crustal accretion only a few kilometers wide. It is unlikely, however, that melt fractions reach this magnitude several tens of kilometers below the ridge axis [Johnson *et al.*, 1990]. Furthermore, Cooper and Kohlstedt [1984, 1986] show that, if the mantle deforms via diffusion creep, the reduction of mantle viscosity is at best a factor of 2–5. The upper mantle deforms via a faster dislocation creep mechanism, however, so the effect of melt upon the viscous deformation of the mantle is likely to be much less. In fact, Scott and Stevenson [1989] showed that a factor of five reduction in the mantle viscosity wherever a melt phase was present resulted in no significant narrowing of the crustal accretion region.

Sparks and Parmentier [1990, 1991] argue that melt flows to the ridge axis along a high-porosity channel that parallels the isotherm below which melt begins to crystallize (i.e. the melt's liquidus). In this mechanism, the solidification of the melt leads to local pressure gradients that drive the melt away from regions where solidification is occurring. The natural buoyancy of the melt and the sloping of the melt liquidus towards the ridge axis will result in focussing of the melt to the ridge axis. The efficacy of this scheme depends upon the balance of two factors: (1) the rate at which melt is transported into the region where melt is crystallizing and (2) the rate at which melt is crystallizing. If the solidification rate of melt is faster than the rate at which melt is brought towards its liquidus, then the channel will not develop and melt will solidify *in-situ*. If the transport rate is greater than the

solidification rate, then the high porosity channel will form and melt will flow to the ridge. The attractions of this mechanism are that it is both dynamically consistent with the full two-phase flow equations and it is testable. Seismic and electromagnetic or magneto-telluric methods could be used to detect the high-porosity layer.

One testable aspect of the freezing-induced high porosity channel is that solidification of the melt along an isotherm should result in the presence of interstitial solidified melt along that isotherm (a solidification front). These fronts will then be advected away from the ridge by the lithosphere. Field studies of the mantle section of ophiolites, however, yield no indication of the solidification front that should result if melt were transported in this fashion. Compositional layering observed in alpine-type peridotites might be interpreted as evidence of migrating/solidifying melt packets, but geochemical and petrologic evidence suggest otherwise. First, geochemical evidence analyses indicate that such peridotites show systematic depletion of Al, Ca, Na, Ti, Al/Cr, and Fe/Mg. This trend is unlike that expected for a melt that is crystallizing but is consistent with melt generation and extraction [Dick and Sinton, 1979]. Second, while trapped melt does exist in some samples of abyssal peridotites [Dick, 1989] it is rare. Investigations of ophiolites further indicate that trapped melt is rare [Dick and Sinton, 1979] and that, moreover, it does not seem to be spatially associated with compositional layering in the mantle.

Stevenson and Scott [1987] argue that if deviatoric stresses are accounted for in determining the morphology of the melt phase, then the melt-filled, grain triple junctions that are the conduits for melt percolation will be dilated in the direction of greatest compressive stress and contracted in the direction of least compressive stress. Permeability depends directly upon the cross-sectional area of channels in the porous network therefore such a mechanism would enhance permeability in the direction of greatest compressive stress. In the sub-ridge mantle, the direction of greatest compressive stress is oriented laterally away from the ridge axis [Sleep, 1984]. Such a mechanism would thus direct melt away from the ridge axis [Stevenson and Scott, 1987].

Transport of Melt due to Dike Propagation

Until now, I have only considered mechanisms in which the melt percolates via porous flow. Attendant with these mechanisms is the assumption that the structural fabric of the mantle in no way effects the route that melt takes on its way to the surface. Field studies of ophiolites belie this assumption, however. Within the peridotite section beneath the overlying gabbro/dike complex, cross-cutting dikes and veins are ubiquitous (Figure 4.2) indicating that, near the surface, the primary mode of melt transport is no longer porous flow.

A number of authors have presented models of melt migration at mid-ocean ridges based around the idea that the primary mode of melt migration throughout the melting regime occurs via dike or vein propagation rather than by porous flow [*Mavko and Nur, 1975; Nicolas and Jackson, 1982; Sleep, 1984; Nicolas, 1986a,b; Nicolas, 1989*]. The basic idea of this mechanism is that melt is retained in the matrix until some critical melt fraction is reached. At this point, the deviatoric stresses on the matrix caused by the differential density between the matrix exceeds the yield stress of the matrix. Melt is then collected into the the dike or vein which then propagates to the surface fairly rapidly.

In the presence of buoyancy forces alone, the dikes transporting the melt will rise vertically. If the melt regime is broad, as shown by a number of authors [*Scott and Stevenson, 1989; Sotin and Parmentier, 1989; Parmentier and Phipps Morgan, 1991, Chapters 1 and 2*] this mechanism will also lead to a broad crustal accretion zone at the surface. The viscous deformation due to mantle flow, however, results in deviatoric stresses that will affect the propagation path of dikes and veins. In an two-dimensional, isotropic medium subjected to deviatoric stress, dikes will propagate along the direction of greatest compressive stress [*Sleep, 1984*]. Beneath a ridge axis, the influence of deviatoric stresses results in dikes propagating away from the ridge axis thereby creating an even broader region of crustal accretion than if dikes propagated under the influence of buoyancy forces alone [*Phipps Morgan, 1987*].

An argument might be made that dikes are only created in a relatively narrow zone about the ridge axis. Once a dike is created, the pressure drop between the mantle and the melt in the dike will cause melt to be drawn to the dike via porous flow. However, the compaction length in the mantle is only a few hundred meters and the melting regime beneath a mid-ocean ridge is of order 100 km wide. Given that the pressure drop caused by the presence of the dike will decrease rapidly with distance, it does not seem likely that a narrow band of dikes about the ridge axis will be extremely efficient at extracting melt over distances of several tens of kilometers.

Nicolas [1986a,b,1989] argues that the depth at which the yield stress of the mantle is exceeded is about 50 km if melt is not allowed to percolate until a critical melt fraction is obtained. This estimate of the depth of dike initiation depends upon how much the presence of melt reduces normal stresses in the mantle. *Nicolas [1989]* overestimates this effect by assuming that the resulting difference in the mantle normal stress between melted and an unmelted mantle is $\delta\rho gh$ where $\delta\rho$ is the density difference between the mantle and the melt and h is the depth. This is an estimate of the pressure difference at the base of a melt column of height h and a similar unmelted mantle column. However, melt fractions in the mantle are not likely to be larger than 1–2% within the melting region. A better estimate

would be the integral $(\rho_m - \rho)$ where ρ_m is the unmelted mantle density and ρ is the density of the melt/mantle aggregate. If the melt fraction in a column of mantle is 1%, then the resulting pressure difference at a depth h is only $0.01 \cdot \delta\rho gh$ which would yield a much shallower depth of dike initiation for a given yield stress. Moreover, the displacement caused by the initiation of dikes should be detectable seismically. Studies of mid-ocean ridge seismicity, however, indicate that little seismic activity occurs below a depth of about 6–10 km [Toomey *et al.*, 1988].

Anisotropy in the Mantle and its Effect upon Melt Migration

The inability of dynamic forces in the mantle to focus melt to the ridge axis and the defocussing effect of dikes requires that an alternate melt migration mechanism be sought. The presence of the dikes and veins in ophiolites strongly implies, however, that much of the melt is transported to the ridge axis via a mechanism other than porous flow, at least at shallow depths beneath the ridge. These dikes and veins provide a clue for an efficient mechanism for focussing melt.

In any porous medium, the permeability will be controlled by a number of factors. Two of the most important are the cross-sectional area of the channels through which the fluid flows and a factor known as the tortuosity T_{ij} .

Though the analogy is not strictly correct, dikes and veins may be considered as exceptionally wide melt channels with some orientation. Consider for a moment the plate-driven mantle flow field beneath the ridge axis. If at some point in this flow field a vein is created, the vein will be oriented in the direction of greatest compressive stress. As shown by *Sleep* [1984], the vein will propagate in a direction away from the ridge axis (Figure 4.3a). However, if the vein propagates slowly, shear strain in the mantle will reorient the vein such that it is directed towards the ridge axis (Figure 4.3b). Such a reorientation of veins may also occur because the vein lowers the effective mantle viscosity. Simple numerical experiments for fluids with an anisotropic viscosity [Christensen, 1987, Stevenson, 1989; Phipps Morgan, unpublished data] show that bands of low viscosity material embedded in a higher viscosity matrix will eventually be reoriented by the flow towards the plane of shear and eventually along flowlines. Phipps Morgan [1987] postulated that if a preexisting isotropic network of veins exists in the mantle, then the network will progressively deform such that veins will be aligned parallel to the shear plane in the mantle. Within a few tens of kilometers from the onset of melting, most veins will be oriented towards the ridge axis (Figure 4.4a). The high “porosity” of the veins relative to the surrounding porous matrix would provide an efficient means of directing melt to the ridge.

Recent experiments on partially-molten olivine-basalt systems may yield another means of enhancing melt percolation in the direction of the ridge axis. The traditional theory of crystal-melt interfaces states that, for an isotropic system, the liquid-crystal interface curvature is constant [Bulau *et al.*, 1979]. This result predicts the cross-section of a melt-channel is prismatic with inward-curving faces (Figure 4.4b). Waff and Faul [1991] observe that while this morphology does exist in olivine-basalt systems, flat crystal-melt interfaces are often observed coexisting with curved interfaces (Figure 4.4c). The resulting increase in the cross-sectional area of the melt-channel will significantly enhance permeabilities along that melt-channel. Furthermore, Waff and Faul [1991] identify the faceted crystal face as the (010) slip plane of olivine. It is well-established that (010) is the dominant slip plane in olivine and is the means by which it deforms under the influence of an imposed shear. Theoretical studies of the lattice preferred orientation of olivine (LPO) predict that the (010) slip plane will align itself parallel to the plane of mantle shear [Ribe, 1989a,b]. Observations of the ultramafic sections of ophiolites indicate that olivine does behave as the theory predicts [cf. Christensen, 1987]. Beneath a mid-ocean ridge, therefore, the (010) plane of olivine will align itself such that the observed high-porosity channels will be oriented towards the ridge axis [Waff and Faul, 1991].

The progressive deformation (finite strain) of the mantle under the the influence of shear strain leads to another kind of anisotropy in the melt channel network. Consider an equigranular solid wherein melt channels are of equal cross-sectional area and randomly oriented (shown somewhat diagrammatically in Figure 4.4c). Next, define a distance l , aligned with either the horizontal or vertical axis, over which a pressure change δp occurs. The effective path length l_e is the distance over which the fluid actually travelled in order to move a distance l along the horizontal axis. The ratio of these two lengths gives a measure of the medium's tortuosity. In an isotropic solid, the ratio is the same in all directions and the permeability may be defined by a scalar value k_ϕ . For an anisotropic medium, however, the effective path length will be different depending upon orientation and thus the permeability becomes a second-order tensor. This effect is often observed in materials such as micaceous or slaty rock.

Bear [1972] argues that for a given pressure drop δp , the tortuosity T_{ij} is proportional to $(l/l_e)^2$. Consider now that our crystalline solid undergoes a pure shear event such that individual crystals are elongated in the horizontal direction. In this case, the ratio l/l_e in the direction of shortening decreases and the permeability in that direction drops markedly relative to the permeability in the direction of greatest elongation. Beneath a mid-ocean ridge, the direction of greatest elongation is parallel to the shear plane [e.g. Nicolas, 1989] which, again, is oriented towards the ridge axis. For a simple crystalline

solid like that shown in Figure 4.4c, the change in l_e scales linearly with the amount of elongation (strain) of the crystal. By the above relation between tortuosity and the effective path length, the change in tortuosity scales with the square of the amount of strain and thus so will the permeability [*Phipps Morgan, 1987*].

Objectives

My goal in this chapter is to incorporate a model of anisotropic permeability into the thermo–fluid dynamic model of melt migration and mantle convection I developed in the previous chapter. I will compare the results of these numerical experiments with identical experiments from the previous chapter wherein the mantle permeability was assumed to be isotropic (i.e. scalar–valued).

MODEL DEVELOPMENT

In the previous chapter, I developed a set of simplified governing equations for two–phase flow and melt generation in the oceanic upper mantle. In this chapter, I will use the same equations with only one modification. Recall that the permeability–melt viscosity ratio tensor \mathbf{K} was written

$$\mathbf{K} = k_\mu \mathbf{A} \quad (4.3)$$

where $k_\mu = k_\mu(x, z)$ is the scalar permeability–melt viscosity ratio and \mathbf{A} is a symmetric, non–dimensional anisotropy tensor with the property that $|A_{ij}| \leq 1$. In order to examine the relative strength of mantle pressure gradients to buoyancy forces, the anisotropy tensor was previously assumed to be isotropic or $\mathbf{A} = \mathbf{I}$ where \mathbf{I} is the identity tensor. Here, I remove this assumption and allow \mathbf{A} to have off–diagonal terms and diagonal terms of different magnitude.

Recalling the differential equation for the permeability–melt viscosity ratio

$$f_1 \frac{\partial k_\mu}{\partial x} + f_2 \frac{\partial k_\mu}{\partial z} + f_3 k_\mu = R_m \Gamma \quad (4.4a)$$

where the coefficients f_1, f_2 and f_3 are as follows

$$f_1 = A_{xx} \left(-\frac{\partial p}{\partial x} \right) + A_{xz} \left(-\frac{\partial p}{\partial z} + R_m \delta \rho \right) \quad (4.4b)$$

$$f_2 = A_{xz} \left(-\frac{\partial p}{\partial x} \right) + A_{zz} \left(-\frac{\partial p}{\partial z} + R_m \delta \rho \right) \quad (4.4c)$$

$$f_3 = -A_{xx} \frac{\partial^2 p}{\partial x^2} + A_{xz} \left(-2 \frac{\partial^2 p}{\partial x \partial z} \right) - A_{zz} \frac{\partial^2 p}{\partial z^2} \\ - \left(\frac{\partial A_{xx}}{\partial x} + \frac{\partial A_{xz}}{\partial z} \right) \frac{\partial p}{\partial x} + \left(\frac{\partial A_{xz}}{\partial x} + \frac{\partial A_{zz}}{\partial z} \right) \left(-\frac{\partial p}{\partial z} + R_m \delta \rho \right) \quad (4.4d)$$

The addition of anisotropy affects the magnitude of the permeability–melt viscosity ratio in two ways. First, the coefficients f_1 and f_2 are similar to velocities in an advection equation since the first two terms on the left–hand side of equation (4.4a) can be written $(f_1 f_2) \cdot \nabla k_\mu$. Anisotropy effects relative magnitudes of these two coefficients which in turn reflect the direction in which melt is propagating. The third term on the left–hand side of equation (4.4a) provides a mechanism for increasing or decreasing the permeability in response to anisotropy.

To complete the equation for k_μ , I need to specify the anisotropy tensor \mathbf{A} . As mentioned above, *Phipps Morgan* [1987] suggested that anisotropy in the mantle will be proportional to the square of the finite strain \mathbf{E} under simple shear. To calculate the finite strain, I use the continuum theory of *McKenzie* [1979] who showed that the finite strain tensor \mathbf{E} satisfies the following differential equation

$$\frac{\partial \mathbf{E}}{\partial t} + \mathbf{V} \cdot \nabla \mathbf{E} = \mathbf{L} \mathbf{E} \quad (4.5)$$

where \mathbf{V} is the mantle velocity, and $\mathbf{L} = \partial V_i / \partial x_j$ is the mantle velocity gradient tensor. The boundary conditions on equation (4.5) are that the mantle is isotropic ($\mathbf{E} = \mathbf{I}$) along the bottom boundary of the computational regime ($z = 150$ km). The side boundaries are free outflow boundaries. The strain along the top boundary is set to the strain at the level beneath it. The anisotropy tensor \mathbf{A} is symmetric since \mathbf{K} is symmetric [Bear, 1972]. However, the finite strain tensor \mathbf{E} is not symmetric. A particular coordinate transformation for the finite strain tensor can be found though where \mathbf{E} is diagonal. Transforming \mathbf{E} into this principal coordinate system, squaring the principal axes of the strain ellipse and rotating back into the original coordinate system yields a symmetric tensor \mathbf{A} that is related to the square of the finite strain by the following equation

$$\mathbf{A} = \mathbf{R}^T \mathbf{\Lambda}^2 \mathbf{R} \quad (4.6)$$

where \mathbf{R} is a rotation matrix describing the orientation of the principal axes of the strain ellipse and $\mathbf{\Lambda}$ is the diagonal matrix containing the normalized eigenvalues of \mathbf{E} . Each eigenvalue in $\mathbf{\Lambda}$ is normalized by the largest eigenvalue i.e. $\lambda_i' = \lambda_i / |\lambda_{max}|$.

In this chapter, I present a suite of numerical models which incorporate the above anisotropy tensor into D'Arcy's Law and into the permeability–melt viscosity ratio equation. Numerical solutions of the full thermo–fluid dynamic equations presented in Chapters 2 and 3 and using the above modifications to the permeability are obtained using the finite–element method. The computational domain has dimensions 400 km (horizontal) x 150 km (vertical) and in all other respects (e.g. boundary conditions) is identical to that used in Chapter 3.

RESULTS

Herein I present the results of three numerical experiments that incorporate the anisotropic permeability parameterization given above. For reference, I also present the three experiments from the previous chapter with identical parameters but without anisotropy. Parameters for all numerical experiments are listed in Table 4.1.

The results for models without anisotropy in the permeability are shown in Figures 4.5 (1 cm yr⁻¹), 4.6 (4 cm yr⁻¹), and 4.7 (8 cm yr⁻¹). The salient features in this suite of runs are (1) that the melt rises vertically resulting in a broad zone of crustal accretion (2) mantle pressure gradients have little effect upon melt flow paths because of the low mantle viscosity, (3) narrowing of the melt regime, and thus narrowing of the melt regime, due compositionally–driven convection is only important at slow spreading rates and is not a sufficient mechanism for focussing melt to the ridge axis.

A salient discussion of the anisotropic models requires a brief discussion of their associated finite strain fields. Steady–state finite strain ellipses for experiments 4 (1 cm yr⁻¹), 5 (4 cm yr⁻¹) and 6 (8 cm yr⁻¹) are shown in Figure 4.8. These experiments are the same in all respects to those shown in Figures 4.5–4.7 except that the mantle permeability is allowed to be anisotropic. The differences between the strain fields at the slowest and fastest spreading rates is quite remarkable and unexpected. These differences are due to enhanced mantle upwelling due to convection at the slower spreading rates. It is worthwhile, therefore, to examine the faster spreading rate models first so that this additional complication can be understood. At 8 cm yr⁻¹ (Figure 4.8c) flow in the mantle is primarily driven by the divergence of the lithosphere. Along a mantle flowline, finite strain ellipses show that an initially isotropic crystalline aggregate will become

progressively deformed in such a way as to cause individual crystals to elongate in the direction of the shear plane. Beneath a ridge axis, this effect results in a pervasive ridge-directed anisotropy in the crystalline lattice. Within the rigid lithosphere, deformation ceases and any preexisting strain is frozen in. The general form and orientation of the ellipses is in agreement with the finite strain results of *McKenzie* [1979] and *Phipps Morgan* [1987] and the lattice preferred orientation theory of *Ribe* [1989a,b].

As the spreading rate decreases, convection enhances the flow of mantle material through the melting regime (Chapter 3). The effect of this enhanced flow results in a mantle strain field that is markedly different from the strain field at faster spreading rates (Figure 4.8a). In the deep mantle, beneath the lithospheric lid, the strain field is much like that for simple plate-driven flow. From the base of the lithosphere to the surface, however, the mantle strain field changes orientation and magnitude. This result can best be understood by the nature of the non-plate driven flow. The density driven flow basically imposes a strong recirculation flow on the plate-driven flow field that is very local to the ridge axis [*Rabinowicz et al.*, 1987; *Scott and Stevenson*, 1989; *Sotin and Parmentier*, 1989]. This recirculation cell component acts to reorient the shear such that the axis of greatest extension points away from the ridge axis rather than towards it. The efficacy of this flow at altering the orientation and magnitude of the mantle strain depends upon the point at which any mantle flow line becomes part of the rigidly translating lithosphere. At this point, the mantle strain ceases to change.

For all spreading rates, the effect of the strain upon the the mantle permeability is quite marked. I note, however, that the overall patterns of flow, density and temperature are unchanged between the isotropic and anisotropic permeability models. This is reflected in there being little difference in crustal thickness (total melt production) between models at the same spreading rate.

Concentrating again upon the faster spreading rate models where the strain field is simple, the ridge directed anisotropy at 4 cm yr^{-1} (Figure 4.10) and 8 cm yr^{-1} (Figure 4.11) clearly show that the melt flux vectors are strongly oriented towards the ridge axis even though the driving force for the melt is almost solely due to melt buoyancy. The melt flux at the ridge axis relative to that off-axis is much stronger than in the isotropic models indicating that larger quantities of melt are being delivered to the ridge axis. Contours of the mantle permeability that slope towards the ridge axis envelope most of the region over which significant melting occurs. Evidence that this melt is then channeled laterally several tens of kilometers to the ridge axis is shown by the convergence to the ridge axis of permeability contours directly above the melting regime.

The results for the 1 cm yr^{-1} model (Figure 4.9) are perplexing. Unlike the faster spreading rate models, mantle strain throughout the melting regime has a strong nearly-vertical orientation. Within a few kilometers of the surface, the strain orientation changes abruptly such that major axis of the strain ellipse is oriented towards the ridge axis. Thus, melt would rise rapidly towards the surface along the vertically-oriented high-permeability network and then be deflected laterally towards the ridge. The result appears to be a layer of high permeability near the surface. The presence of this layer seems to me implausible. In fact, the algorithm I use to solve this equation (Appendix A) seems to have some difficulty solving for k_{μ} in this particular model.

Further evidence that the solution algorithm for the permeability equation is having some difficulty with the strong anisotropy in these models can be seen in the curves of crustal thickness versus distance from the ridge axis (Figure 4.12). First, the width of the crustal accretion region is rather broad (Table 4.2) given the strong anisotropy in these models. This seems to result from the fact that the integrated flux of melt out of the surface does not equal the total amount of melt produced by the melting regime. A check of these two values for the isotropic models indicate a discrepancy of at most 10%. For the anisotropic calculations, the flux of mass across the surface is systematically lower than the mass of melt produced by about 50%. Part of this discrepancy may have to do with the solution algorithm.

DISCUSSION

The presence of pervasive dike structures in ophiolites strongly suggests that the assumption of melt migration via porous flow breaks down at some depth. *Nicolas* [1989] suggests that dike propagation initiates at a depth of about 50 km. This is likely to be a gross overestimate considering that it is based upon the assumption that the melt overpressure is given by $\delta\rho gz$ where z is the depth and $\delta\rho$ is the difference in density between the mantle and melt. However, the melt fraction is small throughout much of the melting regime and is distributed in an interconnected network. The overpressure given by the above relation is the difference in pressure between a column of melt and column of mantle both of height z . Given the extreme assumptions leading to this result, the actual overpressure is likely to be much less and therefore the depth at which the rock fails to form a dike is likely to be much less than 50 km as well.

I suggest that melt preferentially travels towards the ridge axis either by passage through veins, differences in the melt channel widths due to surface energy anisotropy, and/or by strain-induced anisotropies in the tortuosity of the mantle. Melt will migrate rapidly towards the ridge axis where it will accumulate to within a few kilometers of the

ridge and at a few kilometers depth. The amount of melt in any volume of mantle will steadily increase as the ridge axis is approached causing the mantle rock to be overpressured. As the volume of mantle rises to the surface, its yield stress is exceeded and the resulting dike flushes the mantle free of any local melt. By transporting the melt to the ridge axis in this fashion, I avoid the problem of requiring dikes to be prevalent throughout the broad melting regime and oriented towards the ridge axis [*Sleep, 1984; Phipps Morgan, 1987*].

The marked differences in mantle anisotropy in the models presented here have important implications for seismic studies of the upper mantle beneath the ocean basins. It is a well established fact that travel times in fast spreading ocean basins such as the Pacific depend upon the azimuth of the seismic raypath. Raypaths oriented in the direction of plate spreading are faster than raypaths oblique to that direction [e.g. *Nishimura and Forsyth, 1985*]. This effect results from flow-induced anisotropy in the crystallographic orientation of olivine in the mantle. Within the lithosphere, the seismically-fast axis of olivine is assumed to be aligned with the direction of plate spreading. Theoretical studies of mantle strain [*McKenzie, 1979; Ribe, 1989a, 1989b*] beneath mid-ocean ridges agree with this assumption as do observations of grain deformation in ophiolites [e.g. *Nicolas, 1989*]. The results of this chapter show (Figure 4.8) that at fast spreading rates this assumption is valid. However, at slower spreading rates, where compositionally-driven convection has imprinted the mantle strain field with an additional component of strain, this assumption is not necessarily valid. The strain field is seen to change both orientation and magnitude with depth through the lithosphere. These differences between slower and faster spreading rates may help explain why seismic anisotropy is clearly observed in the Pacific Ocean basin and is very difficult to detect in the slower-spreading Atlantic basin [e.g. *Sheehan and Solomon, 1991*]. Future seismic studies of ocean basins and mid-ocean ridges that attempt to map anisotropy in the upper mantle should take these possible differences into account.

CONCLUSIONS

(1) A model for transporting melt to the ridge axis is presented that takes advantage of strain-induced mantle anisotropy. Regardless of the exact mechanism, the resulting anisotropy in the mantle permeability strongly focuses melt to the ridge axis, in accordance with observation. This result is in contrast to models which rely upon dynamic forces to drive melt to the ridge.

(2) A marked difference in patterns of finite strain exists between models with different spreading rates. At medium to fast spreading rates, flow is predominantly plate-driven resulting in a strong yet uniform pattern of mantle anisotropy. At slow spreading rates, a strong component of flow due to compositionally-driven convection results in a pattern of lithospheric anisotropy that varies in both orientation and magnitude. This result may help explain why a pervasive mantle anisotropy oriented in the direction of plate spreading is relatively easy to detect beneath the Pacific and difficult to detect beneath the Atlantic.

FIGURE CAPTIONS

Fig. 4.1 Oceanic crustal thickness versus half-spreading rate. Data from seismic studies done since 1970. Asterisks mark average crustal thickness from each seismic profile. Thin vertical bars at slow and intermediate spreading rates show variations in crustal thickness along several seismic profiles. Note the significant variations in crustal thickness at slow spreading rates which reflects crustal thinning towards fracture zones and non-transform offsets. Heavy vertical bar at 70 mm/yr shows range in crustal thickness from 100 seismic refraction results near the southern East Pacific Rise [McClain and Atallah, 1986]. Heavy vertical lines show crustal thickness variations inferred from recent along-axis gravity surveys [Figure courtesy John Chen].

Fig. 4.2 Intrusive gabbro dikes in the harzburgite section of the Oman ophiolite [Photos from Nicolas, 1989].

Fig. 4.3 (a) Solid lines with large arrows show mantle flowlines beneath a ridge axis. Line segment is a newly formed vein. Small arrows about the vein show axes of least compressive stress. (b) Same as (a) except shear flow has rotated dike so that it now points towards ridge axis.

Fig. 4.4 (a) Diagrammatic sketch of a pervasive vein network with a preferred orientation. (b) Left: Diagram from Waff and Faul [1991] showing the shape and cross-sectional area of the melt-channel along a grain triple-junction when all three interfaces between the crystalline solid and melt have the same mean curvature. Right: Diagram from Waff and Faul [1991] showing the shape and cross-sectional area of the melt-channel along a grain triple-junction with two curved and one faceted interface. (c) Left: Diagram showing an idealized crystalline solid in an initially undeformed state. Right: After a pure shear deformation, the crystals are elongated in the direction of minimum compressive stress.

Fig. 4.5 Experiment #1 (1 cm yr⁻¹ half-rate, $\eta = 10^{18}$ Pa s). (a) Dimensional melt production rate is shown as levels of grey. Contours of melt production rate are {0.25 (lightest gray shown), 0.50, 0.75, 1.0 (darkest gray shown)} $\times 10^{-11}$ kg m⁻³ s⁻¹. Solid black contour lines show contours of the permeability–melt viscosity ratio $k_{\mu} = k_{\phi}/\mu$. Contours are {0.50, 1.0, 1.5, 2.0} $\times 10^{-14}$ m². Black arrows show direction and magnitude of melt flux q . Melt flux vectors are scaled to the labelled arrow above the plot. The label next to the arrow shows the scaling flux for the remaining arrows as a fraction of the plate velocity U_0 . The scaling flux is taken to be the maximum flux magnitude. (b) Filled arrowheads show direction and magnitude of mantle velocity (V). Mantle flow vectors are scaled to the arrow above the plot. The scaling velocity is shown next to the arrow. Solid lines are contours of mantle temperature with dimensional contour values of 200, 400, 600, 800, 1000, and 1200 °C. Mantle density is shown as levels of grey. Contours of density are 3326 (lightest gray shown), 3324, 3322, 3320 (darkest gray shown) kg m⁻³.

Fig. 4.6 Experiment #2 (4 cm yr⁻¹ half-rate, $\eta = 10^{18}$ Pa s). (a) Dimensional melt production rate is shown as levels of grey. Contours of melt production rate are {0.01 (lightest gray shown), 0.50, 1.0, 1.50 (darkest gray shown)} $\times 10^{-11}$ kg m⁻³ s⁻¹. Solid black contour lines show contours of the permeability–melt viscosity ratio $k_{\mu} = k_{\phi}/\mu$. Contours are (0.5, 1.0, 1.5, 2.0, 2.5, 3.0) $\times 10^{-14}$ m². (b) Solid lines are contours of mantle temperature with dimensional contour values of 200, 400, 600, 800, 1000, and 1200 °C. Mantle density is shown as levels of grey. Contours of density are 3326 (lightest gray shown), 3324, 3322, and 3320 (darkest gray shown) kg m⁻³.

Fig. 4.7 Experiment #3 (8 cm yr⁻¹ half-rate, $\eta = 10^{18}$ Pa s). (a) Dimensional melt production rate is shown as levels of grey. Contours of melt production rate are {0.05 (lightest gray shown), 1.0, 2.0, 3.0 (darkest gray shown)} $\times 10^{-11}$ kg m⁻³ s⁻¹. Solid black contour lines show contours of the permeability–melt viscosity ratio $k_{\mu} = k_{\phi}/\mu$. Contours are (1.0, 2.0, 3.0, 4.0, 5.0, 6.0) $\times 10^{-14}$ m². (b) Solid lines are contours of mantle temperature with dimensional contour values of 200, 400, 600, 800, 1000, and 1200 °C. Mantle density is shown as levels of grey. Contours of density are 3326 (lightest gray shown), 3324, 3322, and 3320 (darkest gray shown) kg m⁻³.

Fig. 4.8 Plot of the steady–state finite strain field for (a) Experiment #4 (1 cm yr⁻¹), (b) Experiment #5 (4 cm yr⁻¹), and (c) Experiment #6 (8 cm yr⁻¹).

Fig. 4.9 Experiment #4 (1 cm yr⁻¹ half-rate, $\eta = 10^{18}$ Pa s, anisotropic permeability). (a) Dimensional melt production rate is shown as levels of grey. Contours of melt production rate are {0.25 (lightest gray shown), 0.50, 0.75, 1.0 (darkest gray shown)} $\times 10^{-11}$ kg m⁻³ s⁻¹. Solid black contour lines show contours of the permeability–melt viscosity ratio $k_{\mu} = k_{\phi}/\mu$. Contours are {1, 2, 3, 4, 5} $\times 10^{-14}$ m². (b) Solid lines are contours of mantle temperature with dimensional contour values of 200, 400, 600, 800, 1000, and 1200 °C. Mantle density is shown as levels of grey. Contours of density are 3326 (lightest gray shown), 3324, 3322, 3320 (darkest gray shown) kg m⁻³.

Fig. 4.10 Experiment #5 (4 cm yr⁻¹ half-rate, $\eta = 10^{18}$ Pa s, anisotropic permeability). (a) Dimensional melt production rate is shown as levels of grey. Contours of melt production rate are {0.01 (lightest gray shown), 0.50, 1.00, 1.50 (darkest gray shown)} $\times 10^{-11}$ kg m⁻³ s⁻¹. Solid black contour lines show contours of the permeability–melt viscosity ratio $k_{\mu} = k_{\phi}/\mu$. Contours are (4,6,8,12,16,20) $\times 10^{-14}$ m². (b) Solid lines are contours of mantle temperature with dimensional contour values of 200, 400, 600, 800, 1000, and 1200 °C. Mantle density is shown as levels of grey. Contours of density are 3326 (lightest gray shown), 3324, 3322, and 3320 (darkest gray shown) kg m⁻³.

Fig. 4.11 Experiment #6 (8 cm yr⁻¹ half-rate, $\eta = 10^{18}$ Pa s, anisotropic permeability). (a) Dimensional melt production rate is shown as levels of grey. Contours of melt production rate are {1.0 (lightest gray shown), 2.0, 3.0, 4.0 (darkest gray shown)} $\times 10^{-11}$ kg m⁻³ s⁻¹. Solid black contour lines show contours of the permeability–melt viscosity ratio $k_{\mu} = k_{\phi}/\mu$. Contours are (10, 20, 30, 40, 50) $\times 10^{-14}$ m². (b) Solid lines are contours of mantle temperature with dimensional contour values of 200, 400, 600, 800, 1000, and 1200 °C. Mantle density is shown as levels of grey. Contours of density are 3326 (lightest gray shown), 3324, 3322, and 3320 (darkest gray shown) kg m⁻³.

Fig. 4.12 Normalized crustal thickness vs. distance from the ridge axis for anisotropic permeability models only. Each curve is calculated by integrating the flux of melt, q , at the surface ($z=0$ km) and assuming that the total integrated flux of melt from the ridge axis ($x=0$ km) to the edge of the box ($x=200$ km) equals the crustal thickness, h . Curves are shown for three different spreading rates: 1 cm/yr, 4 cm/yr, and 8 cm/yr.

TABLE 4.1 Experimental Parameters

| Run # | U_0^a (cm yr ⁻¹) | ΔT (°C) | Pe^b | R_m^c ($\times 10^3$) | η (Pa s) |
|-------|-----------------------------------|--------------------|--------|------------------------------|------------------|
| 1 | 1 | 1340 | 47 | 2,320 | 10 ¹⁸ |
| 2 | 4 | 1340 | 190 | 580 | 10 ¹⁸ |
| 3 | 8 | 1340 | 380 | 290 | 10 ¹⁸ |
| 4 | 1 | 1340 | 47 | 2,320 | 10 ¹⁸ |
| 5 | 4 | 1340 | 190 | 580 | 10 ¹⁸ |
| 6 | 8 | 1340 | 380 | 290 | 10 ¹⁸ |

^a U_0 is the half-spreading rate of the surface plates.

^b Peclet number : $U_0 d / \kappa$.

^c R_m : $\rho_m g d^2 / U_0 \eta_0$.

Note: Runs 1,2, and 3 are experiments with isotropic permeability. Runs 4, 5, and 6 are experiments with anisotropic permeability.

TABLE 4.2 Physical Dimensions of Crust and Melting Regime

| Run # | η Pa s | h^a (km) | w^b (km) | Pressure of Melting | | |
|-------|----------------|---------------|---------------|---------------------|-------------------|--------------------------------|
| | | | | Minimum (kbar) | Maximum (kbar) | Average ^c (kbar) |
| 1 | 10^{18} | 6.1 | 50 | 3.9 | 15.7 | 9.6 |
| 2 | 10^{18} | 6.3 | 114 | 3.9 | 15.7 | 9.8 |
| 3 | 10^{18} | 6.4 | 162 | 3.9 | 15.7 | 9.8 |
| 4 | 10^{18} | 5.8 | 25 | 3.9 | 15.7 | 9.6 |
| 5 | 10^{18} | 5.8 | 73 | 3.9 | 15.7 | 9.9 |
| 6 | 10^{18} | 5.8 | 107 | 3.9 | 15.7 | 9.8 |

^a Crustal thickness. To form the crust, all melt is assumed to contribute to the total crustal thickness. By simple mass balance, the total thickness of the crust h is given by

$$h = \frac{1}{2\rho_f U_0} \iint \Gamma \, dx dz$$

^b The width of the neovolcanic zone, w , is defined by the flux of melt out of the top of the computational regime. If the total integrated flux of melt out of half of the box is equal to the crustal thickness h , then the neovolcanic zone width may be defined as twice the distance x_0 ($w = 2x_0$) such that the following integral has a value of $0.90h$

$$f = h \int_0^{x_0} \|q(x, z=0)\| \, dx / \int_0^{200 \text{ km}} \|q(x, z=0)\| \, dx$$

^c The average pressure of melting, \bar{p} , is the integral over the hydrostatic pressure weighted by the melt production rate

$$\bar{p} = \iiint \Gamma \rho_m g z \, dx dz / \iiint \Gamma \, dx dz$$

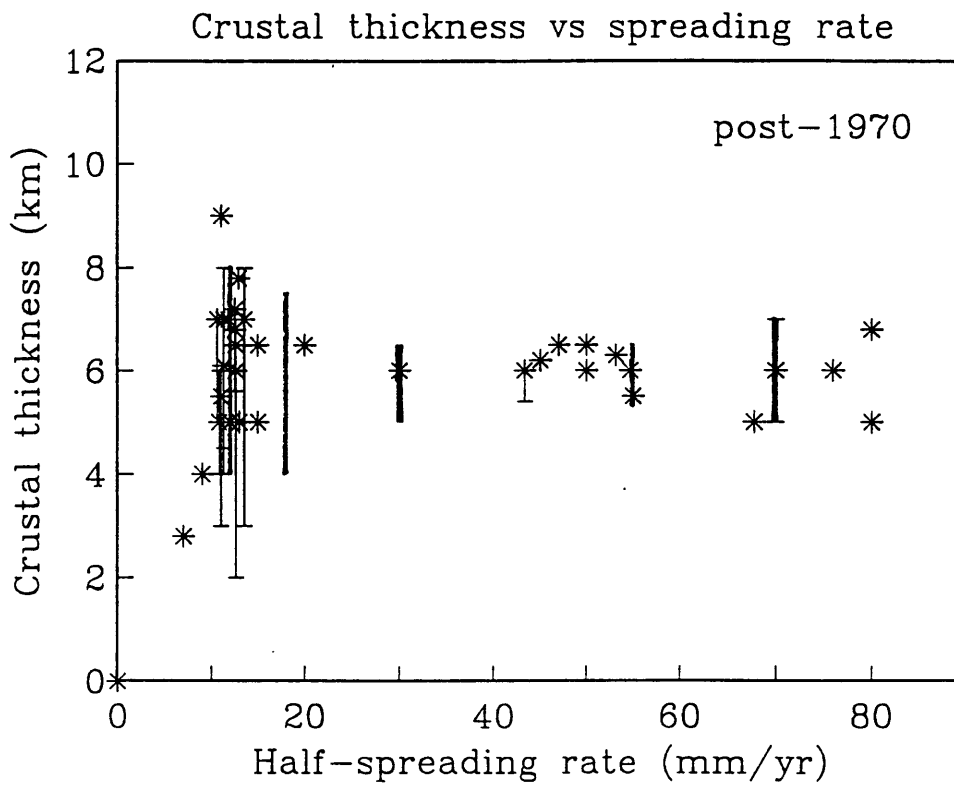


Figure 4.1

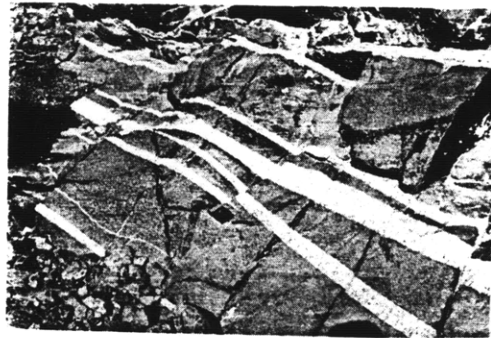
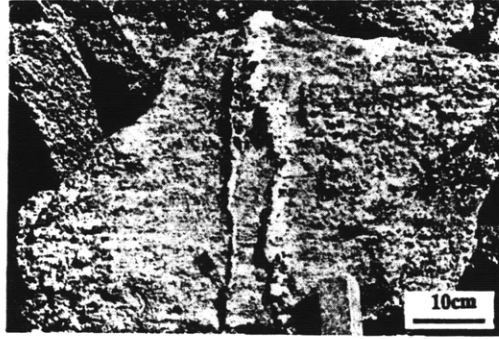


Figure 4.2

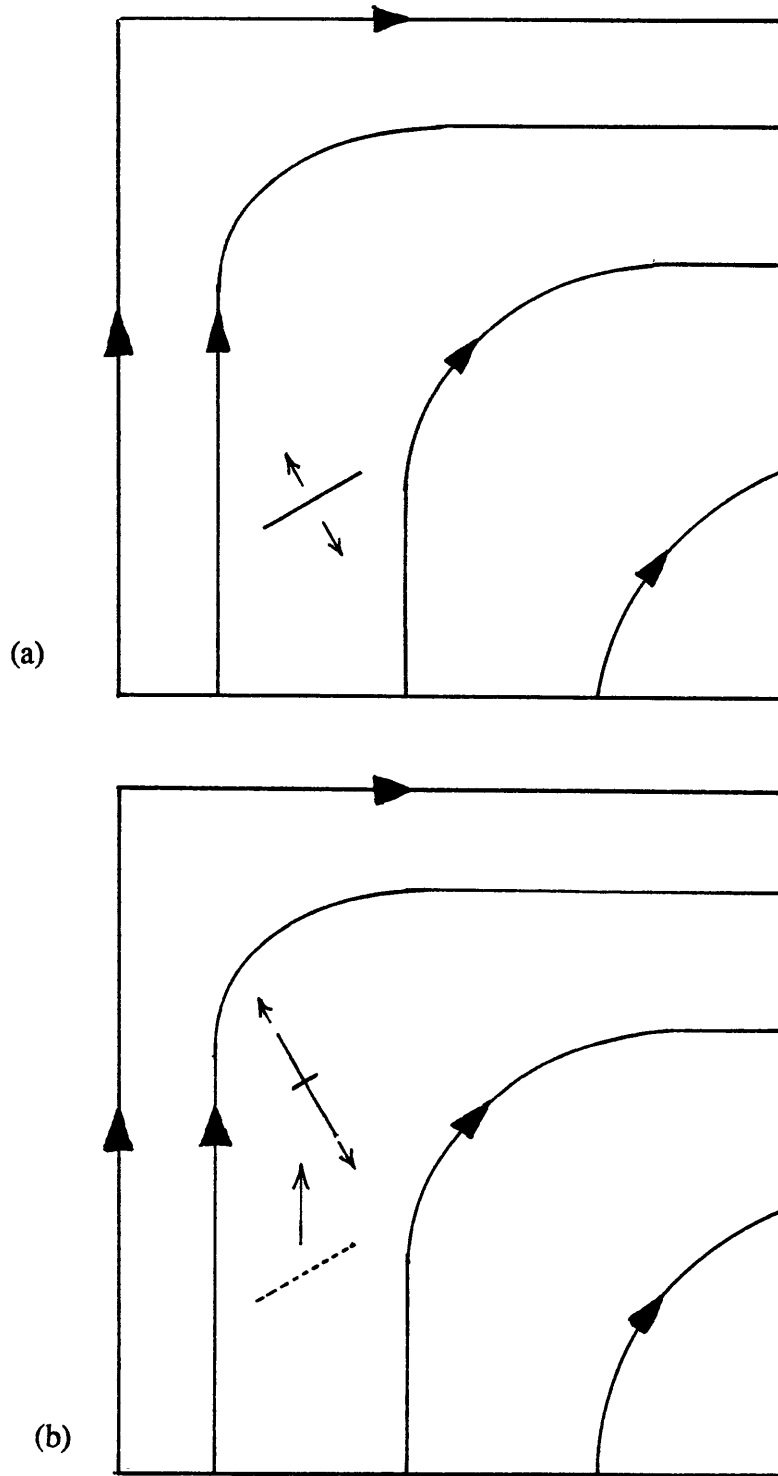


Figure 4.3

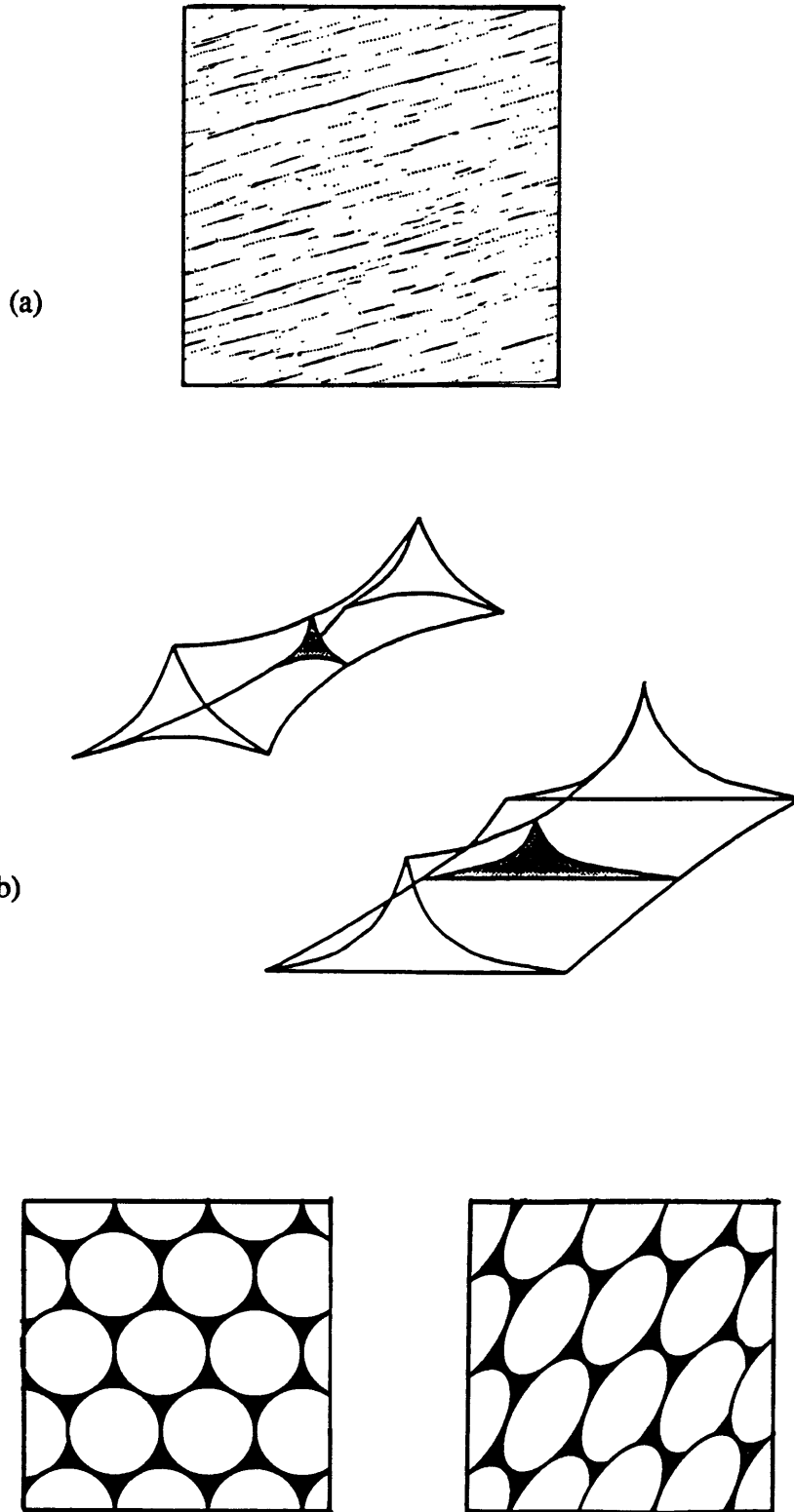


Figure 4.4

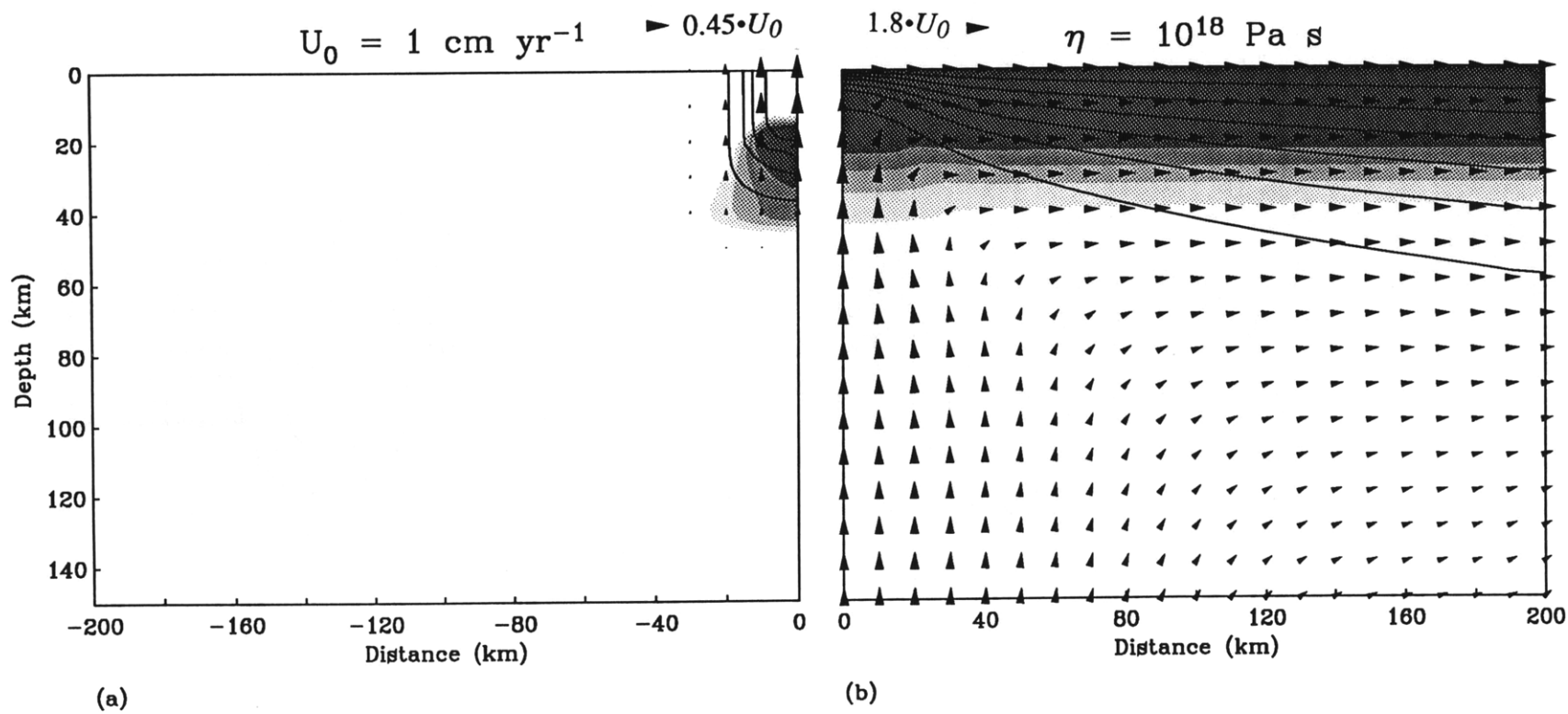


Figure 4.5

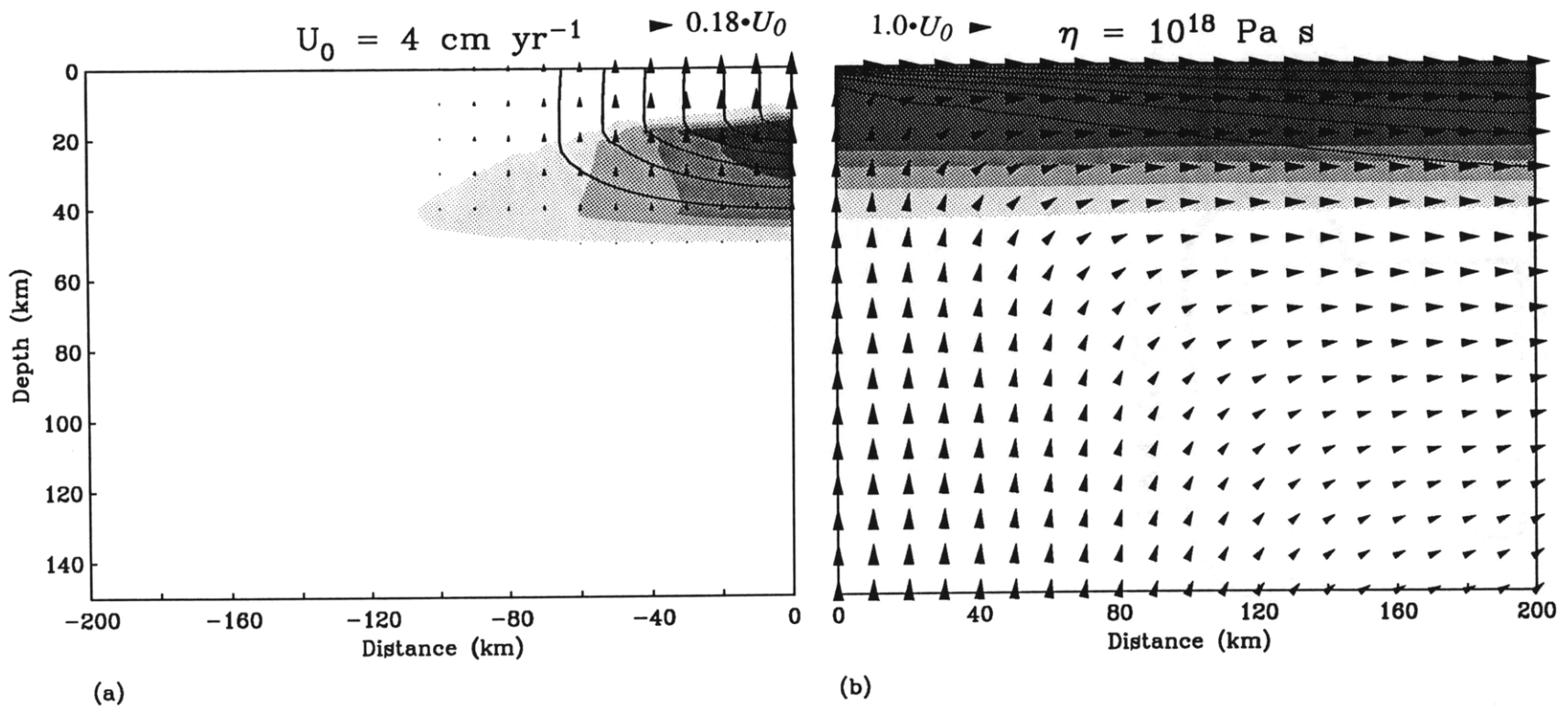


Figure 4.6

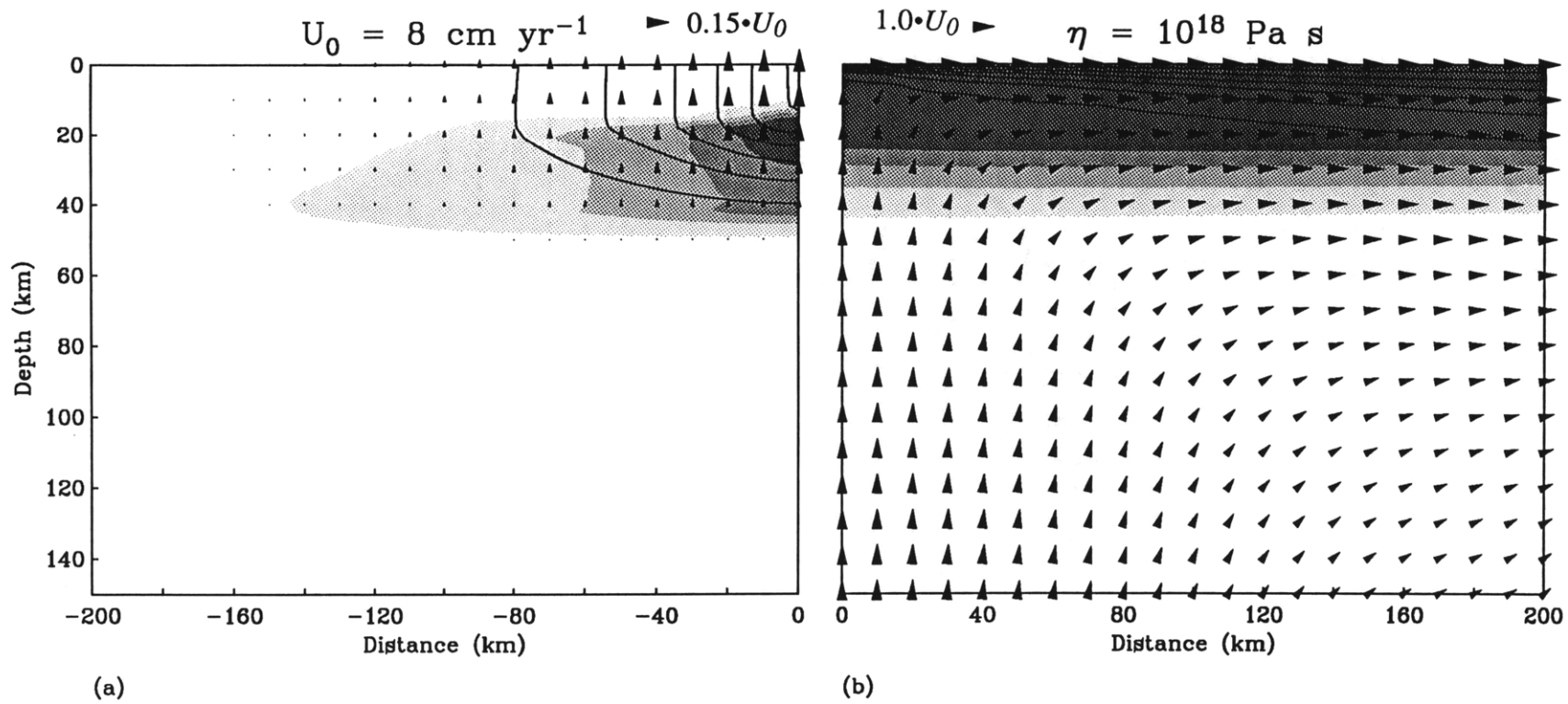
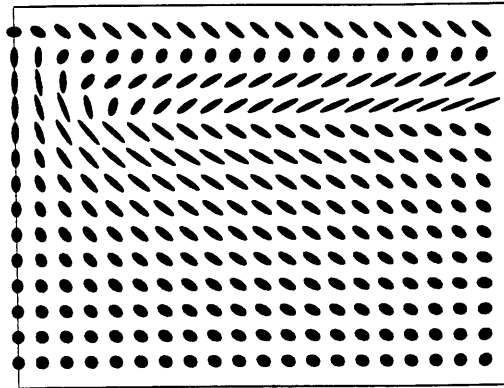
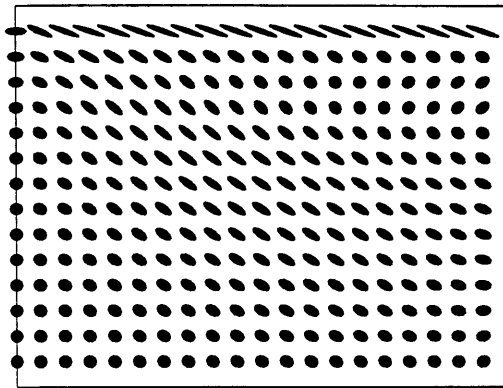


Figure 4.7

(a) $U_0 = 1 \text{ cm yr}^{-1}$



(b) $U_0 = 4 \text{ cm yr}^{-1}$



(c) $U_0 = 8 \text{ cm yr}^{-1}$

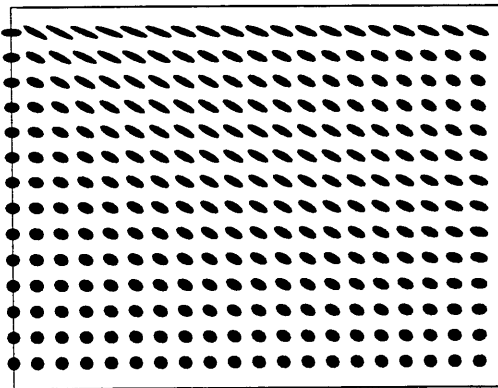


Figure 4.8

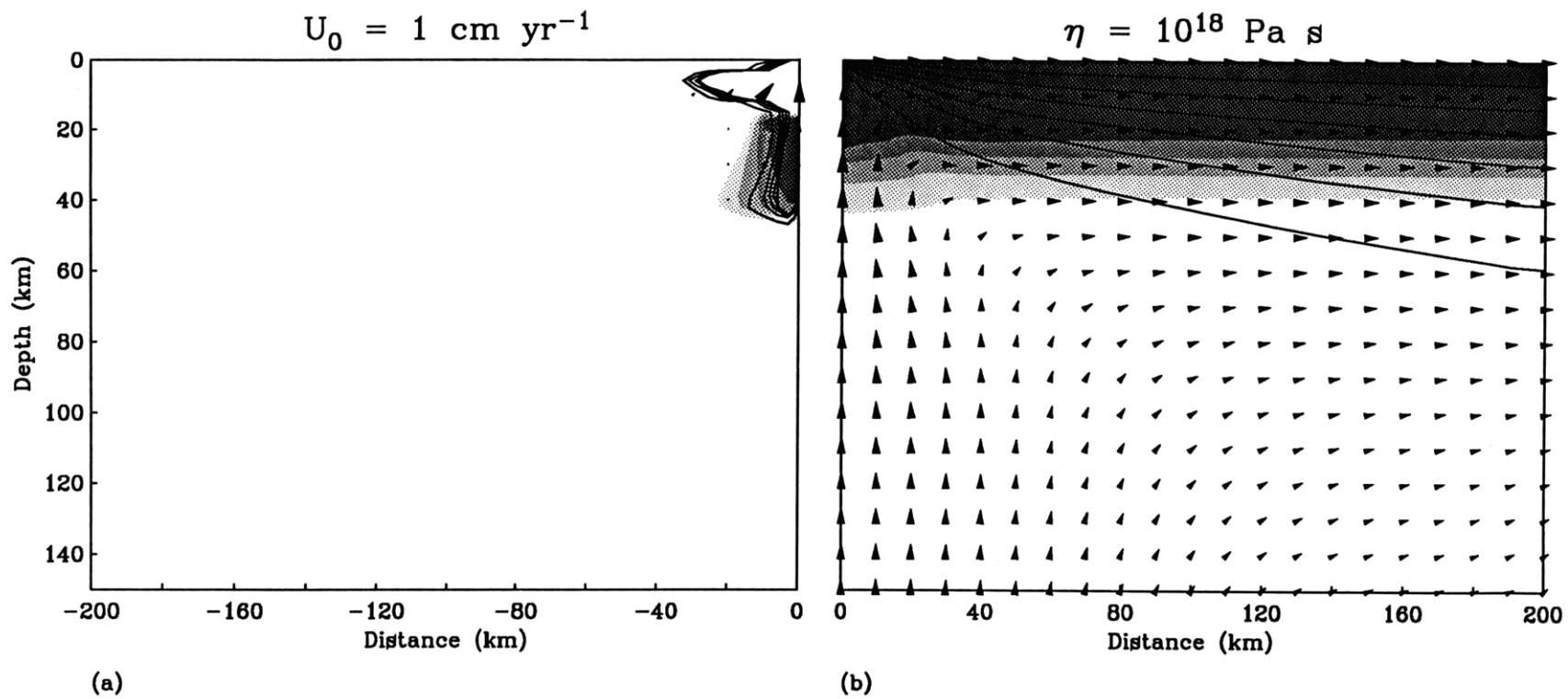


Figure 4.9

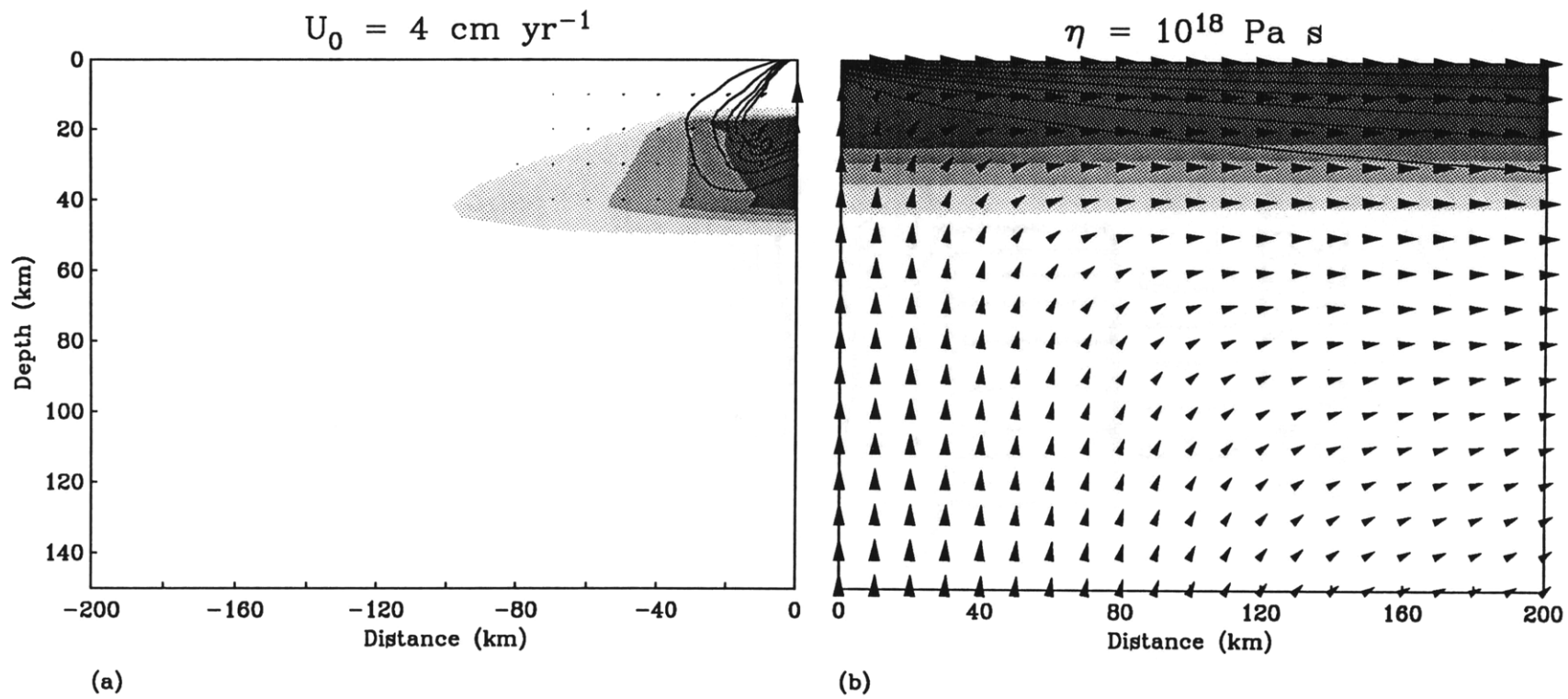


Figure 4.10

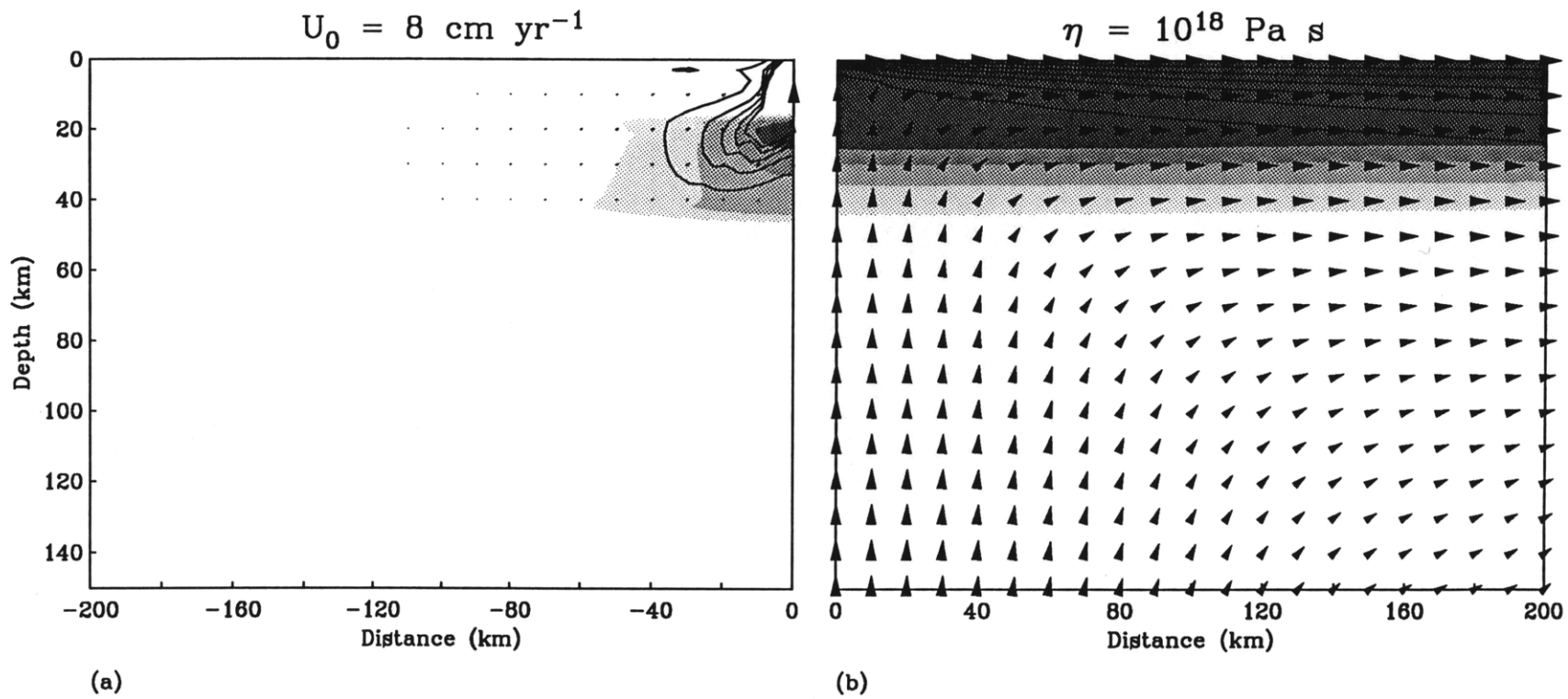


Figure 4.11

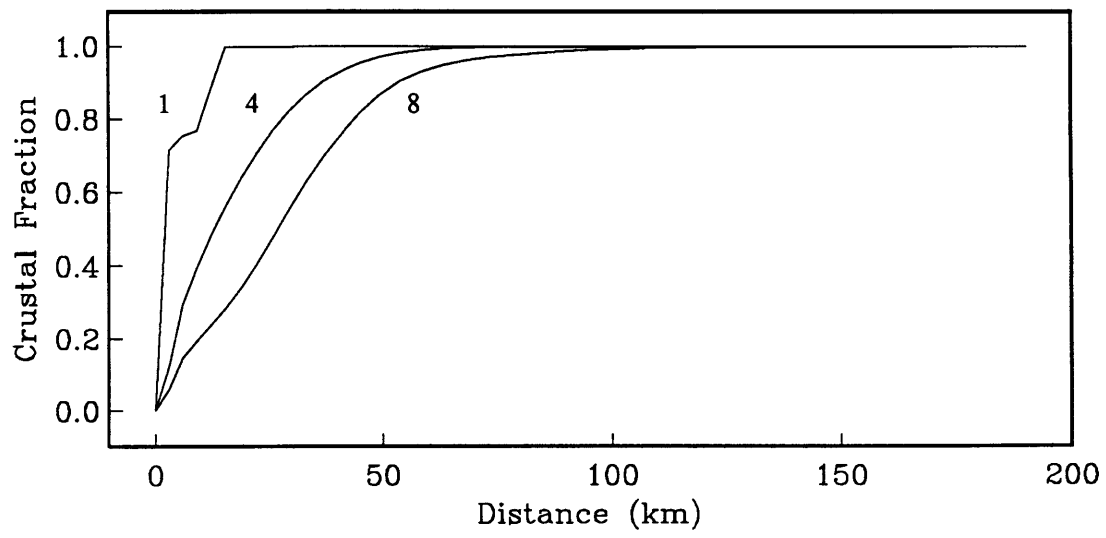


Figure 4.12

Chapter Five

Conclusions

We are usually convinced more easily by reasons we have found ourselves than by those which have occurred to others.

Pascal
Pensées

In this thesis, I develop a unique finite–element computer program that calculates the following variables in the mantle beneath a mid–ocean ridge: (1) the mantle flow field, (2) the melt flow field, (3) the mantle temperature, (4) the rate of melt production, (5) the mantle density, (6) the modal mineralogy and oxide composition of the mantle, (7) the oxide composition of the melt, and (8) the ratio of permeability to melt viscosity. Optionally, the finite strain in the mantle is also calculated. I then apply this model to a suite of numerical experiments designed to examine the interactions of melting, melt migration and mantle flow in the subridge mantle.

Flow in the mantle is driven by two–mechanisms: (1) the divergence of the rigid lithosphere that results in a broad stagnation point flow beneath the ridge axis and (2) convection driven by melting–induced variations in the residual mantle density. Deformation of the mantle due to compaction is ignored. Melt flow paths are obtained using D’Arcy’s Law for the flow of a Newtonian fluid through a viscous matrix. The driving forces for melt migration are (1) the natural buoyancy due the density contrast between melt and mantle and (2) mantle flow derived pressure gradients. The direction of the flow of melt may also be changed by allowing for anisotropy in the mantle.

The steady–state temperature structure of the mantle is determined by balancing the flux of heat due to the mantle and melt against thermal diffusion and the loss of latent heat due to melting. Melt production rate is determined by the rate at which energy is advected above a mantle solidus. The solidus used in this study is a function of pressure, modal mineralogy and oxide composition where the assumed mantle mineralogy that of a spinel lherzolite which is defined by the following modes: olivine, orthopyroxene, clinopyroxene and spinel. Mantle and melt oxide compositions are given by concentrations of the following eight oxides: K_2O , Na_2O , CaO , FeO , MgO , TiO_2 , SiO_2 , Al_2O_3 . The density of the mantle, which drives buoyant flow, is calculated using the weight percentages of each mineral present and their Fe/Mg ratio.

In order to close D’Arcy’s Law, the ratio of the permeability to mantle viscosity is required. In other studies, a value is assumed for the mantle viscosity and the permeability is assumed to have a functional dependence upon the mantle porosity. This latter functional

dependence is not well-constrained. Rather than assume a functional form for the permeability, I derive an expression for the ratio of permeability to melt viscosity using D'Arcy's Law and the equation describing conservation of melt mass. Mantle permeabilities obtained using this equation yield reasonable results based upon available data and other theoretical studies.

In general, a D'Arcy Law formulation requires a second order (anisotropic) tensor in order to describe the permeability. The presence of a crystallographic preferred orientation in mantle minerals found in ophiolites as well as veins and dikes all imply that, at some depth, the mantle permeability is anisotropic. In this thesis, I present a method for mapping the finite strain of the mantle into the mantle permeability to allow for this anisotropy.

The program described above was applied towards (1) characterizing the interaction of a thermodynamically self-consistent mantle/melt system, (2) testing the efficacy of various mechanisms for focussing melt to the axis of a mid-ocean ridge. Specific conclusions from this thesis are as follows;

(1) In a thermodynamically self-consistent model of melting, melt migration and mantle convection beneath a mid-ocean ridge melting is explicitly controlled by the flux of thermal energy above a mantle solidus. The mantle solidus depends upon pressure, mantle mineralogy and mantle composition. As the extent of melting increases, the mantle solidus temperature rises and its pressure derivative changes as the mantle becomes more depleted in its basaltic components. The latent heat of melting controls how much melting occurs locally for a given temperature increase. Advection of heat by the melt will increase melting rates as will the buoyantly-driven component of upwelling.

(2) A large impediment to further progress in studies of melt migration at mid-ocean ridges is our uncertainty in the functional dependence of permeability upon melt fraction. The rate at which both mass and heat may be transported by the the melt are critically dependent upon the permeability. As the transport of heat via the melt may effect melt production rates, the extent of melting, etc., it is important that this parameter be well determined. For steady-state melt migration, one may derive an equation for the ratio of permeability to melt viscosity from a set of simplified governing equations. This equation lets the permeability adjust for both local production of melt and the advection of melt from other regions.

(3) The effect of latent heat of melting is to reduce mantle temperatures to the solidus wherever sufficient heat is advected to cause melting. Lowering the latent heat of melting

causes both the total amount of melting and the melt production rates to increase. The latent heat also has an effect on the variation of melt production rate with depth. Small latent heats yield high melt production rates. More mantle-like latent heats decrease melt production rates because less heat is required to keep the mantle temperature on its solidus for a given amount of melt. As a result, differences in the latent heat of a factor of two can lead to large differences in the thickness of the crust. For low latent heats ($250 \text{ J kg}^{-1} \text{ }^\circ\text{C}^{-1}$), melt production rates are high and melting continues until clinopyroxene is lost as a phase. Since most of the basaltic component is melted out for this value of the latent heat, the crustal thickness is higher than for a high-latent heat model ($450 \text{ J kg}^{-1} \text{ }^\circ\text{C}^{-1}$) where melting ceases due to the onset of conductive cooling.

(4) The advection of heat due to the melt increases melt production rates by providing additional energy for melting at shallower depths. Outside the melting region, melt heat advection raises isotherms and provides a means for changing the thickness and width of the melting region. These may be an important effects where melt is focussed into a narrow region. In my simple plate spreading models, the combined effects of low melt production and vertically rising melt combine to produce a small effect on the temperature and melt production rate fields. However, when crustal thicknesses become appreciable ($\sim 6 \text{ km}$), the advection of melt heat may be a factor that cannot be ignored in any self-consistent study.

(5) The pattern of melt production will depend both upon (1) the rate of heat advection and therefore local mantle and melt velocities and (2) changes in the solidus temperature and its pressure derivative. This latter effect provides an explanation for the increase of melt production rate with height from the pressure of initial melting. This effect is initially counter-intuitive because the solidus temperature actually increases as the low-melting point components are extracted. However, what is important in the generation of melt is the rate at which heat is advected across the solidus. The important parameter for then is not the mantle temperature, but the spatial gradient of temperature ($V \cdot \Delta T$). Since the pressure derivative of the mantle solidus increases as pressure decreases throughout the melting regime, the melt production rate increases.

(6) Beneath the ridge axis, melting ceases at the depth where clinopyroxene is lost as a phase. This effect results in a depleted harzburgitic layer above the minimum depth of melting. The harzburgite layer acts as a barrier to further melting away from the ridge axis.

In these experiments, melting occurs between 4 and 16 kbar depth with an average pressure of melting of 10 kbar.

(7) Compositionally-driven convection increases crustal production by a factor of 1.5–2 over models where mantle flow is driven solely by the divergence of the lithosphere.

(8) At fast spreading rates (4–8 cm yr⁻¹), compositionally-driven convection does not significantly enhance mantle flow beneath the ridge. At these velocities, viscous stresses are high and lateral variations in mantle density are small and, thus, little buoyantly-driven upwelling occurs. At slower spreading rates, the effect of buoyancy forces on the mantle flow becomes increasingly important for two reasons. First, the lateral dimensions of the melting regime are increasingly delimited by the onset of conductive cooling. The smaller width leads to larger lateral variations in density which are the driving force for convection. Second, the magnitude of viscous stresses decreases relative to buoyancy forces because of their dependence upon spreading rate

(9) Most of the melt that forms the oceanic crust is created within several tens of kilometers of the ridge axis where significant mantle upwelling occurs thus strongly delimiting the lateral dimensions of the melting regime. The maximum pressure of melting is constant if the mantle temperature and initial mantle composition are also constant. The minimum pressure of melting is constant in all models in which clinopyroxene is lost as a phase. The limits placed upon the size of the melting regime by the mantle flow field and the depth range over which significant melting occurs explains why the crustal thickness remains constant as spreading rate increases beyond about 4 cm yr⁻¹.

(10) The narrowing of the melt regime and the additional pressure gradients resulting from compositional convection are insufficient to focus melt to the ridge axis when the sub-ridge viscosity is low enough for significant compositionally driven flow to occur.

(11) If mantle viscosities are of order 10¹⁸–10¹⁹ Pa s, then the flowpaths of the melt phase will be little affected by pressure gradients due to viscous stresses and the melt will rise vertically resulting in a broad region of crustal accretion. Enhancement of these pressure gradients by the use of a temperature- and pressure-dependent viscosity is not a sufficient mechanism for focussing melt to the ridge axis.

(12) Comparing several geophysical observables (bathymetry, gravity, seismic travel time) shows that, for any given spreading rate, there are no physically detectable differences between models with different viscosity structures. A comparison of mantle residual mineralogy and aggregate primary melt compositions show that there is also little difference in these observables between models with different spreading rates and viscosity structures. The fact that significant differences in these variables do exist between mid-ocean ridges implies that changes are required in other parameters, such as mantle temperature, composition and perhaps variations in the mantle flow field due to ridge-transform offsets, ridge migration, or asymmetric spreading.

(13) Several of these numerical experiments explore the effects of strain-induced mantle anisotropy as a mechanism for transporting melt to the ridge axis. Regardless of the exact mechanism, the resulting anisotropy in the mantle permeability strongly focuses melt to the ridge axis, in accordance with observation that the entire volume of melt forming the oceanic crust is emplaced there. This result is in contrast to models which rely upon dynamic forces to drive melt to the ridge.

(14) A marked difference in patterns of finite strain exists between models with different spreading rates. At medium to fast spreading rates, flow is predominantly plate-driven resulting in a strong yet uniform pattern of mantle anisotropy. At slow spreading rates, a strong component of flow due to compositionally-driven convection results in a pattern of lithospheric anisotropy that varies in both orientation and magnitude. This result may help explain why a pervasive mantle anisotropy oriented in the direction of plate spreading is relatively easy to detect beneath the Pacific and difficult to detect beneath the Atlantic.

*Our little systems have their day;
They have their day and cease to be;
They are but broken lights of thee,
And thou, O Lord, art more than they.*

*We have but faith: we cannot know,
For knowledge is of things we see;
And yet we trust it comes from thee,
A beam in darkness, let it grow.*

*Let knowledge grow from more to more,
But more of reverence in us dwell;
That mind and soul, according well,
May make one music as before.*

But vaster.

Appendix A

Finite Element Formulation of the Governing Equations and their Solution via Digital Computers

Nature hates calculators...

Ralph Waldo Emerson

Introduction

In this thesis, I derived several equations that described (1) creeping fluid flow in the Earth's upper mantle, (2) melt migration via two-phase flow, and (3) the generation of a partial melt beneath a mid-ocean ridge and the related time-evolution of the mantle composition and mineralogy. Each of the non-linear equations required to describe the behavior of the coupled mantle-melt system are too complicated to be solved analytically. Rather, numerical techniques are used to solve the resulting system of non-linear equations on digital computers. Of the techniques available to us, we have a choice of two relatively robust candidates: finite differences and finite elements.

The main advantages of finite differences are that it is relatively easy to implement and generally results in memory- and time-efficient algorithms. For example, consider the one-dimensional heat equation

$$\kappa \frac{\partial^2 T}{\partial x^2} + f(x) = 0 \quad (A1)$$

where T is temperature, κ is the thermal diffusivity, and $f(x)$ is a source function. We wish to solve this equation on the closed interval $[0,1]$ subject to some appropriate boundary conditions. Since we can only solve the equation at a finite number of points, we divide the interval into $n-1$ equally spaced intervals and solve the equation at their n intersections (nodes). To solve this problem via finite differences, we simply discretize the first term in the equation by the standard centered difference approximation to the second derivative

$$\kappa \left[\frac{T_{i-1} - 2T_i + T_{i+1}}{\Delta x^2} \right] = -f(x_i) \quad (A2)$$

where Δx is the node spacing and the subscript i indicates the i th node. Writing one of these equations for each degree of freedom results in an $3 \times n$ system of linear equations which may then be solved by one of various methods (Gaussian elimination, for example).

Clearly, this ease of implementation is part of the strong attraction of the finite difference technique. Moreover, certain types of problems are extremely easy to solve using finite differences because they do not require the solution of a matrix problem via some sort of inversion scheme. Despite these advantages, finite difference methods are often difficult to implement on irregular meshes or for problems with spatially variable material properties. This last quality is particularly desirable in the problem we wish to solve. In these problems, we would like to have a fine mesh near the ridge axis where strong gradients exist in several of the variables we are calculating. Second, we will be investigating the effects of lateral variations in viscosity and density. Hence, we would like to have a method which handles these problems with ease. For these reasons (amongst others we will mention in passing at the appropriate times) we generally choose to discretize our equations with the method of finite elements.

Unfortunately, the theoretical development of finite elements is less intuitive than that for finite differences. Therefore, we will begin this section with a preliminary discussion of the idea of finite elements and shape functions. Next, we will outline the method of conjugate gradients which forms the basis of the algorithms used to solve most of equations. This discussion will lead us into a novel method of storing the resulting system of equations. This technique, known as the Element-By-Element (EBE) method, provides us with an efficient scheme (both in terms of computation time and storage) for solving our equations on a vector-parallel computer. From there, we will proceed to discretize each of the equations presented in the body of the thesis.

The Finite Element Method

In this section, we give a brief description of the basis of the finite element method, using similar notation and descriptions found in *Hughes* [1987] which should be consulted for a more thorough and lucid explanation.

Consider again for a moment the one-dimensional diffusion equation with a source term (equation A1). We have already stated the equation we wish to solve and the domain over which we wish to solve it. The only things we need declare in order to complete the *strong* or *classical* form of this problem are boundary conditions. If we choose to employ both fixed (Dirichlet) and flux (Neumann) boundary conditions, then the strong form of this problem is as follows:

$$(S) \left\{ \begin{array}{l} \text{Given } f: \bar{\Omega} \rightarrow \mathfrak{R}^1 \text{ and constants } g \text{ and } h, \text{ find } u: \bar{\Omega} \rightarrow \mathfrak{R}^1 \text{ such that} \\ u_{,xx} + f = 0, \forall x \in \bar{\Omega} \\ u(1) = g \\ -u_{,x}(0) = h \end{array} \right.$$

where $\bar{\Omega}$ is the closed interval $[0,1]$ (without the overbar it would indicate the open interval $(0,1)$), \mathfrak{R}^1 is the set of real numbers, and the subscript comma indicates differentiation (i.e. $u_{,xx} = d^2u/dx^2$).

To define the *weak* or *variational* form of (S) we first need to describe two classes of functions. The first is a collection of *trial solutions* denoted by U which consists of all functions which have square-integrable first derivatives and take on the value of the fixed boundary conditions. In our example, this is stated as follows

$$U = \{ u \mid u \in H^1, u(1) = g \}$$

where H^1 implies that u is a function such that

(A3)

$$\int_0^1 (u_{,x})^2 dx < \infty.$$

The second collection of functions we must define are the so called *weighting functions* or *variations*. The definition of the weighting functions is very similar to the definition of the trial functions (A3) but with the exception that the weighting functions w are identically zero on fixed boundaries. The collection of these functions, denoted V , is defined as follows

$$V = \{ w \mid w \in H^1, w(1) = 0 \}$$
(A4)

The weak form of (S) is obtained by integration by parts of the integral

$$\int w(u_{,xx} + f) dx$$

and is

$$(W) \left\{ \begin{array}{l} \text{Given } f, g, \text{ and } h, \text{ as before. Find } u \in U \text{ such that } \forall w \in V \\ \int_0^1 w_x u_x dx = \int_0^1 wf dx + w(0)h \end{array} \right.$$

We now make an essential distinction between usual finite difference and finite element formulations. Finite differences are usually based upon discretizing the strong form (S), whereas finite elements is based upon a discretization of (W), the weak form.

From here we proceed to the method of discretizing the weak form. In finite differences, recall, we merely wrote down the discrete form of the differential operator and the source term. In finite elements we are required to be a bit more explicit since we are dealing with classes of functions. That is, in finite differences, nothing about the variation of say, u , between nodes was explicitly mentioned. The definitions of our trial function and weighting function spaces (U and V , respectively), require us to ensure that a function in either space is at least continuous and that its first derivative is square-integrable. Therefore, we need to specify how our variables will change between nodes and within elements. At the very least, this can be seen by the need to have some way of calculating the integrals in the weak form. This is where the idea of *shape* or *interpolation* functions comes into play. We need to make one more critical step, however, before we can proceed to defining these functions explicitly.

Now, we define the finite-dimensional approximations to U and V , U^h and V^h , and associate them with a mesh or discretization of the domain Ω which is characterized by a mesh spacing h . These approximations are thus subsets of their parent spaces, *i.e.* $U^h \subset U$ and $V^h \subset V$. Note here that one consequence of this definition is that the finite-dimensional analogues of u and w will satisfy their respective boundary conditions, *e.g.* $u^h(1) = g$ and $w^h(0) = 0$.

Assume that the set of discrete weighing functions, V^h , is given. We now construct a function $u^h \in U^h$ by

$$u^h = v^h + g^h \tag{A5}$$

where $v^h \in V^h$ and g^h is a given function satisfying the Dirichlet boundary conditions, *i.e.* $g^h(1) = g$. Note that (A4) satisfies this boundary condition as well. The important point here is that, up to a function g^h , U^h and V^h are composed of identical collections of functions. Upon inserting (A5) into the weak form (W), we are left with the Galerkin form of our problem

$$(G) \left\{ \begin{array}{l} \text{Given } f, g, \text{ and } h, \text{ as before, find } u^h = v^h + g^h \text{ where } v^h \in V^h, \\ \text{such that } \forall w^h \in V^h \\ \int_0^1 w^h_{,x} v^h_{,x} dx = \int_0^1 w^h f dx + w(0)h - \int_0^1 w^h_{,x} g^h_{,x} dx \end{array} \right.$$

Let V^h be the collection of all linear combinations of given functions denoted by N_A where $A = 1, 2, \dots, n$. Thus

$$w^h = \sum_{A=1}^n c_A N_A \quad (A6)$$

The N_A 's are referred to as shape functions and the c_A 's are constants. We require that at each Dirichlet boundary the shape functions are homogeneous i.e. $N_A(1) = 0$, $A = 1, 2, \dots, n$. To complete U^h , we need to specify g^h . To accomplish this, we introduce an additional shape function N_{n+1} with the property that at each Dirichlet boundary $N_{n+1} = 1$. Then $g^h = gN_{n+1}$ and thus $g^h = g$. With these definitions, we may write u^h as follows

$$\begin{aligned} u^h &= v^h + g^h \\ &= \sum_{A=1}^n d_A N_A + g N_{n+1} \end{aligned} \quad (A7)$$

where the d_A 's are constants. Inserting this equation into the Galerkin form of our problem, plus a little algebra, yields the following equation

$$\sum_{B=1}^n \int_0^1 \frac{\partial N_A}{\partial x} \frac{\partial N_B}{\partial x} dx d_B = \int_0^1 N_A f dx + N_A(0)h - g \int_0^1 \frac{\partial N_A}{\partial x} \frac{\partial N_{n+1}}{\partial x} dx \quad (B8)$$

Everything in (A8) is known except the d_B 's. Thus, equation (A8) is a system of n equations in n unknowns. We may simplify equation (A8) by compressing our notation thus

$$\sum_{B=1}^n K_{AB} d_B = F_A, \quad A = 1, 2, \dots, n \quad (A9)$$

If we adopt matrix notation, then (A9) may be further simplified into

$$\mathbf{Kd} = \mathbf{F} \quad (\text{A10})$$

It is common practice to refer to the matrix \mathbf{K} as the *stiffness matrix*, and the vectors \mathbf{d} and \mathbf{F} as the *displacement* and *force vectors*, respectively, reflecting the elasticity origins of the first finite element formulations.

Before we immerse ourselves in shape functions, let us make mention of two minor but important bookkeeping tools. Consider the bounded region in Figure A1 which is divided into a number of subregions. A node exists at the vertices of each subregion. We may assign a *global node number* to each node by assigning the node in the lower left-hand corner a value of one. From this point we number the remaining nodes in increasing order from left-to-right, bottom-to-top. Our ordering could have been arbitrary, as long as each node has a unique value but for the rectangular regions we will be considering, this type of ordering is natural and useful.

We now ask ourselves what is an element? An element is the region bounded by a finite collection of nodes. In our examples (Figure A1), the nodes may be only at the corners of an element (as in the case of the four node element) or along the sides and interior as well (as in the case of the nine node element). Elements only share nodes along their edges. Within each element, we may assign a *local node number* to each node. In the case of the four-node element, we assign to an arbitrary node the value one and number the rest in increasing order in a counter-clockwise direction. It does not matter which node we pick to be first, as long as we are consistent in our ordering. In this thesis, we use both the global and local node orderings shown in Figure A1.

The distinction between global and local coordinates is an important one because the stiffness matrix \mathbf{K} and force vector \mathbf{F} are essentially the sum of elemental contributions. That is, the integrals in, say, equation (A8) are calculated at an element level and then summed into \mathbf{K} and \mathbf{F} .

In this thesis, we use two basic elements, the four node bilinear quadrilateral element and the nine-node biquadratic element. The four node element, perhaps the most basic of all elements, is shown in Figure A2. The domain of each element is referred to with the symbol Ω^e . In general, element domains are irregular and of unequal size, making the calculation of multidimensional integrals rather tedious. We would like to have a standard integration scheme and be able to apply it to all elements. We may accomplish this by mapping all elements to a *parent domain*. In two dimensions, the parent domain is the

biunit square shown in Figure A2. We can now relate the coordinates of our original four-node quadrilateral, x , to those of the parent domain, ξ by mappings of the form

$$x(\xi, \eta) = \sum_{a=1}^4 N_a x_a^e \quad (\text{A11})$$

$$y(\xi, \eta) = \sum_{a=1}^4 N_a y_a^e \quad (\text{A12})$$

where ξ and η are called the *natural coordinates*. It can be shown that the shape function N_a has the form

$$N_a(\xi) = N_a(\xi, \eta) = \frac{1}{4} (1 + \xi_a \xi) (1 + \eta_a \eta) \quad (\text{A13})$$

where $-1 \leq \xi, \eta \leq 1$ and the premultiplication factors ξ_a and η_a are given in the following table

TABLE A1

| a | ξ_a | η_a |
|-----|---------|----------|
| 1 | -1 | -1 |
| 2 | 1 | -1 |
| 3 | 1 | 1 |
| 4 | -1 | 1 |

The form of the bilinear shape function is shown in Figure A3. Because the shape functions we have used to map coordinates are *isoparametric* we may use them as our interpolation functions as well, *i.e.*

$$u^h(\xi) = \sum_{a=1}^{n_{en}} N_a(\xi) d_a^e \quad (\text{A14})$$

where n_{en} is the number of nodes per element.

We may also define the higher-order nine-node element shown in Figure A4. Rather than go through the above process, we may construct the nine-node element by beginning

with the four node element and then adding on nodes and correcting previously defined nodes as required. This process is shown in Figure A5.

To calculate the entries in our stiffness matrix and force vector, we need to calculate the integrals resulting from the Galerkin approximation to the weak form of our problem. For example, given a function f and an element domain Ω^e we wish to calculate

$$\int_{\Omega^e} f(x) d\Omega \quad (A15)$$

First we must map our integral to our parent domain as follows

$$\int_{\Omega^e} f(x) d\Omega = \iint_{-1}^1 f(x(\xi,\eta),y(\xi,\eta))J(\xi,\eta) d\xi d\eta \quad (A16)$$

where $J(\xi,\eta) = \det(\partial x/\partial \xi)$, the Jacobian of our coordinate transformation. To actually integrate equation (A16) we use the method of Gaussian quadrature. In one-dimension, Gaussian quadrature may be stated as follows

$$\int_{-1}^1 f(\xi) d\xi \equiv \sum_{l=1}^{n_{int}} f(\tilde{\xi}_l)W_l \quad (A17)$$

where n_{int} is the number of integration points, $\tilde{\xi}_l$ is the coordinate of the l th integration point, and W_l is the ‘weight’ of the l th integration point. In multiple dimensions, the method is basically the same with, of course, the added factor of our Jacobian. In this thesis, we rely most heavily on the one-, 2x2-, and 3x3-point Gaussian quadrature rules given in Table A2 and shown in Figure A6.

The Conjugate Gradient Algorithm

In this section, we describe the classic conjugate gradient algorithm for solving problems of the form $Ax = b$. Why conjugate gradients? Basically we wish to avoid either inverting the matrix A or using the computationally intensive Gaussian elimination method. In conjugate gradients, the most computationally intensive tasks we need perform are the inner-product of two vectors and matrix-vector multiplies. If coded properly, this algorithm is very efficient on vector-parallel machines (see next section).

We will begin by showing how the conjugate gradient algorithm is derived from the method of steepest descents and then finish by discussing the biconjugate gradient algorithm and methods of preconditioning to achieve further speedup. In the following discussion, we assume that A is an $n \times n$ symmetric, positive-definite matrix. The description here is basically that found in *Hageman and Young* [1981] (see also *Press et. al.*, 1986).

The method of steepest descents begins with the quadratic functional

$$F(x) = \frac{1}{2}(x, Ax) - (b, x) \quad (A18)$$

where the parentheses indicate taking the following inner product

$$(f, g) = \int f \cdot g \, dx \quad (A19)$$

Thus, the problem we encounter is that of trying to minimize $F(x)$. The gradient of the functional is given by

$$\nabla F(x) = b - Ax \quad (A20)$$

The direction of ∇F is the direction for which $F(x)$ has the greatest rate of change at the point x . If x^n is an approximation to the true answer x_0 , then moving in a direction parallel to ∇F from the point x^n to a point x^{n+1} where the functional $F(x^{n+1})$ is a minimum will give us an improved estimate of x_0 . Thus

$$x^{n+1} = x^n + \lambda_n r^n \quad (A21)$$

where λ_n is chosen to minimize $F(x^{n+1})$. Using equations (A18) and (A20), the method of steepest descents is

$$\begin{aligned} x^0 & \text{ arbitrary,} \\ x^{n+1} & = x^n + \lambda_n r^n, \text{ for } n = 0, 1, \dots, \\ r^n & = b - Ax^n, \\ \lambda_n & = \frac{(r^n, r^n)}{(r^n, Ar^n)} \end{aligned} \quad (A22)$$

However, for ill-conditioned matrices, the convergence rate of this method is slow. The basic problem is that in moving from x^n to x^{n+1} it is possible to degrade previous minimizations. What we want is a method that moves us towards the minimum of F without affecting the minimizations of all our previous guesses. This is basically the idea of the conjugate gradient algorithm. In conjugate gradients, we still move in a direction that minimizes F (through the parameter λ_n) but we choose a correction vector p^n (through the parameter α_n) that is 'A-conjugate' to p^{n-1} , i.e. $(p^n, Ap^{n-1}) = 0$. By correctly choosing p^n rather than r^n , we can avoid the problems caused by the steepest descents method. The conjugate gradient algorithm is given by the following formula

$$\begin{aligned}
 & x^0 \text{ arbitrary,} \\
 & x^{n+1} = x^n + \lambda_n p^n, \quad n = 0, 1, \dots, \\
 & p^n = \begin{cases} r^n, & \text{if } n = 0 \\ r^n + \alpha_n p^{n-1}, & n = 1, 2, \dots, \end{cases} \\
 & \alpha_n = -\frac{(r^n, Ap^{n-1})}{(p^{n-1}, Ap^{n-1})}, \quad n = 1, 2, \dots, \\
 & r^n = b - Ax^n, \quad n = 0, 1, \dots, \\
 & \lambda_n = \frac{(p^n, r^n)}{(p^n, Ap^n)}, \quad n = 0, 1, \dots
 \end{aligned} \tag{A23}$$

Fixed (Dirichlet) boundary conditions are implemented by setting the correction vectors $p^n = 0$ at each iteration.

If a matrix is ill-conditioned, that is the ratio of its largest to smallest eigenvalues is large, then iterative methods tend to have some difficulty converging to a solution. A common technique is to precondition the matrix A by another matrix Q such that the spectral separation of the product QA is smaller than that of the matrix A alone. Furthermore, such a preconditioner should not change the nature of the solution while enhancing convergence rates. A number of good preconditioners exist, however, implementing them in an Element-By-Element framework is difficult. One method that seems to work reasonably well and is easy to implement with the EBE data structure is diagonal preconditioning. Consider a diagonal matrix Q with the following properties

$$Q_{ij} = \begin{cases} 1/A_{ij}, & i = j \\ 0, & i \neq k \end{cases} \tag{A24}$$

The conjugate gradient algorithm (A23) can be modified to incorporate this preconditioning matrix resulting in the following PCG (preconditioned conjugate gradient) algorithm

$$\begin{aligned}
 & \mathbf{x}^0 \text{ arbitrary,} \\
 & \mathbf{x}^{n+1} = \mathbf{x}^n + \lambda_n \mathbf{p}^n, \quad n = 0, 1, \dots, \\
 & \mathbf{p}^n = \begin{cases} \mathbf{r}^n, & \text{if } n = 0 \\ \mathbf{r}^n + \alpha_n \mathbf{p}^{n-1}, & n = 1, 2, \dots, \end{cases} \\
 & \alpha_n = -\frac{(\mathbf{r}^n, \mathbf{Q} \mathbf{A} \mathbf{p}^{n-1})}{(\mathbf{p}^{n-1}, \mathbf{Q} \mathbf{A} \mathbf{p}^{n-1})}, \quad n = 1, 2, \dots, \\
 & \mathbf{r}^n = \mathbf{b} - \mathbf{Q} \mathbf{A} \mathbf{x}^n, \quad n = 0, 1, \dots, \\
 & \lambda_n = \frac{(\mathbf{p}^n, \mathbf{r}^n)}{(\mathbf{p}^n, \mathbf{Q} \mathbf{A} \mathbf{p}^n)}, \quad n = 0, 1, \dots
 \end{aligned} \tag{A25}$$

When a matrix is not unsymmetric and not positive definite, then one must resort to using a class of algorithms often referred to as Generalized Conjugate Gradients or Biconjugate Gradients. A number of algorithms exist and each have their own convergence properties. One might consider simply multiplying both sides of $\mathbf{A} \mathbf{x} = \mathbf{b}$ by \mathbf{A}^T ; the result being a symmetric system of equations. However, if the condition number of \mathbf{A} is large, then this procedure only serves to further worsen the convergence properties of the system. For this reason, we choose to use biconjugate gradients to solve systems of equations that are unsymmetric. The algorithm we use in this thesis is a basically the ORTHOMIN procedure [Hageman and Young, 1981] and is as follows

$$\begin{aligned}
 & \mathbf{r}_0 = \mathbf{p}_0 = \mathbf{r}_0^T = \mathbf{p}_0^T = \mathbf{b} - \mathbf{A} \mathbf{x}_0 \\
 & \alpha_n = \frac{(\mathbf{p}_n^T, \mathbf{r}_n)}{(\mathbf{p}_n^T, \mathbf{A} \mathbf{p}_n)} \\
 & \mathbf{x}_{n+1} = \mathbf{x}_n + \alpha_n \mathbf{p}_n \\
 & \mathbf{r}_{n+1} = \mathbf{r}_n - \alpha_n \mathbf{A} \mathbf{p}_n \\
 & \mathbf{r}_{n+1}^T = \mathbf{r}_n^T - \alpha_n \mathbf{A}^T \mathbf{p}_n^T \\
 & \beta_n = \frac{(\mathbf{r}_n^T, \mathbf{A} \mathbf{p}_n)}{(\mathbf{p}_n^T, \mathbf{A} \mathbf{p}_n)} \\
 & \mathbf{p}_{n+1} = \mathbf{r}_n + \beta_n \mathbf{r}_n \\
 & \mathbf{p}_{n+1}^T = \mathbf{r}_n^T + \beta_n \mathbf{r}_n^T
 \end{aligned} \tag{A26}$$

Computations on Vector-Concurrent Computers and the Element-By-Element Concept

The fact that finite-elements is based upon integrals over elements (such as those in equation A15) leads us to develop programs based on element structure and logic. This is

in contrast to finite differences where programs are based on nodal structure and logic. The main bulk of a finite element program would thus involve looping over all elements, computing the element matrix contributions, accumulating these element contributions into the stiffness matrix, and solving the resulting system. Depending upon the problem to be solved, the bandwidth of the matrix may be quite large even though the matrix itself has mostly zero-valued entries. For large problems with numerous degrees of freedom per node, the bandwidth of the stiffness matrix may rapidly become prohibitive. Ideally, we would like to store only the non-zero entries of the stiffness matrix, while retaining information on which degrees of freedom are associated with which entries in the matrix.

Another consideration is that we wish to solve our system on a digital computer featuring a vector-concurrent architecture. On a standard serial computer, operations on data structures are executed sequentially. For example, consider the following Fortran loop

```
DO 10 I = 1, 8192
10 A(I) = A(I) + S
```

where A is a double precision array and S is a double precision scalar. On a serial computer, only one array entry may be updated for each iteration of the loop. Thus, the time to execute the loop is 8192 times the amount of time required for one iteration.

A computer operating concurrently can execute the same loop over multiple processors. For example, on a concurrent computer with eight processors, we can update eight entries of the array in one iteration of the loop, i.e.

```
A(1) = A(1) + S
A(2) = A(2) + S
A(3) = A(3) + S
A(4) = A(4) + S
A(5) = A(5) + S
A(6) = A(6) + S
A(7) = A(7) + S
A(8) = A(8) + S
```

Thus, in our example loop, each processor executes 1024 iterations; completing the loop in about 13% of the time required to perform the same instructions on a serial computer.

On the Alliant FX/Series of computers, each processor is also capable of performing the same instruction across multiple pieces of data. Working in this vector mode, each

processor on an Alliant is capable of working on 32 elements of data at once. Processing 32 elements with a vector instruction is about two to four times faster than processing the same 32 elements in scalar mode.

If we combine these two ideas and operate in a vector-concurrent mode, our example loop is broken up into groups of 32 elements, then these 32 element groups are allotted to each processor. Using eight processors, the total time to execute our loop is now 3% of the time required in scalar mode.

Most of the computational effort in solving our finite element system via conjugate gradients (see previous section) is the formulation of matrix-vector products of the form $Ax = b$. We would like to write our program such that the formation of such products takes full advantage of the vector-concurrent nature of the computer we will be using (an Alliant FX/40). If we could break up the process of forming matrix vector products, we could easily distribute the task across multiple processors and vector pipelines. This idea, along with our desire to minimize the demands of the stiffness matrix upon the core memory, leads us to the Element-By-Element concept [Carey *et al.*, 1988].

Let us define A_e and b_e as the element matrix and vector contributions to the stiffness matrix. If we take these element contributions, expand them to the size of the stiffness matrix (i.e. the entries of A_e and b_e are mapped to their appropriate global row and column positions with all other entries being zero) then we may rewrite the system $Ax = b$ as follows

$$\left(\sum_{e=1}^E \hat{A}_e \right) x = \left(\sum_{e=1}^E \hat{b}_e \right) \quad (A27)$$

where E is the number of elements and \hat{A}_e and \hat{b}_e are the elemental contributions expanded to system size. If we know how to map from local node orderings to global node orderings we need not store the non-zero entries of A . Thus, we store \hat{A}_e as dense local element contributions without summing them into a stiffness matrix.

The other half of the conjugate gradient algorithm is the formation of matrix-vector products Ax . Recalling equation (A24) we may write this product as follows

$$Ax = \left(\sum_{e=1}^E \hat{A}_e \right) x = \left(\sum_{e=1}^E \hat{A}_e \hat{x}_e \right) = \left(\sum_{e=1}^E \hat{b}_e \right) = b \quad (A28)$$

Only the non-zero entries of each element matrix and vector enter term-by-term into the above sum. Hence, the non-zero entries \hat{b}_e can be computed as dense element matrix vector-products $A_e x_e$ rather than in the expanded form shown above. That is we may calculate

$$b_e = A_e x_e \quad (A26)$$

and each element matrix-vector product can be calculated independently and then summed into the global vector b .

We now ask the question: what is the optimal procedure for forming these matrix vector products on a vector-concurrent computer? Our first thought would be to loop over all elements, calculate each element matrix-vector product by looping over the nodes in the element, and then sum the result into the global force vector. However, a vector-concurrent Fortran compilers will try to optimize the inner-most loops in this scheme resulting in rather short vector lengths (basically, the number of nodes in an element). Rather, we need to rearrange our loops such that the all or most of the vectors on a given processor are filled. Here we use our knowledge that, in a typical finite-element problem, the number of elements is generally much larger than the number of nodes per element. If we rearrange our loops such that our outer loops are over the number nodes per element and the innermost loop is over the number of elements, then we achieve the longest vector lengths possible in a simple and efficient coding scheme. To make this more explicit, let the element matrices be stored as a four-dimensional array $A_{kl}(i,j) \equiv A_{klij}$ and the element vectors b_e in a one-dimensional array $b(i) = b_i$. The above scheme may then be written

```

For  $i = 1, 2, \dots, N$  nodes do
  For  $j = 1, 2, \dots, N$  nodes do
    For  $l = 1, 2, \dots, E_y$  elements do
      For  $k = 1, 2, \dots, E_x$  elements do
         $b_i = b_i + A_{klij} x_j$ 
      End do
    End do
  End do
End do.

```

This scheme is very efficient on vector-concurrent computers and yields very nearly linear speedup as the number of available processors increases.

As we mentioned before, the element-by-element method of storing the stiffness matrix results in a savings of allocated core memory thus either freeing up available memory and allowing for the solution of larger problems or eliminating page swapping from RAM to disk. How much of a savings may we expect? Consider a finite element mesh spanning a square domain. The banded stiffness matrix for this problem will have roughly $n^{3/2}$ entries where n is the total number of nodes in the grid. By contrast, storing the element contributions separately requires approximately $n(n_{pe})^2$ entries where n_{pe} is the number of nodes per element. The ratio of the memory required by the stiffness matrix versus the element-by-element method is thus $n^{1/2}/(n_{pe})^2$. Typically, elements have four or nine-nodes. The following table shows the above ratio as a function of n for these values of n_{pe} .

TABLE A3

| $n_{pe} \setminus n$ | 16 | 32 | 64 | 128 | 256 | 512 | 1024 |
|----------------------|-----|-----|-----|-----|-----|-----|------|
| 4 | 1 | 2 | 4 | 8 | 16 | 32 | 64 |
| 9 | 0.2 | 0.4 | 0.8 | 1.6 | 3.2 | 6.3 | 12.6 |

In this case, the element-by-element storage method is clearly more memory efficient large problems.

Discrete Form of the Momentum Equations

A number of methods exist for solving Stoke's equation for viscous flow. In the earth sciences, a likely choice is the penalty function method because of its ability to handle large variations in viscosity. However, the penalty function method often performs poorly when the system of equations is solved iteratively, e.g. by conjugate gradient relaxation techniques. However, the direct solvers used with the penalty function method require a large amount of computer memory relative to the Element-By-Element data structure. Memory requirements may or may not be an issue for two-dimensional problems. Three-dimensional problems are another matter, however, with direct solution algorithms becoming rapidly untenable due to their large storage requirements. Furthermore, some complicated data accessing schemes must be devised if direct algorithms are to be made efficient on vector-parallel computers. Fortunately, both the data storage issue and the data

access issue are straight forward if Element-By-Element data structures are used in conjunction with iterative solvers. The desirability of a robust iterative solver for the Stoke's problem led us to choose from a new class of algorithms that have as their basis a conjugate gradient solution process. This class of algorithms are generally referred to as global iterative Uzawa algorithms. The algorithm presented below is that of *Maday and Patera* [1989] and the presentation follows theirs closely.

For a constant viscosity fluid, the Stoke's problem for an incompressible fluid is

$$\begin{aligned}\eta\nabla^2\mathbf{V} - \nabla p &= \mathbf{f} \\ \nabla\cdot\mathbf{V} &= 0\end{aligned}\tag{A29}$$

where \mathbf{V} is the fluid velocity, p is the fluid pressure, and \mathbf{f} encompasses any forcing terms (i.e. buoyancy). Equation (A29) may be written in a discrete form as

$$\begin{aligned}\mathbf{A}\mathbf{V} - \mathbf{D}^T p &= \mathbf{B}\mathbf{f} \\ -\mathbf{D}\mathbf{V} &= 0\end{aligned}\tag{A30}$$

where \mathbf{A} and \mathbf{B} are discrete Laplacian and mass matrices, respectively and \mathbf{D} is a discrete gradient operator. The superscript T indicates the matrix transpose. Equation (A30) can be solved for \mathbf{V} directly from the momentum equation

$$\mathbf{V} = \mathbf{A}^{-1}\mathbf{D}^T p + \mathbf{A}^{-1}\mathbf{B}\mathbf{f}\tag{A31}$$

Substituting the discrete divergence equation into this yields

$$-\mathbf{D}\mathbf{V} = -\mathbf{D}\mathbf{A}^{-1}\mathbf{D}^T p - \mathbf{D}\mathbf{A}^{-1}\mathbf{B}\mathbf{f}\tag{A32}$$

Thus, the original statement of the discrete Stoke's problem may be written

$$\mathbf{A}\mathbf{V} - \mathbf{D}^T p = \mathbf{B}\mathbf{f}\tag{A33a}$$

$$\mathbf{S}p = -\mathbf{D}\mathbf{A}^{-1}\mathbf{B}\mathbf{f}\tag{A33b}$$

where

$$\mathbf{S} = \mathbf{D}\mathbf{A}^{-1}\mathbf{D}^T\tag{A34}$$

Note that the matrix S is symmetric and positive semi-definite. One advantage of this formulation is that velocity and pressure are decoupled in the solution process. Equation (A33b) is first solved for pressure and then equation (A33a) is solved for the velocities once p is known. Note that I need not have assumed a constant viscosity fluid in order to arrive at equations (A33a,b).

Solving for the pressure involves several iterations of the following conjugate gradient loop

$$\left\{ \begin{array}{l} \text{Guess } p_0 \\ r_0 = -DA^{-1}Bf - Sp_0, q_0 = r_0 \\ \alpha_m = \frac{(r_m, r_m)}{(q_m, Sq_m)} \\ p_{m+1} = p_m + \alpha_m q_m \\ r_{m+1} = r_m - \alpha_m Sq_m \\ \beta_m = \frac{(r_{m+1}, r_{m+1})}{(r_m, r_m)} \\ q_{m+1} = r_{m+1} + \beta_m q_m \end{array} \right. \quad (A35)$$

The matrix-vector product Sq within this loop is evaluated via the following sequence of discrete problems

$$y = D^T q \quad (A36)$$

$$Az = y \quad (A37)$$

$$Sq = Dz \quad (A38)$$

Equation (A37) is solved using a preconditioned conjugate gradient algorithm with diagonal preconditioning. The other two equations in this sequence are merely a vector-vector multiply and a vector-vector dot-product. Note that the residual r is the above conjugate gradient loop is actually the discrete divergence $-DV$ which can be used as an error criteria for stopping iteration. In this thesis, iteration for the pressure ceases when $\|r\| < 10^{-4}$ (note that this is a non-dimensional value) which usually requires $O(1)$ iterations of the main pressure solution loop. Once the pressure is determined, the velocities may be solved for directly using equation (A33a) which is solved using a preconditioned conjugate gradient algorithm with diagonal preconditioning.

An issue that has not been addressed so far is the type of element used to interpolate the velocities and pressures between nodes. One choice might be the Q_2-P_1 element in which velocities are specified on 9 (3x3) node, biquadratic element and pressure is specified on 4 (2x2) node bilinear (Figure A7a). A property of this element is that velocities and pressure are both continuous across element boundaries. This element also works well with the velocity-pressure algorithm of *Maday and Patera* [1989]. While continuity of the bilinear functions across element boundaries results in a smooth pressure field, the incompressibility condition ($\nabla \cdot \mathbf{V} = 0$) cannot be easily satisfied for each element individually. In order to circumvent this problem and satisfy incompressibility in each element separately, we adopt a pressure interpolation that is discontinuous across element boundaries. We assume that the pressure within each element can be described by the following linear function

$$f(\zeta, \eta) = \alpha_0 + \alpha_1 \zeta + \alpha_2 \eta \quad (\text{A39})$$

Unlike the Q_2-P_1 element where pressure is specified at the corner nodes of the nine-node macroelement, we now specify pressure at three nodes all located at the center of the nine-node macroelement (Figure A7b). Since the pressure functions are not matched at the element boundaries, pressure is discontinuous across element boundaries.

A further change is made to the shape functions that interpolate the velocities across the nine-node element. Rather than use the standard biquadratic Galerkin shape functions at each node, we use what are known as *hierarchical* shape functions. In this scheme, full velocities are only specified at the corner nodes and bilinear shape functions are used to interpolate velocities within the rest of the element. The remaining five nodes in the element contain correction terms to the linear velocity interpolation (Figure A7c). These correction terms are themselves linearly interpolated throughout the remainder of the element resulting in velocities that vary quadratically over the element. While this procedure seems unnecessary, it turns out that this formulation of the velocity element actually improves the condition of the resulting element stiffness matrix. As a result, noticeable improvements in convergence rates are observed in the velocity-pressure iteration described above.

Discrete Form of the Energy Equation

In this thesis, we have two forms of the discrete energy equation. The first is a steady-state advection-diffusion equation without any source terms. We use this equation to provide a reasonable initial starting guess to the temperature field. The second equation is

our time-dependent advection-diffusion equation with a source term given by the melt production rate (equation A26). Our non-dimensional steady-state equation is as follows

$$P_e \mathbf{V} \cdot \nabla T - \nabla^2 T = 0 \quad (\text{A40})$$

The stiffness matrix A_e for this problem is given by

$$A_e = \int_{\Omega_e} \nabla N^T \nabla N \, d\Omega + P_e \int_{\Omega_e} N^T \cdot \mathbf{V} \nabla N \, d\Omega \quad (\text{A41})$$

where N is the four-node bilinear shape function and the integrals are computed using the 2x2 point integration rule shown in Table A2. The velocity field for the steady state problem is simply the plate-driven flow due to the divergence of the rigid lithosphere. Because advection terms are present in this equation, the resulting stiffness matrix is not self-adjoint, hence we must use the biconjugate gradient algorithm (equation A26) to solve the resulting system of equations.

After an initial guess to the temperature field is made, advection of heat by the melt, changes in the mantle velocity field and the initiation of melting begin to alter the temperature field. In order to reach a steady-state solution, we solve the non-dimensional time-dependent advection-diffusion equation

$$P_e \left(\frac{\partial T}{\partial t} + \mathbf{V} \cdot \nabla T + \frac{\rho_f}{\rho_m} \mathbf{q} \cdot \nabla T \right) = \nabla^2 T - \frac{\Delta S_m \rho_f}{C_p \rho_m} P_e \Gamma \quad (\text{A42})$$

As mentioned above, the presence of advection terms in the energy equation makes the resulting stiffness matrix nonself-adjoint, thus forcing us to use a biconjugate gradient algorithm. However, the biconjugate gradient method is more computationally intensive compared to its simpler cousin, conjugate gradients. A problem arises however if we attempt to solve an equation discretized with standard Galerkin elements via the conjugate gradient algorithm. Basically, solutions resulting from such a scheme exhibit a noticeable amount of non-physical diffusion and spatial oscillations. To eliminate such numerical artifacts, some workers [e.g. *Hughes and Brooks*, 1982] developed the streamline upwind/Petrov-Galerkin (SUPG) method for dealing with the advection terms. The basic idea of the SUPG method is that the standard Galerkin shape functions are modified by adding a streamline upwind perturbation to the weighting functions which acts only in the flow direction. While this method ameliorates the above numerical artifacts, it does not free

us from the constraint of using the biconjugate gradient algorithm to solve the resulting system. What we would like is a method that allows us to use the self-adjoint Galerkin shape functions (and thus a simpler solution algorithm) while incorporating the desirable qualities of the SUPG method. Such an algorithm exists and is referred to as the Taylor-Galerkin method. The Taylor-Galerkin method [Zienkiewicz *et al.*, 1984] essentially consists of approximating the temperature at the next time step via Taylor expansions of the associated variables, viz

$$T(\xi, t^n) = T(x, t^n) - \Delta t (\bar{V} - \tilde{V}) \frac{\partial T^n}{\partial x} + \frac{\Delta t^2}{2} (\bar{V} - \tilde{V}) \frac{\partial^2 T^n}{\partial x^2} - \dots \quad (\text{A43})$$

where \hat{V} is the velocity of the mesh and \bar{V} is the average velocity of a particle in the element. Similar expansions can be written for the remaining variables in our energy equation, resulting in the following one-dimensional example (neglecting terms of higher order)

$$\begin{aligned} T^{n+1} - T^n = & -\Delta t (\bar{V} - \tilde{V}) \frac{\partial T^n}{\partial x} + \frac{\Delta t^2}{2} (\bar{V} - \tilde{V}) \frac{\partial^2 T^n}{\partial x^2} \\ & + \Delta t \cdot \left\{ \theta \left[\frac{\partial}{\partial x} k \frac{\partial T^{n+1}}{\partial x} + Q^{n+1} \right] + (1-\theta) \left[\frac{\partial}{\partial x} k \frac{\partial T^n}{\partial x} \right. \right. \\ & \left. \left. + Q^n - \Delta t (\bar{V} - \tilde{V}) \frac{\partial Q^n}{\partial x} + \frac{\Delta t^2}{2} (\bar{V} - \tilde{V}) \frac{\partial^2 Q^n}{\partial x^2} \right] \right\} \end{aligned} \quad (\text{A44})$$

where Q is a volumetric source function. According to Zienkiewicz *et al.* [1984] this is still the representation of a self-adjoint problem and can be discretized using the standard Galerkin shape functions yielding

$$[M + \theta \Delta t K] T^{n+1} = [M - \Delta t \{V + \bar{K} + (1-\theta)K\}] T^n + f^\theta \quad (\text{A45})$$

where

$$M = \int_{\Omega_e} N^T N d\Omega \quad (\text{A46})$$

$$K = \int_{\Omega_e} \frac{\partial N^T}{\partial x} k \frac{\partial N}{\partial x} d\Omega \quad (\text{A47})$$

$$\mathbf{V} = \int_{\Omega_e} N^T (\bar{V} - \tilde{V}) \frac{\partial N}{\partial x} d\Omega \quad (\text{A48})$$

and

$$\bar{\mathbf{K}} = \frac{\Delta t}{2} \int_{\Omega_e} (\bar{V} - \tilde{V}) \frac{\partial N^T}{\partial x} \frac{\partial N}{\partial x} d\Omega \quad (\text{A49})$$

Lastly, f^θ is a term containing the appropriate boundary conditions and Q values. We note that M is the ‘standard’ mass matrix, K is the ‘standard’ diffusivity matrix, V is a non-symmetric Galerkin convective matrix, and \bar{K} is a new matrix incorporating the effects of upwind diffusion (cf. SUPG method). Note that the velocity terms in equation (A48-A49) are the average velocities evaluated at the center of an element. If we discretize our energy equation (A42) via this technique and non-dimensionalize using the methods describe in the body of the thesis, we obtain the following discrete equation

$$\begin{aligned} [PeM + \theta \Delta t K] T^{n+1} &= [PeM - \Delta t \{ PeV + \bar{K} + (1-\theta)K \}] T^n \\ - \Delta t \frac{\rho_f \Delta S_m}{\rho_m C_p} [PeM \{ \theta T^{n+1} + (1-\theta)T^n \} + (1-\theta) \Delta t \{ PeV + \bar{K} \} T^n] \end{aligned} \quad (\text{A50})$$

In our use of equation (A50) we assume that $\theta = 1$ (implicit time-stepping) and $\tilde{V} = 0$.

Our final problem is in selecting an appropriate time step Δt . Here, I use the method recommended by *Zienkiewicz et al.* [1984] for the case where $\theta = 0$ (explicit time-stepping). For every element, I calculate the average velocity, U_{avg} in a four-node element and the minimum element dimension $dl = \min(dx, dz)$. The element Peclet number is then given by $Pe_h = Pe \cdot dl \cdot U_{avg}$. For optimal results, *Zienkiewicz et al.* [1984] calculate an ‘upwinding number’ $C_0 = 1/\tanh(Pe_h/2) - 2/Pe_h$. The time step is then given by

$$\Delta t = \min \left(\frac{dl \cdot C_0}{U_{avg}} \right) \quad (\text{A51})$$

To solve our discrete equation (A50) we use the approximate inverse technique of *Donea et al.* [1984] which is known to work well with the Taylor-Galerkin method. Consider the system $Ax = b$. Let us write the following identity for A

$$A = D + (A - D) \quad (\text{A52})$$

where D is the diagonal and positive matrix of A . Since D is diagonal and has positive entries, it is possible to write

$$A = D^{1/2}(I + X)D^{1/2} \quad (A53)$$

where

$$X = D^{-1/2}(A - D)D^{-1/2} \quad (A54)$$

Under the assumption that $\|X\| \leq 1$, the inverse of A can be expressed by the following series

$$A^{-1} = L^{-1/2}(I - X + X^2 - X^3 + \dots)L^{-1/2} \quad (A55)$$

In practice, successive approximations to A^{-1} can be generated iteratively using the following multipass algorithm. Consider the sequence of approximate solutions x^g , $g = 0, 1, \dots, G$, defined as follows: start from a guess to x^0 , then for $g = 0, 1, \dots, G-1$, determine x^{g+1} from x^g by the following linear system

$$Dx^{g+1} = b - (A - L)x^g \quad (A56)$$

Finally, assume that $x = x^G$. In this thesis, we assume that $G = 5$.

Discrete Form of the Melt Production Rate

The amount of melting that must occur at each time-step can be calculated using the melting equation for a spinel lherzolite given by *Kinzler and Grove* [1991]

$$1155 + 16p - 50Fe\# - 129NaK\# - T = 0 \quad (A57)$$

where p is the pressure in kilobars and T is the mantle temperature in degrees Centigrade. The two compositional parameters, $Fe\#$ and $NaK\#$, are non-dimensional parameters describing the compositional state of the melt. These two parameters are non-linear functions of the melt fraction [*Kinzler and Grove*, 1991]. Since the functional dependence is non-linear, the melt fraction must be solved for iteratively. I iterate for the melt fraction using a simple bisection algorithm [*Press et al.*, 1986]. The bisection

technique requires that upper and lower search bounds be specified. The lower bound for the melting problem is no melting whatsoever, or $\varphi = 0$. The upper bound is determined from the simple thermodynamic statement

$$\rho_m C_p \delta T = \varphi \rho_f L \quad (\text{A58})$$

where C_p is the specific heat capacity of the mantle, ρ_f is the melt density, L is the latent heat of melting, and δT is the difference between the mantle temperature and the solidus temperature at the current time. If $\delta T > 0$, then melting occurs and the amount (melt fraction) is given by equation (A57). Iteration for the melt fraction continues until the difference between successive guesses is less than or equal to 10^{-4} .

Discrete Form of the Permeability-Melt Viscosity Ratio Equation

The non-dimensional equation for the permeability-melt viscosity ratio k_μ is

$$f_1 \frac{\partial k_\mu}{\partial x} + f_2 \frac{\partial k_\mu}{\partial z} + f_3 k_\mu = R_m \Gamma \quad (\text{A59a})$$

where the coefficients f_1, f_2 and f_3 are as follows

$$f_1 = A_{xx} \left(-\frac{\partial p}{\partial x} \right) + A_{xz} \left(-\frac{\partial p}{\partial z} + R_m \delta \rho \right) \quad (\text{A59b})$$

$$f_2 = A_{xz} \left(-\frac{\partial p}{\partial x} \right) + A_{zz} \left(-\frac{\partial p}{\partial z} + R_m \delta \rho \right) \quad (\text{A59c})$$

$$f_3 = -A_{xx} \frac{\partial^2 p}{\partial x^2} + A_{xz} \left(-2 \frac{\partial^2 p}{\partial x \partial z} \right) - A_{zz} \frac{\partial^2 p}{\partial z^2} - \left(\frac{\partial A_{xx}}{\partial x} + \frac{\partial A_{xz}}{\partial z} \right) \frac{\partial p}{\partial x} + \left(\frac{\partial A_{xz}}{\partial x} + \frac{\partial A_{zz}}{\partial z} \right) \left(-\frac{\partial p}{\partial z} + R_m \delta \rho \right) \quad (\text{A59d})$$

The implementation of this equation via finite elements presents its own particular difficulties as it essentially describes the pure advection of a scalar variable. Our desire is that k_μ be a spatially smooth variable albeit it may exhibit rapid changes near its source region. When dealing with equations possessing a relatively large advection term, it is common to discretize the equation using SUPG methods [e.g. *Hughes and Brooks, 1982*]. However, in the presence of strong boundary layers or discontinuities, both Petrov-

Galerkin and anisotropic diffusivity methods exhibit unacceptable oscillatory behavior in the calculated variable. The obvious solution is to refine the grid in the regions we expect boundary layers or discontinuities. This approach is undesirable because grid refinement only increases computation time and, even for fine grids, oscillations in the solution will persist. What we need is an algorithm that incorporates the basic features of SUPG methods (i.e. upwinding) yet is specifically tailored to exhibit no oscillatory errors.

One might imagine that higher order elements or techniques would yield the desired result. Yet both these paths lead to additional computational complexity. In this thesis, we use the method of *Schnipke* [1986] who developed an extremely simple but effective non-oscillatory upwinding technique using four-node elements. In the remainder of this section, we will describe how *Schnipke* [1986] deals with the advection terms in equation (A59a), then we will describe how we discretize the remaining mass and advection terms. All integrals in this section are calculated using the 2x2-point Gaussian quadrature rule.

Following the notation and discussion in *Schnipke* [1986], pure advection of a scalar variable ϕ may be written

$$u \frac{\partial \phi}{\partial x} + v \frac{\partial \phi}{\partial y} = 0 \quad (\text{A60})$$

where u and v are the horizontal and vertical velocity components. For the permeability-melt viscosity equation, the velocity components $(u,v) = (f_1, f_2)$. To calculate f_1 and f_2 , first derivatives of the mantle pressure and finite strain are required as well as second derivatives of the mantle pressure. The first derivatives of the mantle pressure and finite strain are calculated at the center of each element [Barlow, 1976]. The gradients are then weighted and assigned to each node in the element using the smoothing scheme described by *Hughes* [1987]. Once the pressure gradients are interpolated onto the finite element grid, these values are then used to calculate the second derivatives of pressure by the method just described.

If we align our coordinate system with the velocity field (see Figure A8) equation (A60) becomes

$$u_s \frac{\partial \phi}{\partial s} = 0 \quad (\text{A61})$$

Within an element, we now need to determine which nodes are “downwind”. A “downwind” node is one for which the velocity vector at that node points away from the

interior of the element under consideration [Figure A9, *Schnipke* Figure 3-3]. From Figure A10 (*Schnipke* Figure 3-5) a downwind node is one for which

$$\tan \theta^- \leq \tan \theta \leq \tan \theta^+ \quad (\text{A62})$$

This may be rewritten as

$$\begin{aligned} -v_j \Delta x^- + -u_j \Delta y^- &\geq 0 \\ -v_j \Delta x^+ + -u_j \Delta y^+ &\geq 0 \end{aligned} \quad (\text{A63})$$

Both of these conditions must be satisfied at a downwind node.

Once the downwind node is identified, the streamline through that node must be traced back through the element to find the point (x', y') where the streamline intersects the side of the element (Figure A10). At this point, *Schnipke* [1986] assumes that the upwind point (x', y') must intersect one of the opposite sides of the element. In the case of Figure A10, the point lies either on side 2 or side 3. As we shall see, this leads to the result that downwind nodes in an element contribute only that element when we form the advection contribution to the stiffness matrix. For flow that is parallel to the grid, however, this condition is violated and nodes may be “downwind” in two elements. This leads to the problem that such nodes are overweighted in the stiffness matrix and may lead to spurious results. Later in this section, we describe a simple and effective method of overcoming this problem. Now, the location of the upstream point is determined using the factors F_p and F_n shown in Figure A10. The F_p factor is used if the upstream point lies on side 2 and F_n is used if the point lies on side 3. Note that the difficulty mentioned above does not affect the choice of either factor. The selection of F_p or F_n is implicit in the following calculation based on mass flux through the sides of the element

$$\begin{aligned} F_p &= \max \left\{ \min \left\{ \frac{F_2}{F_1}, 1 \right\}, 0 \right\} \\ F_n &= \max \left\{ \min \left\{ \frac{F_4}{F_3}, 1 \right\}, 0 \right\} \end{aligned} \quad (\text{A64})$$

where

$$F_1 = - \int_{x_1}^{x_2} \rho v \, dx + \int_{y_1}^{y_2} \rho u \, dy \quad (\text{A65})$$

$$F_2 = - \left\{ - \int_{x_{I2}}^{x_{I3}} \rho v \, dx + \int_{y_{I2}}^{y_{I3}} \rho u \, dy \right\} \quad (A66)$$

$$F_3 = - \left\{ - \int_{x_{I3}}^{x_{I4}} \rho v \, dx + \int_{y_{I3}}^{y_{I4}} \rho u \, dy \right\} \quad (A67)$$

$$F_4 = - \int_{x_{I4}}^{x_{I1}} \rho v \, dx + \int_{y_{I4}}^{y_{I1}} \rho u \, dy \quad (A68)$$

In calculating these factors, we assume that ρ is constant.

The upstream point is calculated as

$$x' = (1-F_p)x_{I2} + (1-F_n)x_{I4} + F_p F_n x_{I3} \quad (A69)$$

$$y' = (1-F_p)y_{I2} + (1-F_n)y_{I4} + F_p F_n y_{I3} \quad (A70)$$

Similarly, φ' is determined by

$$\varphi' = (1-F_p)\varphi_{I2} + (1-F_n)\varphi_{I4} + F_p F_n \varphi_{I3} \quad (A71)$$

With these definitions, the advective term (equation A61) can be evaluated for the element in Figure A10 as

$$u_s \frac{\partial \varphi}{\partial s} = \frac{u_s}{\Delta s} [\varphi_{I1} - \{(1-F_p)\varphi_{I2} + (1-F_n)\varphi_{I4} + F_p F_n \varphi_{I3}\}] \quad (A72)$$

where

$$u_s = (u_{I1}^2 + v_{I1}^2)^{1/2} \quad (A73)$$

$$\Delta s = [(y_{I1} - y')^2 + (x_{I1} - x')^2]^{1/2} \quad (A74)$$

The advection coefficient matrix A for this element is shown in Table A4 where A_f represents the effective area of the downwind node. In our case, we are using a rectangular four-node elements on a rectangular grid. Hence, the effective area of a node is the total area of the elements around a node divided by four.

One contribution to the source terms is from the melt production rate. Since we are essentially dealing with an advection problem, we choose to discretize this term using the SUPG weighting functions of *Hughes and Brooks* [1982]. Therefore, our source term S may be written

$$S = R_m \int_{\Omega_e} \tilde{w} \Gamma d\Omega \quad (A75)$$

where the SUPG shape function \tilde{w} is given by

$$\tilde{w} = N_A + \tilde{k} \frac{\mathbf{V} \cdot \nabla N}{\|\mathbf{V}\|^2} \quad (A76)$$

The variable \tilde{k} in equation (A76) is an artificial diffusivity term whose value depends upon the local grid size and local velocity

$$\tilde{k} = \frac{(\tilde{\xi} V_\xi h_\xi + \tilde{\eta} V_\eta h_\eta)}{\sqrt{15}} \quad (A77)$$

where ξ and η refer to the local coordinates of our parent domain. For our problem, the velocity terms are merely the mantle velocities $\mathbf{V} = (U, V)$ and the terms h_ξ and h_η are Δx and Δy for the element, respectively. The remaining two factors in equation (A77) are given as follows

$$\begin{aligned} \tilde{\xi} &= \coth(\alpha_\xi) - 1/\alpha_\xi, & \tilde{\eta} &= \coth(\alpha_\eta) - 1/\alpha_\eta \\ \alpha_\xi &= Pe \frac{U \Delta x}{2}, & \alpha_\eta &= Pe \frac{V \Delta y}{2} \end{aligned} \quad (A78)$$

The final contribution enters in on the left hand side our discrete equation as a mass term. The result is a mass matrix of the form

$$M = \int_{\Omega} \tilde{w}^T N d\Omega \quad (A79)$$

Combining the mass matrix, the advection matrix and the source term results in the following system of equations

$$[M + A]k_{\mu} = S \quad (A80)$$

which is solved using the Taylor-Galerkin algorithm that is used above to solve the time-dependent temperature equation.

Discrete Form of the Advection Equation for Mineralogy and Oxide Composition

Each oxide and mineral in the mantle must satisfy the following time-dependent advection equation

$$\frac{\partial f}{\partial t} + V \cdot \nabla f = 0 \quad (A81)$$

where f is an oxide or mineral component and V is the mantle velocity. A good way to discretize this equation would be with the same advection algorithm devised by *Schnipke* [1986] and used above to solve for the permeability -melt viscosity ratio. The presence of the stagnation point at the ridge axis presents a special numerical problem that results in numerical instabilities unless *ad hoc* methods are adopted at that point. Furthermore, the need to solve equation (A81) for each of the thirteen oxide and mineral components consumes a great deal of computer time. In a simple experiment, we tried simple bilinear interpolation. Consider a particular component f_i at a particular node at a position x . At any time step, the new value of that component at every node can be calculated by determining the value of that component at a position $x - V \cdot \Delta t$. At this point, the new value is determined using bilinear interpolation. Surprisingly, this method compares well with the *Schnipke* [1986] algorithm on the meshes we use and has the further advantage of being much faster.

Discrete Form of the Finite Strain Equation

The finite strain tensor \mathbf{E} satisfies the following time-dependent advection equation

$$\frac{\partial \mathbf{E}}{\partial t} + \mathbf{V} \cdot \nabla \mathbf{E} = \mathbf{L} \mathbf{E} \quad (\text{A82})$$

where \mathbf{V} is the mantle velocity and $L_{ij} = \partial V_i / \partial x_j$. Again, the almost pure advection nature of this equation presents some special numerical difficulties. Given the success of simple interpolation when applied to composition, this method is used here to solve for the finite strain tensor. As with the permeability tensor equation, the first derivatives of the mantle velocity are calculated at the center of each element [Barlow, 1976]. The pressure gradients are then weighted and assigned to each node in the element using the smoothing scheme described by Hughes [1987].

The permeability tensor requires that the mantle strain be symmetric. In general, however, \mathbf{E} is unsymmetric. A symmetric version of the strain tensor is calculated in the following way. At every node, one can obtain the principal axes of deformation from the components of the strain tensor. The ratio of the major axis a to the minor axis b is

$$\frac{a}{b} = \gamma + \sqrt{\gamma^2 - 1} \quad (\text{A83})$$

where

$$\gamma = \frac{(E_{xx}^2 + E_{zz}^2 + E_{zx}^2 + E_{zz}^2)}{2} \quad (\text{A84})$$

A diagonal matrix Λ is then constructed containing the major and minor axes along the diagonal. This matrix is, essentially, the eigenvalue matrix of \mathbf{E} . This matrix is squared and then rotated back into the original cartesian frame of reference

$$\mathbf{A} = \mathbf{R} \Lambda \mathbf{R}^T \quad (\text{A85})$$

where the matrix \mathbf{R} is a two-dimensional rotation matrix with the entries

$$\mathbf{R} = \begin{bmatrix} \cos\theta & -\sin\theta \\ \sin\theta & \cos\theta \end{bmatrix} \quad (\text{A86})$$

The correct rotation angle θ is found by a simple numerical search.

Discrete Form of the Melt Flux Equation

Melt velocities are calculated using D'Arcy's Law for the percolation of an interstitial fluid through a porous medium. The non-dimensional form of this equation developed in the body of the thesis is

$$\mathbf{q} = -\mathbf{K} \left(\frac{\nabla p}{R_m} - \delta \rho \hat{\mathbf{z}} \right) \quad (\text{A87})$$

where \mathbf{q} is the melt velocity, p is the deviatoric mantle pressure, $\delta\rho$ is the density difference between the mantle and the melt, and \mathbf{K} is the permeability-melt viscosity ratio tensor. The melt velocity \mathbf{q} is trivial to calculate because the mantle pressure p and the permeability tensor \mathbf{K} are known at each node. The density difference is simply a constant thus all that remains is to calculate the directional derivatives of the pressure. As with the permeability tensor equation, the first derivatives of the mantle pressure are calculated at the center of each element [Barlow, 1976]. The pressure gradients are then weighted and assigned to each node in the element using the smoothing scheme described by Hughes [1987].

FIGURE CAPTIONS

Fig. A1 A finite element grid with 9 nodes (black circles). Global node numbers for each node are given by boldface numbers. Nodes within each element (local node ordering) are ordered as shown by the smaller, italic numbers.

Fig. A2 (a) A four node, bilinear element. (b) A nine node, biquadratic element. (c) A diagram showing the transformation between the natural coordinates of the element (right hand side) and the natural coordinates of the parent quadrilateral element (left hand side) (Figure from *Hughes* [1987]).

Fig. A3 A diagram showing the form of a bilinear shape function for a node a (Figure from *Hughes* [1987]).

Fig. A4 A diagram showing the form of various shape functions within a nine node biquadratic element (Figure from *Hughes* [1987]).

Fig. A5 A flow chart showing the sequence of steps for constructing higher-order elements from a parental, four node element (Figure from *Hughes* [1987]).

Fig. A6 Diagrams showing the location of quadrature points within an element that has been transformed into its parental coordinates. Quadrature points are shown as small crosses within each element. (a) 1 point integration, (b) 2×2 point integration, (c) 3×3 point integration.

Fig. A7 (a) Figure showing the location of the nine velocity nodes (black circles) and four pressure nodes (open squares) in the Q_2-P_1 element. (b) Figure showing the location of the nine velocity nodes (black circles) and three pressure nodes (open squares) in the modified velocity-pressure element used in this thesis. All three pressure nodes are located at the element's center of mass. (c) Figure illustrating the idea of hierarchical elements. The black circles show the location of velocity nodes the edge of an element. The nodes at the end of the element have values a and b , respectively. The node located between these two end nodes has a value δc . The nodes at the ends of the element are interpolated throughout the rest of the element using bilinear shape functions. Summing the contributions of these two nodes along the edge of the element yields the straight dashed line. If the value at the center node is interpolated along the edge using bilinear shape

functions and then added to the linear variation, then the result is the solid, curved line between the edge nodes.

Fig. A8 The streamline coordinate system. Figure from *Schnipke* [1986]. See text.

Fig. A9 The definition of the downwind node. Figure from *Schnipke* [1986]. See text.

Fig. A10 Downwind node identification. Figure from *Schnipke* [1986]. See text.

TABLE A2

Gaussian Quadrature Rules

One-Point Rule

| l | $\tilde{\xi}_l$ | $\tilde{\eta}_l$ | W_l |
|-----|-----------------|------------------|-------|
| 1 | 0 | 0 | 4 |

2x2 Point Rule

| l | $\tilde{\xi}_l$ | $\tilde{\eta}_l$ | W_l |
|-----|-----------------|------------------|-------|
| 1 | $-1/\sqrt{3}$ | $-1/\sqrt{3}$ | 1 |
| 2 | $1/\sqrt{3}$ | $-1/\sqrt{3}$ | 1 |
| 3 | $1/\sqrt{3}$ | $1/\sqrt{3}$ | 1 |
| 4 | $-1/\sqrt{3}$ | $1/\sqrt{3}$ | 1 |

3x3 Point Rule

| l | $\tilde{\xi}_l$ | $\tilde{\eta}_l$ | W_l |
|-----|-----------------|------------------|-------|
| 1 | $-\sqrt{3/5}$ | $-\sqrt{3/5}$ | 25/81 |
| 2 | $\sqrt{3/5}$ | $-\sqrt{3/5}$ | 25/81 |
| 3 | $\sqrt{3/5}$ | $\sqrt{3/5}$ | 25/81 |
| 4 | $-\sqrt{3/5}$ | $\sqrt{3/5}$ | 25/81 |
| 5 | 0 | $-\sqrt{3/5}$ | 40/81 |
| 6 | $\sqrt{3/5}$ | 0 | 40/81 |
| 7 | 0 | $\sqrt{3/5}$ | 40/81 |
| 8 | $-\sqrt{3/5}$ | 0 | 40/81 |
| 9 | 0 | 0 | 72/81 |

TABLE A4
Streamline Upwind Advection Matrix

| | | | |
|--|--|---------------------------------|--|
| 0 | 0 | 0 | 0 |
| 0 | 0 | 0 | 0 |
| $-F_p F_n \frac{\rho u_s}{\Delta s} A_f$ | $-(1-F_n) \frac{\rho u_s}{\Delta s} A_f$ | $\frac{\rho u_s}{\Delta s} A_f$ | $-(1-F_p) \frac{\rho u_s}{\Delta s} A_f$ |
| 0 | 0 | 0 | 0 |

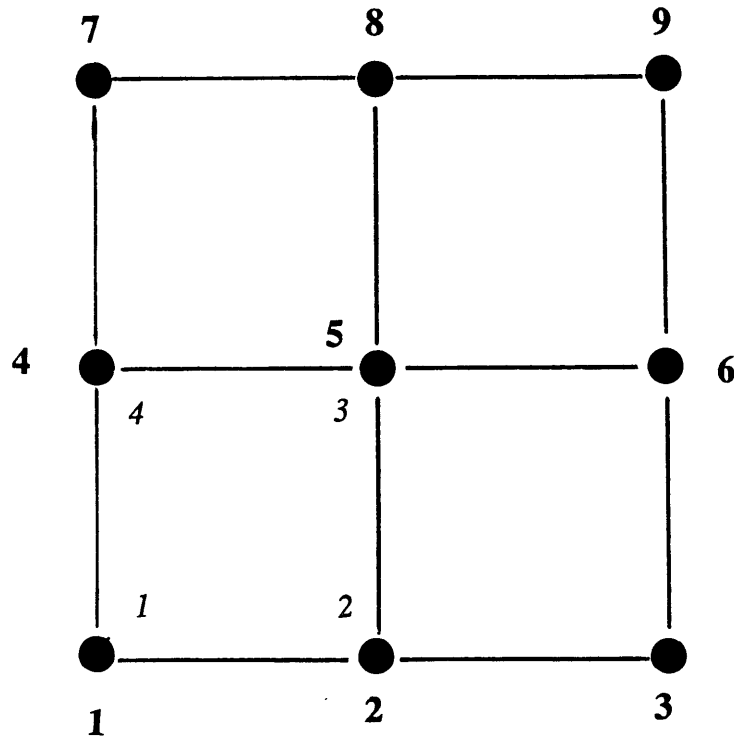


Figure A1

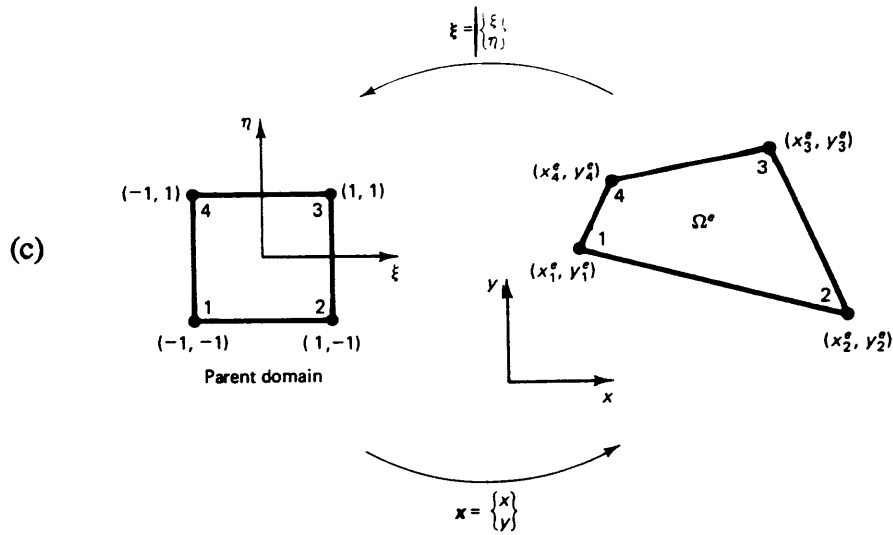
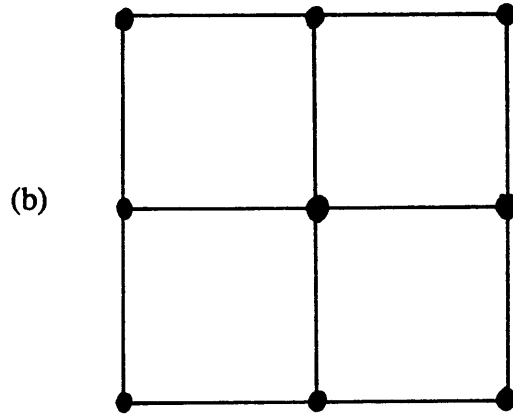
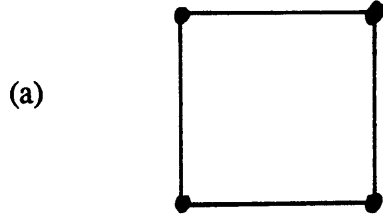


Figure A2

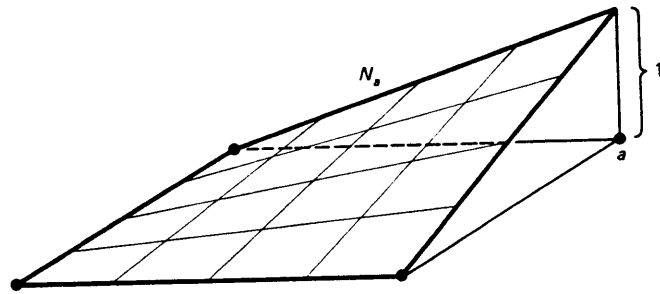


Figure A3

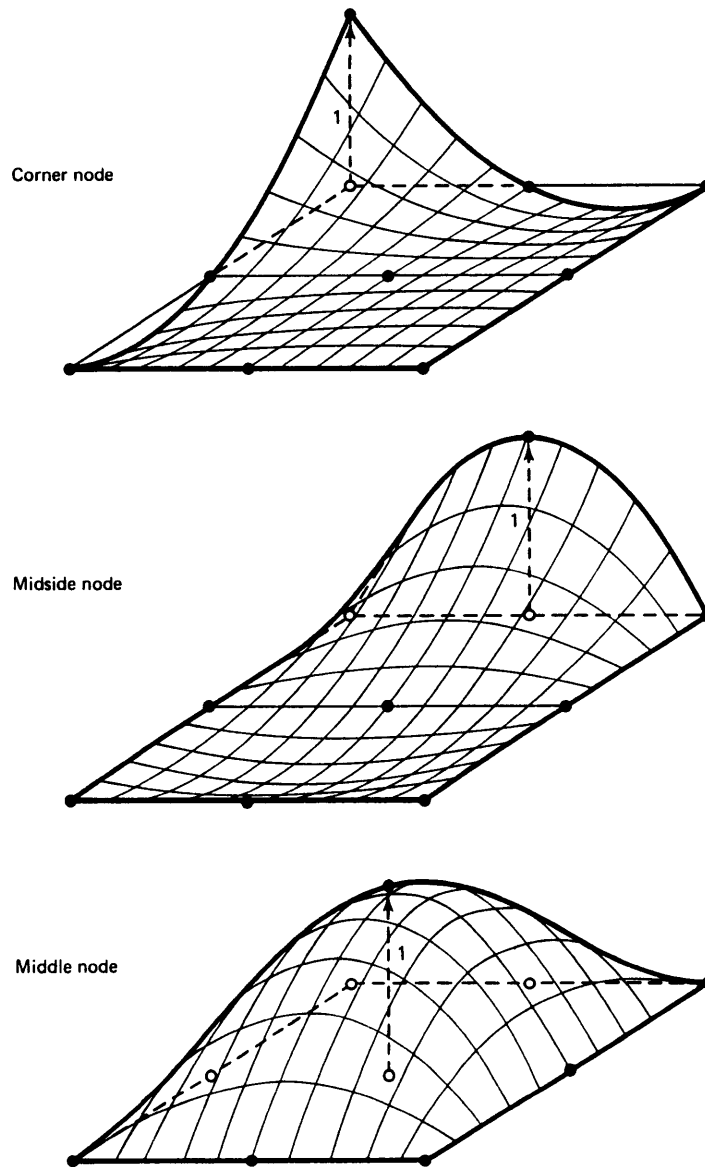


Figure A4

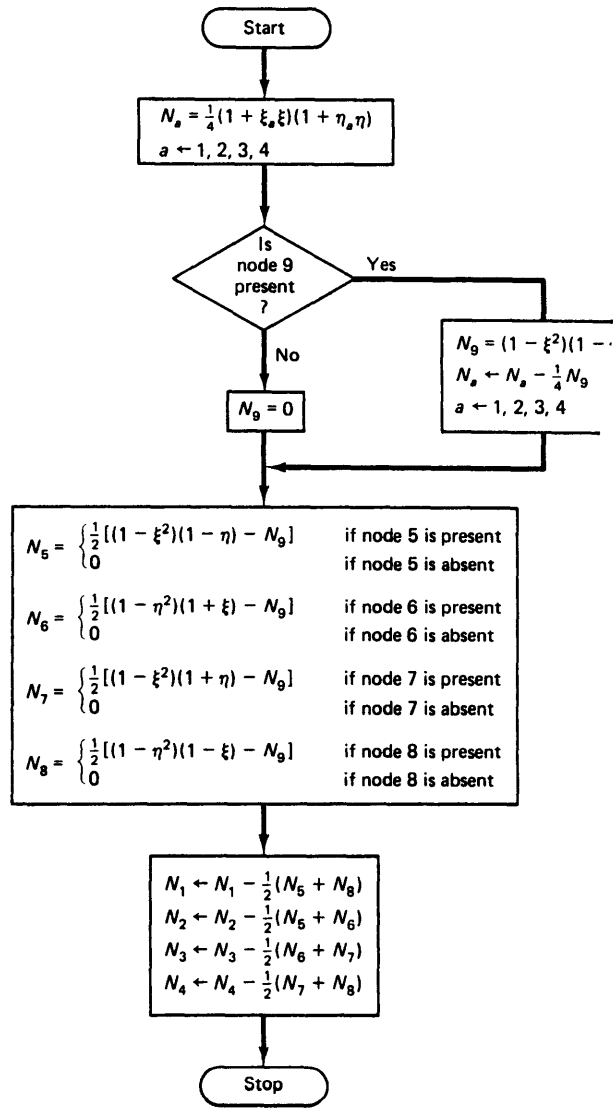


Figure A5

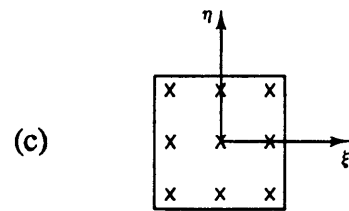
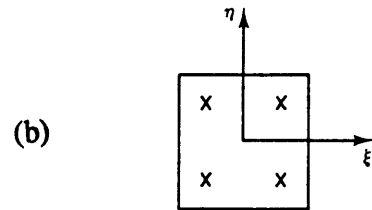
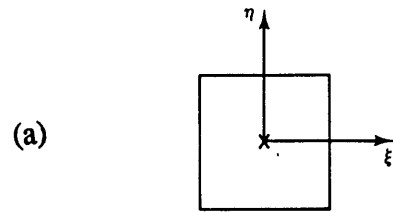


Figure A6

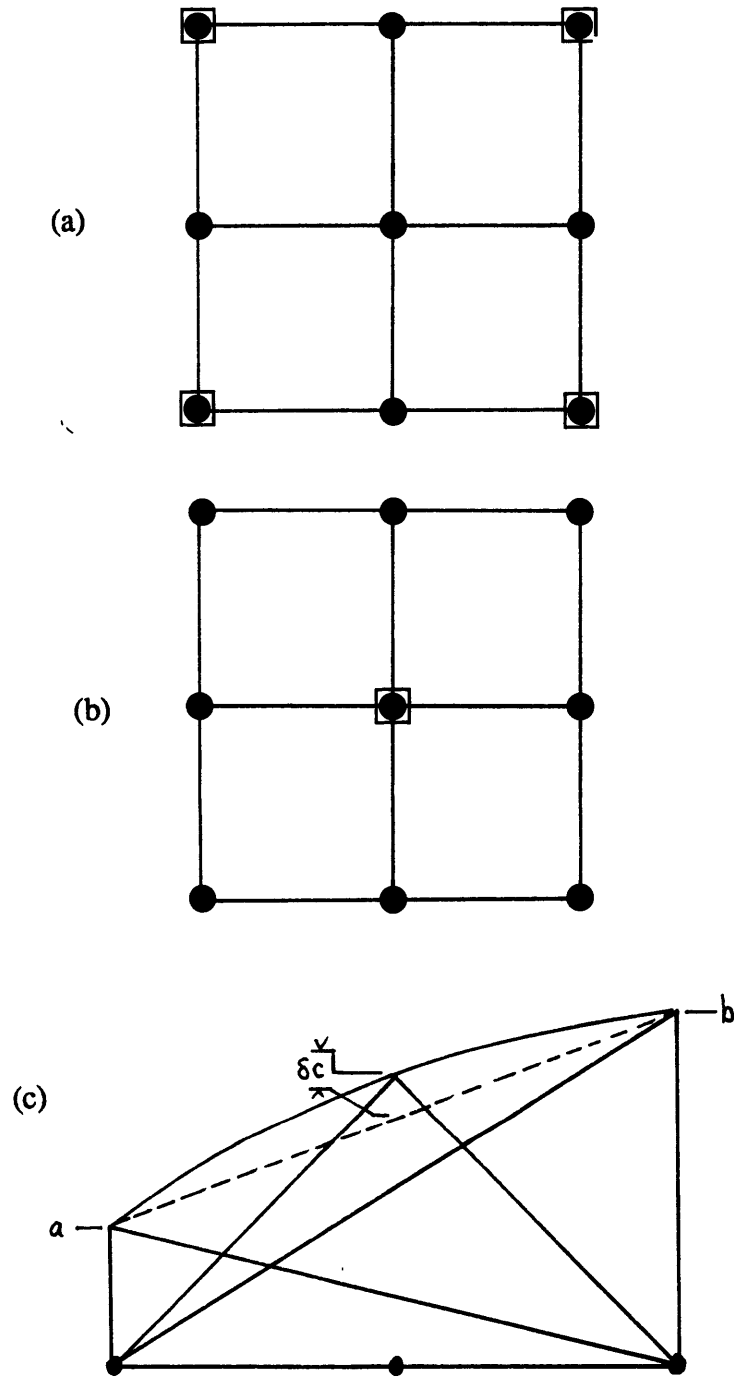


Figure A7

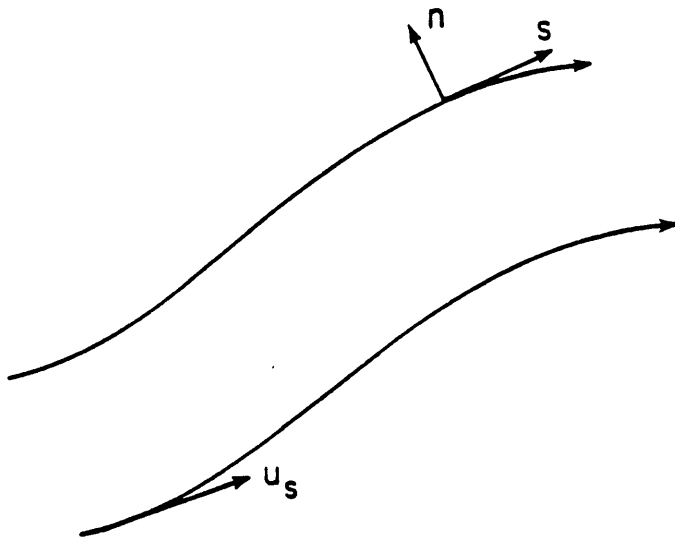


Figure A8

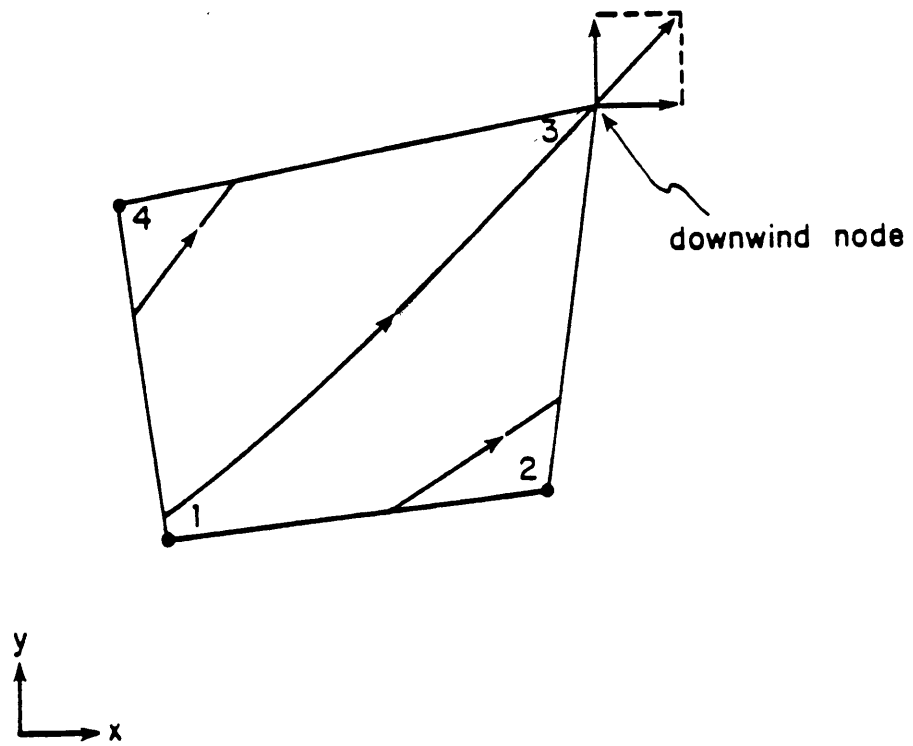


Figure A9

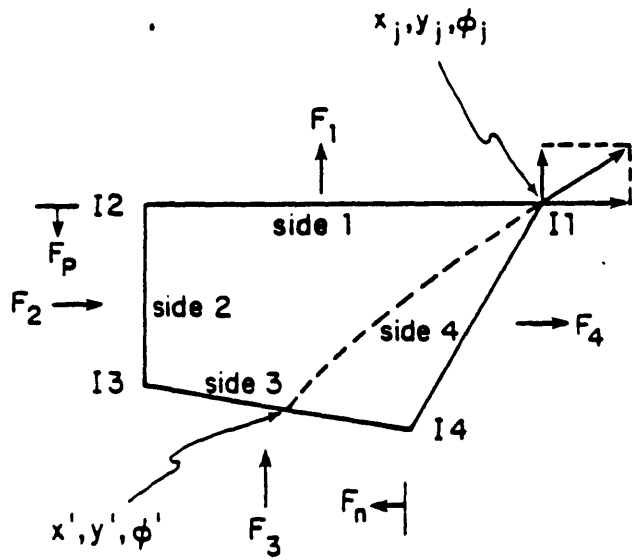
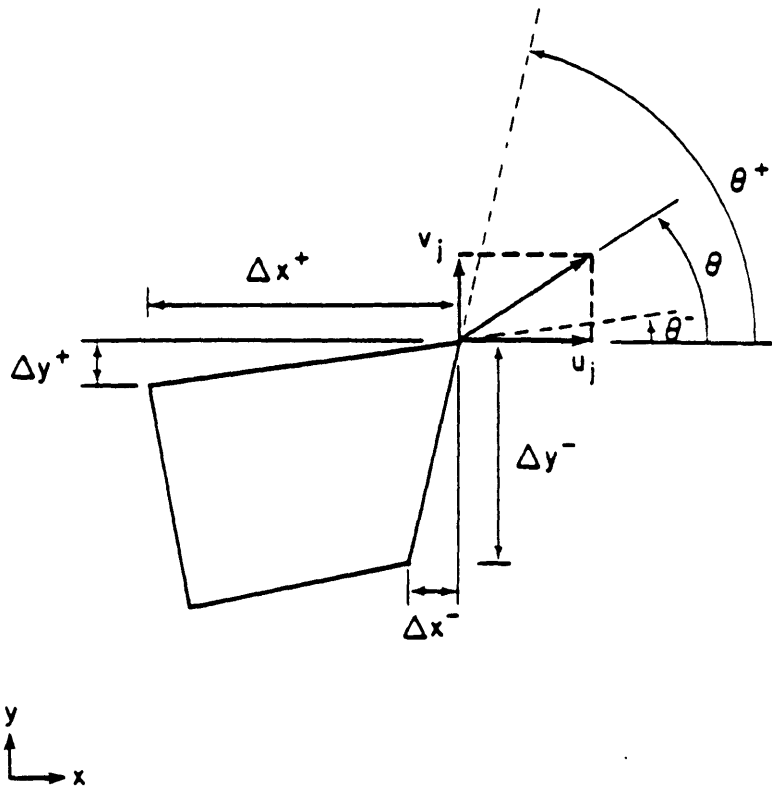


Figure A10

*It happens like this: a kind of languor;
A ceaseless striking of a clock is heard;
Far off, a dying peal of thunder.
I somehow sense the groaning and the sorrows
Of unrecognized, imprisoned voices,
A kind of secret circle narrows;
But in the abyss of whispers and ringing
Rises one triumphant sound.
Such an absolute stillness surrounds it
That one can hear the grass growing in the woods,
How misfortune with a knapsack plods the earth...
But now words are beginning to be heard
And the signalling chimes of light rhymes—
Then I begin to comprehend,
And the simply dictated lines
Lie down in place on the snow-white page.*

Bibliography

All instruction given or received by way of argument proceeds from preexistent knowledge.

Aristotle
Analytica Posteriora

- Ahearn, J. L. and D. L. Turcotte, Magma migration beneath an ocean ridge, *Earth Planet. Sci. Lett.*, 45, 115–122, 1979.
- Ashby, M. F. and R. A. Verrall, Micromechanisms of flow and fracture, and their relevance to the rheology of the upper mantle, *Phil. Trans. R. Soc. Lond. A.*, 288, 59–95, 1977.
- Barlow, J., Optimal stress locations in finite element models, *Int. J. num. Meth. Engrg.*, 10, 243–251, 1976.
- Batchelor, G. K., An introduction to fluid dynamics, Cambridge University Press, Cambridge, Britain, pp. 615, 1967.
- Bear, J., *Dynamics of Fluids in Porous Media*, American Elsevier Publishing Co., New York, NY, 1972.
- Blackman, D. K., and D. W. Forsyth, Isostatic compensation of tectonic features of the Mid–Atlantic Ridge: 25–27° 30′ S., *J. Geophys. Res.*, *in press*.
- Boyd, F. R. and R. H. McCallister, Densities of fertile and sterile garnet peridotites, *Geophys. Res. Lett.*, 3, 509–512, 1976.
- Brooks, A. N. and T. J. R. Hughes, Streamline upwind/Petrov–Galerkin formulations for convection dominated flows with particular emphasis on the incompressible Navier–Stokes equations, *Comput. Meths. Appl. Mech. Engrg.*, 32, 199–259, 1982.
- Bryan, W. B. and H. J. B. Dick, Contrasted abyssal basalt liquidus trends: evidence for mantle major element heterogeneity, *Earth Planet. Sci. Lett.*, 58, 15–26, 1982.
- Buck, W. R. and E. M. Parmentier, Convection beneath young oceanic lithosphere: Implications for thermal structure and gravity, *J. Geophys. Res.*, 91, 1961–1974, 1986.
- Buck, W. R. and W. Su, Focussed mantle upwelling below mid–ocean ridges due to feedback between viscosity and melting, submitted to *Geophys. Res. Lett.*, 1988.
- Bulau, J. R., H. S. Waff and J. A. Tyburczy, Mechanical and thermodynamic constraints on the fluid distribution in partial melts, *J. Geophys. Res.*, 84, 6102–6108, 1979.
- Carey, G. F., E. Barragy, R. McLay and M. Sharma, Element–by–element vector and parallel computations, *Comm. Appl. num. Meths.*, 4, 299–307, 1988.

- Ceuleneer, G., M. Rabinowicz, M. Monnereau, A. Cazenave and C. Rosemberg, Viscosity and thickness of the sub-lithospheric low-viscosity zone: constraints from geoid and depth over oceanic swells, *Earth Planet. Sci. Lett.*, *89*, 84–102, 1988.
- Chen, Y., and D. Sandwell, Oceanic crustal thickness versus spreading rate, *Eos, Transactions of the American Geophysical Union* (abstract), *71*, 1573, 1990.
- Christensen, N. I., The magnitude, symmetry, and origin of upper mantle anisotropy based on fabric analysis of ultramafic tectonites, *Geophys. J. Roy. astr. Soc.*, *76*, 89–111, 1984.
- Christensen, U. R., Some geodynamical effects of anisotropic viscosity, *Geophys. J. R astr. Soc.*, *91*, 711–736, 1987.
- Cooper, R. F. and D. L. Kohlstedt, Solution-precipitation enhanced diffusional creep of partially molten olivine-basalt aggregates during hot-pressing, *Tectonophysics*, *107*, 207–233, 1984.
- Cooper, R. F. and D. L. Kohlstedt, Rheology and structure of olivine-basalt partial melts, *J. Geophys. Res.*, *91*, 9315–9323, 1986.
- Cormier, M.-H., R. S. Detrick and G. M. Purdy, Anomalously thin crust in oceanic fracture zones: New seismic constraints from the Kane fracture zone, *J. Geophys. Res.*, *89*, 10,249–10,266, 1984.
- Craig, C. H. and D. McKenzie, The existence of a thin low-viscosity layer beneath the lithosphere, *Earth Planet. Sci. Lett.*, *78*, 420–426, 1986.
- Daines, M. J. and F. M. Richter, An experimental method for directly determining the interconnectivity of melt in a partially molten system, *Geophys. Res. Lett.*, *15*, 1459–1462, 1988.
- Detrick, R. S. and G. M. Purdy, The crustal structure of the Kane fracture zone from seismic refraction studies, *J. Geophys. Res.*, *85*, 3759–3777, 1980.
- Detrick, R. S., P. Buhl, E. Vera, J. Mutter, J. Orcutt, J. Madsen and T. Brocher, Multi-channel seismic imaging of a crustal magma chamber along the East Pacific Rise, *Nature*, *326*, 35–41, 1987.
- Dick, H. J. B., Abyssal peridotites, very slow spreading ridges and ocean ridge magmatism, in *Magmatism in the Ocean Basins*, eds. A. D. Saunders and M. J. Norry, Geological Society Special Publication No. 42, pp. 71–105, 1989.
- Dick, H. J. B. and J. M. Sinton, Compositional layering in alpine peridotites evidence for pressure solution creep in the mantle, *J. Geology*, *87*, 403–416, 1979.
- Dick, H. J. B. and R. L. Fisher, Mineralogic studies of the residues of mantle melting: Abyssal and alpine-type peridotites, in *Kimberlites. II: The Mantle and Crust-*

- Mantle Relationships*, ed. J. Kornprobst, Elsevier Science Publishers B. V., Amsterdam, pp. 295–308, 1984.
- Dick, H. J. B., R. L. Fisher and W. B. Bryan, Mineralogic variability of the uppermost mantle along mid-ocean ridges, *Earth Planet. Sci. Lett.*, *69*, 88–106, 1984.
- Donea, J., S. Giuliani, H. Laval and L. Quartapelle, Time-accurate solution of advection-diffusion problems by finite elements, *Comput. Meths. Appl. Mech. Engrg.*, *45*, 123–145, 1984.
- Elthon, D., Pressure of origin of primary mid-ocean ridge basalts, In *Magmatism in the Ocean Basins*, eds.: Saunders, A. D., and Norry, M. J., Geol. Soc. Spec. Publ. No. 42, pp. 125–136, 1989.
- Frank, F. C., Two-component flow model for convection in the Earth's upper mantle, *Nature*, *220*, 350–352, 1968.
- Fujii, T. and I. Kushiro, Density, viscosity, and compressibility of basaltic liquid at high pressures, *Carnegie Inst. of Wash. Yearbook*, *76*, 419–424, 1977.
- Goetze, C., The mechanisms of creep in olivine, *Phil. Trans. R. Soc. Lond. A.*, *288*, 99–119, 1978.
- Hageman, L. A., and D. M. Young, *Applied Iterative Methods*, Academic Press, New York, 386 p., 1981.
- Hughes, T. J. R., *The Finite Element Method*, Prentice Hall, Inc., 803 p., 1987.
- Hughes, T. J. R., and A. Brooks, A theoretical framework for Petrov-Galerkin methods with discontinuous weighting functions: Application to the streamline-upwind procedure, *Finite Elements in Fluids*, *4*, ed. R. H. Gallagher, D. H. Norrie, J. T. Oden, and O. C. Zienkiewicz, John Wiley and Sons, Ltd., 47–65, 1982.
- Johnson, K. T. M., H. J. B. Dick and N. Shimizu, Melting in the oceanic upper mantle: An ion microprobe study of diopsides in abyssal peridotites, *J. Geophys. Res.*, *95*, 2661–2678, 1990.
- Jordan, T. H., Mineralogies, densities, and seismic velocities of garnet lherzolites and their geophysical implications, in *Proceedings of the Second International Kimberlite Conference*, vol. 2, eds. F. R. Boyd and H. O. A. Meyer, American Geophysical Union, Washington, D. C., 1979.
- Jurewicz, S. R. and A. J. G. Jurewicz, Distribution of apparent angles on random sections with emphasis on dihedral angle measurements, *J. Geophys. Res.*, *91*, 9277–9282, 1986.
- Karato, S., Does partial melting reduce the creep strength of the upper mantle?, *Nature*, *319*, 309–310, 1986.

- Kinzler, R. J. and T. L. Grove, Primary magmas of mid-ocean ridge basalts, submitted to *J. Geophys. Res.*.
- Klein, E. M. and C. H. Langmuir, Global correlations of ocean ridge basalt chemistry with axial depth and crustal thickness, *J. Geophys. Res.*, *92*, 8089–8115, 1987.
- Klein, E. M. and C. H. Langmuir, Local versus global variations in ocean ridge basalt composition: A reply, *J. Geophys. Res.*, *94*, 4241–4252, 1989.
- Kuo, B.-Y., and D. W. Forsyth, Gravity anomalies of the ridge-transform system in the South Atlantic between 31 and 34.5 °S: Upwelling centers and variations in crustal thickness, *Mar. Geophys. Res.*, *10*, 205–232, 1988.
- Kushiro, I., Viscosity of partial melts in the upper mantle, *J. Geophys. Res.*, *91*, 9343–9350, 1986.
- Langmuir, C. H., and G. N. Hanson, An evolution of major element heterogeneity in the mantle sources of basalts, *Phil. Trans. R. Soc. Lond. A*, *297*, 383–407, 1980.
- Lin, J. and E. M. Parmentier, Mechanisms of lithospheric extension at mid-ocean ridges, *Geophys. J.*, *96*, 1–22, 1989.
- Lin, J., G. M. Purdy, H. Schouten, J.-C. Sempere and C. Zervas, Evidence from gravity data for focused magmatic accretion along the Mid-Atlantic Ridge, *Nature*, *344*, 627–632, 1990.
- Maaløe, S. and Å. Scheie, The permeability controlled accumulation of primary magma, *Contrib. Mineral. Petrol.*, *81*, 350–357, 1982.
- Macdonald, K. C., Mid-ocean ridges: fine scale tectonic, volcanic, and hydrothermal processes within the plate boundary zone, *Ann. Rev. Earth. Planet. Sci. Lett.*, *10*, 155–190, 1982.
- Maday, Y. and A. T. Patera, Spectral element methods for the incompressible Navier-Stokes equations, *State of the art surveys on computational mechanics*, ed. A. K. Noor and J. T. Oden, Amer. Soc. of Mech. Eng., United Engineering Center, New York, New York, pp. 71–144., 1989.
- Mavko, G. and A. Nur, Melt squirt in the asthenosphere, *J. Geophys. Res.*, *80*, 1444–1448, 1975.
- McClain, J. S. and C. Atallah, Thickening of the oceanic crust with age, *Geology*, *14*, 574–576, 1986.
- McNutt, M. K. and A. V. Judge, The Superswell and mantle dynamics beneath the South Pacific, *Science*, *248*, 969–975, 1990.
- McKenzie, D., Finite deformation during fluid flow, *Geophys. J. Roy. astr. Soc.*, *58*, 689–715, 1979.

- McKenzie, D., The generation and compaction of partially molten rock, *J. Petrology*, 25, 713–765, 1984.
- McKenzie, D., ^{230}Th – ^{238}U disequilibrium and the melting processes beneath ridge axes, *Earth Planet. Sci. Lett.*, 72, 149–157, 1985.
- McKenzie, D. and M. J. Bickle, The volume and composition of melt generated by extension of the lithosphere, *J. Petrology*, 29, 625–679, 1988.
- Michael, P. J. and E. Bonatti, Peridotite compositions from the North Atlantic: regional and tectonic variations and implications for partial melting, *Earth Planet. Sci. Lett.*, 73, 91–104, 1985.
- Mutter, J. C. and R. S. Detrick, and the NAT Study Group, Multichannel seismic evidence for anomalously thin crust at Blake Spur fracture zone, *Geology*, 12, 534–537, 1984.
- Nakada, M. and K. Lambeck, Late Pleistocene and Holocene sea-level change in the Australian region and mantle rheology, *Geophys. J.*, 96, 496–517, 1989.
- Nakano, T. and N. Fujii, The multiphase grain control percolation: Its implications for a partially molten rock, *J. Geophys. Res.*, 94, 15,653–15,661, 1989.
- Nicolas, A., A melt extraction model based on structural studies in mantle peridotites, *J. Petrology*, 27, 999–1022, 1986a.
- Nicolas, A., Structure and petrology of peridotites: Clues to their geodynamic environment, *Rev. Geophys.*, 24, 875–895, 1986b.
- Nicolas, A., *Structures of Ophiolites and Dynamics of Oceanic Lithosphere*, Kluwer Academic Publishers, 367 pp., 1989.
- Nicolas, A. and M. Jackson, High-temperature dikes in peridotites: origin by hydraulic fracturing, *Tectonophysics*, 23, 568–582, 1982.
- Nishimura, C. E., and D. W. Forsyth, The anisotropic structure of the upper mantle in the Pacific, *Geophys. J.*, 96, 203–229, 1989.
- O'Hara, Is there an Icelandic mantle plume?, *Nature*, 253, 708–710, 1975.
- Oxburgh, E. R. and E. M. Parmentier, Compositional and density stratification in oceanic lithosphere—causes and consequences, *J. geol. Soc. Lond.*, 133, 343–355, 1977.
- Parmentier, E. M. and J. Phipps Morgan, Spreading rate dependence of three-dimensional structure in oceanic spreading centres, *Nature*, 348, 325–328, 1991.
- Parsons, B. and J. G. Sclater, An analysis of the variation of ocean floor bathymetry and heat flow with age, *J. Geophys. Res.*, 82, 803–827, 1977.
- Phipps Morgan, J., Melt migration beneath mid-ocean spreading centers, *Geophys. Res. Lett.*, 14, 1238–1241, 1987.

- Phipps Morgan, J. and D. W. Forsyth, Three-dimensional flow and temperature perturbations due to a transform offset: Effects on oceanic crustal and upper mantle structure, *J. Geophys. Res.*, *93*, 2955–2966, 1988.
- Phipps Morgan, J., E. M. Parmentier, and J. Lin, Mechanisms for the origin of mid-ocean ridge axial topography: Implications for the thermal and mechanical structure at accreting plate boundaries, *J. Geophys. Res.*, *92*, 12,823–12,836, 1987.
- Press, W. H., B. P. Flannery, S. A. Teukolsky, W. T. Vetterling, *Numerical Recipes: The Art of Scientific Computing*, Cambridge University Press, 818 pp., 1986.
- Rabinowicz, M., G. Ceuleneer and A. Nicolas, Melt segregation and flow in mantle diapirs below spreading centers: Evidence from the Oman ophiolite, *J. Geophys. Res.*, *92*, 3475–3486, 1987.
- Reid, I. and H. R. Jackson, Oceanic spreading rate and crustal thickness, *Mar. Geophys. Res.*, *5*, 165–172, 1981.
- Ribe, N. M., The deformation and compaction of partial molten zones, *Geophys. J. R. astr. Soc.*, *83*, 487–501, 1985a.
- Ribe, N. M., The generation and composition of partial melts in the earth's mantle, *Earth Planet. Sci. Lett.*, *73*, 361–376, 1985b.
- Ribe, N. M., A continuum theory for lattice preferred orientation, *Geophys. J.*, *97*, 199–207, 1989a.
- Ribe, N. M., Seismic anisotropy and mantle flow, *J. Geophys. Res.*, *94*, 4213–4223, 1989b.
- Richter, F. M. and S. F. Daly, Dynamical and chemical effects of melting a heterogeneous source, *J. Geophys. Res.*, *94*, 12,499–12,510, 1989.
- Richter, F. M. and D. McKenzie, Dynamical models for melt segregation from a deformable matrix, *J. Geology*, *92*, 729–740, 1984.
- Rigden, S. M., T. J. Ahrens and E. M. Stolper, Densities of liquid silicates at high pressures, *Science*, *226*, 1071–1074, 1984.
- Riley Jr., G. N., D. L. Kohlstedt and F. M. Richter, Melt migration in a liquid–olivine system: an experimental test of compaction theory, *Geophys. Res. Lett.*, *17*, 2101–2104, 1990.
- Robinson, E. M., B. Parsons and S. F. Daly, The effect of a shallow low viscosity zone and the apparent compensation of mid-plate swells, *Earth Planet Sci. Lett.*, *82*, 335–348, 1987.
- Salters, V. J. M. and S. R. Hart, The hafnium paradox and the role of garnet in the source of mid-ocean-ridge basalts, *Nature*, *342*, 420–422, 1989.

- Schnipke, R. J., A streamline upwind finite element method for laminar and turbulent flow, Ph.D dissertation, University of Virginia, 1986.
- Scott, D. R., The competition between percolation and circulation in a deformable porous medium, *J. Geophys. Res.*, *93*, 6451–6462, 1988.
- Scott, D. R. and D. J. Stevenson, Magma solitons, *Geophys. Res. Lett.*, *11*, 1161–1164, 1984.
- Scott, D. R. and D. J. Stevenson, Magma ascent by porous flow, *J. Geophys. Res.*, *91*, 9283–9296, 1986.
- Scott, D. R. and D. J. Stevenson, A self-consistent model of melting, magma migration and buoyancy driven circulation beneath mid-ocean ridges, *J. Geophys. Res.*, *94*, 2973–2988, 1989.
- Sheehan, A. F. and S. C. Solomon, Joint inversion of shear wave travel time residuals, geoid, and depth anomalies along the mid-Atlantic ridge: Implications for upper mantle temperature and composition variations, unpublished manuscript, 1991.
- Sleep, N. H., Segregation of magma from a mostly crystalline mush, *Geol. Soc. Amer. Bull.*, *85*, 1225–1232, 1974.
- Sleep, N. H., Tapping of magmas from ubiquitous mantle heterogeneities: An alternative to mantle plumes, *J. Geophys. Res.*, *89*, 10,029–10,041, 1984.
- Sotin, C. and E. M. Parmentier, Dynamical consequences of compositional and thermal density stratification beneath spreading centers, *Geophys. Res. Lett.*, *16*, 835–838, 1989.
- Sparks, D. W., and E. M. Parmentier, 3-D flow beneath spreading centers due to compositional and thermal buoyancy, *Eos, Transactions of the American Geophysical Union*, *71*, 1637, 1990.
- Sparks, D. W., and E. M. Parmentier, Melt extraction from the mantle beneath spreading centers, *Earth Planet. Sci. Lett.*, *in press*, 1991.
- Spiegelman, M. and D. McKenzie, Simple 2-D models for melt extraction at mid-ocean ridges and island arcs, *Earth Planet. Sci. Lett.*, *83*, 137–152, 1987.
- Stevenson, D. J., Spontaneous small-scale melt segregation in partial melts undergoing deformation, *Geophys. Res. Lett.*, *16*, 1067–1070, 1989.
- Stevenson, D. J. and D. R. Scott, Stress-induced anisotropic permeability in partially molten media, submitted to *J. Geophys. Res.*, 1987.
- elford, W. M., L. P. Geldart, R. E. Sheriff, and D. A. Keys, *Applied Geophysics*, Cambridge Univeristy Press, 860 p., 1976.
- Thayer, T. P., Flow-layering in alpine peridotite-gabbro complexes, Mineralogical Society of America, Special Paper 1, *Inter. Miner. Ass. Papers*, 55-61, 1963.

- Toomey, D. R., S. C. Solomon, and G. M. Purdy, Microearthquakes beneath the median valley of the Mid-Atlantic Ridge near 23°N: Tomography and Tectonics, *J. Geophys. Res.*, *93*, 9093–9112, 1988.
- Toramaru, A. and N. Fujii, Connectivity of melt phase in a partially molten peridotite, *J. Geophys. Res.*, *91*, 9239–9252, 1986.
- Turcotte, D. L., Magma migration, *Ann. Rev. Earth Planet. Sci. Lett.*, *10*, 397–408, 1982.
- Turcotte, D. L. and J. L. Ahearn, A porous flow model for magma migration in the asthenosphere, *J. Geophys. Res.*, *83*, 767–772, 1978.
- Vaughan, P. J. and D. L. Kohlstedt, Distribution of the glass phase in hot-pressed, olivine-basalt aggregates: An electron microscopy study, *Contrib. Mineral. Petrol.*, *81*, 253–261, 1982.
- von Bargen, N. and H. S. Waff, Permeabilities, interfacial areas and curvatures of partially molten systems: Results of numerical computations of equilibrium microstructures, *J. Geophys. Res.*, *89*, 9261–9276, 1986.
- Waff, H. S. and J. R. Bulau, Equilibrium fluid distribution in an ultramafic partial melt under hydrostatic stress conditions, *J. Geophys. Res.*, *84*, 6109–6114, 1979.
- Waff, H. S. and U. H. Faul, Coexisting faceted and curved interfaces in partially molten olivine-basalt systems and implications for mantle partial melts, manuscript submitted for publication, 1991.
- Weertman, J., Creep laws for the mantle of the Earth, *Phil. Trans. R. Soc. Lond. A.*, *288*, 9–26, 1978.
- Whitehead Jr., J. A., H. J. B. Dick and H. Schouten, A mechanism for magmatic accretion under spreading centres, *Nature*, *312*, 146–148, 1984.
- Zienkiewicz, O. C., R. Loehner, K. Morgan, and S. Nakazawa, Finite elements in fluid mechanics – a decade of progress, *Finite Elements in Fluids*, eds. R.H. Gallagher, J.T. Oden, O.C. Zienkiewicz, T. Kawai, and M. Kawahara, John Wiley and Sons Limited, vol 5., pp. 1 – 28, 1984.

*Up! up! my Friend and quit your books;
Or surely you'll grow double:
Up! up! my Friend, and clear your looks;
Why all this toil and trouble?*

*The sun, above the mountains head,
A freshening lustre mellow
Through all the long green fields has spread,
His first sweet evening yellow.*

*Books! 'tis a dull and endless strife:
Come, hear the woodland linnet,
How sweet his music! on my life,
There's more of wisdom in it.*

*And hark! how blithe the throstle sings!
He, too, is no mean preacher:
Come forth into the light of things,
Let Nature be your Teacher.*

*She has a world of ready wealth,
Our minds and hearts to bless—
Spontaneous wisdom breathed by health,
Truth breathed by cheerfulness.*

*One impulse from a vernal wood
May teach you more of man,
Of moral evil and of good,
Than all the sages can.*

*Sweet is the lore which Nature brings;
Our meddling intellect
Mis-shapes the beauteous forms of things:—
We murder to dissect.*

*Enough of Science and of Art;
Close up those barren leaves;
Come forth, and bring with you a heart
That watches and receives.*